

Crack path selection and shear toughening effects due to mixed mode loading and varied surface properties in beam-like adhesively bonded joints

Youliang (Leonardo) Guan

Dissertation submitted to the faculty of the Virginia Polytechnic Institute and State University in partial fulfillment of the requirements for the degree of

Doctor of Philosophy

In

Engineering Mechanics

David A. Dillard – Chairman

Romesh C. Batra

John G. Dillard

John J. Lesko

Robert L. West

December 9, 2013

Blacksburg, VA, 24061

Keywords: Strain energy release rate, double cantilever beam (DCB), fracture energy, adhesively bonded joints, crack path selection, mode mixity angle, shear toughening effect, cohesive zone model, fracture mechanics, locally weakened interface, crack steering, maximum traction, damage evolution, softening law, cohesive element, extended finite element method (XFEM), epoxy adhesive, dual actuator load frame, silane treatment

Copyright 2013, Youliang Guan

# Crack path selection and shear toughening effects due to mixed mode loading and varied surface properties in beam-like adhesively bonded joints

Youliang Guan

## Abstract

Structural adhesives are widely used with great success, and yet occasional failures can occur, often resulting from improper bonding procedures or joint design, overload or other detrimental service situations, or in response to a variety of environmental challenges. In these situations, cracks can start within the adhesive layer or debonds can initiate near an interface. The paths taken by propagating cracks can affect the resistance to failure and the subsequent service lives of the bonded structures. The behavior of propagating cracks in adhesive joints remains of interest, including when some critical environments, complicated loading modes, or uncertainties in material/interfacial properties are involved. From a mechanics perspective, areas of current interest include understanding the growth of damage and cracks, loading rate dependency of crack propagation, and the effect of mixed mode fracture loading scenarios on crack path selection. This dissertation involves analytical, numerical, and experimental evaluations of crack propagation in several adhesive joint configurations. The main objective is an investigation of crack path selection in adhesively bonded joints, focusing on in-plane fracture behavior (mode I, mode II, and their combination) of bonded joints with uniform bonding, and those with locally weakened interfaces.

When removing cured components from molds, interfacial debonds can sometimes initiate and propagate along both mold surfaces, resulting in the molded product partially bridging between the two molds and potentially being damaged or torn. Debonds from both adherends can sometimes occur in weak adhesive bonds as well, potentially altering the apparent fracture behavior. To avoid or control these multiple interfacial debonding, more understanding of these processes is required. An analytical model of 2D parallel bridging was developed and the interactions of interfacial debonds were investigated using Euler-Bernoulli beam theory. The numerical solutions to the analytical results described the propagation processes with multiple debonds, and demonstrated some common phenomena in several different joints corresponding to double cantilever beam configurations. The analytical approach and results obtained could prove useful in extensions to understanding and controlling debonding in such situations and optimization of loading scenarios.

Numerical capabilities for predicting crack propagation, confirmed by experimental results, were initially evaluated for crack behavior in monolithic materials, which is also of interest in engineering design. Several test cases were devised for modified forms of monolithic compact tension specimens (CT) were developed. An asymmetric variant of the CT configuration, in which the initial crack was shifted to two thirds of the total height, was tested experimentally and numerically simulated in ABAQUS®, with good agreement. Similar studies of elongated CT specimens with different specimen lengths also revealed good agreement, using the same material properties and cohesive zone model (CZM) parameters. The critical specimen length when the crack propagation pattern abruptly switches was experimentally measured and accurately predicted,

building confidence in the subsequent studies where the numerical method was applied to bonded joints.

In adhesively bonded joints, crack propagation and joint failure can potentially result from or involve interactions of a growing crack with a partially weakened interface, so numerical simulations were initiated to investigate such scenarios using ABAQUS®. Two different cohesive zone models (CZMs) are applied in these simulations: cohesive elements for strong and weak interfaces, and the extended finite element method (XFEM) for cracks propagating within the adhesive layer. When the main crack approaches a locally weakened interface, interfacial damage can occur, allowing for additional interfacial compliance and inducing shear stresses within the adhesive layer that direct the growing crack toward the weak interface. The maximum traction of the interfacial CZM appears to be the controlling parameter. Fracture energy of the weakened interface is shown to be of secondary importance, though can affect the results when particularly small (e.g. 1% that of the bulk adhesive). The length of the weakened interface also has some influence on the crack path. Under globally mixed mode loadings, the competition between the loading and the weakened interface affects the shear stress distribution and thus changes the crack path. Mixed mode loading in the opposite direction of the weakened interface is able to drive the crack away from the weakened interface, suggesting potential means to avoid failure within these regions or to design joints that fail in a particular manner.

In addition to the analytical and numerical studies of crack path selection in adhesively bonded joints, experimental investigations are also performed. A dual actuator load frame (DALF) is used to test beam-like bonded joints in various mode mixity angles. Constant mode mixity angle tracking, as well as other versatile loading functions, are developed in LabVIEW® for use with a new controller system. The DALF is calibrated to minimize errors when calculating the compliance of beam-like bonded joints. After the corrections, the resulting fracture energies ( $G_c$ ) values are considered to be more accurate in representing the energy released in the crack propagation processes. Double cantilever beam (DCB) bonded joints consisting of 6061-T6 aluminum adherends bonded with commercial epoxy adhesives (J-B Weld, or LORD 320/322) are tested on the DALF. Profiles of the  $G_c$  values for different constant mode mixity angles, as well as for continuously increasing mode mixity angle, are plotted to illustrate the behavior of the crack in these bonded joints.

Finally, crack path selection in DCB specimens with one of the bonding surfaces weakened was studied experimentally, and rate-dependency of the crack path selection was found. Several contamination schemes are attempted, involving of graphite flakes, silicone tapes, or silane treatments on the aluminum oxide interfaces. In all these cases, tests involving more rapid crack propagation resulted in interfacial failures at the weakened areas, while slower tests showed cohesive failure throughout. One possible explanation of this phenomenon is presented using the rate-dependency of the yield stress (commonly considered to be corresponding to the maximum traction) of the epoxy adhesives. These experimental observations may have some potential applications tailoring adhesive joint configurations and interface variability to achieve or avoid particular failure modes.

# Acknowledgements

My five-year stay at Virginia Tech, as a PhD candidate, was one of my most important life experiences, and may be one of the most pleasant memories for the rest of my life. I believe that, when I am working somewhere around the world, I will always remember the beautiful town of Blacksburg, my professors' words and experiences that I shared with them.

I would like to thank my advisor, Prof. David A. Dillard, who taught me a lot of things during these five years. He taught me not only in the classroom. He was always teaching me, or showing good examples of how to be a careful and professional researcher, how to be a successful and humorous teacher in the classroom, and how to be a warm-hearted and respectable gentleman. He is gifted with a smart brain and always ready to discuss difficult academic problems, as well as interesting issues in the history of English grammar, customs, human behavior, etc. "Big pictures" and brainstorming are the two problem solving tools that he likes most, in my opinion. First, I learned that whenever and whatever we were discussing, the big picture should be emphasized so as to keep us moving in the right direction. Then, we try some brainstorming to produce many potential solutions, without caring, initially, if they are right or wrong. Then, with a lot of options on our hands, we are ready to use our judgment to select a best solution. From Prof. David Dillard, I also learned how to be a good teacher and give vivid and humorous lectures to the students. I remember another thing he told me: if people with basic knowledge cannot understand what you said, it is your problem, not theirs. In summary, everything I learned from him at Virginia Tech will become precious treasures in my life.

I would also like to show my appreciation to Prof. Romesh C. Batra, who gave me many instructions and suggestions on academic issues related to numerical simulation, repeatability, and consistency in research. We had biweekly or weekly meetings with Prof. Batra and other members of our research team during these five years. He offered fewer suggestions and ideas than my advisor, but much more than other professors. For experimental issues, he often asked me to check with my advisor, first. His ideas about verifying numerical models, repeatability of the tests, and his insights in numerical issues, would also help me to improve my professional performance in future.

I am grateful to Prof. John G. Dillard, Prof. Jack J. Lesko, and Prof. Robert L. West, who gave me assistance in my projects, presentations, and ideas. Prof. John Dillard had spent a lot of time in teaching me chemical treatments, as well as other techniques used in chemistry. Prof. Lesko taught my first class on adhesives and adhesion. His suggestions on how to conduct primary aspects of a project and deserve the title of doctor were also helpful. Prof. West was my first teacher on ABAQUS software and gave me useful ideas on engineering design and evaluations. My ideas on numerical experiments on crack path selection, using both XFEM and cohesive elements, were first inspired by his class.

I would like to thank Dr. Donatus C. Ohanehi, who had attended team meetings frequently. He is always warm-hearted and willing to help me with academic problems and English writing. I appreciate his humorous and friendly suggestions and ideas. I would like to thank Prof. Muhammad R. Hajj for the department's generous financial support, Prof. Surot Thangjitham for his course on fracture mechanics and discussions on

the history of ancient China, Prof. Scott Case for his course on composite materials, Prof. Mark A. Stremmer and Prof. Mark S. Cramer for their courses on fluid mechanics and continuum mechanics. They are all friendly and generous teachers in our Department of Engineering Science and Mechanics.

Another important professor that I would like to thank is Prof. Xu Chen in Tianjin University. Prof. Chen generously offered me the chance to contact Prof. David Dillard, and initiated all the things that happened to me at Virginia Tech. Special thanks would also go to the China Scholar Council for their partial financial support in the first 3 years.

I would like to thank Melissa Nipper, Lisa Smith, Linda Taylor, and Anne-Marie Bracken, who helped me to deal with travel, personal financial matters, reserving meeting rooms, etc. I would like to thank Mac McCord III, Daniel Reed, Darrell L. Link, David Simmons, and Paul K. Siburt, for their help with machine shop, pump, instrument, and other issues related to experiments.

I would like to thank my “big brother” in the lab, Dr. Edoardo Nicoli, for the helpful discussions on experiments, and delicious Italian pasta. I would like to thank “Mr. America,” Geoffrey Tizard III, and the straightforward man, Hitendra K. Singh, for fun times in the lab. Though not listed explicitly, other young friends of mine are also important. To everyone who helped me and supported me during my stay in Blacksburg, I would like to say, thank you very much.

I would like to offer special thanks to Virginia Tech, the town of Blacksburg, National Science Foundation, and the United States of America, for the education, support, and nice environment provided to me during these five years. Atmosphere and environment are very important to researchers, just like the air and water: they are very important to researchers though people would usually forget them. The benefits can be described by the Chinese poem “Good rain knows the best season to fall to the ground, it infiltrates into the earth without any sound.” Personally, I think education is just like rain, it would not affect students suddenly and strongly, but would change them gradually but deeply. For example, Prof. David Dillard would not usually tell his students directly what to do, or what not to do. He will encourage us to try some of the ideas, even if these ideas may not result in useful output. By these trials and rethinking, the students can learn more. Therefore, I think that it is these patient and kind professors who have made high education in the US valuable. I hope that they will be happy and proud of me when I am spreading these ideas on education to other countries, or teaching even younger students in the ways similar to theirs.

Last but not least, I am saying thank you to each of my family members. It is their support that encouraged me to go further. Though their voices and videos came from the other side of the earth through the internet, they are the source of my strength when facing to difficulties.

In summary, my time at Virginia Tech will be one of the most important periods in my life. I appreciate all the help from my family, all the professors, all the staff, and all my friends. I wish all of them happiness and good health.

# Contents

Chapter 1 Introduction .....	1
1.1 General background and introduction to the project .....	1
1.2 Fracture mechanics and cohesive zone models in monolithic materials and layered material systems .....	3
1.3 Fracture analysis method in adhesively bonded joints .....	10
1.4 Problem statement and objectives .....	12
1.5 Dissertation outline.....	13
1.6 References .....	15
Chapter 2 Fracture and crack trajectory in monolithic materials.....	20
2.1 Introduction to crack path selection in monolithic material .....	20
2.2 Material and experiments .....	24
2.3 Simulation with XFEM .....	28
2.4 Conclusions .....	34
2.5 References .....	35
Chapter 3 The intrinsic role of strain energy in 2D bridging problem and the subsequent multiple parallel propagating debonds in beam-like joints.....	37
3.1 Introduction .....	37
3.2 Analysis .....	41
3.2.1 2D bridging DCB model .....	41
3.2.2 Strain energy release rate in the bridging model .....	44
3.3 Results and discussions .....	45
3.3.1 Load and response without crack propagation .....	45
3.3.2 Prediction of the crack propagation sequence .....	51
3.3.3 Discussions on other nonlinear effects .....	56
3.4 Conclusions .....	57
3.5 References .....	59
Chapter 4 Development of the improved controller for the dual actuator load frame.....	60
4.1 Realization of the hardware and software of the controller.....	60
4.2 Calibration of the DALF .....	69
4.3 Summary .....	77

4.4 References .....	79
Chapter 5 Experimental investigation of adhesively bonded joint by tests of double cantilever beam specimens with flexible changes of mode mixity angle applied by dual actuator load frame .....	80
5.1 Introduction .....	80
5.2 Test method .....	81
5.3 Materials and joint preparation.....	82
5.4 Analysis methods for determining fracture energy .....	83
5.4.1 Corrected beam theory .....	83
5.4.2 Compliance-based beam method.....	85
5.4.3 Stability of the crack growth in mixed mode tests .....	88
5.5 Experimental results .....	90
5.6 Discussion .....	102
5.6.1 Friction and contact .....	102
5.6.2 Toughening mechanisms and microcracks in adhesive.....	102
5.6.3 Effect of damage zone size in constrained joints .....	104
5.7 Conclusions .....	105
5.8 References .....	107
Chapter 6 A numerical study of crack path selection in mode I and mixed mode loading conditions using cohesive zone models .....	111
6.1 Introduction .....	112
6.2 Background on crack path selection.....	112
6.3 Background on the CZM.....	114
6.4 Modeling .....	117
6.5 Results with mode I loadings .....	122
6.5.1 Crack path selection with long weakened interface .....	125
6.5.2 Crack path selection with short weakened interface.....	129
6.6 Modelling and results with mixed mode loadings.....	138
6.7 Discussion .....	143
6.8 Conclusions .....	145
6.9 References .....	147

Appendix A Rate dependent tests on crack path selection in epoxy adhesive bonded joints with weakened interfaces .....	151
A.1 Experimental works with graphite and silicone tape contaminated interfaces .....	151
A.2 Experimental works with silane weakened interfaces .....	157
A.3 Summary.....	160
Appendix B Calculation of the T-stress using contour integration in ABAQUS .....	162
B.1 Calculation of the T-stress in front of the crack tip in an infinite plate .....	162
B.2 Calculation of the T-stress in front of the crack tip in the asymmetric CT specimens .....	165
B.3 References.....	168
Appendix C The simulation of 2D bridging problem in ABAQUS using cohesive elements .....	169
C.1 Modelling of the 2D bridging problem in ABAQUS® .....	169
C.2 References.....	172

## List of Tables

### Chapter 3

Table 3.1. Three cases studied in the present work.....	46
---	----

### Chapter 5

Table 5.1. Critical crack lengths at different mode mixity angles.....	90
--	----

### Chapter 6

Table 6.1. CZM parameters for the long weakened areas. ....	120
---	-----

Table 6.2. CZM parameters for the short weakened areas. ....	120
--	-----

Table 6.3. Parameters for the two models used for the study of the effect of mixed mode loadings. ....	139
--	-----

Table 6.4. Displacements and mode mixity angle applied to the models. ....	139
--	-----

## List of figures

### Chapter 1

- Figure 1.1. Stresses near the tip of a crack in an elastic material for William's asymptotic stress expansion.....4
- Figure 1.2. Definition of the zones of interest around the crack tip.....6
- Figure 1.3. Cohesive zone model: (a) crack in bulk material with damage zone of length  $L$ ; (b) simplified model with damage zone thickness of  $h$ , crack opening of  $d$ ; (c) cohesive zone model with crack opening of  $w$ .....7
- Figure 1.4. Typical traction-separation law of a CZM.....8
- Figure 1.5. Schematic of the calculation of fracture energy: area of triangle  $ODD'$  divided by  $dA$ , is the fracture energy when  $P$  is constant but deflection changes from  $D$  to  $D'$  (depends on the material properties,  $OD$  and  $OD'$  can be either linear or nonlinear).....9
- Figure 1.6. Test applications of specimens with beam-like configurations (ENF: End notched flexure, ELS: End loaded split, DCB: Double cantilever beam, FRMM: Fixed-ratio mixed-mode).....10

### Chapter 2

- Figure 2.1. The definitions of stresses near the tip of a crack in elastic materials.....21
- Figure 2.2. The phantom nodes created in the ABAQUS when simulating a crack propagation using XFEM.....23
- Figure 2.3. A typical traction-separation law.....23
- Figure 2.4. PMMA CT Specimen with  $w=25.4$ ,  $a=12.7$ , and thickness = 12.7 (all dimensions in mm).....24
- Figure 2.5. PMMA asymmetric CT specimens with  $w=25.4$ ,  $a=12.7$ , and the ratio of the height of the loading beam is 1:2; specimen thickness = 12.7 (all dimensions in mm)....25
- Figure 2.6. One CT specimen with precrack before a test, another one with a straight crack path after a test.....25
- Figure 2.7. Pre-cracking the CT specimen with a blade and two shims.....26
- Figure 2.8. Load vs. extension curves for three CT specimens.....26
- Figure 2.9. An asymmetric CT specimen: (a) with notch and initial crack before the test, (b) with crack after the test, (c) the 2D projection on a scanner.....27

Figure 2.10. The boundary conditions, initial crack, and opening stress ( $\sigma_{yy}$  in MPa) for the asymmetric CT specimen. ....28

Figure 2.11. Crack path of the asymmetric CT specimen in the numerical simulation using XFEM,  $W$  is the length and  $2H$  is the height of the specimens.....30

Figure 2.12. Simulated crack paths show dramatically different when  $W$  is (a): 25.7 mm, (b): 26.2 mm, (c): 26.4 mm.....32

Figure 2.13. Varied crack paths after the tests of the asymmetric CT specimens machined in the same orientation of the PMMA sheet at the same time, with exactly the same dimensions and the critical specimen length (26.4 mm).....33

Figure 2.14. Trajectories of the crack paths in the specimens with different initial crack lengths (From top to bottom:  $a = 12.7\text{mm}$ ,  $25.4\text{mm}$ , and  $38.1\text{mm}$ ).....33

### Chapter 3

Figure 3.1. Bridging problem in a wedge test of hydrogel with stiff substrates (a schematic is also shown so as to clarify the multiple debonds).....38

Figure 3.2. Bridging problem in DCB test with weak surfaces and strong adhesive layer (flexible aluminum adherends were used to obtain large opening in the picture, but the deflection is usually very small in a real DCB test).....38

Figure 3.3. Model of the adhesive bridging problem with geometric parameters and external loads: (a) Schematic of the initial debond and cavitation; (b) 2D view of the model; (c) Appearance of the bridge and definition of three crack lengths; (d) Cantilever beam models, definition of coordinate system and points.....41

Figure 3.4. Crosshead displacement for bridge and no-bridge model with the same external loads, with a set of crack lengths for Case 1 .....47

Figure 3.5. Comparison of loads for both bridging and no-bridge model for Case 1 when the length of crack 3 is changed from 120 mm to 240 mm, the crosshead displacements are set to be 5 mm for both no-bridge and bridging model.....48

Figure 3.6. Comparison of loads for both bridging and no-bridge model for Case 2 when the length of crack 3 is changed from 120 mm to 240 mm, the crosshead displacements are set to be 5 mm for both no-bridge and bridging model.....48

Figure 3.7. SERR curves for the three cracks as functions of the external load for Case 1.....49

Figure 3.8. SERR curves for the three cracks as functions of the external load for Case 2.....49

Figure 3.9. SERR curves for the three cracks as functions of the external load for Case 3.....	50
Figure 3.10. Intersections with different length of crack 3 (lengths of crack 1 and 2 are fixed).....	51
Figure 3.11. Schematic of the competition between $G_2$ and $G_3$ for two cases ( $G_1$ is always lower than the others, thus crack 1 is never predicted to propagate).....	52
Figure 3.12. Crack propagation sequence calculated when the adherends were opened in Case 1 (with initial crack lengths assumed to be 50 mm, 51 mm, and 52mm for crack 1, 2, and 3, respectively).....	52
Figure 3.13. Crosshead displacement vs. load curves for Case 1 in both bridging and no-bridge model (the plots were stopped when crack length reached 250 mm).....	53
Figure 3.14. Crosshead displacement vs. load curves for Case 2 in both bridging and no-bridge model (the plots were stopped when crosshead displacement reached 10 mm).....	54
Figure 3.15. The relationships between the lengths of crack 2 and crack 3 when propagating from several specified initial crack lengths for Case 1.....	55
Figure 3.16. The relationships between the lengths of crack 2 and crack 3 when propagating with several different initial crack lengths for Case 2.....	55

## Chapter 4

Figure 4.1. Dual actuator load frame.....	61
Figure 4.2. Schematic of the two loops of the controller for the DALF.....	62
Figure 4.3. The main GUI window of the DALF controller: (a) Initiate, (b) Method, (c) Test and monitors, (d) Configuration.....	64
Figure 4.4. Part of the diagram for the initiation of the RT controller.....	65
Figure 4.5. The while-loop for the PID control of the DALF.....	66
Figure 4.6. Sine wave displacement function in the DALF controller.....	66
Figure 4.7. Part of the diagram for the controlling of the constant mode mixity angle tracking.....	67
Figure 4.8. Displacement curve (left adherend) and load curve (right adherend) when controlled in constant mode mixity angle function.....	68
Figure 4.9. Safety monitor module in the programming of the DALF controller.....	69

Figure 4.10. One of the load-free calibrations of an LVDT of the DALF.....	70
Figure 4.11. Superposition of the mixed mode test by pure mode I and pure mode II components.....	71
Figure 4.12. Schematic and picture of the machined aluminum DCB specimens for calibration .....	72
Figure 4.13. Compliances for the DCB specimens with different initial crack lengths, as functions of the pure mode I loads increasing but without yielding in the aluminum beams.....	72
Figure 4.14. Components of the total crosshead displacement in mode I tests on the DALF: the left extension, beam deflections, and the right extension.....	73
Figure 4.15. Comparison of the crack lengths read by the naked eye to those calculated by the corrected CBBM for a normal DCB bonded joint, with mode mixity angle from 30 ° to 75° .....	75
Figure 4.16. Schematic and the photo of setup in the calibration of the rotary error of the bottom clamp.....	76
Figure 4.17. Curve fitting of the displacements for calibration of the rotary error of the bottom clamp.....	77

## Chapter 5

Figure 5.1. One loading path sequence imposed by the two cylinders of the DALF when testing a DCB specimen in mixed mode.....	82
Figure 5.2. Definition of positive and negative loads in mode I and mode II tests.....	85
Figure 5.3. The effect of the error in compliance measurement to the calculation of the equivalent crack lengths.....	87
Figure 5.4. SEM pictures of the crack surfaces after the test of one JB Weld adhesive bonded specimen: (a) deformations were essentially pure mode I; (b) the mode mixity angle was around 60 °.....	91
Figure 5.5. Fracture energy values from one test with mode I followed by constant nominal mode mixity angle of 40 °(LORD): (a) CBT, (b) CBBM.....	92
Figure 5.6. Fracture energy values from one test with mode I followed by constant nominal mode mixity angle 60 °(LORD): (a) CBT, (b) CBBM.....	93
Figure 5.7. Fracture energy values from one test with mode I followed by constant nominal mode mixity angle 80 °(LORD): (a) CBT, (b) CBBM.....	94

Figure 5.8. Fracture energy values from one test with mode I followed by constant nominal mode mixity angle 40 °(JB Weld): (a) CBT, (b) CBBM.....	95
Figure 5.9. Fracture energy values from one test with mode I followed by constant nominal mode mixity angle 60 °(JB Weld): (a) CBT, (b) CBBM.....	96
Figure 5.10. Fracture energy values from one test with mode I followed by constant nominal mode mixity angle 80 °(JB Weld): (a) CBT, (b) CBBM.....	97
Figure 5.11. Fracture energy values from one test with increasing mode mixity angle (LORD): (a) CBT, (b) CBBM.....	99
Figure 5.12. Fracture energy values from one test with increasing mode mixity angle (JB Weld): (a) CBT, (b) CBBM.....	100
Figure 5.13. Combined plot of failure envelopes with $(G_c)_I$ vs. $(G_c)_{II}$ for repeated tests: (a) LORD, (b) JB Weld.....	101
Figure 5.14. Main crack and microcracks observed along the correction fluid covered bondline during a 60 °mixed mode test of a DCB specimen prepared with JB Weld adhesive: different “crack tip” criteria would lead to different crack reading at the location of (1) 117mm, (2) 112mm, and (3) 106.5mm.....	103
Figure 5.15. Diagrams to show the damage zone in (a) monolithic material, (b) thin adhesive layer and its evolution, and (c) different R-curves when using different criteria, the numbers are corresponding to the crack reading in Figure 5.14.....	104

## Chapter 6

Figure 6.1. Typical traction-separation law.....	115
Figure 6.2. Phantom nodes created in the ABAQUS when simulating crack propagation using XFEM. ....	116
Figure 6.3. Location of the weak interface in the DCB specimen model with initial crack.....	118
Figure 6.4. Schematic of the CZM traction-separation laws for the adhesive layer, strong interface, and several weakened interfaces.....	120
Figure 6.5. Mesh connectivity of the DCB model at three levels: Zooming in (in the pictures located from the left to the right).....	122
Figure 6.6. Example of a grown crack path with meshes and normalized coordinate system .....	123
Figure 6.7. Comparison of crack path selection with same geometric and material parameter but different mesh size and element type.....	124

Figure 6.8. The crack path with long weakened interface and maximum traction: (a) 5 J/m <sup>2</sup> , (b) 50 J/m <sup>2</sup> , (c) 250 J/m <sup>2</sup> .....	126
Figure 6.9. Crack path with long weakened interface and maximum traction: (a) 2.5 MPa, (b) 5 MPa, (c) 10 MPa.....	127
Figure 6.10. The main crack propagation and damage evolution of a long weakened interface: (a) the main crack senses and veers to the weakened interface, the interface is damaging, (b) large scale of damage is found when the main crack is closer, (c) the main crack veers into and connects with the interface, interfacial crack is developed.....	129
Figure 6.11. Crack paths with 0.25 mm weakened interface and fracture energy of: (a) 5 J/m <sup>2</sup> , (b) 50 J/m <sup>2</sup> , (c) 250 J/m <sup>2</sup> .....	130
Figure 6.12. Crack paths with 0.25 mm weakened interface and the maximum traction of: (a) 0.25 MPa, (b) 2.5 MPa, (c) 5 MPa.....	132
Figure 6.13. Crack paths with 0.125 mm weakened interface and fracture energy of: (a) 5 J/m <sup>2</sup> , (b) 50 J/m <sup>2</sup> , (c) 250 J/m <sup>2</sup> .....	133
Figure 6.14. Crack paths with 0.125 mm weakened interface and the maximum traction of: (a) 0.25 MPa, (b) 2.5 MPa, (c) 5 MPa.....	134
Figure 6.15. Crack paths with 0.0625 mm weakened interface and fracture energy of: (a) 5 J/m <sup>2</sup> , (b) 50 J/m <sup>2</sup> , (c) 250 J/m <sup>2</sup> .....	135
Figure 6.16. Crack paths with 0.0625 mm weakened interface and the maximum traction of: (a) 0.25 MPa, (b) 2.5 MPa, (c) 5 MPa.....	136
Figure 6.17. The main crack propagation and damage evolution of a short weakened interface: (a) the main crack senses and veers to the weakened interface, the interface starts to damage, (b) the main crack veers more closely to the interface, (c) the main crack passes over the short weakened interface and veers back to the center line, the short interface does not totally fail.....	138
Figure 6.18. The crack paths when loaded in different mode mixities but without any weakened interface in the model in ABAQUS.....	140
Figure 6.19. Location of the crack tip when the weakened interface starts to affect the main crack.....	141
Figure 6.20. The different crack paths resulting when mixed mode loads were applied to model 1 that has a 0.25mm weakened interface on the left hand side. The horizontal red line is shown as a reference for comparisons of crack paths.....	141
Figure 6.21. The different crack paths obtained when the 11 loading cases were applied to model 1 that has a 0.25mm weakened interface on one side. The horizontal dash-dot red line is shown as a reference for the comparisons.....	142

Figure 6.22. The different crack paths when mixed mode loads were applied to model 2 that has a 0.125mm weakened interface on the left hand side. The horizontal red line is shown as a reference for the comparisons of crack paths.....143

Figure 6.23. The different crack paths when the 11 cases of mixed mode loads were applied to model 2 that has a 0.125mm weakened interface on one side. The horizontal dash-dot red line is shown as a reference for the comparisons.....143

Figure 6.24. Shear stress distribution in the adhesive layer when the main crack is propagating .....144

## Appendix A

Figure A.1. Crack path selection at different displacement rates in toughened epoxy adhesive bonded DCB joints: (a) constant crosshead loading rate: 0.1 mm/min, (b) constant crack propagation rate.....153

Figure A.2. Rate dependent detection of weakened interfacial areas in bonded joints prepared by JB Weld epoxy adhesive, the crosshead displacement rate is 0.1 mm/min, and the crack propagation rate is decreasing.....154

Figure A.3. Rate dependent detection of weakened interfacial areas in bonded joints prepared by JB Weld epoxy adhesive, the crosshead displacement rate is 0.002 mm/min and no clear detection in this case.....155

Figure A.4. Rate dependent detection of weakened interfacial areas in bonded joints prepared by the JB Weld epoxy adhesive, the crosshead displacement rates are 0.01mm/min, and 100 mm/min, respectively.....156

Figure A.5. Fracture energy curve for one high propagation rate tests of specimens bonded with the JB Weld epoxy.....156

Figure A.6. Rate dependent detection of weakened interfacial areas in bonded joints prepared by the LORD epoxy adhesive, the crosshead displacement rates are 0.01mm/min, and 100 mm/min, respectively.....157

Figure A.7. Relationships between the water drop contact angle and the failure modes: cohesive failure when the contact angle is smaller than 67 °; interfacial failure when the contact angle is larger than 83° .....158

Figure A.8. One fracture energy curve of the DCB specimens prepared by the LORD epoxy tested at: (a) 0.01 mm/min (cohesive failure); (b) 100 mm/min (interfacial failure).....160

Figure A.9. Schematic of the explanation to the rate dependency of the crack path selection using the CZM for adhesive layer, and weakened interface.....160

## Appendix B

Figure B.1. The symmetrically loaded block with a symmetric initial crack in the middle, (a): fixed bottom plane and the 0.01 mm displacement applied to the top plane, (b): zoom-in of the mesh ( $0.1 \times 0.1 \times 3$  mm) near the crack.....163

Figure B.2. The T-stress calculated by contour integration in ABAQUS for the symmetric model shown in Figure B.1.....164

Figure B.3. The T-stress calculated by contour integration in ABAQUS for the symmetric model but with the initial crack moved up to  $2/3$  of the height.....164

Figure B.4. T-stress obtained from ABAQUS during the crack propagations when  $W$  is: (a) 25.7 mm, (b) 26.2 mm, (c) 26.4 mm.....167

## Appendix C

Figure C.1. Geometry, boundary conditions, and mesh connectivity of the 2D bridging model in ABAQUS®.....170

Figure C.2. When the initial  $a_1$  values are assumed, the relationship between the crack lengths  $a_3$  and  $a_2$  is fixed during the propagation process.....171

# Chapter 1 Introduction

---

## 1.1 General background and introduction to the project

The need for lighter-weight, higher performance, and less expensive products has driven significant increases in the use of adhesives for joining components for several decades. Improvements in surface preparation, bonding techniques, adhesive performance, and joint design have been important for enabling advances in this technology. In spite of substantial progress, however, a number of uncertainties remain, especially as related to long term durability, surface roughness or treatments ADDIN EN.CITE [, locus of failure [1-3], and the effect of mixed mode loading[4, 5]. The presence and propagation of cracks in the adhesively bonded joints is of continuing concern, and is the focus of this dissertation.

Fundamental concepts in fracture mechanics have proven to be an essential entry to the understanding of these questions and concerns. Several centuries ago, experiments conducted by Leonardo da Vinci presented some clues as to the root cause of fracture. Modern fracture mechanics is often considered to have been first developed by Griffith around one century ago [6]. After the Second World War, the Griffith model was reviewed and advanced by several researchers for analyzing ductile metals. Some other progresses were made so as to describe crack tip stress fields in nonlinear materials. Some details of the history were shown in the next section.

Besides nonlinear materials, there are also a lot of natural, and more recently, engineered layered material systems, where discontinuities in thermal and elastic properties exist. The applications of fracture mechanics of layered materials range over a broad spectrum of interesting and beneficial areas including coating materials, electronic packaging, and bonded joints, etc. Crack paths in bonded joints have been observed to propagate in a variety of ways, such as straight paths, wavy paths, along one interface, or alternating from one interface to another[3]. In bonded joints, which are the focus of this dissertation, the fracture process is often complex due to the mismatch of the material properties, the presence of interfaces, and local inconsistencies such as contamination, etc. Stress singularities due to geometries, as well as loading modes (with combined shear and tension stresses), are also important factors affecting crack initiation and propagation. All these issues have made the crack path selection in adhesively bonded joints a challenging area, and more understanding of the damage and fracture processes is required.

One of the important studies is the behavior of cracks in imperfectly bonded joints. Crack path selection is one interesting area relevant for understanding the performance, predicting the behavior, and estimating service life of the adhesively bonded joints, though it is still a basic research area at present. Some relevant questions are listed as follows:

- (1) What options do engineers have in designing joint geometries or altering loading mode to either steer cracks towards weakened zones for ease of disassembly or avoid weak areas and resist failure?
- (2) When there is a small locally weakened interface in front of the main crack tip, how does the main crack interact with the weakened area: would it pass over the weakened area, or would it veer into the weakened area?
- (3) How weak should the weakened area be, or how large should it be, so that the main crack in the adhesive layer can sense it?
- (4) Is it possible to apply mixed mode loading to drive the main crack away from the weakened interface in front of it?
- (5) Would the crack path be altered if the bonded joints are opened in different loading rates?
- (6) If the crack paths can be altered by certain methods, can engineers make use of it so as to develop longer crack paths, increase the fracture energy, and extend the service life of the bonded joint?

These questions need to be answered by fundamental studies on crack path selection. The answers to them could potentially inspire new design methods for bonded joints, avoid sudden or catastrophic failures, improve the performance, and extend the service life of bonded structures.

Indeed, the path of a growing crack is determined by a number of factors in addition to the relative strength or fracture energy of the adhesive layer and the interfaces or interphases. These factors include the loading mode, the thicknesses of the adherends and adhesive layer, the moduli and ductility of the adherends and adhesive, the presence of localized flaws, and the residual stress state within the adhesive layer. Some of these factors are focused in this project and discussed in this dissertation:

- (1) Fracture mode mixity angle is one of the important factors discussed in this dissertation. Mixed mode loadings are applied to specimens by a custom-built instrument, the dual actuator load frame (DALF), which has been developed through a prior NSF IMR project. The DALF is capable of providing and changing mode mixity angles arbitrarily on the fly to beam-like specimens by the use of two independent actuators. Updates made to the controller over the course of this dissertation research enabled constant mode mixity angle tracking during the tests.
- (2) Material properties need to be clarified when discussing fracture processes. In this project and dissertation, linear elastic homogeneous isotropic (LEHI) materials are assumed in most of the discussion, unless specified. To evaluate the behavior of the damage at the crack tips, a cohesive zone model (CZM), including damage evolution and softening laws, is employed. Based on the CZM, there are two methods for the numerical simulation in ABAQUS®: cohesive elements and extended finite element method (XFEM). Cohesive elements are widely used to simulate the debonding of interfaces. XFEM is a relatively new method for simulating crack propagation with an arbitrary crack path within bulk materials. These simulations enable the comparison with experimental results, and show some important results that are not yet experimentally available (e.g. stress distribution, damage evolution).

- (3) Locally weakened interfaces were developed experimentally using several physical and chemical methods. The interaction of the initial crack and the weakened interface is also discussed in this dissertation. One of the interesting problems considered is 2D bridging in a bonded joint with an initial interfacial crack and a debond on the opposite interface. The process of the multiple debond propagation can provide more understanding to demolding processes, and prediction of the behavior of bridging beam-like specimens. These results may also provide some useful information to develop strategies to control debond propagation. The other one is to see how the crack is affected by local weakened zones when the crack is grown under a range of mode mixities. This will provide important insights into how a spatially varying interface will affect the locus of a growing crack. Because of the ability to carefully tailor the surface properties over a desired range of adhesion, a systematic investigation can be conducted, with broad implications for surface variations associated with inadequate adherend preparation.

## **1.2 Fracture mechanics and cohesive zone models in monolithic materials and layered material systems**

Although there were several relevant prior studies, modern fracture mechanics is often considered to have been first developed by Griffith around one century ago for ideal brittle in monolithic solid materials. He provided a quantitative connection between fracture stress and flaw size[6]. He invoked the First Law of Thermodynamics to formulate a fracture theory based on a simple energy balance. According to this theory, fracture occurs when the change in strain energy associated with crack growth is sufficient to overcome the surface energy of the material. This model correctly predicted the relationship between the strength and flaw size in glass specimens. Initial attempts to apply the Griffith model to more ductile metals, however, were not successful.

Starting from 1948, Griffith's model was reviewed and pushed forward by Irwin[7], Dugdale[8], Barenblatt[9], and Wells[10] by correcting for yielding at the crack tip, which was of key importance for analyzing ductile metals. The Irwin plastic zone correction was a relatively simple extension of LEFM, while Dugdale and Barenblatt each developed more elaborate models based on a narrow strip of yielded material at the crack tip. Wells proposed the displacement of the crack faces as an alternative fracture criterion when significant plasticity precedes failure. His observation led to the development of the parameter now known as the crack tip opening displacement (CTOD). Williams[11] also derived a crack tip solution using different method, but essentially identical to Irwin's. In 1968, Rice[12] developed another parameter, the J integral, which Hutchinson[13] and Rice and Rosengren[14] related to crack tip stress fields in nonlinear materials. Reviews of the classical literature of Griffith and Irwin in fracture mechanics of homogeneous and isotropic materials, latest approaches, and description of testing techniques can also be found in [15-17].

In order to apply the concepts in fracture mechanics to design, a mathematical relationship between toughness, stress, and flaw size was required. In 1976, Shih and Hutchinson[18] provided the theoretical framework based on the J integral for fracture

design analysis. Shih also illustrated that both the J integral and CTOD are equally valid for characterizing fracture. This achievement has made the two methodologies begin to merge, with positive aspects of each combined to yield improved analyses.

According to William's expansion[11], the stress state is characterized as

$$\begin{aligned}
 \begin{bmatrix} \sigma_{xx} & \sigma_{xy} \\ \sigma_{xy} & \sigma_{yy} \end{bmatrix} &= \frac{K_I}{\sqrt{2\pi r}} \cos\left(\frac{\theta}{2}\right) \begin{bmatrix} 1 - \sin\left(\frac{\theta}{2}\right)\sin\left(\frac{3\theta}{2}\right) & \sin\left(\frac{\theta}{2}\right)\sin\left(\frac{3\theta}{2}\right) \\ \sin\left(\frac{\theta}{2}\right)\sin\left(\frac{3\theta}{2}\right) & 1 + \sin\left(\frac{\theta}{2}\right)\sin\left(\frac{3\theta}{2}\right) \end{bmatrix} \\
 &+ \frac{K_{II}}{\sqrt{2\pi r}} \begin{bmatrix} -\sin\left(\frac{\theta}{2}\right)\left[2 + \cos\left(\frac{\theta}{2}\right)\cos\left(\frac{3\theta}{2}\right)\right] & \cos\left(\frac{\theta}{2}\right)\left[1 - \sin\left(\frac{\theta}{2}\right)\sin\left(\frac{3\theta}{2}\right)\right] \\ \cos\left(\frac{\theta}{2}\right)\left[1 - \sin\left(\frac{\theta}{2}\right)\sin\left(\frac{3\theta}{2}\right)\right] & \sin\left(\frac{\theta}{2}\right)\cos\left(\frac{\theta}{2}\right)\cos\left(\frac{3\theta}{2}\right) \end{bmatrix} \\
 &+ \begin{bmatrix} T & 0 \\ 0 & 0 \end{bmatrix} + O(\sqrt{r})
 \end{aligned} \tag{1.1}$$

where the origin of the coordinate system is located at the crack tip with x-axis directing along the crack plane,  $r$ , and  $\theta$  are the variables of the polar coordinates.  $K_I$  and  $K_{II}$  are the stress intensity factors (SIFs) in mode I and mode II, respectively.

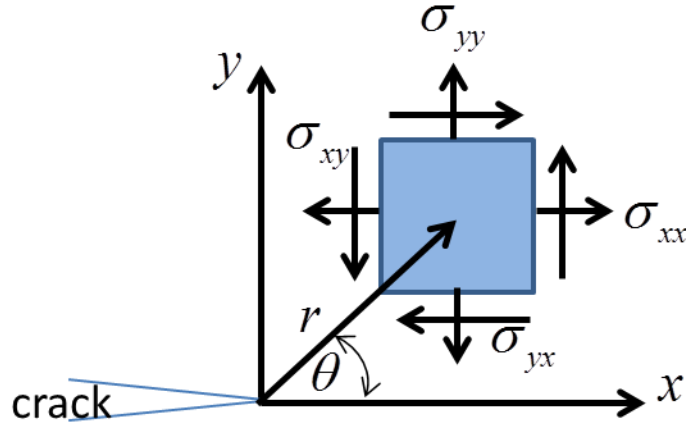


Figure 1.1. Stresses near the tip of a crack in an elastic material for William's asymptotic stress expansion.

The first and second terms on the right hand side are singular stresses that dominate the stress state and the onset of fracture in the vicinity of the crack tip. The third term on the right hand side with  $T$  is non-singular and only the component along the crack plane is not zero. This non-zero term is commonly referred to as the T-stress, and is considered to dominate the stability of the direction of crack propagation. Cotterell and Rice[19] studied the slightly curved or kinked cracks in homogeneous material, and showed that cracks will converge back to the original path, resulting in a directionally stable crack

trajectory, if the T-stress is negative (compressive). On the other hand, cracks will veer further away from the original path and the resultant crack path is directionally unstable if the T-stress is positive (tensile).

Besides the effect of the T-stress on crack path stability, local mode mixity is another parameter affecting crack propagation. Usually, when loaded in one mode, if the crack propagates in a non-straight path, the local stress state will be modified such that the mode mixity adjacent to the crack tip will be changed, as shown by Leever et al. for quasi-static[20] and fatigue[21] tests of PMMA (Polymethylmethacrylate), by Streit & Finnie for aluminum[22], and by Cotterell[23] for various other materials.

Three criteria have been used to determine the direction of crack propagation.

- (1) The direction that is perpendicular to the maximum opening stress at the crack tip (Erdogan & Sih[24]).
- (2) The direction that maximizes the strain energy release rate as a function of the angle of crack kinking or steering (Palaniswamy & Knauss[25]).
- (3) The direction such that pure mode I fracture is maintained at the crack tip where local  $K_{II} = 0$  (Goldstein & Salganik[26], Cotterell & Rice[19]).

Though seemingly very different criteria, they all yield similar results. No experimentally distinguishable differences have been observed [27-29]. According to these criteria, a crack path can be steered in different directions if the local stress state at the crack tip is mixed mode.

Though developed primarily for cracks in homogeneous materials, these criteria can be readily applied to bi-material systems, such as adhesively bonded joints[29]. This thesis is limited to linear elastic behavior. However, attention should be paid when applying them to the cracks located in the vicinity of an interface, where interfacial fracture mechanics is required[30]. Chen and Dillard[2] provided an example to show how to use these criteria to determine the direction when the crack is located at the interface.

For the cracks in adhesives, where the plastic zone size is relatively large, there are more difficulties to be overcome when simulating their behavior. When subjected to a unique stress field, fracture often initiates from some microscopic flaw or tiny nucleation in the bulk material, which subsequently grows and then leads to total failure and crack propagation. Viscoelasticity, discontinuities, and the presence of voids, flaws, and other irregularities can also influence the nucleation and propagation processes. More sophisticated microstructural models for fracture were developed beginning in the 1960s. One of the most important and successful approaches is the cohesive zone model (CZM). This dissertation is limited to linear elastic behavior, and the CZM is employed to describe material behavior at crack tips. The following paragraphs will show the details about it, starting from Williams' expansion of stresses at a crack tip.

Williams' approach of fracture mechanics is widely used to analyze the correlation among crack growth, material properties, and input test parameters, which include the imposed displacements or loads. Rewriting equation (1.1) in compact form with only the

first order terms (i.e. the terms with  $K_I, K_{II}, K_{III}$ ) in a polar coordinate system, one obtains:

$$\sigma(r, \theta) = \sum K_i \frac{1}{\sqrt{2\pi r}} f_i(\theta) \quad (1.2)$$

Since the stress field adjacent to the crack tip shows a  $1/\sqrt{r}$  singularity, the stresses in linear elastic materials tend to go infinity when  $r \rightarrow 0$ . Based on the first order solution, three areas can be distinguished in the vicinity of crack tip.

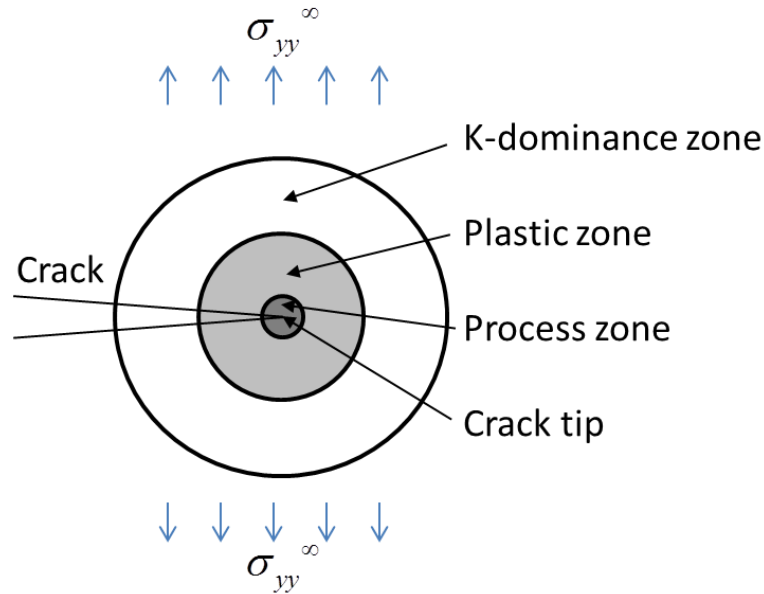


Figure 1.2. Definition of the zones of interest around the crack tip.

When  $r$  is relatively small in equation (1.2), the K-dominant zone is defined, where the asymptotic development terms in the right hand side are very big, and the stress intensity factors (SIFs) are sufficient to characterize the stresses in this zone. Within the K-dominant zone, there is a smaller zone where the material exhibits nonlinear behavior such as plastic behavior. This region is referred to as the plastic zone. Finally, in the immediate vicinity of crack tip, the material undergoes extensive damage that allows the crack to propagate. This is usually defined as the process zone as shown in Figure 1.2. The dimension of this process zone is very small, within which continuum mechanics of plasticity is no longer applicable. The process zone is usually neglected in both linear or nonlinear fracture mechanics, but considered to be important if the local mechanisms of crack propagation have to be taken into account in the simulation[31]. For example, fracture processes in polymers are usually quite complicated, with the movement and breakage of molecular chains, initiation of microcracks, as well as other inelastic behaviors. It is often very useful to define a softening law and damage evolution model in the process zone at the crack tip. This model is usually called a cohesive process zone model, or cohesive zone model (CZM).

The basis for CZM can be traced back to the works of Dugdale (1960)[8] and Barenblatt (1962)[9]. This model ignores the details of complicated mechanisms by

replacing them with a prescribed “traction-separation law” that effectively models the response. The CZM is a general model which can deal with the nonlinear process zone ahead of the crack tip, due to plasticity or microcracking, present in many materials[32]. Figure 1.3 shows the idea of a possible traction-separation model at a crack tip. Usually, a bilinear traction-separation law is taken as a material property that describes the constitutive behavior of the elements near the crack tip. Calculations of crack initiation and crack growth are possible for both ductile and brittle materials. By defining the maximum tractions, and fracture energy, (or maximum traction and maximum displacement), the CZM is commonly used in the simulation of fracture-related behavior. Figure 1.4 shows the traction-separation of a CZM. The symbols  $t^o$  and  $\delta^o$  are the traction and separation, respectively, when damage starts.  $\delta^f$  is the final separation when the crack totally fails. Thus, the area beneath the two lines represents the value of the fracture energy.

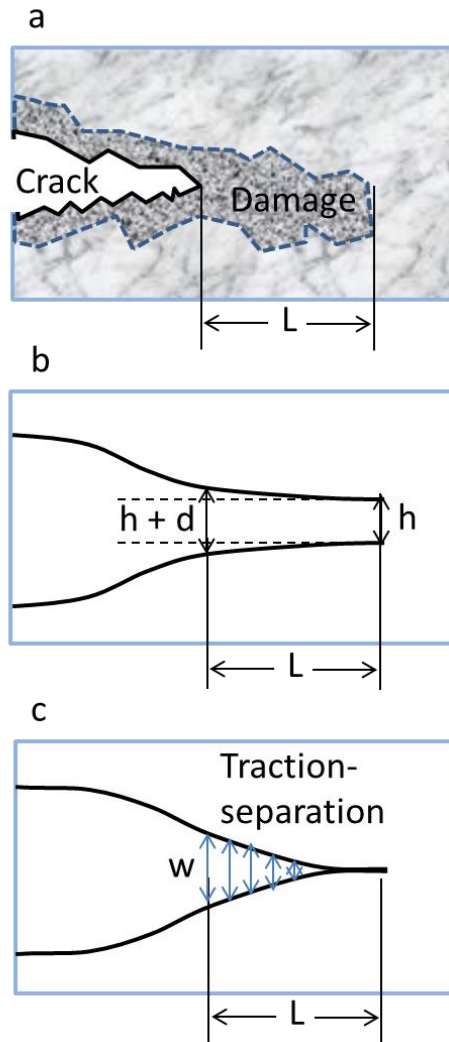


Figure 1.3. Cohesive zone model: a) crack in bulk material with damage zone of length  $L$ ; b) simplified model with damage zone thickness of  $h$ , crack opening of  $d$ ; c) cohesive zone model with crack opening of  $w$ .

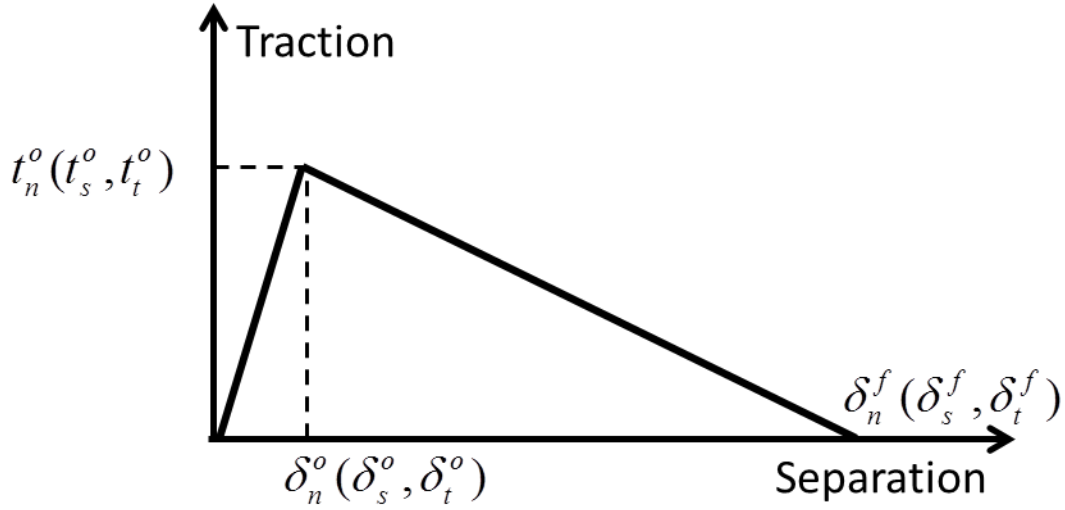


Figure 1.4. Typical traction-separation law of a CZM.

The CZM is still closely related to traditional fracture mechanics, so one of the important parameter is the fracture energy, which is commonly used in traditional fracture mechanics. In fracture mechanics, strain energy release rate (SERR), and critical SERR (or fracture energy) are frequently used. SERR, or  $\mathcal{G}$ , is the driving force for fracture, while fracture energy, or  $\mathcal{G}_c$ , is the materials' resistance to fracture. Crack propagation occurs when the energy available for crack growth is adequate to overcome the resistance of the material, which includes the surface energy, plastic work, viscoelastic dissipation, or other dissipation associated with this propagation. From the viewpoint of energy conservation, assuming no plastic or viscoelastic dissipation, the available energy for crack propagation is

$$\mathcal{G} = \frac{dW - dU}{dA} \quad (1.3)$$

where  $dA$  is the infinitesimal area of the new crack surface,  $dW$  is the work of the internal forces in the infinitesimal propagation process, and  $dU$  is the variation of the stored elastic strain energy. The expression of  $\mathcal{G}$  for linear load-deflection behavior in terms of load, known as Irwin-Kies relationship[7] is shown as follows:

$$\mathcal{G} = \frac{P^2}{2} \frac{dC}{dA} \quad (1.4)$$

where  $P$  is the applied external load and  $dC$  is the change of the compliance.

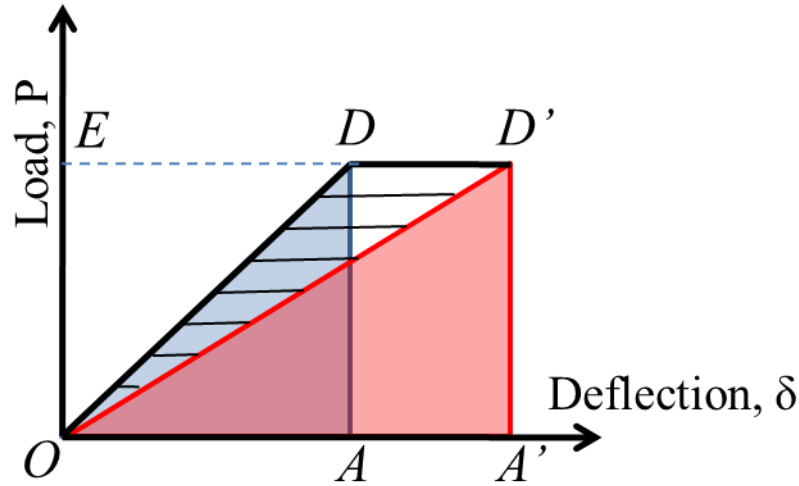


Figure 1.5. Schematic of the calculation of fracture energy: area of triangle ODD' divided by  $dA$ , is the fracture energy when  $P$  is constant but deflection changes from  $D$  to  $D'$  (depends on the material properties,  $OD$  and  $OD'$  can be either linear or nonlinear).

Mode mixity is likely to occur in real applications, due to the nature of both the structural configuration and various loading scenarios. Asymmetric loading or a multi-axial stress state would usually bring mode mixity to the system as well. Partitioning techniques for  $\mathcal{G}$  have been developed by Williams[33], Schapery & Davidson[34], and Hutchinson & Suo[29], though with different results[35]. These techniques are commonly applied to geometries such as beams and plates subjected to different mixed mode loading conditions. With the hypotheses of elastic deformation, the stress field resulted from mixed mode loading is equivalent to a linear superposition of that from pure modes. In particular, the applied  $\mathcal{G}$  is a scalar and can be obtained as the summation of the pure mode components. Thus, we have:

$$\mathcal{G} = \mathcal{G}_I + \mathcal{G}_{II} + \mathcal{G}_{III} \quad (1.5)$$

This study has focused on mode I and mode II, the in-plane fracture modes. Therefore, the mode mixity angle,  $\psi$ , is denoted as in[29], and defined as follows:

$$\psi = \arctan \sqrt{\frac{\mathcal{G}_{II}}{\mathcal{G}_I}} \quad (1.6)$$

Whereas  $\mathcal{G}$  represents the applied SERR,  $\mathcal{G}_c$ , or the fracture energy, is regarded as a material property, and thus is usually evaluated experimentally.  $\mathcal{G}_c$  is sometimes referred to pure mode I or mode II in literatures and standards[16, 17, 36]. However,  $\mathcal{G}_c$  for the crack propagation at different mode mixity angles is usually quite different[37]. Thus, interpretation of fracture energy under mixed mode loading is required. A large number of publications addressed the experimental techniques that used to measure mixed mode fracture properties of materials using Brazil-nut specimens[38], Arcan specimens[37, 39].

Usually, one of the most important parameter for the CZM is the fracture energy of the material.  $G_c$  in pure mode I and mode II, as well as a failure criterion will be assigned to the material model, which can help to calculate the fracture energy value at an arbitrary mode mixity angle.

The other important parameter for the CZM is the maximum traction, which is defined as the critical value of stress when the damage process initiates. The value of the maximum traction cannot be directly obtained from experiments, but is usually estimated by comparison of numerical simulation to the experiments[40]. For example, Blackman[40] noted that, for crack propagation in the DCB (double cantilever beam) specimen, the load versus displacement curve is independent of the value of maximum traction; but the crack initiation point is dependent upon the chosen value of maximum traction. In summary, there are still some uncertainties and arguments on the evaluation and interpretation of maximum traction.

### 1.3 Fracture analysis method in adhesively bonded joints

For fracture studies of bonded joints, double cantilever beam (DCB) test is common for characterizing mode I behavior of bonded joints[41] and has been codified in standards [42, 43]. Because of its simplicity and the perception that mode I loading often results in the smallest fracture energy, DCB test is useful for conservative design purposes. Other loading modes can be achieved using similar bonded beam-like specimens loaded in different fixtures. For example, fracture energy in mode II can be obtained from the end notch flexure (ENF) [44] or end load split [45] tests. Fracture energy in other discrete mode mixities can be obtained using specimens such as the fixed-ratio mixed-mode (FRMM) test[46] or crack lap shear (CLS) test[47]. Some of them were shown in Figure 1.6. Discrete [48] or continuous[49] variations in mode mixity over relatively narrow ranges about these specific loading modes can be achieved with asymmetric specimens. Reeder & Crews[50-52], and Fernlund & Spelt[5, 53, 54] developed special loading jigs that can be adjusted to conduct fracture tests on bonded beam specimens over a wide range of mode mixities.

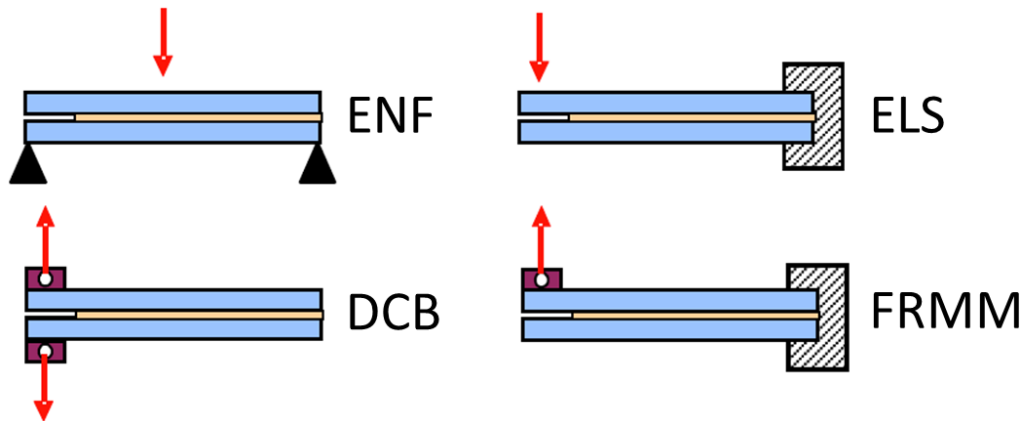


Figure 1.6. Test applications of specimens with beam-like configurations (ENF: End notched flexure, ELS: End loaded split, DCB: Double cantilever beam, FRMM: Fixed-ratio mixed-mode).

All these techniques have been broadly applied to characterize failures in adhesively bonded joints, answering fundamental scientific questions as well as providing engineering data for design purposes. However, the material behavior of adhesives in mixed modes or pure mode II were not clearly understood. Studies of Singh *et al.* [55] and Dillard *et al.* [4] showed that for certain material systems, however, the fracture energy values for some levels of mode mixity are lower than that in pure mode I. Chen and Dillard found that, the locus of failure in adhesive bonds is dependent on the fracture mode mixity at the crack tip, the failure tends to be more interfacial as the mode II fracture component increases [1-3].

In bonded joints, Chai[56-58] first discussed the directional stability of cracks and observed a unique form of crack trajectory in the mode I delamination failure of graphite reinforced epoxy composite laminates and aluminum/epoxy bonds. Fleck, Hutchinson and Suo[59], and Akisanya and Fleck[60] investigated this issue analytically and indicated that, as with homogeneous materials, the directional stability of cracks in adhesively bonded joints also depends on the T-stress level. Cracks in bonded joints tend to be directionally stable if the T-stress is negative and unstable of positive. For an adhesive bond of sandwich geometry with semi-infinite adherends, Fleck, Hutchinson and Suo[59] obtained the T-stress as

$$T = \frac{1-\alpha}{1+\alpha} T^\infty + \sigma_0 + C_I(c/t, \alpha, \beta) \frac{K_I^\infty}{\sqrt{t}} + C_{II}(c/t, \alpha, \beta) \frac{K_{II}^\infty}{\sqrt{t}} \quad (1.7)$$

where  $\sigma_0$  is the residual stress in the adhesive and  $t$  is the thickness of the adhesive layer.  $C_I(c/t, \alpha, \beta)$  and  $C_{II}(c/t, \alpha, \beta)$  are non-dimensional functions tabulated in Fleck, Hutchinson, and Suo.  $c$  is defined as the distance of the crack tip to the interface.  $\alpha$  and  $\beta$  are Dundurs' parameters reflecting the material mismatch, and are defined as

$$\alpha = \frac{\mu_1(\kappa_2 + 1) - \mu_2(\kappa_1 + 1)}{\mu_1(\kappa_2 + 1) + \mu_2(\kappa_1 + 1)} \quad (1.8)$$

$$\beta = \frac{\mu_1(\kappa_2 - 1) - \mu_2(\kappa_1 - 1)}{\mu_1(\kappa_2 + 1) + \mu_2(\kappa_1 + 1)}$$

where the subscripts 1 and 2 refer to the materials for the adherends and adhesive, respectively;  $\mu_i (i=1,2)$  are shear moduli,  $\kappa_i = 3 - 4\nu_i$  for plane strain and  $\kappa_i = (3 - \nu_i) / (1 + \nu_i)$  for plane stress;  $\nu_i (i=1,2)$  are the Poisson's ratios.

In summary, in adhesively bonded joints, besides the complicated material property of adhesive itself, the mismatch of material properties of adherends and adhesives, residual stress in the adhesive (though not discussed much in this thesis), the existence of interfaces, as well as contaminations and flaws on the interfaces, etc., all of these factors can complicate the analysis of bonded joints.

## 1.4 Problem statement and objectives

The goal of this project is to study the crack path selection problem in beam-like adhesively bonded joints. Starting from monolithic materials, an asymmetric geometry was applied in the specimens that are similar to the standard compact tension (CT) specimen so as to obtain the crack path. Then simulation with CZM is used in ABAQUS to predict crack path selection. The objective of this work was to verify the CZM model, develop appropriate parameters for damage evolution and softening laws, and obtain fundamental understanding of it, which is of interest in engineering design.

Crack path selection in the adhesive layer of bonded joints is more complex than in monolithic materials, because the adhesive layer is constrained by stiff adherends. The behavior of the fracture responses of DCB specimens at different mode mixity angles, or with increasing mode mixity angle needs to be characterized. These fracture energy curves would be useful to the engineers to understand fracture profiles of two toughened epoxy adhesives, the influence of the size of the damage zone to the fracture energy, the shear toughening effect, as well as some other complex mechanisms in adhesively bonded joints.

Besides crack path selection in bulk material, interfacial debonding can also occur in some bonded joints. The multiple debonding processes along interfaces, as well as their interaction, is also an interesting area in the study of crack path selection. The propagation processes of the multiple debonds can provide more understanding to demolding processes, and prediction of the behavior of bridging beam-like specimens. These results. The study focused on the 2D bridging problem, simulating an anomalous debonding phenomenon that can occur in DCB specimens. The objective of this section is to investigate the competition of the multiple debonds on the interfaces and the resulting crack path selection and propagation processes, which can provide some useful information to develop strategies to control debond propagation.

For crack path selection in bonded joints, the interaction between the interfaces and the adhesive layer is another interesting topic. The objective of this section is to investigate how would the mixed mode loading and the interaction of interface and adhesive influence the crack path selection if some preset weakened interfaces are made when the main crack is proceeding. Studying of the stress fields influenced by the damage evolution of interfaces is also an important objective. The goal of this simulation is to study the sensitivity of crack path to weakened areas, the effect of the maximum traction, fracture energy, and size of the weakened areas on the crack path selection.

To apply varied loading modes to all the specimens experimentally as planned in this project, the performance of the DALF was improved by applying LabVIEW in the controlling system. Calibrations were required to correct the errors that come from the loading rod extension and bottom clamp rotations so as to obtain the beam deflections precisely and determine the fracture energy or intermediate SERR values correctly. The objective was to obtain the compliances or stiffness of the loading rods, as well as the rotary compliance of the clamp at the bottom. Then, these corrections can be applied to the experimental study of bonded joints.

## 1.5 Dissertation outline

This dissertation is mainly organized as a series of papers to be submitted to journals, as will be addressed at the beginning of those specific chapters intended for publication. An outline of the chapters is as follows:

- Chapter 1 provides a general background of this project and an introduction to fracture mechanics, including applications to adhesively bonded joints. Problem statements and objectives are also stated at the end of this chapter.
- Chapter 2 presents a study of crack path selection in a relatively brittle, monolithic polymer (PMMA). Models similar to compact tension specimens but with asymmetric arms were simulated with XFEM in ABAQUS. Crack paths were predicted by the numerical simulations. Specimens with the same dimensions were also prepared and tested so as to verify the predictions to the crack path trajectories. The comparison with numerical results showed good agreement.
- Chapter 3 addresses a study of the 2D bridging problem in DCB specimens, which is also related to crack path selection with multiple interfacial debonds. Equations were derived from Euler-Bernoulli beam theory. Numerical integrations were conducted in Mathematica® to determine the expected sequence of propagation of the three cracks and the mechanism of bridging was clarified.
- Chapter 4 provides the details on the controller and calibration improvements of the DALF. Hardware configuration and software programming in LabVIEW are shown in detail. Development of more versatile control functions such as constant mode mixity angle function is presented. Calibration of the DALF was executed so as to minimize the error from extension of loading rods and end rotation at the clamp.
- Chapter 5 provides the details on mixed mode beam-like specimen tests using the DALF. Fracture energy and intermediate SERR curves are plotted so as to characterize the behavior of the crack in bonded joints. Effects of the size of the damage zone and shear toughening are discussed.
- Chapter 6 provides the numerical study of crack path selection with weakened areas on part of the interfaces. By applying different lengths and parameters to the damage evolution and softening laws of the weakened area, influences of the weakened areas are summarized. The maximum traction in the CZM is considered to play a very important part in the crack path selection process. Fracture energy is found to be of secondary importance, though can affect the results when it is particularly small (e.g. 1% of the adhesive toughness). Under globally mixed mode loadings, the competition between the loading and weakened interface is affecting the shear stress distribution and thus changes the crack path in the adhesive layer. Higher mixed mode loadings in the opposite direction of the weakened interface are predicted to drive the crack away from the weak interface, avoiding failure within these regions.
- Appendix A shows the tests of rate dependent crack path selection conducted by using DCB specimens with one of the bonding surfaces weakened by some physical and chemical methods. It is discovered that high loading rate can

help the main crack to discover those partially weakened areas, but low loading rate can not. These results were explained by the competition between the CZMs of the adhesive and the weakened interface.

- Appendix B show the discussion for the T-stress calculated by ABAQUS®.
- Appendix C show the numerical simulation of the 2D problem analyzed in Chapter 3 using ABAQUS®.

## 1.6 References

- [1] H. J. Choi and G. H. Paulino, "Interfacial cracking in a graded coating/substrate system loaded by a frictional sliding flat punch," *Proceedings of the Royal Society A: Mathematical, Physical and Engineering Sciences*, vol. 466, pp. 853-880, 2009.
- [2] J. M. A. Reina, J. J. N. Prieto, and C. A. Garcia, "Influence of the Surface Finish on the Shear Strength of Structural Adhesive Joints and Application Criteria in Manufacturing Processes," *Journal of Adhesion*, vol. 85, pp. 324-340, 2009.
- [3] B. Chen, D. A. Dillard, J. G. Dillard, and R. L. Clark, "Crack path selection in adhesively bonded joints: the roles of external loads and specimen geometry," *International Journal of Fracture*, vol. 114, pp. 167-190, Mar 2002.
- [4] B. Chen and D. A. Dillard, "Numerical analysis of directionally unstable crack propagation in adhesively bonded joints," *International Journal of Solids and Structures*, vol. 38, pp. 6907-6924, SEP 2001.
- [5] B. Chen, D. A. Dillard, J. G. Dillard, and R. L. Clark, "Crack path selection in adhesively-bonded joints: The role of material properties," *Journal of Adhesion*, vol. 75, pp. 405-434, 2001.
- [6] D. A. Dillard, H. K. Singh, D. J. Pohlit, and J. M. Starbuck, "Observations of Decreased Fracture Toughness for Mixed Mode Fracture Testing of Adhesively Bonded Joints," *Journal of Adhesion Science and Technology*, vol. 23, pp. 1515-1530, 2009.
- [7] G. Fernlund and J. K. Spelt, "Mixed-Mode Energy-Release Rates for Adhesively Bonded Beam Specimens," *Journal of Composites Technology & Research*, vol. 16, pp. 234-243, JUL 1994.
- [8] A. A. Griffith, "The Phenomena of Rupture and Flow in Solids," *Philosophical Transactions, Royal Society Series A*, vol. 221, pp. 582-593, 1921.
- [9] G. R. Irwin, "Fracture dynamics," *Fracturing of Metals, American Society for Metals*, pp. 147-166, 1948.
- [10] D. S. Dugdale, "Yielding in Steel Sheets Containing Slits," *Journal of the Mechanics and Physics of Solids*, vol. 8, pp. 100-104, 1960.
- [11] G. I. Barenblatt, "The Mathematical Theory of Equilibrium Cracks in Brittle Fracture," *Advances in Applied Mechanics*, vol. 7, pp. 55-129, 1962.
- [12] A. A. Wells, "Unstable Crack Propagation in Metals: Cleavage and Fast Fracture," *Proceedings of the Crack Propagation Symposium*, vol. 1, 1961.
- [13] M. L. Williams, "On the stress distribution at the base of a stationary crack," *Journal of Applied Mechanics*, vol. 24, pp. 109-114, 1957.

- [14] J. R. Rice, "A Path Independent Integral and the Approximate Analysis of Strain Concentration by Notches and Cracks," *Journal of Applied Mechanics*, vol. 35, pp. 379-386, 1968.
- [15] J. W. Hutchinson, "Singular behaviour at the end of a tensile crack in a hardening material," *Journal of the Mechanics and Physics of Solids*, vol. 16, pp. 13-31, 1// 1968.
- [16] J. R. Rice and G. F. Rosengren, "Plane strain deformation near a crack tip in a power-law hardening material," *Journal of the Mechanics and Physics of Solids*, vol. 16, pp. 1-12, 1// 1968.
- [17] L. P. Pook, *Linear Elastic Fracture Mechanics for Engineers: Theory and Applications*. Southampton, UK: Boston: WIT Press, 2000.
- [18] N. E. Dowling, *Mechanical Behavior of Materials: Engineering Methods for Deformation, Fracture, and Fatigue*, 3rd ed. Upper Saddle River, NJ: Pearson/Prentice Hall, 2007.
- [19] T. L. Anderson, *Fracture Mechanics: Fundamentals and Applications*, 2nd ed. Boca Raton: CRC Press, 1995.
- [20] C. F. Shih and J. W. Hutchinson, "Fully Plastic Solutions and Large-Scale Yielding Estimates for Plane Stress Crack Problems," *Journal of Engineering Materials and Technology-Transactions of the Asme*, vol. 98, pp. 289-295, 1976.
- [21] B. Cotterell and J. R. Rice, "Slightly Curved or Kinked Cracks," *International Journal of Fracture*, vol. 16, pp. 155-169, 1980.
- [22] P. S. Leevvers, J. C. Radon, and L. E. Culver, "Fracture Trajectories in a Biaxially Stressed Plate," *Journal of the Mechanics and Physics of Solids*, vol. 24, pp. 381-395, 1976.
- [23] P. S. Leevvers and J. C. Radon, "Inherent Stress Biaxiality in Various Fracture Specimen Geometries," *International Journal of Fracture*, vol. 19, pp. 311-325, 1982.
- [24] R. Streit and I. Finnie, "Experimental Investigation of Crack-Path Directional Stability," *Experimental Mechanics*, vol. 20, pp. 17-23, 1980.
- [25] B. Cotterell, "On fracture path stability in the compact tension test," *International Journal of Fracture Mechanics*, vol. 6, pp. 189-192, 1970.
- [26] V. F. Erdogan and G. C. Sih, "On Crack Extension in Plates Under Plane Loading and Transverse Shear," *Trans. ASME J. Bas. Eng.*, vol. 85, pp. 519-527, 1963.
- [27] K. Palaniswamy and W. G. Knauss, "On the Problem of Crack Extension in Brittle Solids Under General Loading," *Mechanics Today*, vol. 4, pp. 87-148, 1978.
- [28] R. V. Goldstein and R. L. Salganik, "Brittle Fracture of Solids with Arbitrary Cracks," *International Journal of Fracture*, vol. 10, 1974.

- [29] A. R. Akisanya and N. A. Fleck, "Brittle-Fracture of Adhesive Joints," *International Journal of Fracture*, vol. 58, pp. 93-114, NOV 15 1992.
- [30] P. H. Geubelle and W. G. Knauss, "Crack-Propagation at and near Bimaterial Interfaces - Linear-Analysis," *Journal of Applied Mechanics-Transactions of the Asme*, vol. 61, pp. 560-566, SEP 1994.
- [31] J. W. Hutchinson and Z. Suo, "Mixed-Mode Cracking in Layered Materials," *Advances in Applied Mechanics, Vol 29*, vol. 29, pp. 63-191, 1992.
- [32] J. R. Rice, "Elastic Fracture-Mechanics Concepts for Interfacial Cracks," *Journal of Applied Mechanics-Transactions of the Asme*, vol. 55, pp. 98-103, Mar 1988.
- [33] S. Pommier, A. Gravouil, A. Combescure, and N. Moes, *Extended finite element method for crack propagation*. Hoboken, NJ 07030: John Wiley & Sons, Inc., 2011.
- [34] M. Elices, G. V. Guinea, J. Gomez, and J. Planas, "The cohesive zone model: advantages, limitations and challenges," *Engineering Fracture Mechanics*, vol. 69, pp. 137-163, Jan 2002.
- [35] J. G. Williams, "On the Calculation of Energy-Release Rates for Cracked Laminates," *International Journal of Fracture*, vol. 36, pp. 101-119, Feb 1988.
- [36] R. A. Schapery and B. D. Davidson, "Prediction of Energy Release Rate for Mixed-Mode Delamination Using Classical Plate Theory," *Applied Mechanics Reviews*, vol. 43, pp. S281-S287, 1990.
- [37] N. Choupani, "Interfacial mixed-mode fracture characterization of adhesively bonded joints," *International Journal of Adhesion and Adhesives*, vol. 28, pp. 267-282, Sep 2008.
- [38] ASTM-D5045-99e1, "Standard Test Methods for Plane-Strain Fracture Toughness and Strain Energy Release Rate of Plastic Materials," in *Annual Book of ASTM Standards*, ed West Conshohocken, PA, 2007.
- [39] J. S. Wang and Z. Suo, "Experimental-Determination of Interfacial Toughness Curves Using Brazil-Nut-Sandwiches," *Acta Metallurgica Et Materialia*, vol. 38, pp. 1279-1290, Jul 1990.
- [40] N. Choupani, "Mixed-mode cohesive fracture of adhesive joints: Experimental and numerical studies," *Engineering Fracture Mechanics*, vol. 75, pp. 4363-4382, Oct 2008.
- [41] B. R. K. Blackman, H. Hadavinia, A. J. Kinloch, and J. G. Williams, "The use of a cohesive zone model to study the fracture of fibre composites and adhesively-bonded joints," *International Journal of Fracture*, vol. 119, pp. 25-46, Jan 2003.
- [42] A. J. Kinloch, *Adhesion and Adhesives: Science and Technology*. London: Chapman and Hall, 1987.

- [43] BS-7991, "Determination of the Mode I Adhesive Fracture Energy,  $G_{Ic}$ , of Structural Adhesives Using the Double Cantilever Beam (DCB) and Tapered Double Cantilever Beam (TDCB) Specimens," ed, 2001.
- [44] ASTM-D3433-99, "Standard Test Method for Fracture Strength in Cleavage of Adhesives in Bonded Metal Joints," in *Annual Book of ASTM Standards*, ed West Conshohocken, PA, 1999 (Reapproved in 2005).
- [45] F. Ducept, P. Davies, and D. Gamby, "Mixed mode failure criteria for a glass/epoxy composite and an adhesively bonded composite/composite joint," *International Journal of Adhesion and Adhesives*, vol. 20, pp. 233-244, Jun 2000.
- [46] B. R. K. Blackman, A. J. Kinloch, and M. Paraschl, "The determination of the mode II adhesive fracture resistance,  $G_{IIc}$ , of structural adhesive joints: an effective crack length approach," *Engineering Fracture Mechanics*, vol. 72, pp. 877-897, Apr 2005.
- [47] A. J. Kinloch, Y. Wang, J. G. Williams, and P. Yayla, "The Mixed-Mode Delamination of Fiber Composite-Materials," *Composites Science and Technology*, vol. 47, pp. 225-237, 1993.
- [48] Y. H. Lai, M. D. Rakestraw, and D. A. Dillard, "The cracked lap shear specimen revisited - A closed form solution," *International Journal of Solids and Structures*, vol. 33, pp. 1725-1743, May 1996.
- [49] S. Mall and N. K. Kochhar, "Criterion for Mixed Mode Fracture in Composite Bonded Joints," *NASA/CR-178112*, 1986.
- [50] S. Park and D. A. Dillard, "Development of a simple mixed-mode fracture test and the resulting fracture energy envelope for an adhesive bond," *International Journal of Fracture*, vol. 148, pp. 261-271, Dec 2007.
- [51] J. R. Reeder and J. H. Crews, "Mixed-Mode Bending Method for Delamination Testing," *Aiaa Journal*, vol. 28, pp. 1270-1276, Jul 1990.
- [52] J. R. Reeder and J. H. Crews, "Redesign of the Mixed-Mode Bending Delamination Test to Reduce Nonlinear Effects," *Journal of Composites Technology & Research*, vol. 14, pp. 12-19, Spr 1992.
- [53] J. R. Reeder and J. J. H. Crews, "Non-linear Analysis and Redesign of the Mixed-mode Bending Delamination Test," *NASA/TM-102777*, 1991.
- [54] G. Fernlund and J. K. Spelt, "Mixed-Mode Fracture Characterization of Adhesive Joints," *Composites Science and Technology*, vol. 50, pp. 441-449, 1994.
- [55] M. Papini, G. Fernlund, and J. K. Spelt, "The Effect of Geometry on the Fracture of Adhesive Joints," *International Journal of Adhesion and Adhesives*, vol. 14, pp. 5-13, Jan 1994.
- [56] H. K. Singh, A. Chakraborty, C. E. Frazier, and D. A. Dillard, "Mixed mode fracture testing of adhesively bonded wood specimens using a dual actuator load frame," *Holzforschung*, vol. 64, pp. 353-361, Apr 2010.

- [57] H. Chai, "The Characterization of Mode-I Delamination Failure in Non-Woven, Multidirectional Laminates," *Composites*, vol. 15, pp. 277-290, 1984.
- [58] H. Chai, "On the Correlation between the Mode-I Failure of Adhesive Joints and Laminated Composites," *Engineering Fracture Mechanics*, vol. 24, pp. 413-&, 1986.
- [59] H. Chai, "A Note on Crack Trajectory in an Elastic Strip Bounded by Rigid Substrates," *International Journal of Fracture*, vol. 32, pp. 211-213, Nov 1986.
- [60] N. A. Fleck, J. W. Hutchinson, and Z. G. Suo, "Crack Path Selection in a Brittle Adhesive Layer," *International Journal of Solids and Structures*, vol. 27, pp. 1683-1703, 1991.
- [61] A. R. Akisanya and N. A. Fleck, "Analysis of a Wavy Crack in Sandwich Specimens," *International Journal of Fracture*, vol. 55, pp. 29-45, May 1 1992.
- [62] H. K. Singh, P. Soojae, D. C. Ohanehi, and D. A. Dillard, "A design space for a novel dual-actuator mixed-mode test frame," *Proceedings of the 29th Annual Adhesion Society Meeting, Jacksonville, FL, 2006*.

# Chapter 2 Fracture and crack trajectory in monolithic materials

---

Since experimental and numerical studies of crack growth within one bulk material is simpler than those in multi-layered material systems such as bonded joints, the investigation of crack path selection initially focused on cracks in monolithic materials. Also, the XFEM (extended finite element method) with damage evolution and a softening law in ABAQUS® were applied to the numerical model with monolithic fracture so as to investigate this relatively new method before applying it to model adhesively bonded joints.

## 2.1 Introduction to crack path selection in monolithic material

Crack path selection in monolithic material is one of the interesting problems in fracture mechanics, and is affected by material uniformity, external constraints, external loads, residual stress, etc. More understanding of crack path selection can potentially help to avoid harmful crack propagation or drive crack in a different direction or towards a tougher region that leads to longer service life. Therefore, this study could be very useful for the understanding and controlling crack propagation thus benefiting engineering design in multiple industries.

In linear fracture mechanics for homogeneous isotropic monolithic materials, the crack tip stresses are characterized by Williams' expansion using coordinate system for the crack tip shown in Figure 2.1.

$$\begin{aligned}
 \begin{bmatrix} \sigma_{xx} & \sigma_{xy} \\ \sigma_{xy} & \sigma_{yy} \end{bmatrix} &= \frac{K_I}{\sqrt{2\pi r}} \cos\left(\frac{\theta}{2}\right) \begin{bmatrix} 1 - \sin\left(\frac{\theta}{2}\right)\sin\left(\frac{3\theta}{2}\right) & \sin\left(\frac{\theta}{2}\right)\sin\left(\frac{3\theta}{2}\right) \\ \sin\left(\frac{\theta}{2}\right)\sin\left(\frac{3\theta}{2}\right) & 1 + \sin\left(\frac{\theta}{2}\right)\sin\left(\frac{3\theta}{2}\right) \end{bmatrix} \\
 &+ \frac{K_{II}}{\sqrt{2\pi r}} \begin{bmatrix} -\sin\left(\frac{\theta}{2}\right)\left[2 + \cos\left(\frac{\theta}{2}\right)\cos\left(\frac{3\theta}{2}\right)\right] & \cos\left(\frac{\theta}{2}\right)\left[1 - \sin\left(\frac{\theta}{2}\right)\sin\left(\frac{3\theta}{2}\right)\right] \\ \cos\left(\frac{\theta}{2}\right)\left[1 - \sin\left(\frac{\theta}{2}\right)\sin\left(\frac{3\theta}{2}\right)\right] & \sin\left(\frac{\theta}{2}\right)\cos\left(\frac{\theta}{2}\right)\cos\left(\frac{3\theta}{2}\right) \end{bmatrix} \\
 &+ \begin{bmatrix} T & 0 \\ 0 & 0 \end{bmatrix} + O(\sqrt{r})
 \end{aligned} \tag{2.1}$$

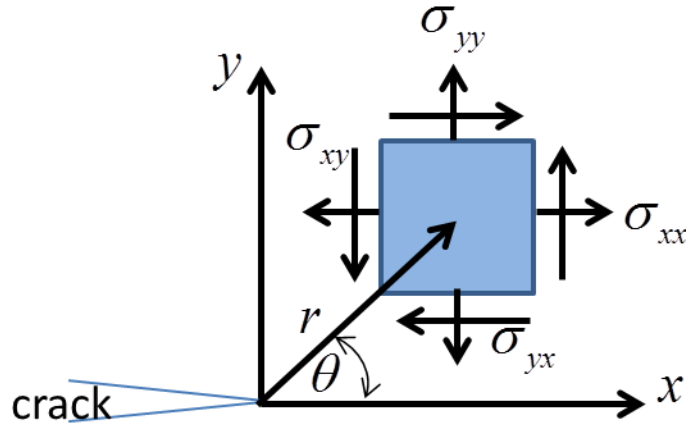


Figure 2.1. The definitions of stresses near the tip of a crack in elastic materials.

From equation (2.1), the T-stress along the crack tip, obtained by setting  $\theta = 0$ , is given by:

$$T = \sigma_{xx} - \sigma_{yy} \quad (2.2)$$

Though the T-stress term is much smaller than the singular terms at the crack tip, its magnitude controls the directional stability of a crack. Cotterell and Rice [1] concluded that a crack tends to be directionally unstable if the T-stress is positive (tensile) and directionally stable if it is negative (compressive).

There are three criteria to determine the direction of crack propagation. The first criteria, proposed by Erdogan & Sih[2], is that a crack will propagate in the direction that is perpendicular to the maximum opening stress. Palaniswamy & Knauss[3] suggested that propagation would occur in the direction that maximizes the strain energy release rate. The third criteria, advocated by Goldstein & Salganik[4] and Cotterell & Rice[1], is that a crack will grow in a direction such that mode I fracture is maintained at the crack tip, i.e. such that the local  $K_{II} = 0$ . Though seemingly very different criteria, they all yield similar results. No experimentally distinguishable differences have been observed [5-7]. According to these criteria, a propagating crack can veer or kink into a different direction depending on the mode mixity of the local stress state at the crack tip.

Analytical solutions can only provide results of the direction and trajectory of crack propagation for simple geometries. However, in most of the applications, simulations with the finite element method (FEM) are widely used to obtain quick and accurate results with the assistance of computers.

However, with the assumptions of linear elastic fracture mechanics, the stress tends to infinity when the distance to the crack tip tends to zero. The definitions of the stress and strain at the crack tip are not valid anymore. A more complicated constitutive

relationship, such as the elastic-plastic law with damage evolution, is required. In this case, the stress at the crack tip is limited by the nonlinear property of the material.

In the simulation of a models with fracture, as briefly introduced in Chapter 1, the CZM (cohesive zone model) has been widely applied in the simulation of crack propagation. ABAQUS is commonly used software for with extensive capabilities for analyzing nonlinear material behavior and fracture mechanics. Actually, there are three applications of the CZM in ABAQUS: cohesive element method, XFEM (extended finite element method), and CZM-based contact. The first one is widely used for the simulation of interface and will be described in detail in Chapter 6. The second is mainly used for the simulation of crack propagation within bulk materials, where the crack path is not known a priori, and don't need to be correspondent to the element boundaries. The third one introduces CZMs when simulating contact problems of two surfaces and will not be discussed in this dissertation.

Based on the CZM framework, the XFEM is an extension of the conventional finite element method based on the concept of partition of unity [8, 9]. It allows the presence of discontinuities in an element by enriching degrees of freedom with special displacement functions, but does not require the mesh to match the geometry of the discontinuities. In brief, XFEM is a relatively new application that enables crack propagation within elements and determination of crack path automatically by some criteria. Therefore, XFEM can be used to simulate crack initiation and propagation along an arbitrary, solution-dependent path in bulk materials, since the crack propagation is not tied to the element boundaries in a mesh. In this case the near-tip asymptotic singularity is not needed, and only the displacement jump across a cracked element is considered. In ABAQUS®, the XFEM does not need remeshing after each crack propagation step. But some phantom nodes, which are superposed on the original real nodes, are introduced to represent the discontinuity of the cracked elements, as illustrated in Figure 2.2. When the element is intact, each phantom node is completely constrained to its corresponding real node. When one element is broken by a crack, the cracked element splits into two parts. Each part is formed by a combination of real and phantom nodes depending on the orientation of the crack. Each phantom node and its corresponding real node are no longer tied together and can move apart. These capabilities greatly facilitate simulations of crack path selection. By default in ABAQUS, the crack propagates normal to the direction of the maximum tangential stress. This process can be repeated several times within one element by small increments of the crack, so as to provide a relatively continuous crack path.

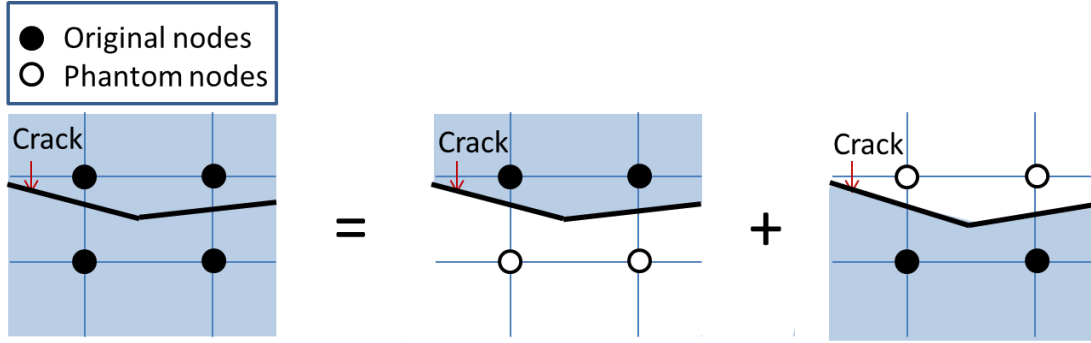


Figure 2.2. The phantom nodes created in the ABAQUS when simulating a crack propagation using XFEM.

In the XFEM, besides Young's modulus and Poisson's ratio, the profile of the softening law and the parameters of the damage evolution are also defined as material properties. Figure 2.3 shows an example of the CZM. Subscripts n, s, and t, indicate normal, in-plane shear, and out-of-plane shear directions, respectively. The symbols  $t^o$  and  $\delta^o$  are the traction, and separation, respectively, when damage starts.  $\delta^f$  is the final separation when the crack totally fails. The first stage of the behavior of this model,  $\delta < \delta_n^o$ , is elastic until the stress approaches the maximum traction. The slope of this line is related to Young's modulus. Since there's only elastic strain in this stage, no damage is initiated. The second stage,  $\delta_n^o < \delta < \delta_n^f$ , is the softening law, which defines how the traction drops to zero as the displacement increases to the critical value (or the SERR approaches its critical value). Basically, there are two key parameters for the CZM: one is the maximum traction that defines the highest stress when a damage process starts, and the other is the fracture energy value that controlling the total damage of an element and the crack propagation. Actually, the area beneath the lines is the critical strain energy release rate (or fracture energy), as seen in Figure 2.3.

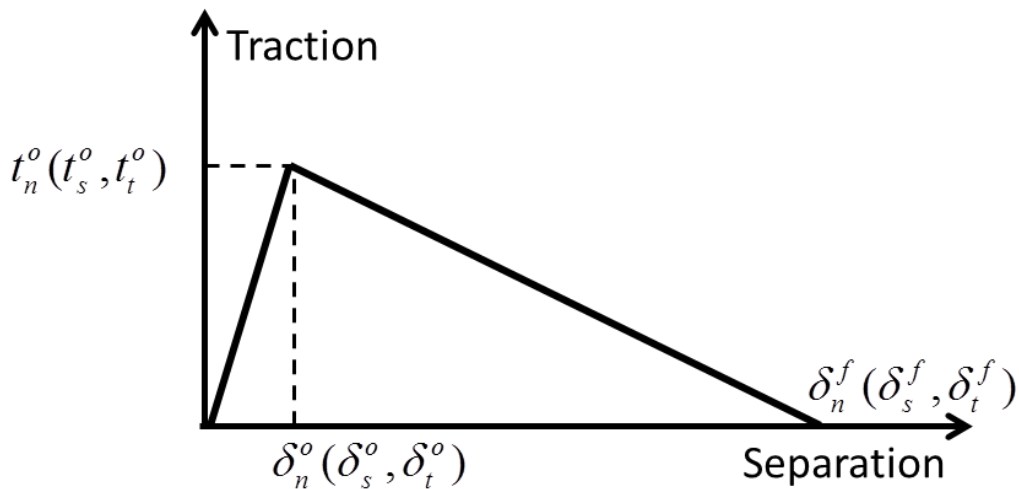


Figure 2.3. A typical traction-separation law.

The CZM is a theoretical approach to fracture process that consider scales larger than atomic or molecular, but smaller than macro-scale dimensions of the problem. Extraction of the maximum traction is evaluated empirically by comparison with the experimental results, and modified by further simulations. There are many ways to get the fracture energy value experimentally.

## 2.2 Material and experiments

The monolithic material, poly(methylmethacrylate) (PMMA), is a transparent thermoplastic, often used as a light weight alternative to glass. It is recommended because of its moderate properties, easy handling and processing, low cost, though is known for its brittle behavior. Therefore, linear elastic fracture mechanics can be applied to this material. The critical stress intensity factor of the PMMA was obtained by compact tension (CT) tests as suggested in ASTM D5045-99e1[10]. All tests were conducted on an Instron 5800R machine using a 5kN load cell. With one arm of the CT specimen fixed by a pin and clevis, the other arm of the specimen was displaced downwards by the other pin and clevis.

CT specimens were prepared with dimensions defined in Figure 2.4. Also, modified specimens, similar to the CT specimen but with different initial crack locations, initial crack lengths, and specimen lengths were prepared. In the latter specimens, the heights of the two loading beams are different, thus the loading is asymmetric (see Figure 2.5). The stress distribution near the crack tip involves a mixed fracture mode, and therefore different crack trajectories are observed. This simple modification of the standard CT configuration permitted investigation of several fracture phenomena. For each of the cases with different specimen lengths or initial crack lengths, three replicates were tested, which were machined from the same PMMA sheet by the same machine at almost the same time, and cut in the same orientation so as to avoid significantly different material properties.

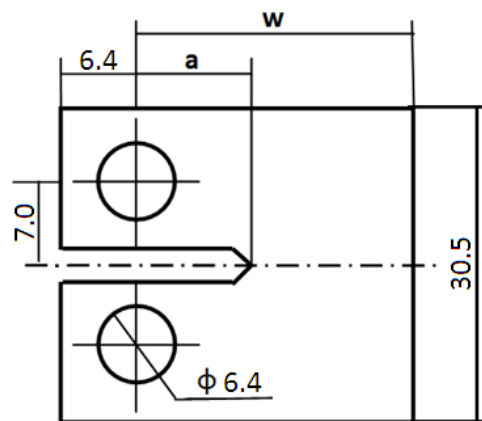


Figure 2.4. PMMA CT Specimen with  $w=25.4$ ,  $a=12.7$ , and thickness = 12.7 (all dimensions in mm).

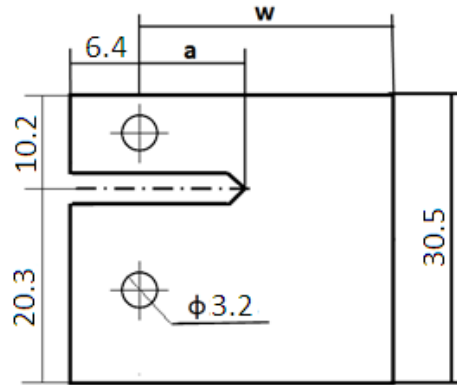


Figure 2.5. PMMA asymmetric CT specimens with  $w=25.4$ ,  $a=12.7$ , and the ratio of the height of the loading beam is 1:2; specimen thickness = 12.7 (all dimensions in mm).

A standard CT specimen is shown in Figure 2.6, with thickness,  $B=12.7\text{mm}$ ,  $w=25.4\text{mm}$  and  $a=12.7\text{mm}$ [10]. The tests were conducted using a crosshead displacement rate of 10 mm/min, as recommended in ASTM D5045-99e1. To ensure consistency in  $K_{Ic}$  values for all specimens, sharp initial cracks were required. The initial cracks were made carefully with a razor blade and a wooden hammer after machining the notches. One blade and two shims were inserted into a notch to center the blade and to keep it parallel to the centroidal axis of the notch, as seen in Figure 2.7. Then, gentle hammer blows were applied to the back of the blade, initiating a small crack, only a few millimeters in front of the blade. This process of precracking prevented a large initial crack from propagating too far into the specimen. The relationships between the load and the crosshead displacement for these specimens are shown in Figure 2.8. From these results, the average value of  $K_{Ic}$  is  $1.056 \pm 0.029 \text{MPa}\sqrt{\text{m}}$  was obtained. As expected, the crack trajectories remain straight as crack propagates across an entire specimen.

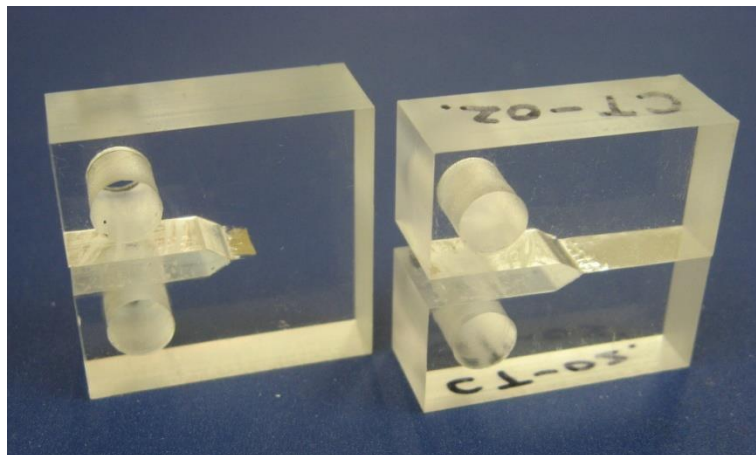


Figure 2.6. One CT specimen with precrack before a test, another one with a straight crack path after a test.

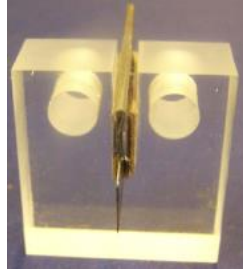


Figure 2.7. Pre-cracking the CT specimen with a blade and two shims.

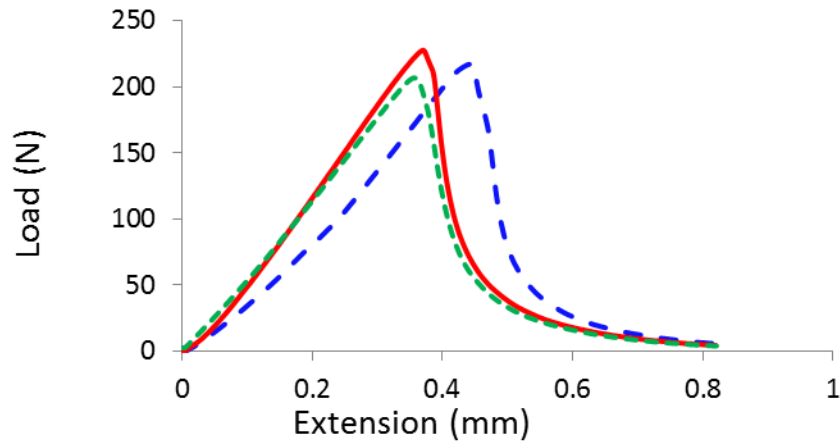
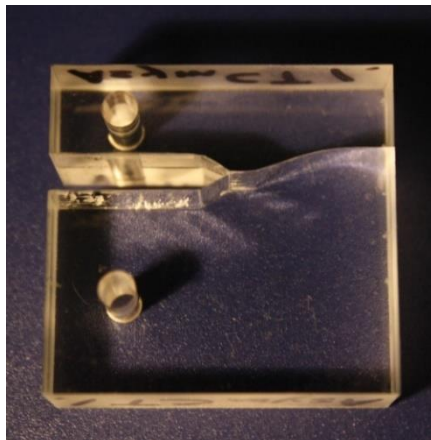


Figure 2.8. Load vs. extension curves for three CT specimens.

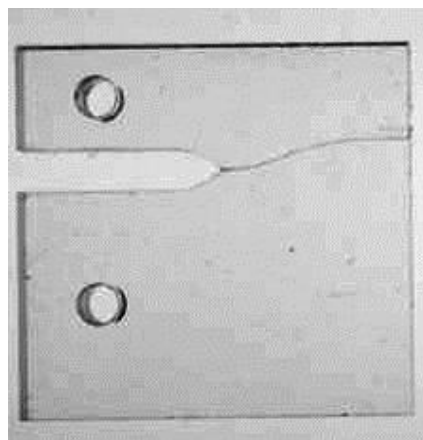
Unlike the specimens described above that have a notch placed along the horizontal centroidal axis, “modified” or “asymmetric” specimens with the notch and the starting crack not located along the horizontal centroidal axis were also tested. The ratio of the height of the loading beams is 2, and an untested specimen is shown in Figure 2.9a. In the modified specimen with stationary cracks, mode mixity exists because of asymmetry. Also, the diameter of the holes was reduced to 3.2 mm to make room for the notch. Because of the mode mixity, the crack veered in the direction of the thinner arm (on the top in Figure 2.9b). However, the crack path changed its direction and became straight (almost perpendicular to the right edge in Figure 2.9c) before the crack terminated at the edge. Additional details on this observation will be discussed in the following section on the simulations, and comparisons will be made with the numerical results.



(a)



(b)



(c)

Figure 2.9. An asymmetric CT specimen: (a) with notch and initial crack before the test, (b) with crack after the test, (c) the 2D projection on a scanner.

## 2.3 Simulation with XFEM

In this section, a similar configuration was modeled in the ABAQUS and the crack trajectory was simulated using the XFEM with traction-separation law, which is one of the applications of the CZM (cohesive zone model). The dimensions and material properties of the CT specimen are:  $W = 25.4\text{mm}$ ,  $2H = 30.5\text{mm}$ ,  $a = 12.7\text{mm}$ ,  $E = 3\text{GPa}$  and  $\nu = 0.4$ . The plane strain state was assumed to prevail in the CT specimens. We employed the crack initiation criterion used by Erdogan [11], i.e., a crack initiates when the maximum principal tensile stress reaches a critical value, which is also the default for the XFEM in ABAQUS.

After applying the parameters for the CZM, the predicted crack path was compared with the experimental results. The curves are quite close to each other and the XFEM worked successfully for the simulation of crack propagation in this monolithic generic polymer.

The XFEM implemented in ABAQUS® v6.9 using 4-node plane strain element, CPE4, was employed to analyze the deformations of the asymmetric CT specimen used in the experimental studies [12, 13]. Assigned boundary conditions is closely related to the test configurations. Two reference points in ABAQUS were assigned corresponding to the two contact points of the pins and holes. These two reference points were attached to the elements in the meshed model in ABAQUS. With the loading points shown in Figure 2.10, the following boundary conditions were used in the numerical simulation.

Load point 1: fixed in x and y directions:  $u_x = 0, u_y = 0$ ;

Load point 2: fixed in the x-direction but displacement in y-direction is prescribed:  $u_x = 0, u_y = -2\text{mm}$ .

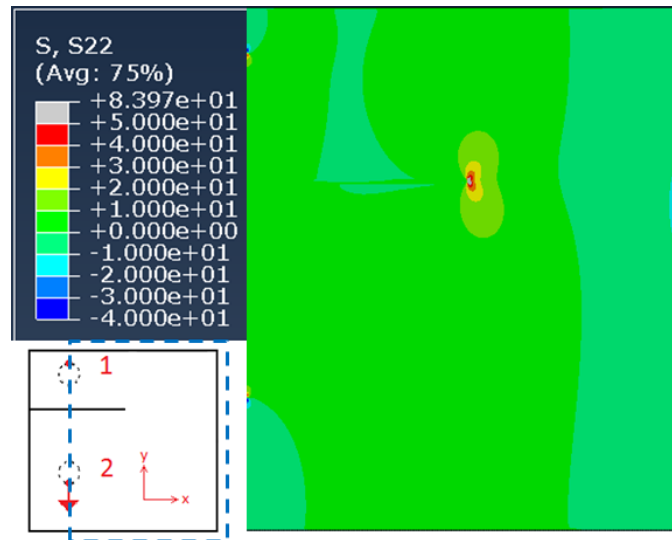


Figure 2.10. The boundary conditions, initial crack, and opening stress (i.e.  $\sigma_{yy}$  in MPa) for the asymmetric CT specimen. The contour showed stress singularity at the crack tip.

The boundary conditions were applied by an increase of -0.1 mm (negative means opening the lower beam downwards) in each steps until the crack propagated to the edge of the specimen (usually -1 mm for the CT specimens, and -2 mm for the asymmetric CT specimens). ABAQUS also provided several increments (or sub-steps, in other words) in each steps. The crack path selection processes is considered to be recorded with reasonable precision. Indeed, since cracking is an irreversible process, the accurate crack path will be recorded in the last step, even if the other steps are deleted.

From tensile tests on PMMA at a strain rate of 0.00014/s and room temperature, Elices and Guinea [14] obtained the following average values: Young's modulus  $E = 3GPa$ , yield limit stress (i.e. the 0.2% offset yield stress)  $\sigma_{0.2} = 43.9 \pm 0.7MPa$ , rupture stress  $\sigma_R = 74.9 \pm 0.2MPa$ , and Poisson's ratio  $\nu = 0.4$ . The maximum principal stress of the damage initiation (i.e. the maximum traction in CZM model) was set equal to the rupture stress  $\sigma_R = 74.9MPa$ . Damage evolution was determined based on the fracture energy

$$(\mathcal{G}_{Ic} = \mathcal{G}_{IIc} = \frac{K_{Ic}^2}{(E / (1 - \nu^2))} = 312.2J / m^2), \text{ linear softening, and mixed mode behavior of}$$

power law ( $\alpha=1$ ), which was commonly used in simulations [14]. The peak stresses in the followed simulations is around 260N when the characteristic element size is 0.2 mm. This peak load is close to the experimental results shown in Figure 2.8. The maximum traction value is chosen because of the agreement of the peak load in the experiments and the simulations, though there are a lot of arguments about whether the rupture stress can be used directly as the maximum traction or not[15]. Since the focus of this study is the crack path, sensitivity study about the maximum traction was not shown in this chapter. Three mesh sizes were applied and compared:  $0.5 \times 0.5$  mm,  $0.2 \times 0.2$  mm, and  $0.1 \times 0.1$  mm. The ABAQUS Documentation showed that, in XFEM with traction-separation laws, several increments will be calculated within one element. Therefore, we can usually find several small turnings in the crack path within single elements in some of the models. So the crack path selection is considered to be not significantly sensitive to the mesh size, because of the capability of changing crack direction when needed in each element. Therefore, as far as observed in these cases, the number of steps did make difference in the crack path or other computed results. Figure 2.11 shows that the crack path simulated with different mesh sizes are very close to each other.

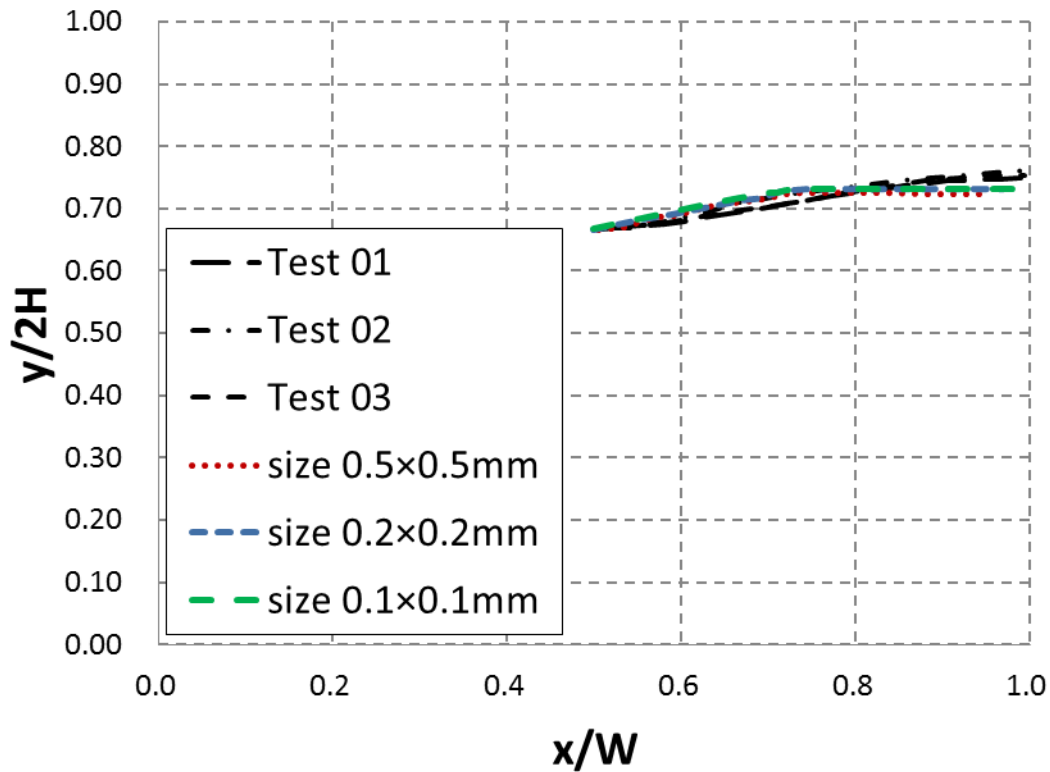


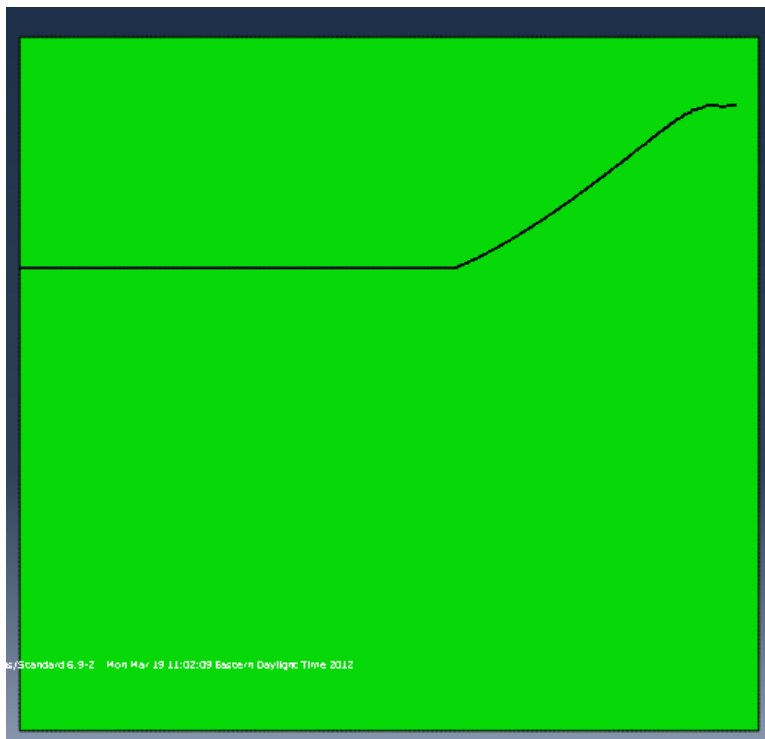
Figure 2.11. Crack path of the asymmetric CT specimen in the numerical simulation using XFEM,  $W$  is the length and  $2H$  is the height of the specimens.

When the crack starts to propagate, the crack veered gradually upwards, where the loading beam is thinner and more flexible. However, because the limitation of the dimensions of the specimen, the crack turns to the right edge thereafter and then stops. Similar to the standard CT specimens, the crack terminated at the right edge in Figure 2.9.

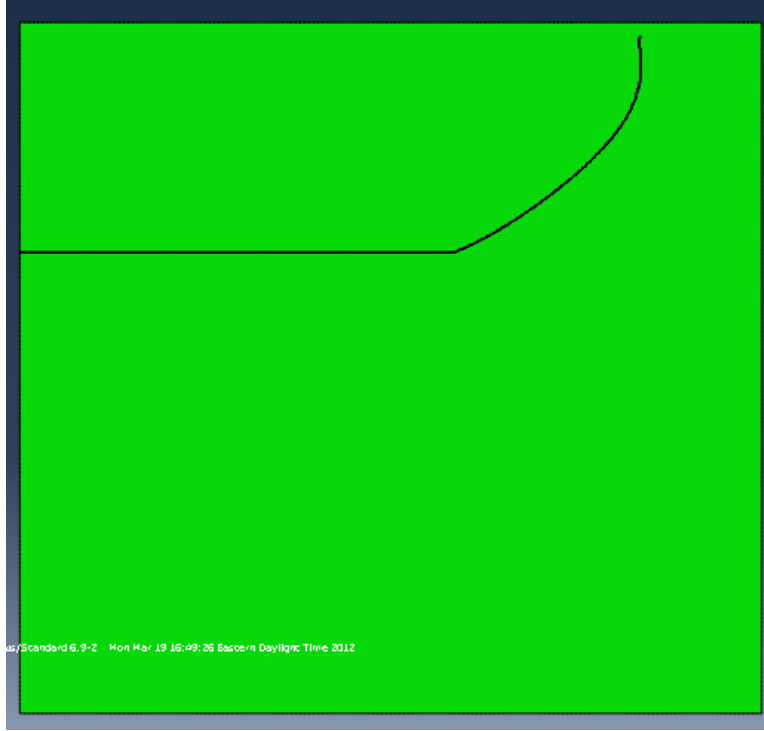
Also, a series of similar specimens were simulated in ABAQUS, with increased  $W$  but all the other lengths were the same, as seen in Figure 2.12. The reason for this increment is to find out a critical value of  $W$  that leads to different crack paths. By default in ABAQUS, the crack propagates normal to the direction of the maximum tangential stress. The numerical results showed that, when the value of  $W$  increases to 26.4 mm, the crack path should change dramatically. The length of the specimen altered the stresses in front of the crack tip: when the length is longer, the crack path tends to terminated on the top edge.



(a)



(b)



(c)

Figure 2.12. Simulated crack paths show dramatically different when  $W$  is (a): 25.7 mm, (b): 26.2 mm, (c): 26.4 mm.

After the prediction, three replicates were tested, and the crack paths are almost the same as those predicted in the simulations. When testing the specimens with the same size in the simulation (as in Figure 2.12c), some of the cracks approached the top edge, while the others approached the right edge. Evidently, this dimension is very close to the critical size for the switch of the crack paths.

The experiments were conducted using the critical specimen length ( $W = 26.4\text{mm}$ ) after the prediction by numerical simulations. By machining in the same orientation and at the same time, the dimensions of these asymmetric CT specimens were nearly identical, the resulting crack paths are shown in Figure 2.13. Due to the uncertainties in the experiments (e.g. the contact points between the pins and holes, the slight differences of the length of the precracks, etc.), some of the cracks terminated on the top, some of them terminated on the right, though the dimensions of these specimens are exactly the same. Thus the critical depth associated with the switch from one crack path to the other by ABAQUS predictions proved accurate for inducing the same effect experimentally.

In summary, since the agreement in the crack path selection is considered to be good, and the critical specimen length was predicted accurately, it is reasonable to conclude that, these models are reasonable for the study of crack path selection in monolithic materials. Of course, since the crack path selection and the critical specimen length are

not sensitive to  $T_{max}$ , the value of  $T_{max}$  may need to be adjusted when studying other topics, such as load-displacement curves.

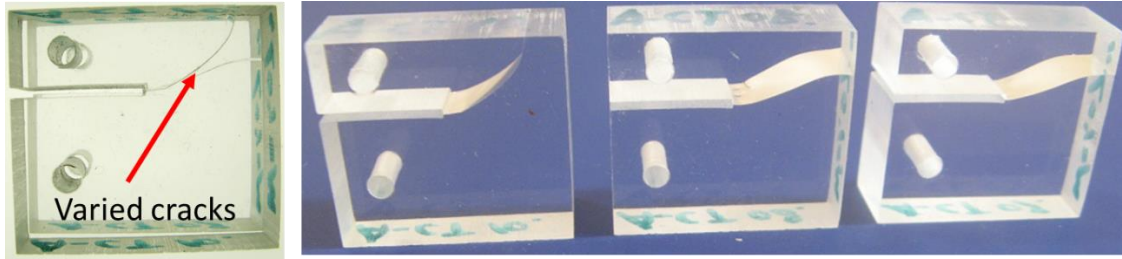


Figure 2.13. Varied crack paths after the tests of the asymmetric CT specimens machined in the same orientation of the PMMA sheet at the same time, with exactly the same dimensions and the critical specimen length (26.4 mm).

To complete the validation study, the effects of longer specimens and shorter initial crack lengths were also evaluated. The ratio of the specimen length and the initial crack length ( $W/a$ ) was expected to be important for the directional stability of cracking, since they would change the sign of the T-stress. Accordingly, more PMMA specimens with different values of  $W/a$  were tested. The crack length was varied from 12.7mm (0.5”), to 25.4mm (1”), and 38.1mm (1.5”) while the value of  $W=101.6$  mm (4”) remained constant; thus  $w/a$  equaled 8, 4, and 2.67. The other dimensions were as same as those of the CT specimen. The crack paths are shown in Figure 2.14.



Figure 2.14. Trajectories of the crack paths in the specimens with different initial crack lengths (From top to bottom:  $a = 12.7$ mm, 25.4mm, and 38.1mm.)

As the ratio,  $W/a$ , was varied from 8, to 4, and 2.67, the crack path deviated towards one side. The curvatures of the three cracks were almost the same. For the specimens with  $a=25.4$ mm and 38.1mm, ( $W/a \leq 4$ ), the crack curved to one side immediately upon propagation. However, when the initial crack length was 12.7mm ( $W/a=8$ ), the crack

propagated along a straight line for almost 20mm before the deviation. Since the critical specimen lengths has been predicted by ABAQUS, some longer specimens were considered to be more or less redundant. The further works in ABAQUS, especially those simulation in longer specimens, were suspended.

## **2.4 Conclusions**

The XFEM in ABAQUS was employed in the simulations of the crack path selection in some CT specimens made of PMMA. It was shown that the parameters, with assumed value of maximum traction and experimental data of fracture energy, work accurately for the simulations of the crack path selection in monolithic material.

Asymmetric CT specimen models were developed in ABAQUS and the influence of the specimen lengths was investigated. To determine the direction of crack propagation in ABAQUS, the direction of crack propagation is determined by the maximum tangential stress.

Due to the asymmetry of the initial crack location, the moving crack veers to the thinner loading beam. When the length of the modified CT specimen is short, the crack path tends to terminate to the edge opposite to the initial crack (the right edge in Figure 2.12). When the longer versions of the modified CT specimen are use, the crack path tends to terminate at the edge of the thinner beam (the top edge in Figure 2.12). The critical specimen length was predicted by the simulation and agree well with the subsequent experimental results.

## 2.5 References

- [1] B. Cotterell and J. R. Rice, "Slightly Curved or Kinked Cracks," *International Journal of Fracture*, vol. 16, pp. 155-169, 1980.
- [2] V. F. Erdogan and G. C. Sih, "On Crack Extension in Plates Under Plane Loading and Transverse Shear," *Trans. ASME J. Bas. Eng.*, vol. 85, pp. 519-527, 1963.
- [3] K. Palaniswamy and W. G. Knauss, "On the Problem of Crack Extension in Brittle Solids Under General Loading," *Mechanics Today*, vol. 4, pp. 87-148, 1978.
- [4] R. V. Goldstein and R. L. Salganik, "Brittle Fracture of Solids with Arbitrary Cracks," *International Journal of Fracture*, vol. 10, 1974.
- [5] A. R. Akisanya and N. A. Fleck, "Brittle-Fracture of Adhesive Joints," *International Journal of Fracture*, vol. 58, pp. 93-114, NOV 15 1992.
- [6] P. H. Geubelle and W. G. Knauss, "Crack-Propagation at and near Bimaterial Interfaces - Linear-Analysis," *Journal of Applied Mechanics-Transactions of the Asme*, vol. 61, pp. 560-566, SEP 1994.
- [7] J. W. Hutchinson and Z. Suo, "Mixed-Mode Cracking in Layered Materials," *Advances in Applied Mechanics, Vol 29*, vol. 29, pp. 63-191, 1992.
- [8] E. Giner, N. Sukumar, J. E. Tarancón, and F. J. Fuenmayor, "An Abaqus implementation of the extended finite element method," *Engineering Fracture Mechanics*, vol. 76, pp. 347-368, 2009.
- [9] R. D. S. G. Campilho, M. D. Banea, F. J. P. Chaves, and L. F. M. da Silva, "eXtended Finite Element Method for fracture characterization of adhesive joints in pure mode I," *Computational Materials Science*, vol. 50, pp. 1543-1549, Feb 2011.
- [10] ASTM-D5045-99e1, "Standard Test Methods for Plane-Strain Fracture Toughness and Strain Energy Release Rate of Plastic Materials," in *Annual Book of ASTM Standards*, ed West Conshohocken, PA, 2007.
- [11] K. Hibbitt, Sorensen, Inc., *ABAQUS/standard user's manual, v.6.9*. Pawtucket, Rhode Island, 2009.
- [12] E. Giner, Sukumar, N., Tarancon, J. E., Fuenmayor, F. J., "An ABAQUS implementation of the extended finite element method," *Engineering Fracture Mechanics*, vol. 76, pp. 347-368, Feb. 2009.
- [13] M. Elices, Guinea, G. V., "The cohesive zone model: advantages, limitations, and challenges," *Engineering Fracture Mechanics*, vol. 69, pp. 137-163, 2002.

- [14] B. R. K. Blackman, H. Hadavinia, A. J. Kinloch, and J. G. Williams, "The use of a cohesive zone model to study the fracture of fibre composites and adhesively-bonded joints," *International Journal of Fracture*, vol. 119, pp. 25-46, Jan 2003.
- [15] F. Erdogan, and Sih, G. C. , "On the crack extension in constraint effects in plates under plane loading and transverse shear," *Trans. ASME, J. Bas. Engng*, vol. 85 D, pp. 525-527, 1963.
- [16] ABAQUS 6.11 Documentation Section 11.4.2 [Online].

# Chapter 3 The intrinsic role of strain energy in 2D bridging problem and the subsequent multiple parallel propagating debonds in beam-like joints

---

(Paper prepared for submission to the *International Journal of Solids and Structures*)

## Abstract:

When layered materials are separated beyond their capacity, in some situations, a debond may occur along one interface for some distance, and then switch to the other one, leaving in the wake an interlayer bridge suspended between the two sides. Such bridges can detrimentally affect demolding in manufacturing processes, alter the apparent fracture energy in test specimens, and induce other anomalous behavior. A framework for analyzing such bridging phenomena is presented and an analysis is then performed for a specific application corresponding to common double cantilever beam specimens (DCBs) or to prying action of molds to remove a product for a manufacturing process. This paper analyzes this scenario and related phenomena by taking the strain energy of the adhesive bridge into account. The strain energies stored in the suspended bridge and the two adherends are added together to calculate the total strain energy release rate (SERR). The differences between the bridging model and no-bridge model were compared. Characteristic increasing SERR curves of the three debond tips were plotted and compared when the external load is increasing. The one with the highest SERR value would prevail in the competition, and will propagate if it reach the fracture energy. This chapter summarized some common phenomena for several given combinations of several initial crack lengths, and stiffness of the adherends. Three cases are presented and discussed, aiming to cover a range of bridging problems found in practical situations covering a range of adherend or mold stiffnesses. The bridging analysis presented herein could be helpful in studying demolding processes for soft materials, e.g. hydrogels, where weak adhesion can result in erratic debonding from both interfaces and possible tearing of the molded product. The discussions could also benefit the analysis of the parallel bridging situations in composite materials.

## Keywords:

Strain energy release rate, double cantilever beam, bridging, fracture energy, simple beam theory, adhesive bond, demolding, mold release.

## 3.1 Introduction

Interfacial failures are not uncommon in certain adhesively bonded structures. When the bonding surfaces are unintentionally weakened by dirt/oil/water, or degraded by long-term or cyclic exposure to critical environments. Specifically, if a weak interfacial area

forms ahead of the initial crack, the debonding process will usually jump to that weak area, leaving a bridge suspended between the two adherends. Related examples can be found in manufacturing of polymer products, where debonding from mold surfaces is typically required (as shown in Figure 3.1). Inconsistent mold surfaces, local temperature variations, curved surfaces, and other factors may lead to bridging of the molded product between the two mold halves. Fracture (tearing) of the product is often an unacceptable outcome. Even if fracture of the bridge does not occur, inelastic deformation of the bridge, including those near the crack tips, can damage sensitive products, leading to higher reject rates.

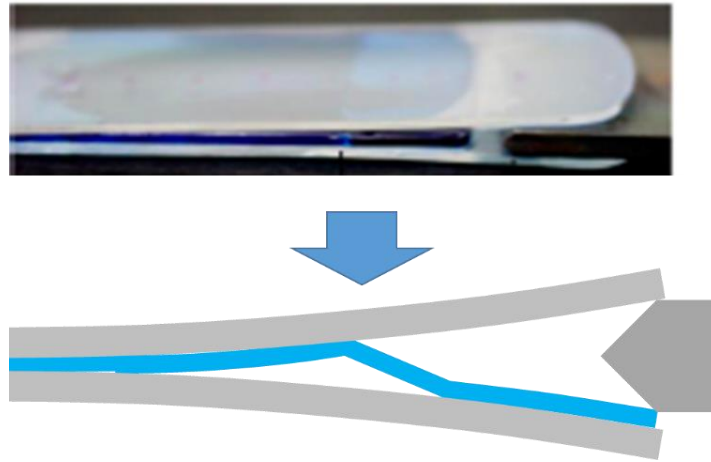


Figure 3.1. Bridging problem in a wedge test of hydrogel with stiff substrates (a schematic is also shown so as to clarify the multiple debonds).

Bridging phenomena have also been observed when splitting orthotropic materials such as wood or composite materials. For example, if  $0^\circ$  laminates are tested as DCB specimens, fiber bridging may significantly increase the apparent interlaminar toughness[1]. In this case, the bridges make relatively small angles with respect to the crack faces, as shown in Figure 3.2. In fact, when the load is removed, these bridges are nominally parallel to the crack.

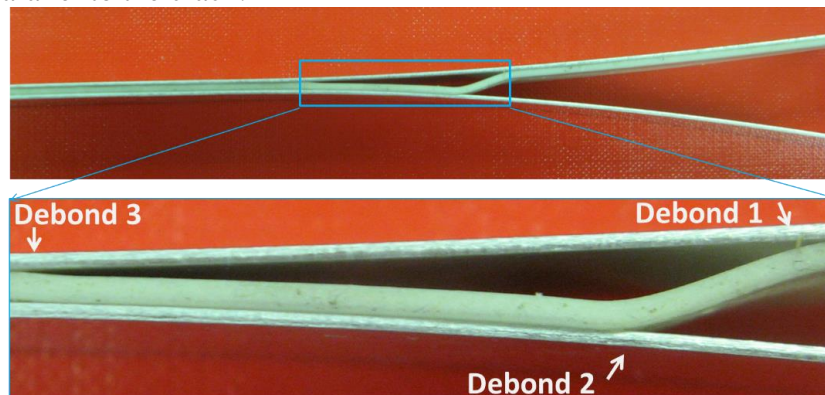
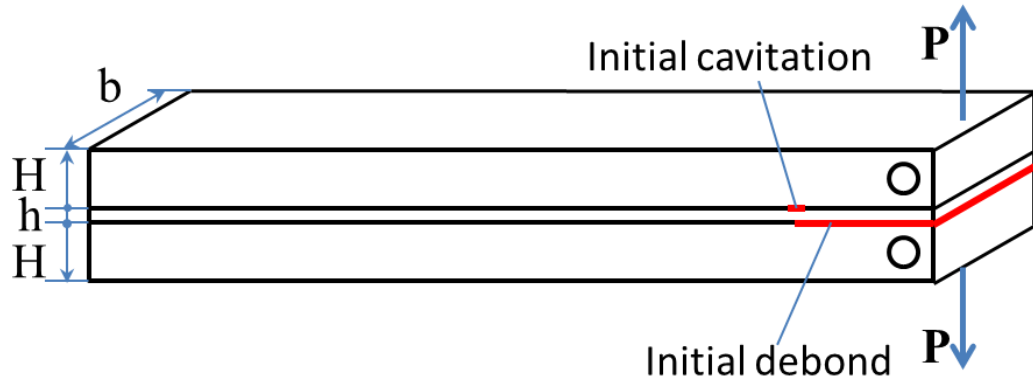


Figure 3.2. Bridging problem in DCB test with weak surfaces and strong adhesive layer (flexible aluminum adherends were used to obtain large opening in the picture, but the deflection is usually very small in a real DCB test). The adhesive layer is VHB® tape purchased from 3M®, St. Paul, MN, USA.

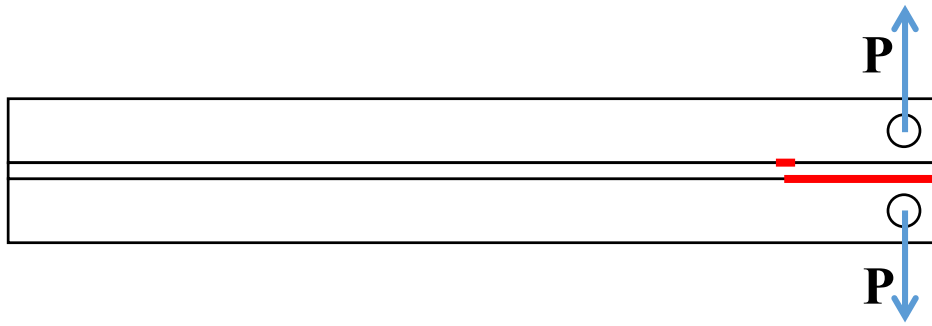
Another area of considerable interest has been in the bridging of cracks by one phase in multiphase materials, including rubber or thermoplastic modified polymers and fiber reinforced composites. Rubber particles, which are widely used to improve the toughness of brittle polymers, may contribute toughness through shear band formation, cavitation, and bridging [2]. Ceramic materials can be significantly toughened by adding fiber reinforcement. In many cases, both the matrix and fibers are quite brittle, and yet a weak interface between the fiber and matrix allows for slippage and substantial energy dissipation in the materials. The fibers that bridge the crack faces exert tractions on the failed surfaces, and reduce the effective stress intensity at the crack tip [3, 4].

Therefore, there is interest in understanding the bridging problem, and for manufacturing process, controlling debond propagation if possible. A useful model for this study is the adhesively bonded, double cantilever beam (DCB) configuration, with relatively weak interfaces and an extensible adhesive layer. When bridging occurs in such geometries, evaluation of the results are complicated by the presence of the bridge. The tractions on the crack faces in the wake of the crack tip can have a significant effect on the strain energy release rate (SERR). The tractions normal to the crack plane have been used for making corrections for plasticity, often assuming that it equals the yield stress of the material [5, 6]. A number of investigators have analyzed various aspects of these fiber bridging phenomena, but most have focused on the case where the fibers are perpendicular to the crack plane [7-9], or have considered a distribution of fiber orientation angles and estimated the averaged effects by statistical means [10, 11]. These fibers or bridges also increase the apparent toughness of the material, but the mechanics are quite different from the bridges that are almost parallel to the crack plane, and only the latter will be considered in the present work.

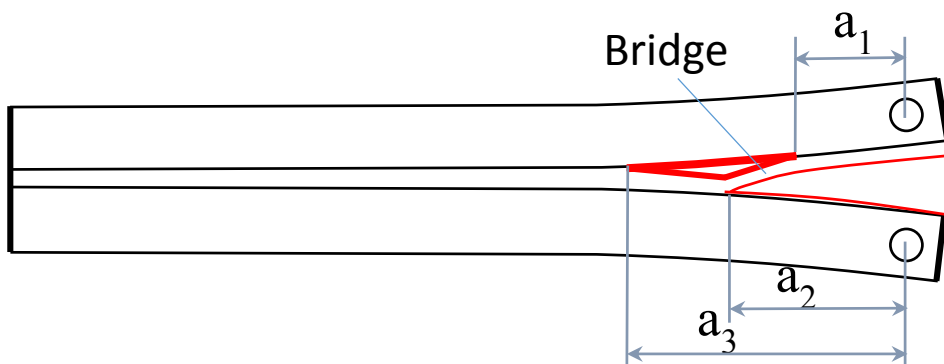
When a DCB specimen is loaded, the crack may propagate along one interface for some distance, and then a second crack may initiate along the opposite interface. Continued loading will result in both cracks propagating, leaving behind a suspended adhesive bridge at a relatively shallow angle with respect to the adherends. This phenomenon is sometimes encountered when testing DCB specimens displaying interfacial failures with an adhesive which has sufficient extensibility to bridge the crack without failure. In this paper, we present an analysis of small angle bridging in DCB adhesively bonded joints, as shown in Figure 3.3. If a two-dimensional representation is appropriate, the bridge results in three debonded interfacial cracks and the crack lengths  $a_1$ ,  $a_2$ , and  $a_3$  are defined as shown in Figure 3.3c. The traction has one vertical component,  $T \sin \alpha$ , that reduces the deflection of the adherends, and one horizontal component,  $T \cos \alpha$ , that results in an eccentric load applied to the adherends that can exert extra bending moments in the adherends. These bending moments will be investigated, although the axial tension or compression in the adherends will be assumed to be negligible. Therefore, the problem can be simplified as shown in Figure 3.3d.



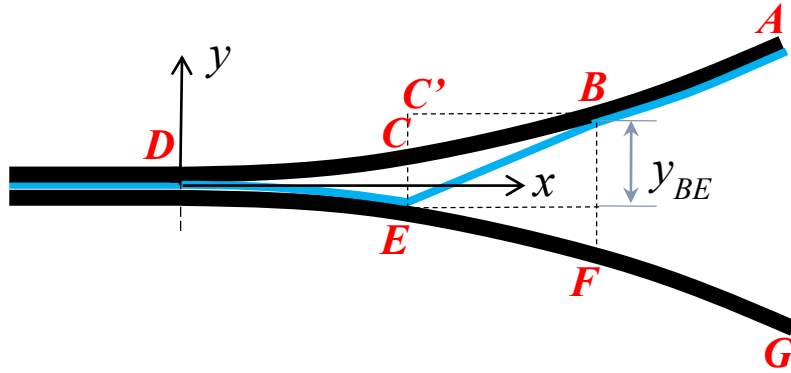
(a)



(b)



(c)



(d)

Figure 3.3. Model of the adhesive bridging problem with geometric parameters and external loads: (a) Schematic of the initial debond and cavitation; (b) 2D view of the model; (c) Appearance of the bridge and definition of three crack lengths; (d) Cantilever beam models, definition of coordinate system and points.

The DCB configuration studied herein may be an idealization of a demolding process, or can represent a common fracture test that is often used to measure adhesion. In practice, this bridge is often relatively uniform across the width of the specimen, permitting a 2D analysis as is presented herein. The bridging mechanism enhances the apparent toughness of the bond because the bridge carries a portion of the load, reducing the applied energy release rate at the longest crack tip. The analysis extends the analysis presented in [12].

In the following section, using Euler-Bernoulli beam theory, the deflections of the beams (adherends) are calculated when the external load, material properties, and geometries are given. The strain energy release rates (SERRs) of the debonds, as well as the strain of the bridging, are calculated by using the deflections of each point. Based on these calculations, the increase of the SERRs and thus the crack propagation sequences are discussed in this chapter.

## 3.2 Analysis

### 3.2.1 2D bridging DCB model

The suspended adhesive bridge is modeled as a linear elastic membrane, assuming that the flexural rigidity is small because of the small thickness of the bridge compared to other dimensions in the model. The two adherends are also assumed to obey linear elastic behavior. As shown in Figure 3.3b, the adhesive bridge exerts equal and opposite tractions  $T$  on the upper and lower adherends. The analysis of this model involves the external load  $P$ , internal force  $T$  exerted by the bridge, and the bridging angle  $\alpha$ . The bridging angle is defined to be the angle between the adhesive bridge and the bond plane of the un-deformed specimen, so  $\alpha$  is the same for both adherends in Figure 3.3b. Note

that this bridging angle is different from and larger than the beam rotation angle  $\theta$ , which is commonly used in beam theories, and assumed to be small.

The adherends are assumed to be identical, resulting in a flat DCB specimen that, except for the bridge, appears to be symmetric and globally loaded in mode I. The adherends as well as the bond are assumed to have a width of  $b$ . The thickness of the adhesive bridge is  $h$ . Ignoring deflections within the bonded adhesive layer, the adherends can be considered to be cantilever beams fixed at the crack tip 3 as root rotation and deflection are not considered. Based on Euler-Bernoulli beam theory, the differential equations can be given and then solved using appropriate boundary conditions at points A, B, D, E, and G.

First consider the upper beam with modulus and second moment of area,  $E$  and  $I$ , respectively. From point D to B,  $0 \leq x \leq (a_3 - a_1)$ , we define  $M^-$ ,  $\theta^-$ , and  $y^-$  to represent the bending moment, rotation angle, and vertical deflection, respectively. Similarly, from point B to A,  $(a_3 - a_1) \leq x \leq a_3$ ,  $M^+$ ,  $\theta^+$ , and  $y^+$  are defined to represent the bending moment, rotation angle, and deflection, respectively. With the coordinate system defined in Figure 3.3 and origin at point D, the derivation can be started from the shear force

equation for Euler-Bernoulli beam theory:  $EI \frac{d^3y}{dx^3} = EI \frac{d^2\theta}{dx^2} = \frac{dM}{dx} = V(x)$ . Therefore,

$$\frac{dM^-}{dx} = -(P - T \sin \alpha) \quad (3.1)$$

$$\frac{dM^+}{dx} = -P \quad (3.2)$$

Applying boundary conditions  $M^+_{x=a_3} = 0$ ,  $M^-_{x=a_3-a_1} = M^+_{x=a_3-a_1} - T \cos \alpha \left(\frac{h}{2} - y_B\right)$ ,

$M^+_{x=a_3} = 0$ ,  $\theta^-_{x=0} = 0$ ,  $\theta^+_{x=a_3-a_1} = \theta^-_{x=a_3-a_1}$ ,  $y^-_{x=0} = 0$  and  $y^+_{x=a_3-a_1} = y^-_{x=a_3-a_1}$ , we obtain the rotation angle and beam deflection by integration in several steps. The solutions of the deflections are given by

$$y_{upper} = \begin{cases} \frac{P}{EI} \left( \frac{a_3 x^2}{2} - \frac{x^3}{6} \right) - \frac{T \sin \alpha}{EI} \left( \frac{(a_3 - a_1) x^2}{2} - \frac{x^3}{6} \right) - \frac{T \cos \alpha}{EI} \left( \frac{H}{2} - y_B \right) \frac{x^2}{2} & (0 < x \leq a_3 - a_1) \\ \frac{P}{EI} \left( \frac{a_3 x^2}{2} - \frac{x^3}{6} \right) - \frac{T \sin \alpha}{EI} \left( \frac{(a_3 - a_1)^2 x}{2} - \frac{(a_3 - a_1)^3}{6} \right) + \frac{T \cos \alpha}{EI} \left( \frac{H}{2} - y_B \right) \left( \frac{(a_3 - a_1)^2}{2} - (a_3 - a_1) x \right) & (a_3 - a_1 < x \leq a_3) \end{cases} \quad (3.3)$$

$$y_{lower} = \begin{cases} -\frac{P}{EI} \left( \frac{a_3 x^2}{2} - \frac{x^3}{6} \right) + \frac{T \sin \alpha}{EI} \left( \frac{(a_3 - a_2) x^2}{2} - \frac{x^3}{6} \right) - \frac{T \cos \alpha}{EI} \left( \frac{H}{2} + y_E \right) \frac{x^2}{2} & (0 < x \leq a_3 - a_2) \\ -\frac{P}{EI} \left( \frac{a_3 x^2}{2} - \frac{x^3}{6} \right) + \frac{T \sin \alpha}{EI} \left( \frac{(a_3 - a_2)^2 x}{2} - \frac{(a_3 - a_2)^3}{6} \right) + \frac{T \cos \alpha}{EI} \left( \frac{H}{2} + y_E \right) \left( \frac{(a_3 - a_2)^2}{2} - (a_3 - a_2) x \right) & (a_3 - a_2 < x \leq a_3) \end{cases} \quad (3.4)$$

Thus deflections at each point can be calculated. In this model, the vertical displacements of points B and E are given by,

$$y_B = \frac{P}{EI} \left( \frac{a_3 (a_3 - a_1)^2}{2} - \frac{(a_3 - a_1)^3}{6} \right) - \frac{T \sin \alpha}{EI} \frac{(a_3 - a_1)^3}{3} - \frac{T \cos \alpha}{EI} \left( \frac{H}{2} - y_B \right) \frac{(a_3 - a_1)^2}{2} \quad (3.5)$$

$$y_E = -\frac{P}{EI} \left( \frac{a_3 (a_3 - a_2)^2}{2} - \frac{(a_3 - a_2)^3}{6} \right) + \frac{T \sin \alpha}{EI} \frac{(a_3 - a_2)^3}{3} - \frac{T \cos \alpha}{EI} \left( \frac{H}{2} + y_E \right) \frac{(a_3 - a_2)^2}{2} \quad (3.6)$$

Similarly, the deflection of points A and G are given by,

$$y_A = \frac{P}{EI} \frac{a_3^2}{3} - \frac{T \sin \alpha}{EI} \left( \frac{(a_3 - a_1)^2 a_3}{2} - \frac{(a_3 - a_1)^3}{6} \right) + \frac{T \cos \alpha}{EI} \left( \frac{H}{2} - y_B \right) \left( \frac{(a_3 - a_1)^2}{2} - (a_3 - a_1) a_3 \right) \quad (3.7)$$

$$y_G = -\frac{P}{EI} \frac{a_3^2}{3} + \frac{T \sin \alpha}{EI} \left( \frac{(a_3 - a_2)^2 a_3}{2} - \frac{(a_3 - a_2)^3}{6} \right) + \frac{T \cos \alpha}{EI} \left( \frac{H}{2} + y_E \right) \left( \frac{(a_3 - a_2)^2}{2} - (a_3 - a_2) a_3 \right) \quad (3.8)$$

In order to simplify the problem, we assume that

$$\tan \alpha = \frac{C'E}{BC'} \approx \frac{y_B - y_E}{a_2 - a_1} \quad (3.9)$$

In this assumption, we neglected the beam foreshortening and took  $BC = BC'$ , which is also consistent with Euler-Bernoulli beam theory with small deflections. Also, it is worth noting that, if the adherend rotation angle  $\theta$  is very small (or  $BC \cong BC'$ ), this 2D model would be accurate enough to simulate the debond propagation, no matter how large the bridging angle  $\alpha$  is.

The axial extension of the bridge is written as

$$\delta_a = \sqrt{(a_2 - a_1)^2 + (y_B - y_E)^2} - (a_2 - a_1) \quad (3.10)$$

The bridging force is

$$T = \sigma A = (E_a \varepsilon)(bh) = (bhE_a) \frac{\delta_a}{(a_2 - a_1)} = bhE_a \left( \sqrt{1 + \left( \frac{y_B - y_E}{a_2 - a_1} \right)^2} - 1 \right) \quad (3.11)$$

where,  $A = bh$  is the cross-sectional area of the bridge and  $E_a$  is the effective modulus. In this equation, plane stress is assumed, though plane strain condition can also be applied by replacing  $E_a$  by  $E_a / (1 - \nu_a^2)$ , where  $\nu_a$  is the Poisson's ratio of the adhesive.

Substituting equations (3.9) and (3.10) into equations (3.5) and (3.6), we have two equations with two variables,  $y_B$ , and  $y_E$ . Though there is no simple analytical solution, the equations can be solved numerically using appropriate software such as Mathematica (Wolfram, Champaign, IL). Then the bridging angle, extension of the bridge, and the traction can be calculated by using equation (3.9), (3.10), and (3.11), respectively.

### 3.2.2 Strain energy release rate in the bridging model

Since the traction  $T$  is an internal force, the external work performed on the specimen enters solely through the displacement of load  $P$ , which was considered to be applied by a load frame with one adherend fixed and the other one moved. Therefore, a quasi-static loading condition is considered in this model, with the external forces assumed to remain constant. Based on the definition, the SERR equals the difference in the variations of the external work and the strain energy in this system.

The strain energy,  $U_s$ , is stored in the two adherends,  $U_{a-up}$  and  $U_{a-low}$ , as well as the bridge,  $U_b$ . The strain energy increment in the linear elastic bridge is

$$dU_b = T d\delta_a = T \left( \frac{d\delta_a}{da_1} da_1 + \frac{d\delta_a}{da_2} da_2 + \frac{d\delta_a}{da_3} da_3 \right) \quad (3.12)$$

In general, the SERR for this system may be given by

$$\mathcal{G} = \frac{1}{b} \left( \frac{dU_e}{da} - \frac{dU_s}{da} \right) = \frac{1}{b} \left( \frac{dU_e}{da} - \frac{dU_{a-up} + dU_{a-low} + dU_b}{da} \right) = \frac{1}{b} \left( \frac{dU_p}{da} \right) - \frac{1}{b} \left( \frac{dU_b}{da} \right) \quad (3.13)$$

where,

$$\frac{1}{b} \frac{dU_p}{da_i} = \frac{1}{b} \frac{dU_e - dU_{a-up} - dU_{a-low}}{da} = \frac{1}{b} \int_0^P \left( \frac{dy_A}{da_i} - \frac{dy_G}{da_i} \right) dP, \quad (i = 1, 2, 3, \text{ no summation.}) \quad (3.14)$$

This equation (3.14) is just the familiar definition of SERR for traditional DCB specimens. Therefore, equation (3.13) is a similar result but with the last term added to

account for the strain energy stored in the bridge. Note that the definition of  $a_1$  is different from the other two crack lengths, and  $a_1$  decreases when this crack propagates (see Figure 3.3). Thus,  $da_1 < 0$  and a negative sign should be added in  $G_1$ . Thus, the SERR for crack 1 is

$$G_1 = \frac{1}{b} \left( \frac{dU_e}{-da_1} - \frac{dU_s}{-da_1} \right) = -\frac{1}{b} \left( \frac{dU_p}{da_1} - \frac{dU_b}{da_1} \right) = -\frac{1}{b} \left( \int_0^P \left( \frac{dy_A}{da_1} - \frac{dy_G}{da_1} \right) dP - T \frac{d\delta_a}{da_1} \right) \quad (3.15)$$

Similarly, the other two SERRs are

$$G_i = \frac{1}{b} \left( \frac{dU_e}{da_i} - \frac{dU_s}{da_i} \right) = \frac{1}{b} \left( \int_0^P \left( \frac{dy_A}{da_i} - \frac{dy_G}{da_i} \right) dP - T \frac{d\delta_a}{da_i} \right), \quad (i = 2, 3, \text{ no summation.}) \quad (3.16)$$

This 2D analysis provides analytical expressions of the bridging problem. These equations were obtained easily by using Euler-Bernoulli beam theory and linear elastic approach without losing much accuracy if the adherend rotation angle is small. Based on the equations presented previously, numerical results and discussions on the factors to the crack propagation sequence are now shown.

### 3.3 Results and discussions

Since it is difficult to solve the equations analytically, numerical results are shown with some assumed materials and geometric properties are applied to the 2D linear elastic model. Numerical solutions for SERRs were found using an incremental approach in Mathematica®, with an assumed numerical crack increment of  $\Delta a = 0.1mm$ . Graphs are shown for several given material properties and crack lengths. Adherends with width  $b = 25.4mm$ , and thickness  $H = 12.7mm$  are used, which is consistent with the DCB specimen with flat adherends used in ASTM D 3433[13]. Also, a thickness  $h = 0.25mm$  is assumed for the adhesive layer, as well as the resulting bridge. The discussion is divided into two parts:

- (1) Response to the external loads when there's no crack propagation;
- (2) The propagation sequence when a fracture energy value is introduced.

#### 3.3.1 Load and response without crack propagation

In this section, the adherends were loaded and the adhesive bridge was extended elastically, but there was no debond propagation and thus each crack kept its initial length. Based on the deflections calculated by the equations shown previously, the SERR curves were also calculated by numerical integration. For illustration purposes in the present section, three cases were studied and details are shown in Table 3.1. The non-

dimensional ratios indicate the stiffness of bridge/adherend ( $\frac{4E_a h a_1^3}{EH^3(a_2 - a_1)}$ ), and the critical debond strain of the bridge ( $\sqrt{\frac{G_c}{E_a h}}$ ). These cases were proposed to cover a range of bridging problems that might be encountered in practice.

Table 3.1. Three cases studied in the present work.

	Adherends	Adhesive & bridge	Simulate	$\frac{4E_a h a_1^3}{EH^3(a_2 - a_1)}$	SRBA *	$\sqrt{\frac{G_c}{E_a h}}$	CDS **
Case 1	70GPa	3GPa	DCB with metal adherends	3.3e-1	medium	5e-3	medium
Case 2	3GPa	3GPa	DCB with polymer adherends	7.6e0	large	5e-3	medium
Case 3	3 GPa	0.3MPa	Demolding process	7.6e-4	small	5e-1	large

\* SRBA: Stiffness ratio of bridge/adhesive;

\*\* CDS: Critical debond strain.

First we consider the differences between the models with and without the bridge. Obviously, the case of no-bridge is the well-known simple beam theory (SBT) result, which can be calculated easily within the present formalism when traction  $T = 0$ . In order to compare these two models by the same criteria, regardless of whether a bridge exists, the crosshead displacement is defined as  $\Delta = y_A - y_G$ . Suppose point G is fixed and the external load P is applied on point A. Since the traction is resisting the separation of point A and G, the deflection is smaller for the bridging model than for the no-bridge model. One of the examples in Case 1 is shown in Figure 3.4 when one set of initial values of the three crack lengths is assumed.

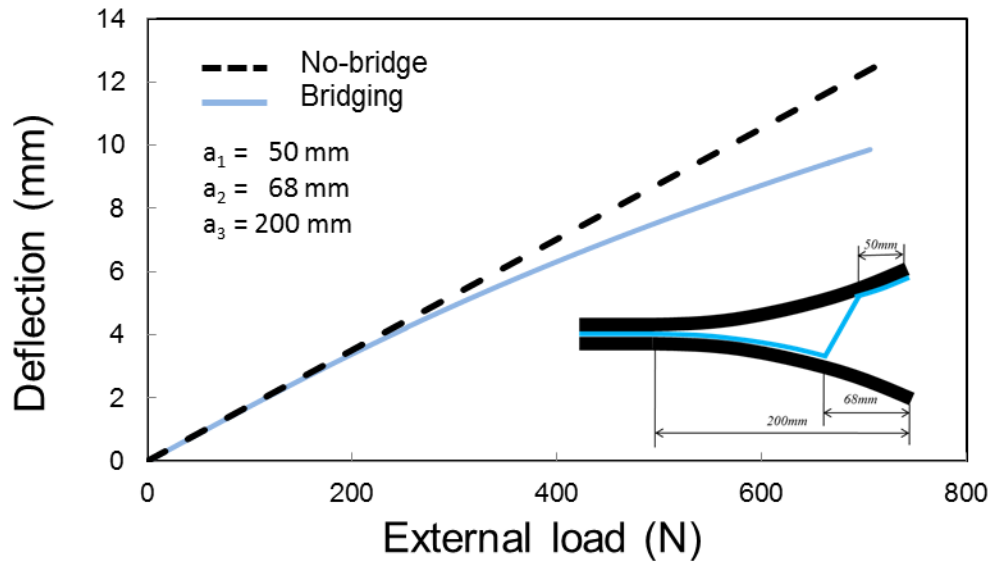


Figure 3.4. Crosshead displacement for bridge and no-bridge model with the same external loads, with a set of crack lengths for Case 1.

Also, the position and length of the bridge are important. When loaded to the same crosshead displacement, the external load required for the bridging model is higher than that of no-bridge model. And also, a more significant difference in the external load in force is found when the bridge is farther away from the tip of crack 3. For example, the crosshead displacements are set to be  $5\text{mm}$  for both no-bridge and bridging model, and cracks 1 and 2 are assumed to be fixed ( $a_1 = 50\text{mm}$ ,  $a_2 = 68\text{mm}$ ), the external load and bridging force were calculated for different values of  $a_3$ . When the length of crack 3 is longer, the external load required is smaller because the specimen is more flexible. Also, the difference in external load is more significant, and the bridge traction is higher when crack 3 is longer. This trend is shown in Figure 3.5 for Case 1, and Figure 3.6 for Case 2.

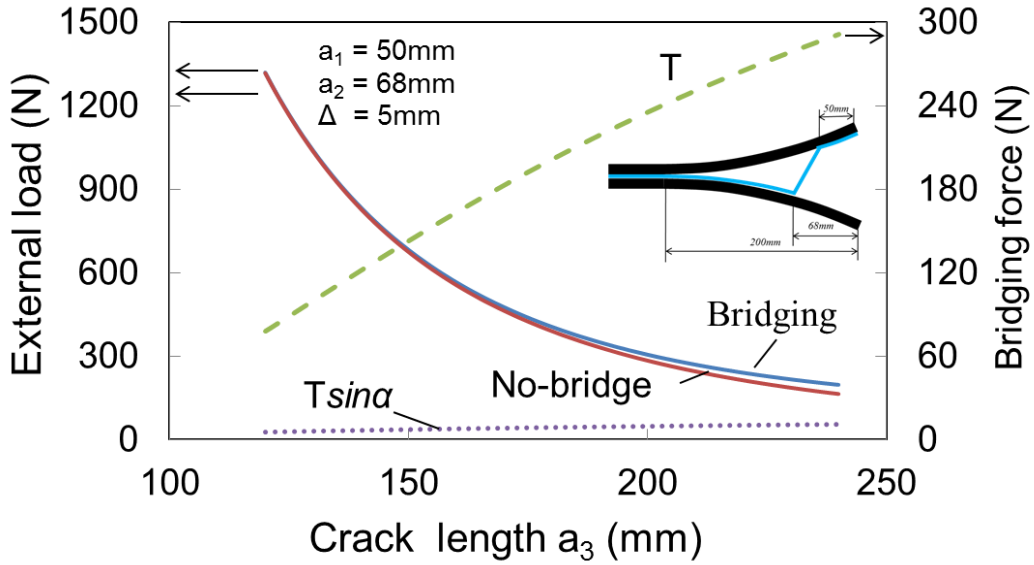


Figure 3.5. Comparison of loads for both bridging and no-bridge model for Case 1 when the length of crack 3 is changed from 120 mm to 240 mm, the crosshead displacements are set to be 5 mm for both no-bridge and bridging model.

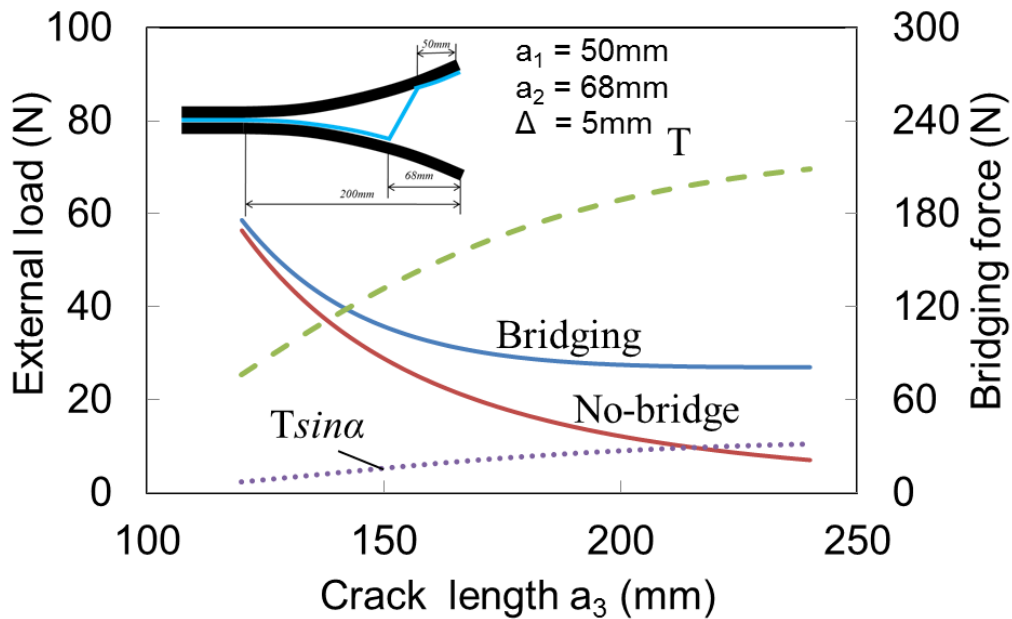


Figure 3.6. Comparison of loads for both bridging and no-bridge model for Case 2 when the length of crack 3 is changed from 120 mm to 240 mm, the crosshead displacements are set to be 5 mm for both no-bridge and bridging model.

If  $a_1 = 50\text{mm}$ ,  $a_2 = 68\text{ mm}$ , and  $a = a_3 = 200\text{mm}$  are assumed, the SERRs of the three cracks as functions of  $P$  are shown in Figure 3.7 (Case 1), Figure 3.8 (Case 2), and Figure 3.9 (Case 3). In these three figures,  $G_i$  is the SERR values at crack  $i$  ( $i = 1, 2, 3$ ),  $G_I$  is the SERR for no-bridge model that is also plotted for comparison.

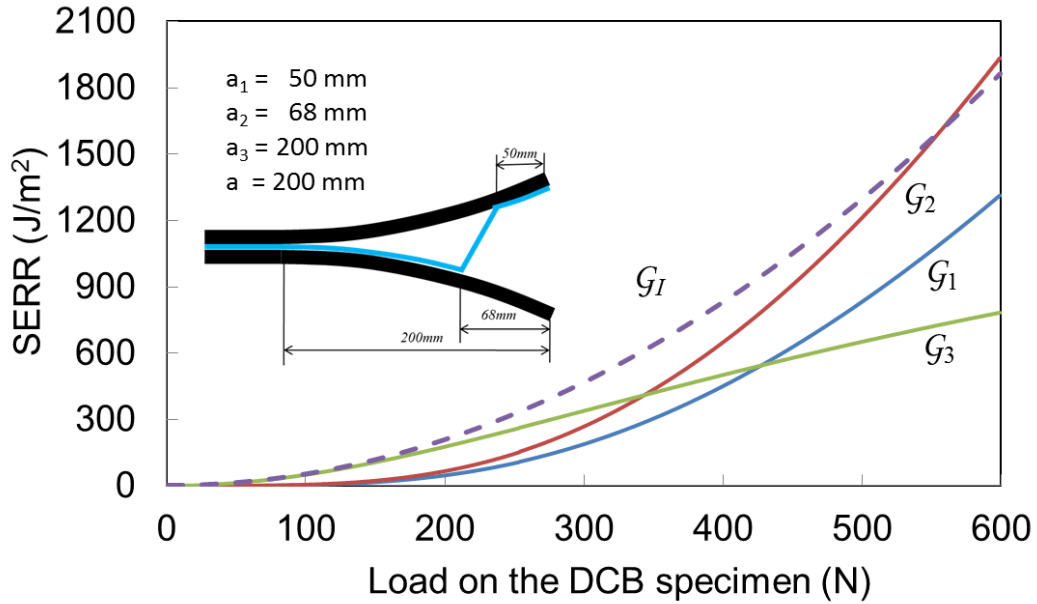


Figure 3.7. SERR curves for the three cracks as functions of the external load for Case 1.

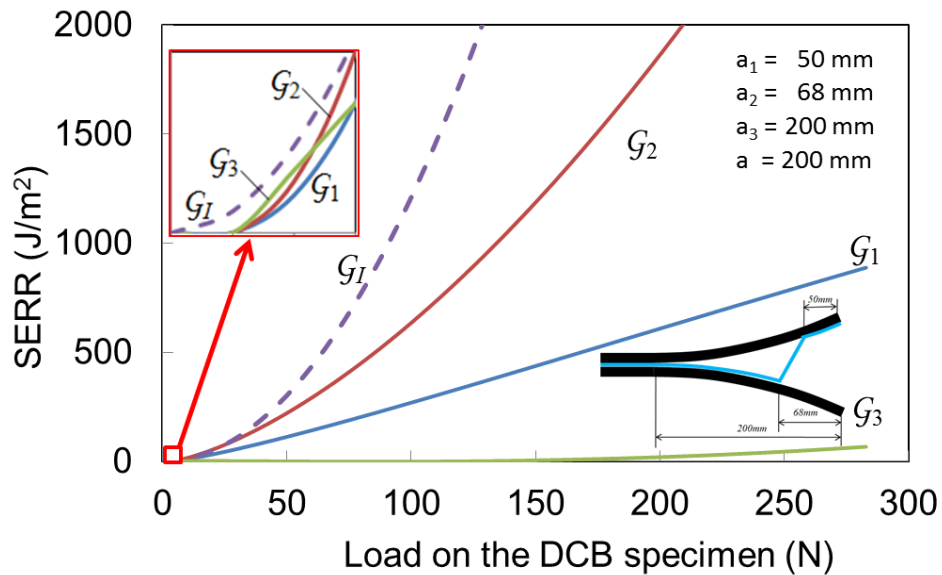


Figure 3.8. SERR curves for the three cracks as functions of the external load for Case 2.

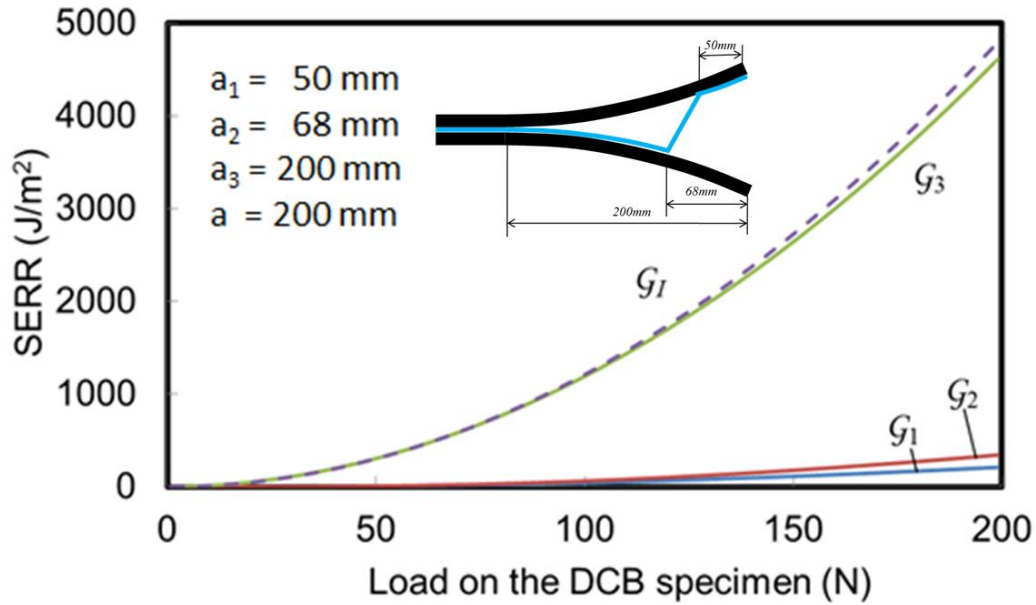


Figure 3.9. SERR curves for the three cracks as functions of the external load for Case 3.

Figure 3.7 shows that, obviously, the three SERR curves are different from each other. Results calculated from other crack length configurations showed similar trends:  $G_2$  is always higher than  $G_1$ ;  $G_3$  is higher than  $G_2$  at the beginning but intersects the other two curves and becomes lower thereafter. With the same geometry, similar trends are found in Figure 3.8 for Case 2, though the intersection is so early that  $G_2$  is mostly the highest curve in Case 2. In Figure 3.9 for Case 3, the bridge is so flexible that the traction is almost negligible,  $G_3$  is always the highest one.

Through a series of calculations with different crack lengths, one observes that, without crack propagation, there is an intersection between curves  $G_2$  and  $G_3$ . These intersections showed the critical value of  $P$  and SERR, where the competition between  $G_2$  and  $G_3$  comes to a draw. Therefore, this point provides another view to summarize the similarity for different cases, independent of the size or stiffness of the adherends or bridge. Between the origin and the intersection,  $G_3$  is higher than  $G_2$ , but lower beyond the intersection. The similar trends facilitate the analysis of the intersections by altering the variables. Some of the examples were calculated by solving equations and then connected in Figure 3.10, where there was no propagation in crack 1 or crack 2. Eleven cases were calculated with  $a_3$  ranged from  $75\text{mm}$  to  $85\text{mm}$ . When altering the crack lengths, stiffness, etc., the shapes and trends of the three SERR curves are similar. This plot is presented to facilitate the understanding, and thus the following discussions on prediction of the crack propagations.

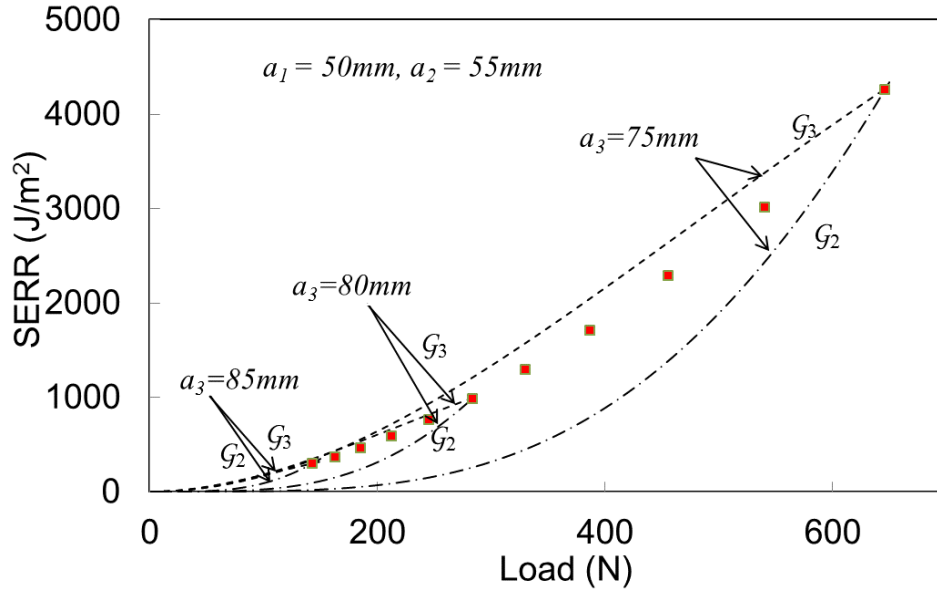


Figure 3.10. Intersections with different length of crack 3 (lengths of crack 1 and 2 are fixed).

### 3.3.2 Prediction of the crack propagation sequence

Since we were studying the bridging problem, only interfacial failure was considered in the present work. In addition to the understanding of the loads, deflections, and individual SERRs of bridged specimens, this bridging model is useful to predict the crack propagation sequence for the three debond tips. When the load is increased, the SERRs at the three debond tips increase but at different rates. If a critical value of the SERR (or fracture energy  $\mathcal{G}_c$ ) that is independent of mode mixity is assumed for the interfaces, the curve that first reaches this limiting value will lead to the initial debonding event. A discussion of this assumption is shown at the end of this chapter. Therefore, if  $\mathcal{G}_c$  for both aluminum/epoxy and polymer/epoxy interfaces are taken to be  $300\text{ J} / \text{m}^2$ , then  $a_3$  will propagate first in Figure 3.7 and 3.9, but  $a_2$  will propagate first in Figure 3.8. In order to plot the full propagation sequence, the calculations have to be repeated using the new set of crack lengths after each step.

One such propagation sequence for Case 1 is shown in Figure 3.12, with interfacial fracture energy  $\mathcal{G}_c = 300\text{ J} / \text{m}^2$ . An initial short bridge and three subsequent crack lengths are assigned before simulation begins. Assume  $a_2 = 51\text{mm}$  when crack 1 and crack 3 emerged on the upper adherend. Therefore, without loss of generality, it is reasonable to assume  $a_1 = 50\text{mm}$  and  $a_3 = 52\text{mm}$  so that there is a small debond on the interface. In these calculations and iterations, the same increment of crack lengths in each numerical step was assumed ( $0.1\text{mm}$ ). When the crosshead displacement increases,  $\mathcal{G}_3$  increases quickly to  $\mathcal{G}_c$  and Crack 3 propagates first. After Crack 3 reaches a critical length,  $\mathcal{G}_3$  will be a

little lower than  $G_2$ . Therefore,  $G_2$  will be the first to reach  $G_c$  and Crack 2 propagates. The process will continue with the competition between  $G_2$  and  $G_3$  driving the propagation of crack 2 and crack 3 in a step by step fashion. This process is similar to a competition among the three crack tips, as shown in the schematic in Figure 3.11: the first one who reaches  $G_c$  wins in the competition and propagates by  $0.1\text{mm}$  in each numerical step. Since the value of  $G_1$  is always smaller than  $G_2$ , crack 1 will never propagate. Also, since the steps of the propagation are very small, it was found that both crack 2 and crack 3 effectively propagate simultaneously but with different rates.

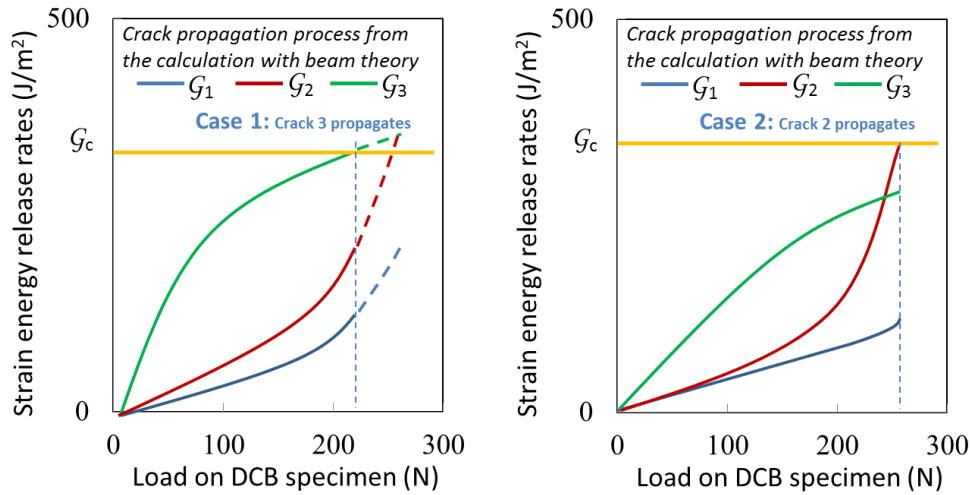


Figure 3.11. Schematic of the competition between  $G_2$  and  $G_3$  for two cases ( $G_1$  is always lower than the others, thus crack 1 is never predicted to propagate).

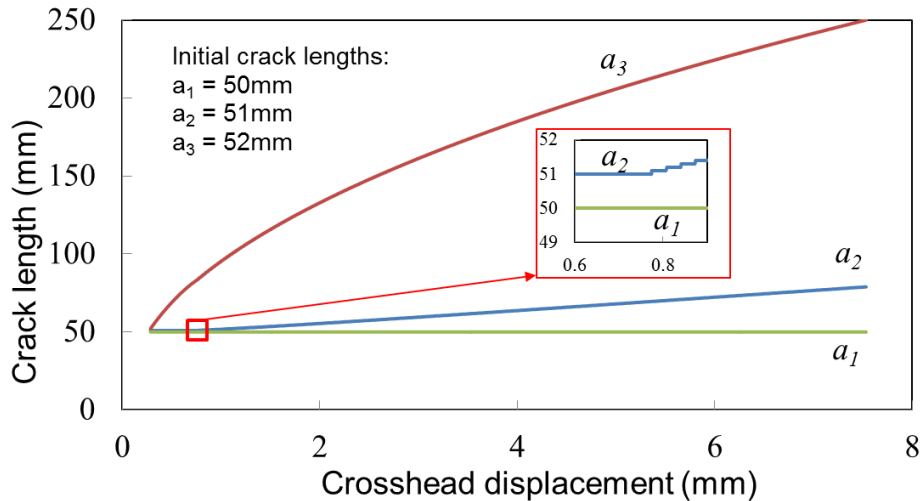


Figure 3.12. Crack propagation sequence calculated when the adherends were opened in Case 1 (with initial crack lengths assumed to be 50 mm, 51 mm, and 52 mm for crack 1, 2, and 3, respectively).

In order to compare the results with the no-bridge model, the relationships of  $\Delta$  vs.  $P$  were plotted in Figure 3.13 for Case 1 and Figure 3.14 for Case 2. Assumptions were the same as those for Figure 3.12, and the relative error of fracture energy was calculated with respect to  $G_c = 300J/m^2$ . Therefore, with a bridging problem, the error of recorded mode I fracture energy will be larger when the distance between crack 2 and crack 3 is longer. Since  $T$  and  $P$  were of the same magnitude in Case 2, the error was even larger. The oscillation of the curves results from the round off in numerical process and the assumption of propagation step of  $0.1mm$ . The kink in the load curves with bridging, and the relative error curves in Figure 3.13 are due to the start of propagation of crack 2 when the crosshead displacement is  $0.77\text{ mm}$  in Case 1. A similar kink is found in Figure 3.14 when crack 2 start to propagate when the crosshead displacement is  $2.2\text{ mm}$  for Case 2.

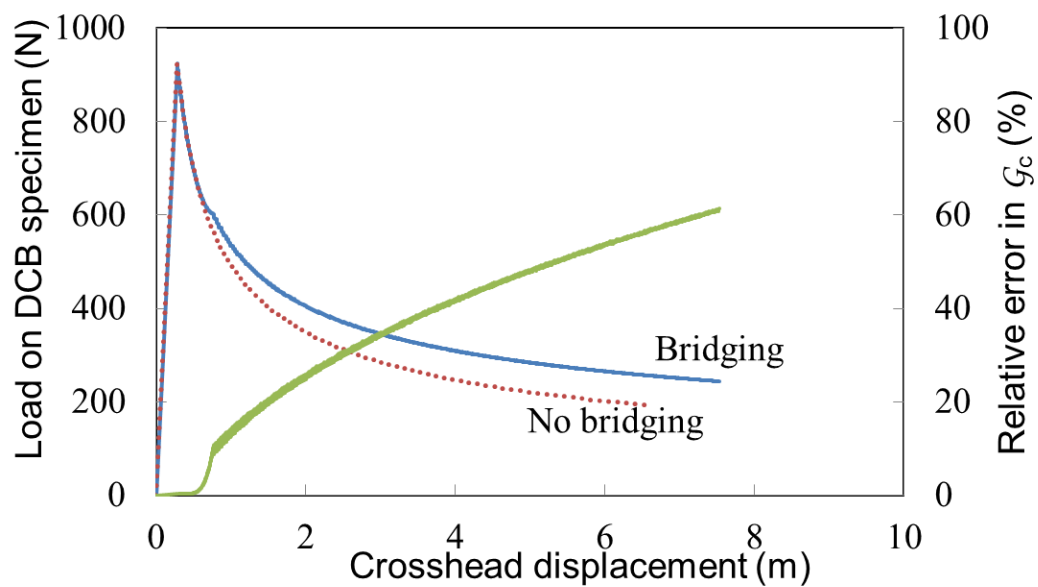


Figure 3.13. Crosshead displacement vs. load curves for Case 1 in both bridging and no-bridge model (the plots were stopped when crack length reached 250 mm).

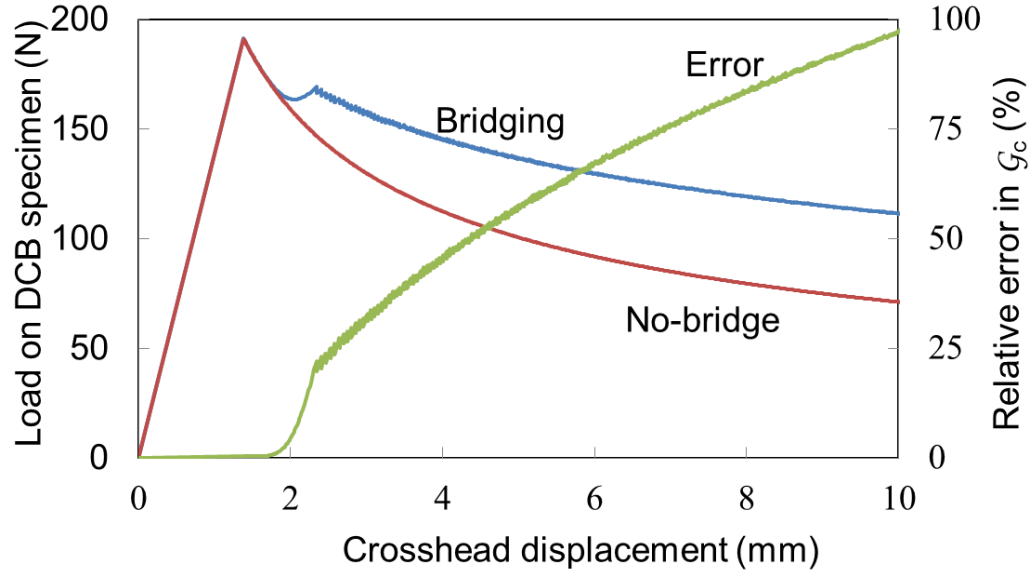


Figure 3.14. Crosshead displacement vs. load curves for Case 2 in both bridging and no-bridge model (the plots were stopped when crosshead displacement reached 10 mm).

Similar plots for Case 2 are also shown in Figure 3.12. Since the modulus of the adherends and bridge are the same, the traction and external load were similar in magnitude, the error was even larger. In Case 3, since  $G_3$  is always the highest one, and the bridging traction is so small, the propagation sequence is almost the same as for no-bridge model. Thus, the plots for Case 3 were not provided in this discussion. For a systems in which the modulus ratio (adherend to adhesive) is very large, the effect of bridging is going to be negligible. In summary, the criterion is provided by comparing the fracture energy  $G_c$  and the  $G$  at interception points. Refer to Figure 3.11, if  $G_c$  is always much lower than  $G$  at all the interception points in the entire propagation sequence, then only crack 3 propagates.

The other similarity can be found if the crack propagation sequences with various initial crack length configurations are plotted (Figure 3.15 for Case 1 and Figure 3.16 for Case 2). Small initial bridging (short debond on the opposite interface) similar to that of Figure 3.12 is assumed. Take  $a_1 = 40mm$  for example, the values of  $a_2$  and  $a_3$  are  $41mm$  and  $42mm$ , respectively. The figures show that, when the model is determined by some fixed  $a_2$ , and a small initial bridging is assumed on the upper adherend, there is theoretically a fixed relationship between  $a_2$  and  $a_3$ . For the cases considered herein, crack 3 will propagate first at the beginning and then the rate will decrease, while crack 2 will usually hold at the beginning and then propagate faster. This point of view can also provide useful predictions to the crack propagation sequences.

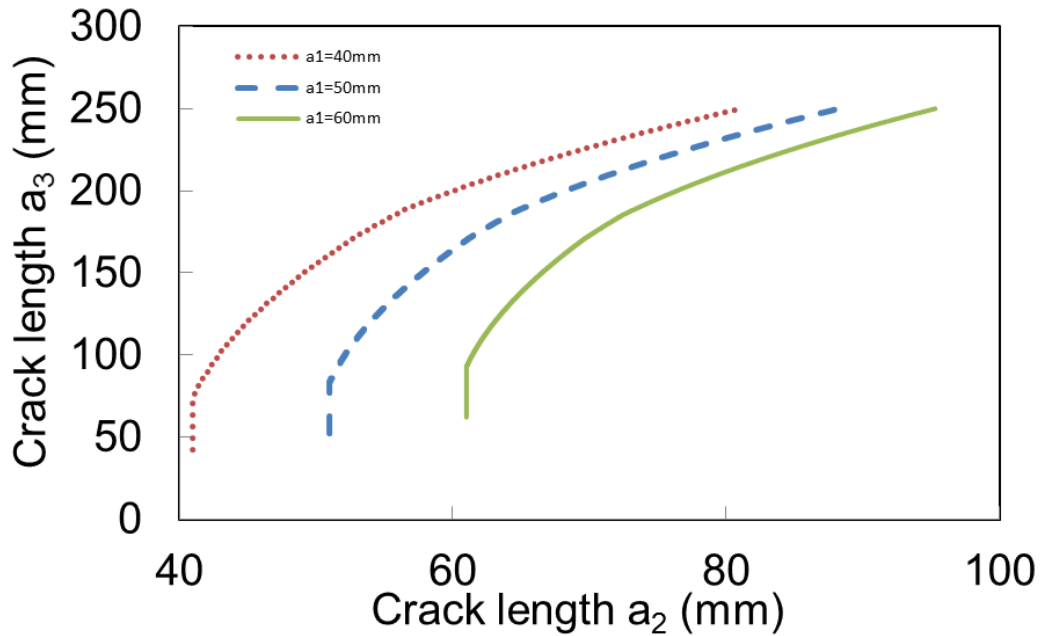


Figure 3.15. The relationships between the lengths of crack 2 and crack 3 when propagating from several specified initial crack lengths for Case 1.

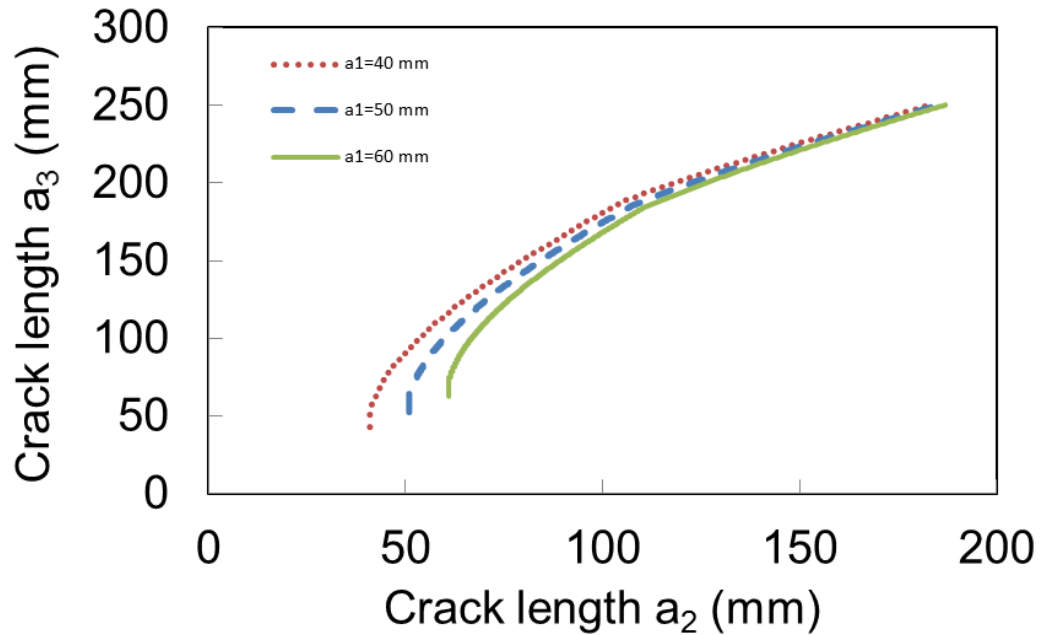


Figure 3.16. The relationships between the lengths of crack 2 and crack 3 when propagating with several different initial crack lengths for Case 2.

This investigation is believed to offer a framework useful for understand the crack propagation sequences for various material and geometric scenarios in many cases. For

example, if there is a bridging problem in the demolding process and we would like to have crack  $a_2$  to propagate first, flexible adherends can be considered (similar to the one in Figure 3.6 for Case 2).

### 3.3.3 Discussions on other nonlinear effects

Note that as stated in the analysis section, the calculations are still valid when the bridging angle is very large provided the beam deflection angles are relatively small. Essentially, the error comes from the overestimation of the length  $(a_2 - a_1)$  and thus the underestimation of  $\tan \alpha$  in equation (3.9). Therefore, in most of the cases, the crosshead displacement openings are small, simple beam theory is still valid, and the error is negligible. The actual length of the beam can be estimated by

$$\int_0^{a_3-a_1} \cos \theta_{upper} dx - \int_0^{a_3-a_2} \cos \theta_{lower} dx \approx \int_{a_3-a_2}^{a_3-a_1} \cos \theta_{upper} dx = (a_2 - a_1) \cos \hat{\theta} \quad (3.17)$$

$\theta_{upper}$  and  $\theta_{lower}$  are beam rotation angle function of the upper and lower adherends, respectively.  $\hat{\theta}$  is the average of them. Obviously,  $\theta_{upper}|_{x=a_3-a_2} < \hat{\theta} < \theta_{upper}|_{x=a_3-a_1}$ . Since the difference between them is very small, estimation can be taken by considering them to be almost equal. For the rotation angles at  $x = (a_3 - a_1)$  smaller than  $10^\circ$ ,  $\cos \hat{\theta} > 0.985$  and the relative error is

$$\frac{(a_2 - a_1) - (a_2 - a_1) \cos \hat{\theta}}{(a_2 - a_1) \cos \hat{\theta}} = \frac{1 - \cos \hat{\theta}}{\cos \hat{\theta}} < \frac{1}{\cos 10^\circ} - 1 \approx 1.5\% \quad (3.18)$$

Due to the geometric nonlinearity, this 2D model could not provide very accurate prediction of crack propagation sequences for the cases when the crosshead displacements are extremely large. The calculations and plots showed that the geometric nonlinearity dominated the relationships and interaction between the three cracks (actually the two longer cracks). And it is noteworthy that some other nonlinear effects could also alter the debonding process. The effects of peeling angle, mode mixity, adhesive layer thickness, and loading rates are some important concerns worth discussing for this bridging problem.

- (1) In this model, crack 3 is constrained by the two stiff adherends and can be still considered to be loaded globally in mode I. The mode mixity due to the mismatch of the two materials exists but will not change, thus the value of the fracture energy will not change during the debonds propagation processes. Crack 2 can be considered to be peeling off from the adherend, and the peeling angle is

$\left( \alpha + \theta_{upper}|_{x=a_3-a_2} \right)$ , which is usually less than  $90^\circ$ . Many researchers have shown that the local peeling angle at the crack tip will be much smaller than the applied peeling angle. Kinloch[14] had discussed the peeling of flexible laminates and the

effect of mode mixity. They tested several material systems and discussed these effects. It was shown that if the dissipated energy due to bending of the peeling arm is taken into account, the values of the corresponding fracture energy values are not significantly dependent upon the applied peeling angle. This local peeling angle is related to the work-hardening representation for the stress vs. strain curve of the adhesive/membrane, and calculated in [14]. Usually, the change of the local peeling angle is limited even if the remote peeling angle changes from  $0^\circ$  to  $180^\circ$ . Therefore in this chapter, since the remote peeling angle is usually less than  $90^\circ$ , the local peeling angle is considered to be very small at the crack tip [14].

- (2) Kinloch also discussed the effects of mode mixity and thickness of the adhesive layer experimentally, showing that these factors will not introduce significant differences in the fracture energy values. Though there is the mismatch of material properties and a mode mixity on the interface due to the Dundur's parameter, the mode mixity angle would not change significantly during the debonding processes. Kinloch stated that, if the pure mode I and mode II values of fracture energy were indeed deduced by some method, it might well be found that they are equal. Hence, no significant effect of the mode mixity would be expected on the measured value of fracture energy[14].
- (3) But the study on the loading rate showed that the fracture energy values for peel tests will decrease when the rate is low[14]. At very low velocities, the values approach that of the thermodynamic work of adhesion, which is a direct measure of the molecular bonding forces[14]. Therefore, the real fracture energy value will be lower when we decrease the crosshead displacement rate. This indicated that, if the crosshead opening rate is very slow for crack 2 (e.g. loaded by some designed jigs, or special methods), it may help crack 2 to propagate farther than expected. Details about this is beyond the focus of this chapter, since more information on the material properties, interface properties, apparatus, etc. need to be specified.

### 3.4 Conclusions

The interlayer bridging problem was studied by using a 2D DCB model with a linear elastic adhesive bridge suspended between the two adherends. Based on simple beam theory and linear elastic material behavior, the beam deflections, bridge strains, and SERRs of the cracks were calculated for aluminum/epoxy, polymer/epoxy, polymer/hydrogel bonded systems for three cases. The effects of bridging on the loads and crosshead displacements of three different DCB specimen cases were studied. Compared with a no-bridge DCB specimen (with the same crosshead displacement but without any bridge), the external load is higher for the bridging models. Therefore, fracture energy recorded in mode I test of those DCB specimens would be overestimated.

Similarities in the interaction of the SERR curves for the three cracks were found. By investigating these trends, the crack propagation sequences were predicted when a constant fracture energy value was assumed for the interfaces. There was also a relationship in the interaction of crack 2 and crack 3. Once the length of  $a_1$ , geometry, and

the material properties is assumed, crack 2 and crack 3 will propagate by following a fixed relationship. In summary, these investigations can be useful for the understanding and prediction of the behavior of bridging beam-like specimens (such as DCB tests or demolding processes). These results can also provide some useful information to develop strategies to control debond propagation. Extensions to other geometries and loading scenarios representative of actual manufacturing processes may prove useful in preventing bridging or controlling deleterious effects that can arise in demolding situations.

### 3.5 References

- [1] W. S. Johnson and P. D. Mangalgi, "Investigation of Fiber Bridging in Double Cantilever Beam Specimens," *Journal of Composites Technology & Research*, vol. 9, pp. 10-13, Spr 1987.
- [2] A. J. Kinloch, *Adhesion and Adhesives: Science and Technology*. London: Chapman and Hall, 1987.
- [3] J. W. Hutchinson and H. M. Jensen, "Models of Fiber Debonding and Pullout in Brittle Composites with Friction (Vol 9, Pg 139, 1990)," *Mechanics of Materials*, vol. 14, pp. 221-221, Jan 1993.
- [4] B. N. Cox and D. B. Marshall, "Crack Bridging in the Fatigue of Fibrous Composites," *Fatigue & Fracture of Engineering Materials & Structures*, vol. 14, pp. 847-861, 1991.
- [5] D. S. Dugdale, "Yielding in Steel Sheets Containing Slits," *Journal of the Mechanics and Physics of Solids*, vol. 8, pp. 100-104, 1960.
- [6] G. I. Barenblatt, "The Mathematical Theory of Equilibrium Cracks in Brittle Fracture," *Advances in Applied Mechanics*, vol. 7, pp. 55-129, 1962.
- [7] R. C. Wetherhold and J. Bos, "Ductile reinforcements for enhancing fracture resistance in composite materials," *Theoretical and Applied Fracture Mechanics*, vol. 33, pp. 83-91, Apr-May 2000.
- [8] M. R. Piggott, "Failure Processes in the Fiber-Polymer Interphase," *Composites Science and Technology*, vol. 42, pp. 57-76, 1991.
- [9] L. M. Zhou, J. K. Kim, and Y. W. Mai, "Interfacial Debonding and Fiber Pull-out Stresses .2. A New Model Based on the Fracture-Mechanics Approach," *Journal of Materials Science*, vol. 27, pp. 3155-3166, Jun 15 1992.
- [10] R. C. Wetherhold and L. K. Jain, "The Effect of Crack Orientation on the Fracture Properties of Composite-Materials," *Materials Science and Engineering a-Structural Materials Properties Microstructure and Processing*, vol. 165, pp. 91-97, Jul 5 1993.
- [11] L. K. Jain and R. C. Wetherhold, "Effect of Fiber Orientation on the Fracture-Toughness of Brittle Matrix Composites," *Acta Metallurgica Et Materialia*, vol. 40, pp. 1135-1143, Jun 1992.
- [12] D. A. Dillard and B. Chen, "A 2-D Analysis of Bridging in Adhesively Bonded DCB Specimens," in *Proceedings of the 1997 SEM Spring Conference*,, 1997, pp. 236-237.
- [13] ASTM-D3433-99, "Standard Test Method for Fracture Strength in Cleavage of Adhesives in Bonded Metal Joints," in *Annual Book of ASTM Standards*. vol. 15.06, ed West Conshohocken: ASTM, 2001, pp. 225-231.
- [14] A. J. Kinloch, C. C. Lau, and J. G. Williams, "The Peeling of Flexible Laminates," *International Journal of Fracture*, vol. 66, pp. 45-70, Mar 1 1994.

# Chapter 4 Development of the improved controller for the dual actuator load frame

---

## Abstract:

This chapter conveys an overview of the implementation of a new LabVIEW®-based controller system for the dual actuator load frame (DALF) that involved replacing the controller with hardware purchased from National Instrument (NI®, Austin, TX). Object-oriented programming idea is employed to facilitate maintenance of the computer program of the controller: each component is relatively independent, thus updates of individual components will not affect the others. Calibration of the controller was performed so that the controller can execute the load and displacement control accurately. Calibrations to the extension of the loading rods and the rotary error were also made so as to measure the displacements of the adherends accurately, ensuring more accurate data analysis.

## Keywords:

LabVIEW, object-oriented programming, real time control, dual actuator load frame (DALF), proportional-integral-derivative (PID) controller.

## Acknowledgement:

The author would like to thank Prof. Alfred L. Wicks and his student Brian A. Cope for their helps in choosing the hardware to be purchased from NI for the DALF, connecting them to the DALF and the computers, providing the programming framework to collect raw data from the DALF and control the pump, and training the author to become familiar with this new controller system. The improvements on the software reported herein could not have been made without these fundamental contributions of them.

## 4.1 Realization of the hardware and software of the controller

The double cantilever beam (DCB) test is one of the most important tests in characterizing the fracture behavior of adhesively bonded joints. Traditional DCB specimens are designed to be loaded in pure mode I (pure opening). However, since mixed mode tests are also important for the design of bonded joints, and the required results cannot be estimated from mode I tests, many test apparatuses have been designed for mixed mode or mode II tests.

The dual actuator load frame (DALF), as seen in Figure 4.1, was designed as an alternative to the range of fixtures required for different kinds of apparatus used in the tests of beam-like bonded joints with different mode mixities by an identical clamping method. Furthermore, the mode mixity can be changed instantly as required, because the

two loading cylinders are independently controlled by the computer. Functions realized in the software reduced the requirements in hardware (including jigs or other complex clamps). In this section, the implementation of more versatile functions for the controller is presented.

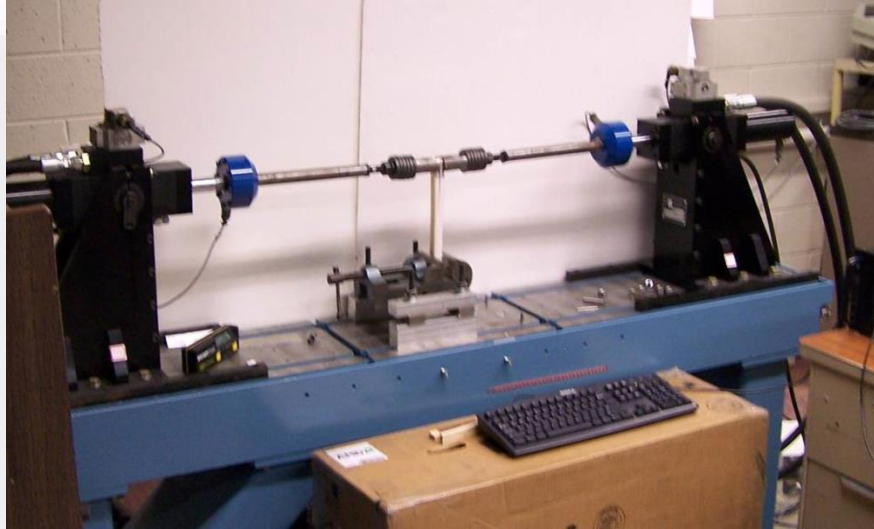


Figure 4.1. Dual actuator load frame.

Beam-like specimen can be installed in the fixed clamp at the bonded end and pinned to the two loading clevises at the end that has an initial debond. The general method for controlling the DALF is to move the two clevises separately in either displacement or load control without collision.

The entire system of the controller and DALF, as seen in Figure 4.2, consists of two controller loops:

- (1) RT-loop, the high frequency loop between the real time (RT) controller and the DALF;
- (2) GUI-loop, the low frequency loop between the graphic user's interface (GUI) and the RT controller.

The former is used to execute control functions and obtain their feedback loads and displacements at high speeds so as to adjust the movement of the loading clevises in real time. The latter is designed to receive a user's commands, send them to the real time controller, and monitor the execution of the DALF at relatively low speeds. The two controlling loops implement the communication between the user and the DALF. The use of two computers operating simultaneously is the commonly recommended protocol for high performance control systems. The commands can be altered instantly as needed during a test. In the following paragraphs, the two controller loops will be described separately so as to give details on how they were implemented.

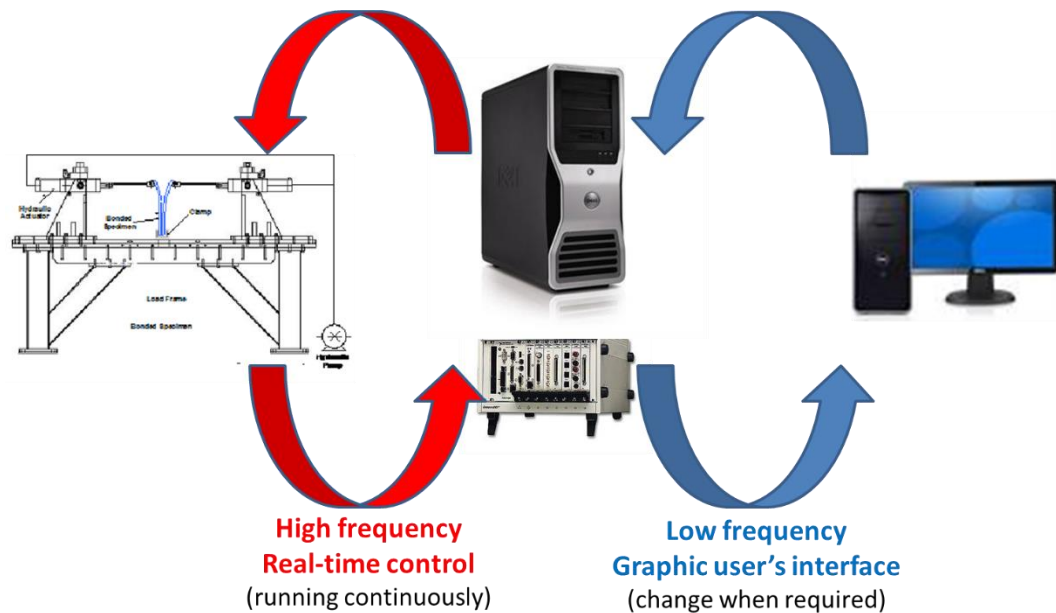
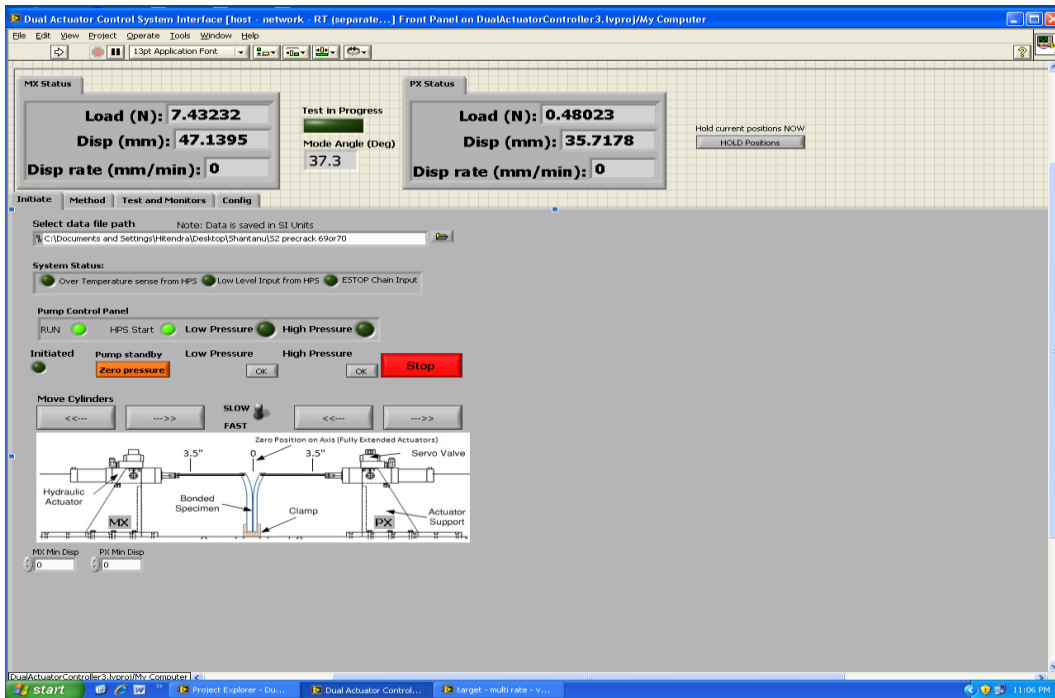


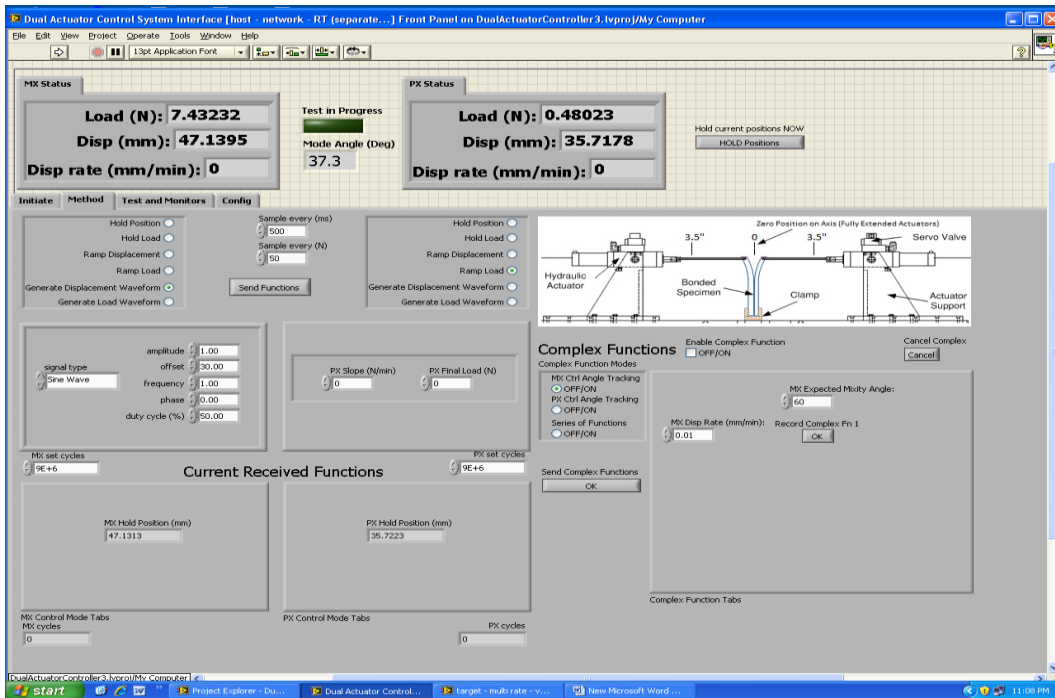
Figure 4.2. Schematic of the two loops of the controller for the DALF.

The RT-loop is designed to read the status of the DALF (loads, displacements), execute the proportional integral and derivative (PID) control, monitor the safety condition so as to avoid collision, and transfer the data at high frequency between the RT-loop and the GUI-loop. The loads and displacements are read from the DALF every 10 microseconds by interpreting the voltages from the transducers. Other variables (as functions of loads and/or displacements, such as loading rates, mode mixity angles, etc.) are also set up to monitor the testing process and facilitate the recording of the data in the two channels for the loads and two channels for the displacements.

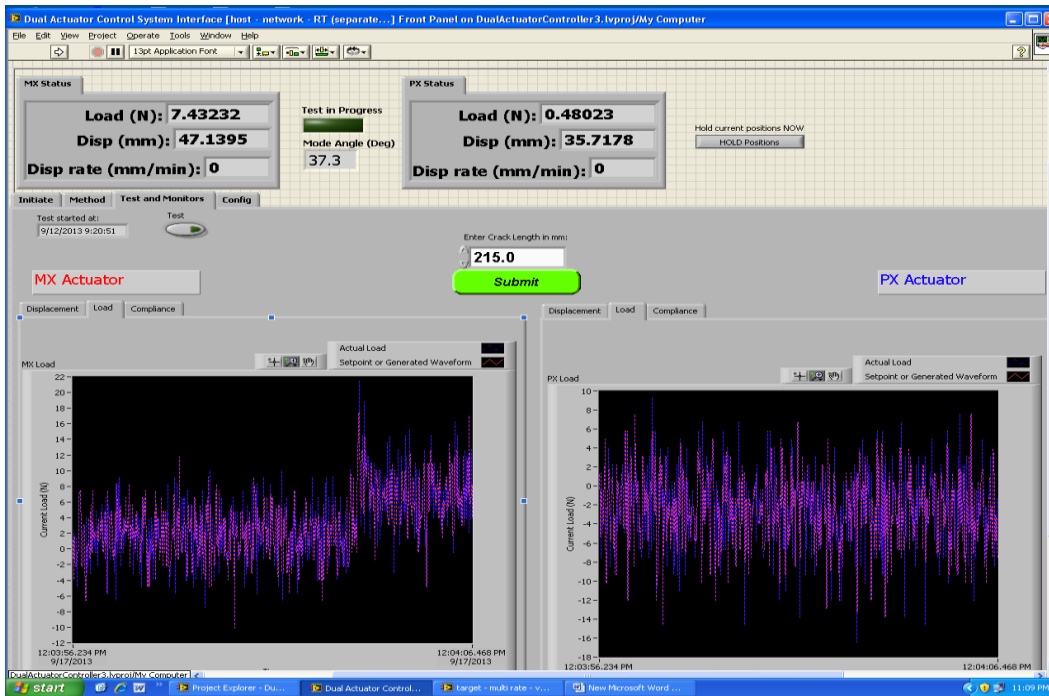
The main window of the GUI is shown in Figure 4.3, illustrating most of the buttons for control of the DALF. In the first tab named “Initiate”, the data file path can be assigned, the pump can be controlled, and movements of the two cylinders can be altered arbitrarily to install/uninstall specimens. The instantaneous values of loads and displacements, as well as mode mixity angle, can also be found there, as shown in Figure 4.3a. Most of the ordinary functions such as maintaining a constant displacement or load, constant slope of displacement/load, and sine/triangle/square waves were realized by using the default functions in the LabVIEW®. These functions are packaged in the second tab named “Method”, as shown in Figure 4.3b. During a test, the loads and displacements can be monitored by using the tab named “Test and monitors”, as seen in Figure 4.3c. Last but not least, the important parameters for PID control are listed in the tab named “Config” if any of the hardware or the pumps changed and a new configuration is required, as shown in Figure 4.3d.



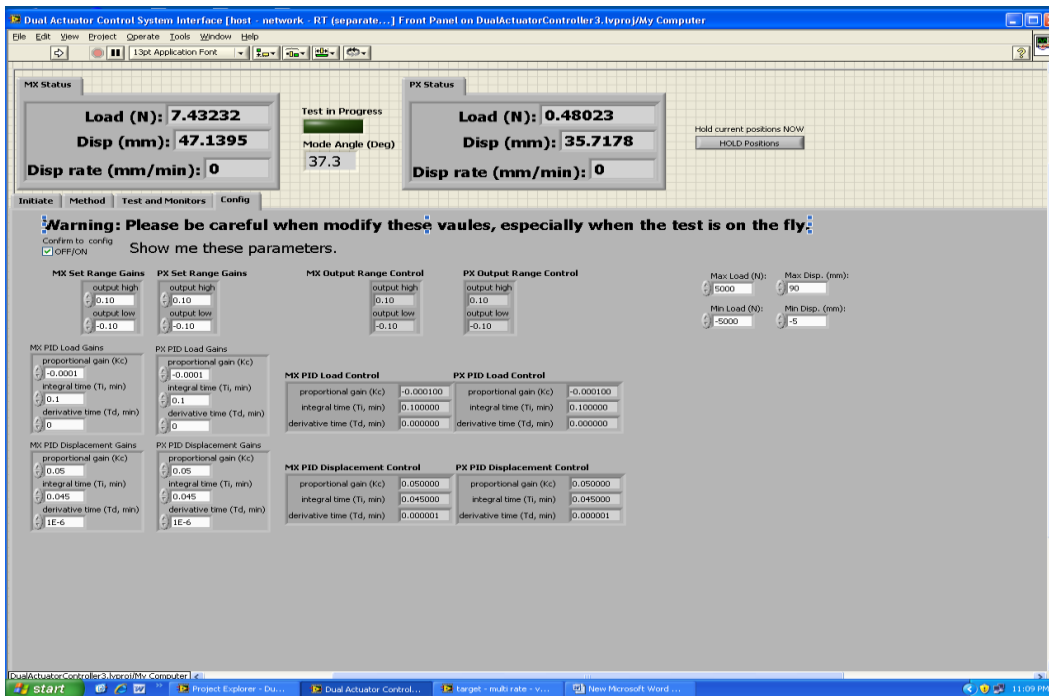
(a)



(b)



(c)



(d)

Figure 4.3. The main GUI window of the DALF controller: (a) Initiate, (b) Method, (c) Test and monitors, (d) Configuration.

The GUI works with the support from the programming in LabVIEW. While the movements of the DALF seem to be simple, the controller is quite complex. Generally, the start, stop, and pressure of the pump should be controlled and monitored carefully on a continuous basis. The oil runs continuously in the pump and valves when the DALF is working. For one of the simplest examples, when the cylinders are holding their positions, the oil flow should be well controlled to be equal in the two chambers of each valve. Besides the pump, the load and displacement signals in volts should also be collected, averaged, and then shown on the screen. There are also some other functions that manage the data recording, PID control, safety checking, etc. One of the most important features of LabVIEW is the view of flowchart-like programming: people can use the mouse and drag the icons to the diagram and connect them with wires to finish most of the programming without writing codes. One example of the initiation of the RT controller is shown in Figure 4.4.

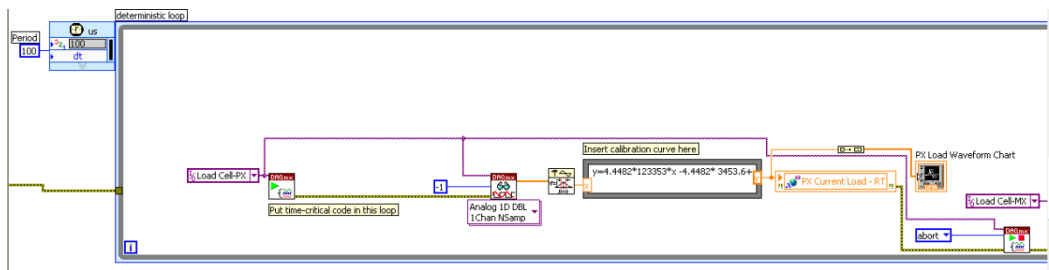


Figure 4.4. Part of the diagram for the initiation of the RT controller.

As seen in Figure 4.4, the while-loop with precise time intervals is one of the most important structures in the programming of the LabVIEW for the DALF controller. Using the while-loop, as well as some other structures, object-oriented programming was realized in the controller. In other words, the programming has been divided into several objects, which are working independently but sending messages to each other. In object-oriented programming, changes in one single object would not affect the others. Therefore, since the user doesn't have to care about details of the other object, this method facilitates the maintenance of the whole system. The other example with a while-loop is the PID control, which has been applied to most of the functions for load or displacement control in the DALF. The diagram with while-loop for the PID control is shown in Figure 4.5.

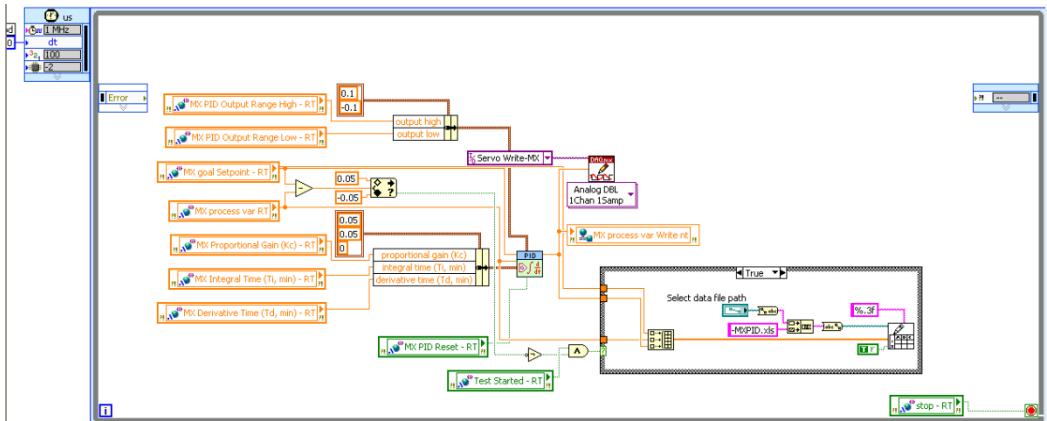


Figure 4.5. The while-loop for the PID control of the DALF.

The kernel of this diagram is the PID module in the middle. Most of the parameters are collected and input to the PID module from the top side and left hand side. By comparing the setpoints and the current points (the values of load or displacement), the PID module adjusts the oil flow and drives the valves to move slightly so as to adjust the setpoints every 10 milliseconds.

With the help of this PID module, the load-control mode and displacement-control mode are achieved in the DALF controller. Not only does the PID hold the operation at some specific point, but the loads and/or displacements can be set at or changed between some constant rates, or programmed to follow some specific functions. A portion of the sine wave function for fatigue tests is shown in Figure 4.6. Parameters of amplitude, frequency, phase angle, and offset, etc., were read and executed instantly after the click of the button “Send Function.”

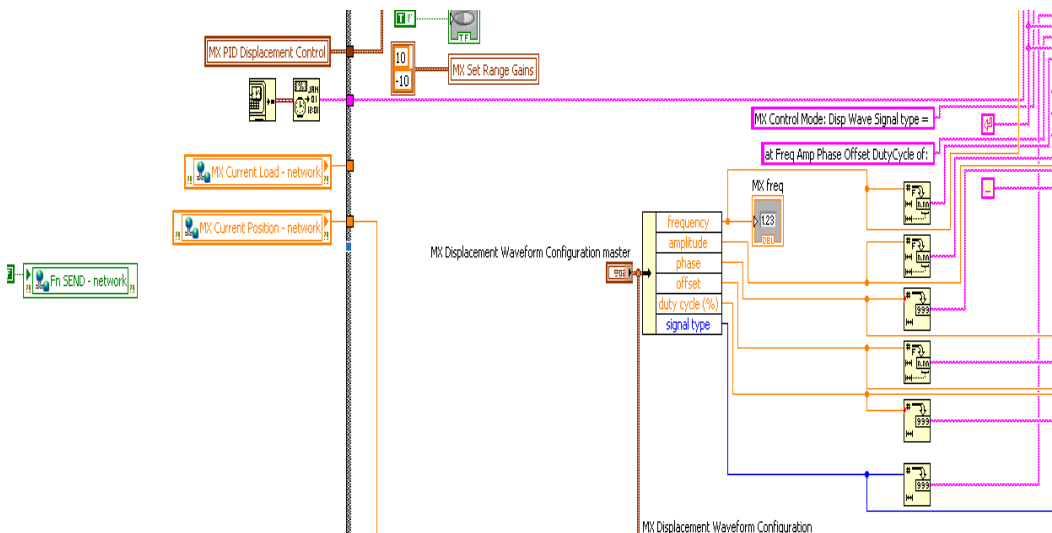


Figure 4.6. Sine wave displacement function in the DALF controller.

Some other functions specifically designed for the DALF were realized manually. One of the examples is the function of “constant mode mixity angle tracking.” Traditionally, the control of one cylinder does not need information of the other cylinder. However, this algorithm would be very difficult to implement for this tracking function. Therefore, another method was used in the controller: adjust one of the cylinders by information received from both. First, the user can choose one of the adherends to be the master and set a constant displacement rate. Then the controller will monitor the load applied to the master cylinder, calculate the required load in the other cylinder (slave) according to the mode mixity angle required by the user. A portion of the diagram for this function is shown in Figure 4.7. In brief, the mode mixity angle can be calculated according to the two loads; details of the equations and derivations are shown in the next chapter. Note that the limits of the voltage for the PID control should be very small ( $\pm 0.1V$ ) so as to prevent fast movements of the DALF. One pair of loading curves for a constant mode mixity angle test is shown in Figure 4.8. On the left hand side, it is a simple ramp-displacement control. On the right hand side, the short red lines are accurate setpoints of the load at each second, while the blue noisy curves are the real load at each moment. Therefore, evidently, the controller is adjusting the loads every second.

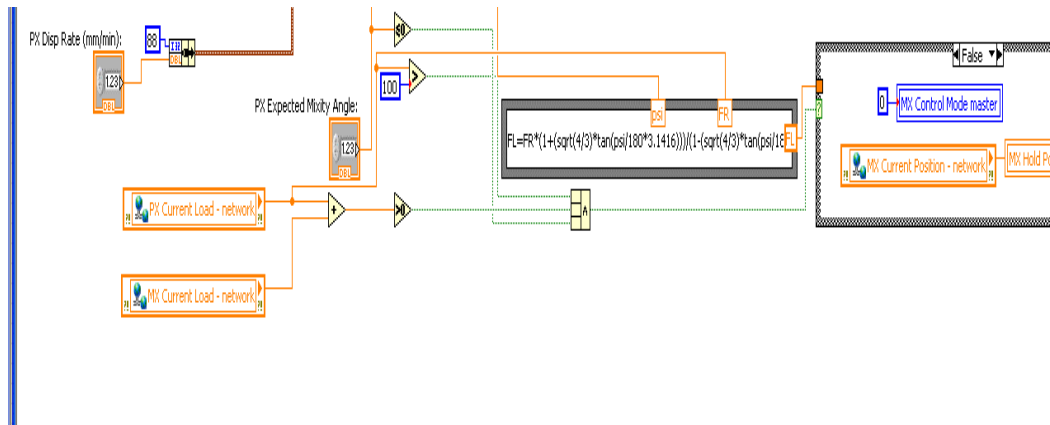


Figure 4.7. Part of the diagram for the controlling of the constant mode mixity angle tracking.

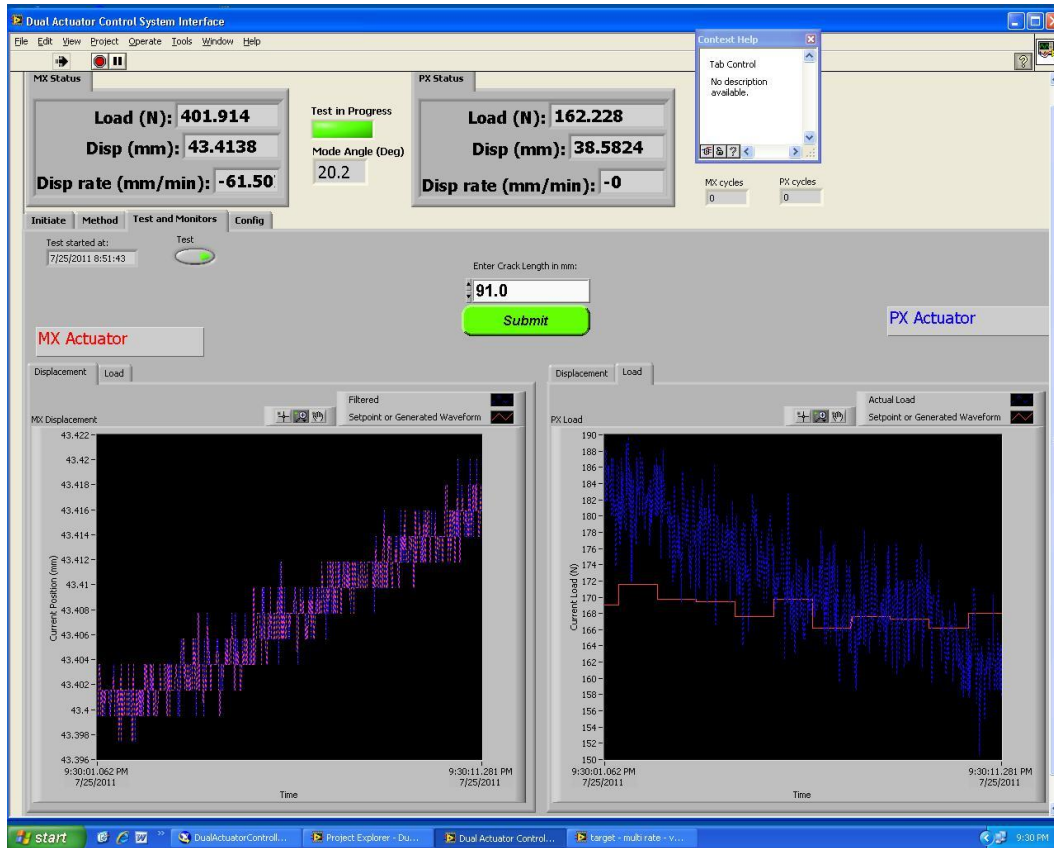


Figure 4.8. Displacement curve (left adherend) and load curve (right adherend) when controlled in constant mode mixity angle function.

There are also some other important functions, though they are not directly related to the routine execution of experiments. One of them is the safety monitor program. Since there are two cylinders in the DALF, it is more complex than single actuator load frames. A major concern in the DALF operation is collision and safety. Therefore, a safety monitor is necessary for the controller.

Whenever a test is running, the safety program should be running continuously in the background. It will monitor the locations of the two loading clamps. Firstly, the location should exceed the limits of the LVDT: not larger than the maximum displacement (88 mm), or smaller than the minimum displacement (0 mm). More importantly, the clamps should not touch each other in a test. There is also a safety loop that detects excessive force: when either of the load exceeds the preset limit ( $\pm 3000$  N for the quasi-static tests, and can be changed by the administrators), the pump will stop automatically.

To realize the collision sensing, the “displacements about the null positions”, i.e. the initial locations of both loading clamps are used and recorded for each test after the installation of the specimen but before the test begins. Based on these two locations, the safety monitor program can calculate whether the clamps are too close to each other or not. Once the current locations indicate that the distance between the loading clamps is

less than the initial value recorded, the pump will be stopped instantly. The diagram of the safety monitor is shown in Figure 4.9.

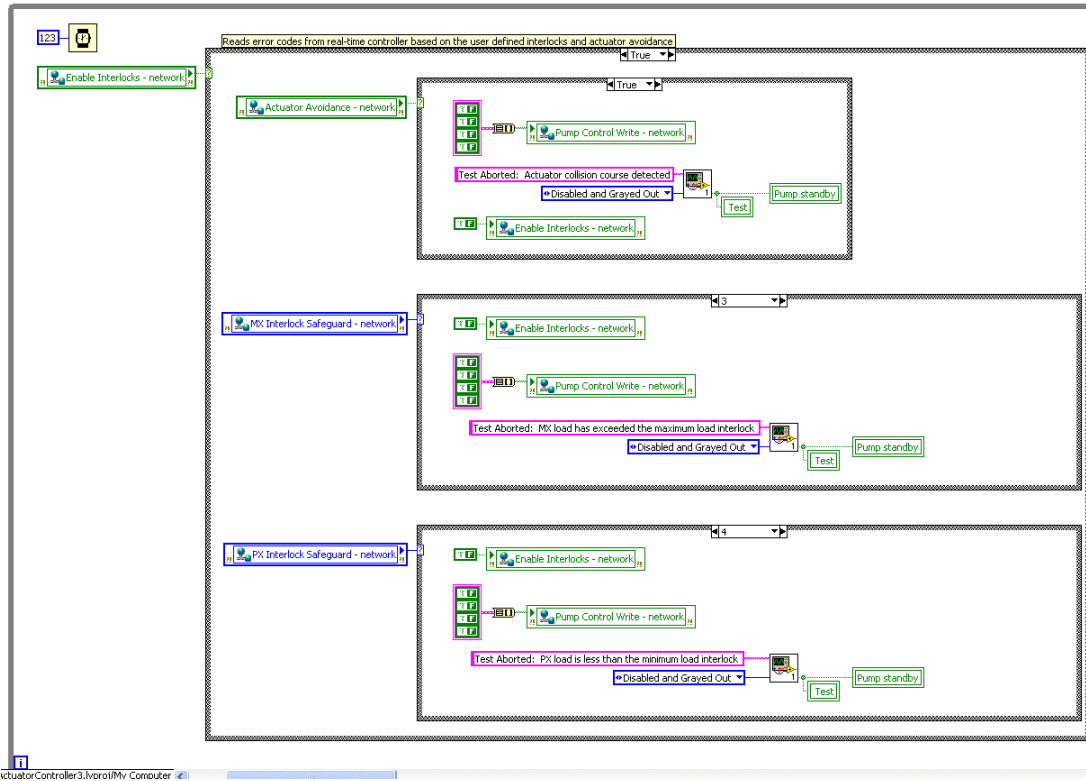


Figure 4.9. Safety monitor module in the programming of the DALF controller.

In summary, with the master cylinder in displacement control, the slave cylinder in load control, and the PID controller adjusting the slave cylinder, constant mode mixity angle tracking tests were conducted smoothly. Of course, the loading speed and the mode mixity angle can also be changed as required any time during the tests.

## 4.2 Calibration of the DALF

The compliance-based beam method (CBBM) is one of the testing methods that do not require crack length readings during a test[1]. This is because the equivalent crack lengths can be calculated from the loads and displacements recorded by the instrument. Two equivalent crack lengths can be calculated:  $a_{eI}$  from the mode I components, and  $a_{eII}$  from the mode II components. This advantage shown above makes this a useful objective testing method. Equations and other details for implementing CBBM will be shown in the next chapter.

However, due to the compliances of the parts of the DALF, and other nonlinear effects in the clamping, etc., the displacements of the adherends would be overestimated if raw displacement values were used. Therefore, the compliance of the adherends would be overestimated as well. Finally, the equations for the CBBM would overestimate the

equivalent crack lengths ( $a_{eI}$ , and  $a_{eII}$ ), and thus overestimate the SERR and fracture energy. Therefore, it is necessary to calibrate the DALF and reduce the errors in the measurement of the real displacements, and thus the compliances of the adherends in bonded joints. Once this correction is made, the CBBM can help the researchers to have a consistent method and also correct some minor crack-reading errors as can easily occur with the naked eye on the rough surfaces or for mode II-dominant loading. Furthermore, if the CBBM correction is adequate, researchers can reduce the time and effort required for crack reading, especially important for long-term tests such as fatigue tests.

The precision of the LVDTs (linear variable differential transformers) for measuring displacements was first calibrated. Figure 4.10 shows excellent agreement and linearity of displacements from one LVDT and as measured by an appropriately mounted dial indicator. The precision would be adequate for fracture tests of beam-like specimens.

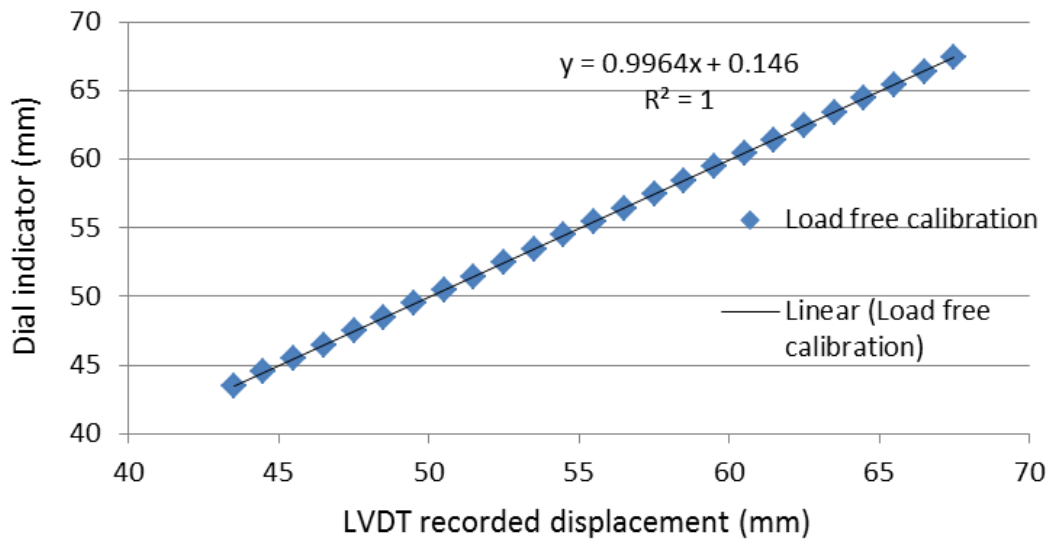


Figure 4.10. One of the load-free calibrations of an LVDT of the DALF.

In the following paragraphs, some corrections to the compliance of the DALF are made by testing some monolithic aluminum 6061-T6 double cantilever beam (DCB) specimens with machined cracks. Initial cracks with different lengths were cut along the center lines of these specimens, and the lengths of the cracks were fixed and there was no crack propagation in these tests.

Under the hypotheses of linear elastic deformation, the stress fields resulting from mixed mode loadings can be obtained as a linear superposition of the stress fields resulting from pure mode I and mode II components[2], as seen in Figure 4.11. In the research done by de Moura and de Morais[3], there are two equivalent crack lengths calculated by the loads and displacements, one is  $a_{eI}$  from mode I component, the other is  $a_{eII}$  from mode II component. Since mode I tests can provide symmetric loading, simplify the analysis, and avoid the nonlinear rotation at the end of the specimens in the bottom clamp, only  $a_{eI}$  was chosen to estimate the crack lengths. The DCB tests on the

DALF showed that, the values of  $a_{eI}$  are closer to the crack lengths read by the naked eye when the mode mixity angle is not very high. The equation for the estimation of  $a_{eII}$  in CBBM requires the values of the specimen compliance in mode II component, which could be affected by the rotary error of the clamping. The values of  $a_{eII}$  are considered to be less accurate than the values of  $a_{eI}$ .

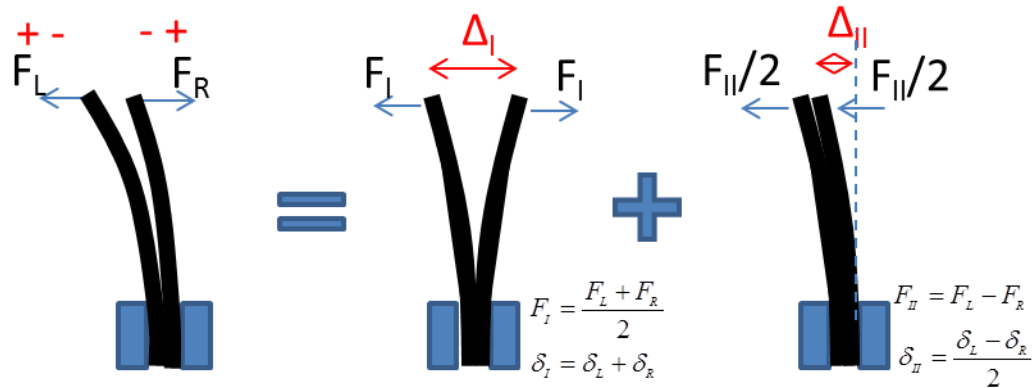


Figure 4.11. Superposition of the mixed mode test by pure mode I and pure mode II components.

Therefore, pure mode I tests were conducted for three specimens made from rectangular 6061-T6 aluminum alloy bars with nominal dimensions of  $305 \times 25.4 \times 12.7$  mm, with machined initial crack lengths of 50mm, 100mm, and 150mm, respectively, as seen in Figure 4.12. Each beam has cross section dimensions of  $12.2 \times 12.7$ mm due to the remove of materials by cutting, because the machining process removed some aluminum. Two symmetric loading holes were drilled for each specimen on the top. The yield stress for this 6061-T6 aluminum alloy is 275MPa; the limits in the loading for each specimen were calculated before the tests.

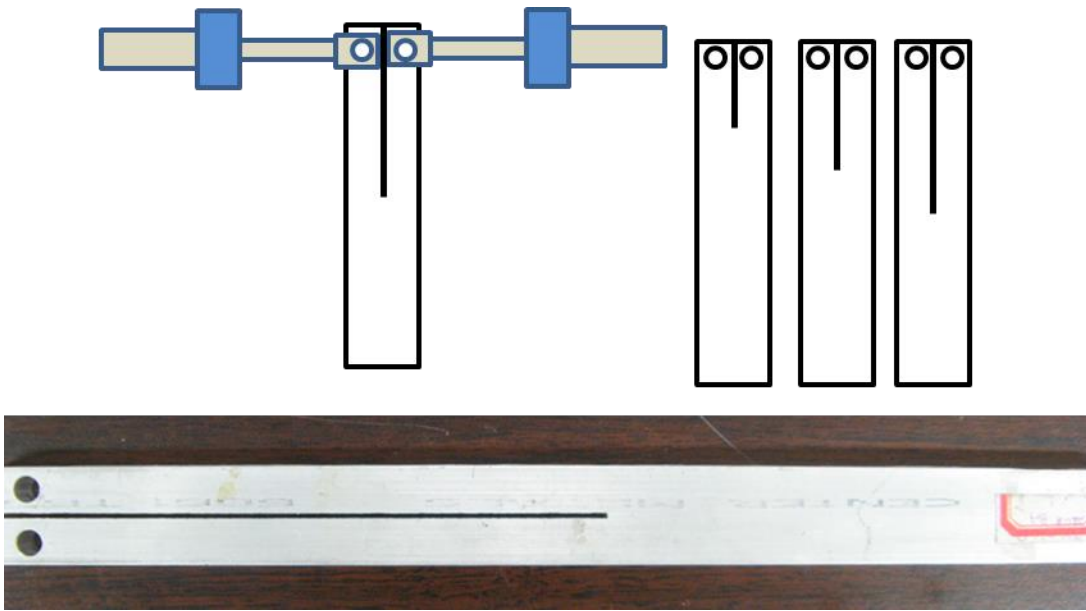


Figure 4.12. Schematic and picture of the machined aluminum DCB specimens for calibration.

Around 500 data points were collected for each of the tests and the compliances were plotted as shown in Figure 4.13. The plots showed that the compliances are almost constant for these specimens, though there was some noise due to the noises in the LVDT and the load cells at the beginning when the load was low. Because the 150 mm thin aluminum bar is very flexible, and the max load is about 300 N, the max displacement is about 6 mm, the noise is about  $\pm 10$  N. So when the displacement is small, the noise in the compliance is quite big, around  $\pm 5\%$ .

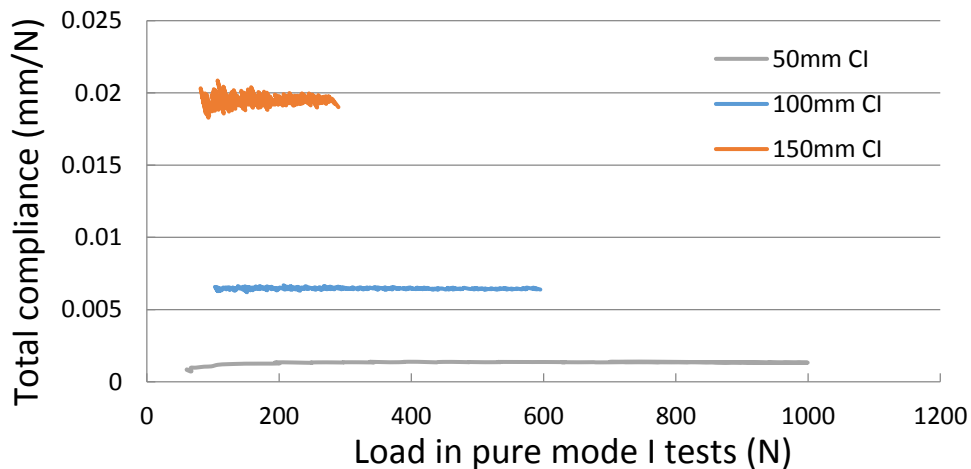


Figure 4.13. Compliances for the DCB specimens with different initial crack lengths, as functions of the pure mode I loads increasing but without yielding in the aluminum beams.

Therefore, the average values of the compliances were used to calibrate the compliance of the DALF. Figure 4.14 shows the assumed model. The total crosshead displacement is equal to  $\Delta_L + \Delta + \Delta_R$ .

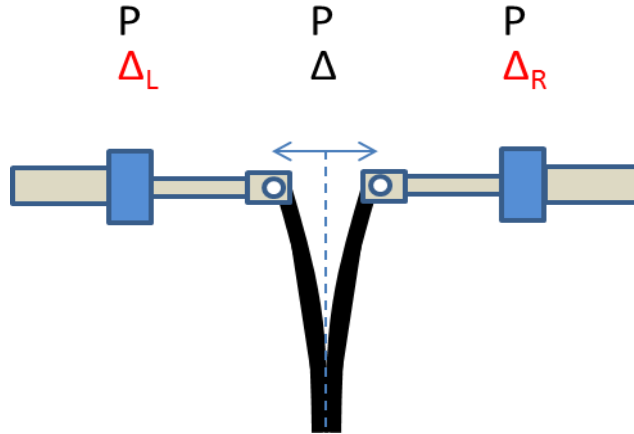


Figure 4.14 Components of the total crosshead displacement in mode I tests on the DALF: the left extension, beam deflections, and the right extension.

Since the specimen was not clamped at the base, the loads applied to the rods and the specimens were in series with the same value, there was only one  $P$  in this model. Besides the crosshead displacement  $\Delta$  in the DCB specimen, the extensions of the two rods were also considered and defined as  $\Delta_L$ , and  $\Delta_R$ . Therefore, the total compliance is divided into two parts, one is from the DALF, and the other is from the specimen:

$$C_{Total} = C_{DALF} + C_{Spec} \quad (4.1)$$

And,  $C_{DALF}$  is defined as:

$$C_{DALF} = (\Delta_L + \Delta_R) / P \quad (4.2)$$

Based on the definition of the terms in equation (4.1),  $C_{spec}$  only includes the theoretical terms from Timoshenko beam theory and assuming that the individual beams are effectively built-in at the crack tip<sup>1</sup>.

Also, from Timoshenko beam theory, including both bending and shearing effects[3], we have:

$$C_{spec} = \Delta / P = \frac{2a^3}{3EI} + \frac{12a}{5BHG} \quad (4.3)$$

where  $a$  is the crack length, and is equal to 50mm, 100mm, or 150mm for the three specimens.  $E = 70GPa$  is Young's modulus of aluminum.  $B = 12.7mm$  is the width of the specimens.  $H = 12.2mm$  is the height of one beam.  $G = 26.3GPa$  is the shear modulus of aluminum.

In order to simplify the equations, we define:

$$A_{50mm} = \frac{2a^3}{3EI} \Big|_{a=50mm} \quad (4.4)$$

$$B_{50mm} = \frac{12a}{5BHG} \Big|_{a=50mm} \quad (4.5)$$

Since we had the shortest crack length of 50mm, the next is double or 100mm, and the third is triple or 150mm, we have

$$A_{100mm} = 8A_{50mm} \quad (4.6)$$

$$A_{150mm} = 27A_{50mm} \quad (4.7)$$

$$B_{100mm} = 2B_{50mm} \quad (4.8)$$

$$B_{150mm} = 3B_{50mm} \quad (4.9)$$

So finally, the three equations for three unknowns are:

---

<sup>1</sup> This solution ignores beam root displacement and rotation of the beams at the crack tip, so these contributions are effectively included in  $C_{DALF}$ , and thus also included in  $\Delta_L$ , and  $\Delta_R$ . Though not considered in the calibration, compliance contributions from beam root displacement and rotation are unavoidable in any real tests, including of the calibration specimen. Realizing this partitioning problem, an attempt to estimate the relative error due to the beam root rotation and displacement was made using the Kanninen model, which considers augmented DCB specimen deflections using a beam on elastic foundation model[4]. The analysis showed that, the three aluminum specimens used herein introduced 10% to 12% error when the beam root rotation and displacement were not considered. Attention should be given to include these contributions when higher accuracy is required.

$$\begin{aligned}
0.001359 &= C_{DALF} + A_{50mm} + B_{50mm} \\
0.006525 &= C_{DALF} + 8A_{50mm} + 2B_{50mm} \\
0.019496 &= C_{DALF} + 27A_{50mm} + 3B_{50mm}
\end{aligned}
\tag{4.10}$$

By solving these equations, we obtain:

$$\begin{aligned}
A_{50mm} &= 0.000650 \\
B_{50mm} &= 0.000613 \\
C_{DALF} &= 0.0000955
\end{aligned}
\tag{4.11}$$

The value of  $C_{DALF}$  was obtained and incorporated in the analysis of adhesively bonded joints. The calibration was only related to mode I component, then the subsequent equivalent crack length is used in the calculation of fracture energy in both mode I and mode II components. One of the examples is shown in Figure 4.15. This mixed mode test was executed by applying the displacement rate of 4:3 (e.g. the left adherend moved at 0.2mm/min, and right adherend moved at 0.15mm/min, in the same direction). The mode mixity angle was increasing from around 30° to 75°. The line is shown as a reference, while the real data is shown with the red diamond marks. The plot showed that, even for tests at higher mixed mode angles, the estimation of the real crack length was quite close to the one read by the naked eyes, though there were some differences when the crack length is smaller than 100mm. A better estimation of the crack length (such as including the beam root displacement and rotation from the Kanninen model[4]) would improve the accuracy of the fracture energy values obtained in the tests.

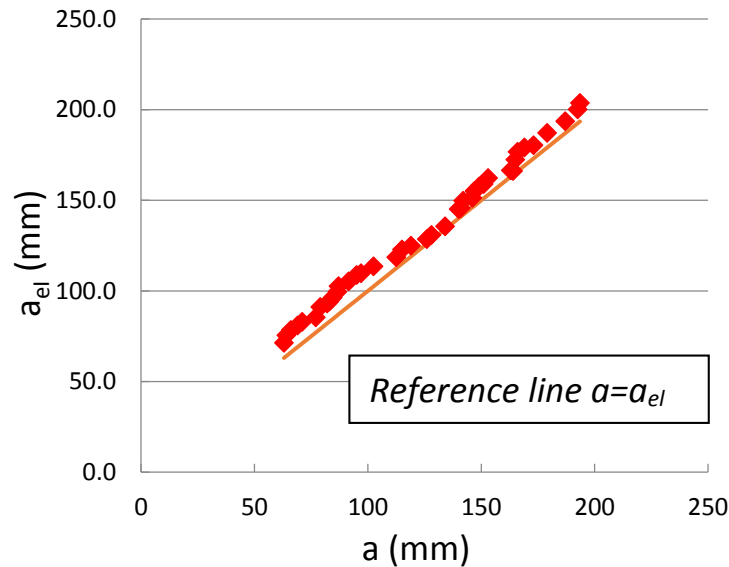


Figure 4.15. Comparison of the crack lengths read by the naked eye to those calculated by the corrected CBBM for a normal DCB bonded joint, with mode mixity angle from 30° to 75°.

In summary, the implementation of the new LabVIEW®-based controller system for the dual actuator load frame (DALF) involved replacing all the hardware of the controller with products purchased from National Instrument (NI®). The mechanism of holding constant displacements, constant displacement rates, constant mode mixity angles, monitoring safety of the instrument and the users have been shown in detail.

The rotary error of the clamp at the bottom of the specimen was also calibrated. In mixed mode tests, the specimen is clamped at the bottom and bent by both cylinders to one side (e.g. left hand side). Therefore, the bending moment at the clamping point is the product of the beam length and the resultant of both forces and it is  $(F_L - F_R)L$  according to the definition in this thesis. It does not matter which cylinder exerted the higher load, since we defined positive moment and mode mixity angle for the bending to the left, and negative moment and mode mixity angle for the bending to the right. The former (bending to the left) is applied to all the specimens tested using the DALF in this dissertation.

As shown in Figure 4.16 by the vertical straight line and the tilted dotted line, due to the rotation at the clamped end, the adherend can rotate by a small angle to the left, which introduces an additional deflection,  $\Delta_o$ , and error in the two displacements that were recorded by the DALF in the tests.

To conduct a base rotation calibration, one adhesively bonded specimen without initial crack (completely bonded through the bondline) was clamped together with a thin steel bar at the bottom, loaded and bent by the left cylinder to the left, as seen in Figure 4.16. Since the stiff steel bar is load free (the reaction force exerted by the dial indicator is ignored), its rotation indicates the rotary error of the clamped end. Therefore by recording the deflection of the steel bar at different loads, the rotary error at the loading pin can be easily calculated.

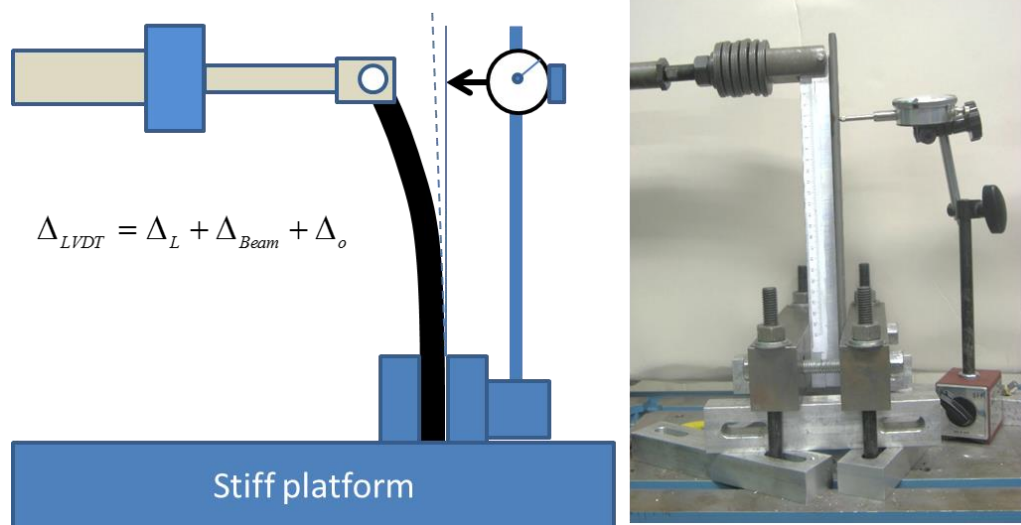


Figure 4.16. Schematic and the photo of setup in the calibration of the rotary error of the bottom clamp.

It is reasonable to inherently assume that the platform remains flat. The displacement was recorded by the dial indicator with the base fixed on the stiff platform at the bottom and the pointer pointing at the length of 186 mm when measured from the clamped end of the specimen. Since the height of the dial indicator was inadequate, corrections were made by using similar triangles. The displacements at the loading pin (effective length of 240 mm measured from the clamped end) due to the rotary error is calculated by multiplying the displacements from the dial indicator by the ratio of 240/186. The calibration was repeated for six times and the averaged slope of the load vs. deflection curve is  $527 \pm 12 \text{ N/mm}$ . One of the load vs. displacement plots is shown in Figure 4.17. Therefore,

$$\Delta_o = P / (527 \text{ N/mm}) \quad (4.12)$$

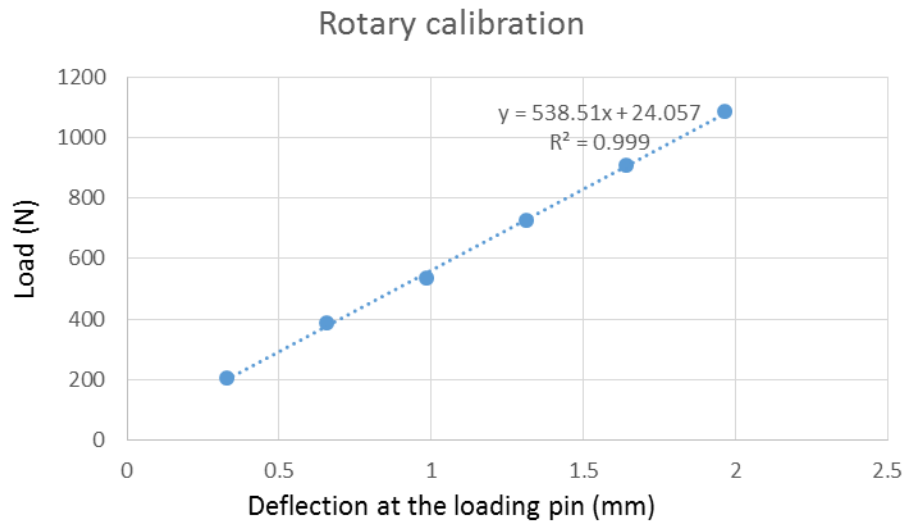


Figure 4.17. Curve fitting of the displacements for calibration of the rotary error of the bottom clamp.

### 4.3 Summary

In summary, the implementation of the new LabVIEW®-based controller system for the dual actuator load frame (DALF) that involved replacing all the hardware of the controller with products purchased from National Instrument (NI®) is shown. The mechanism of holding constant displacements, constant displacement rates, constant mode mixity angles, and monitoring safety of the instrument have been shown in details.

For accurate experimental measurements, the compliance of the DALF is calibrated to minimize the errors in the displacements recorded for loading points of the adherends. The correction to the raw displacements read from the DALF provided an improved method for the measurement of the compliances of the adherends. These corrected

compliances used in the CBBM provided consistent crack estimation. However, it is also worth noting that the equivalent crack lengths obtained by the CBBM are only the prediction of the real crack lengths, and cannot be used directly in the equations for SERR or fracture energy calculation. Another term needs to be added to the  $a_{el}$ , is the corrected crack length in the corrected beam theory (CBT). The CBBM techniques doesn't use this corrected crack length, or the effective stiffness. Therefore, there would still be some error in the results, and both CBT and CBBM are employed and compared in the following chapters so as to provide more information about the fracture energy.

## 4.4 References

- [1] F. J. P. Chaves, M. F. S. F. de Moura, L. F. M. da Silva, and D. A. Dillard, "Numerical analysis of the dual actuator load test applied to fracture characterization of bonded joints," *International Journal of Solids and Structures*, vol. 48, pp. 1572-1578, 2011.
- [2] D. Xie, A. M. Waas, K. W. Shahwan, J. A. Schroeder, and R. G. Boeman, "Fracture criterion for kinking cracks in a tri-material adhesively bonded joint under mixed mode loading," *Engineering Fracture Mechanics*, vol. 72, pp. 2487-2504, Nov 2005.
- [3] M. F. S. F. de Moura and A. B. de Morais, "Equivalent crack based analyses of ENF and ELS tests," *Engineering Fracture Mechanics*, vol. 75, pp. 2584-2596, Jun 2008.
- [4] M. F. Kanninen, "An augmented double cantilever beam model for studying crack propagation and arrest," *International Journal of Fracture*, vol. 9, pp. 83-92, 1973/03/01 1973.

# Chapter 5 Experimental investigation of adhesively bonded joint by tests of double cantilever beam specimens with flexible changes of mode mixity angle applied by dual actuator load frame

---

(Paper prepared for submission to the *International Journal of Adhesion and Adhesives*)

## Abstract:

The process of testing double cantilever beam (DCB) specimen on a dual actuator load frame (DALF) with various discrete mode mixity angle or continuously increasing mode mixity angle to obtain fracture envelopes of structural adhesives is presented. This process is considered to be useful for reducing uncertainties in the data because more mode mixity angles can be applied to individual specimens, the results of which are analyzed in a consistent fashion. The resulting fracture energy as a function of mode mixity angle has been evaluated by corrected beam theory (CBT) and the compliance-based beam method (CBBM). Discussions of the CBBM and beam compliance showed possible ways to improve the accuracy of the CBBM when using it to calculate fracture energy in mixed mode tests of bonded joints. A general equation is derived for stable mixed mode tests of DCB specimens on the DALF, as well as other fixtures with some modification. The tests at constant mode mixity angles showed apparent resistance curves (R-curve), which are explained by shear toughening effect when specimens are bonded with stiff adherends and fixed in the bottom clamp.

## Keywords:

Double cantilever beam, adhesively bonded joint, aluminum epoxy bonds, fracture energy, mode mixity angle, mixed mode fracture dual actuator load frame, bridging, hackle pattern, microcrack, corrected beam theory (CBT), compliance-based beam method (CBBM), base acid treatment

## 5.1 Introduction

The need for lighter weight, higher performance, and less expensive engineered products has driven significant increases in the use of adhesives for joining components over the past few decades. Improvements in surface preparation, bonding techniques, adhesive performance, and joint design have been important for enabling advances in this technology. In spite of substantial progress, a number of uncertainties remain, including the effects of surface roughness or treatments [1, 2], the location of failure [3-5], and the effect of mixed mode fracture loading on fracture resistance [6, 7]. Studies of the fracture

response of adhesively bonded joints under different loading modes remains important to the improvement of engineering designs, and is the focus of this research.

Double cantilever beam (DCB) specimens are common for characterizing the mode I fracture behavior of bonded joints[8] and several forms have been codified in standards [9, 10]. Due to their simplicity and the perception that mode I loading often results in the smallest fracture energy, mode I tests of DCB specimens are widely used and often believed to be useful for conservative design purposes, though exceptions have been noted. [6] Traditionally, other loading modes can be achieved using similar beam-like specimens but loaded in different fixtures. Fracture energy in pure mode II can be obtained from end notch flexure (ENF) tests[11] or end load split (ELS) tests [12]. Fracture energies for other discrete mode mixities can be obtained using specimens such as the fixed ratio mixed-mode tests[13], single leg bend (SLB)[14], or crack lap shear (CLS) test[15, 16]. Discrete [17] or continuous[18] variations in mode mixity over relatively narrow ranges about these specific loading modes can be achieved with asymmetric specimens. Reeder and Crews [19-21] and Spelt and coworkers [7, 22, 23] have developed special loading jigs that can be adjusted to conduct fracture tests on bonded beam specimens over a wide range of mode mixities, and modified forms have been suggested[24]. The above techniques have found wide applications for characterizing failures in adhesive joints, answering fundamental scientific questions, as well as providing engineering data for design purposes. However, concerns may be raised that, if the fracture envelope over the full range of mode mixity angle is desired, different specimen geometries and associated analysis methods may introduce inconsistencies for a given bonding system (i.e. with the same adhesive, adherends, and surface treatment).

Under prior NSF support, a dual actuator, servo-hydraulic load frame (DALF) was developed [25, 26] that is capable of providing variable mode mixity for fracture mechanics studies by imposing asymmetric displacements or loads on a bonded beam specimen mounted rigidly at the bonded end. This effectively imposes a combination of traditional DCB and ELS loading to a specimen. Prior studies using the DALF[6] showed some useful results in mixed mode tests for certain material systems. In the present work, the DALF is also used to study the fracture behavior of two kinds of toughened epoxy adhesives by obtaining fracture energies at different mode mixity angles within a single specimen. Therefore, this approach would offer better consistency and data reliability in the fracture energy values at several mode mixity angles when testing one single specimen with the same chemical treatment, bonding, and curing time.

## 5.2 Test method

The mixed mode loading flexibility is achieved through the independently controlled actuators of the DALF. Each actuator is equipped with a load cell and a displacement sensor to provide information required for quantitative evaluation. The bonded lower end of the specimen is clamped vertically in a vise, while the loads are applied to the pre-cracked and debonded ends of the adherends through clevises and pins[26].

Figure 5.1 shows a typical loading path sequence for the two cylinders. Of course, the paths do not have to be linear as shown, but can be varied arbitrarily by the controller. The

loading rates can be changed on the fly when the loads or displacements meet some criteria in our new controller implemented in LabVIEW® (National Instruments, Austin, TX). The test is usually initiated by using symmetric opening with the same displacement rates. Therefore, the forces applied by the two cylinders will be directed outwards and will be nominally equal to each other. After the crack propagates to a certain length, the cylinders can be returned or moved to a new position if another mode mixity angle or loading is required. Usually, a long initial crack propagated in pure mode I can be used for calibration purposes, and help to avoid unstable propagation when loaded in subsequent mixed mode loading[27]. The specimen is then reloaded at different displacement rates so as to reach the desired mode mixity angle. The displacement rates can be adjusted to increase or decrease the mode mixity angle continuously as required. The relationship between displacements (or forces) and mode mixity angles will be shown in the following section.

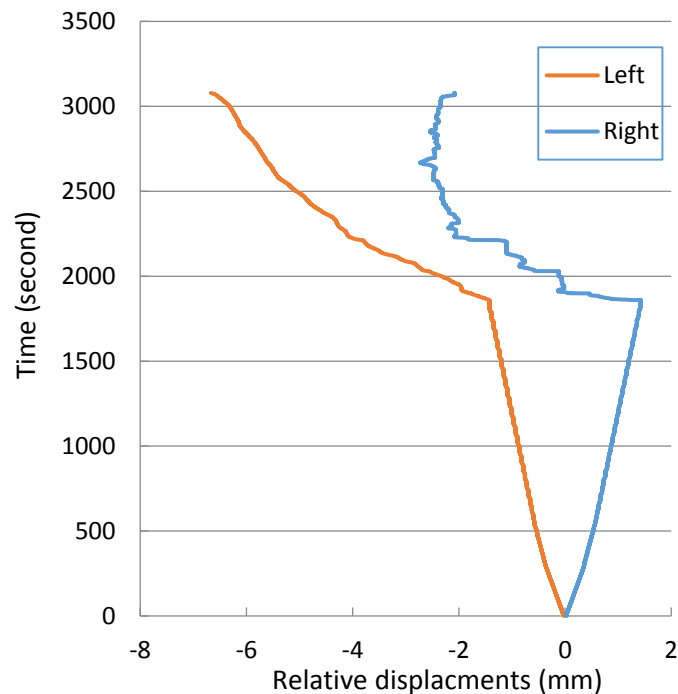


Figure 5.1. One loading path sequence imposed by the two cylinders of the DALF when testing a DCB specimen in mixed mode. The specimen was first opened in mode I to half of the specimen length, then the mode mixity angle was increased to 10°, 20°, 30° gradually (no crack propagation), and finally kept at 40° to crack the rest of the specimen. Since the right cylinder was adjusting itself to meet the requirement of mode mixity angle, and the crack was propagating, the curves were not smooth.

### 5.3 Materials and joint preparation

The DCB adherends were made of rectangular T6061 aluminum bars with the dimensions suggested in ASTM standard[10]. Yielding of the adherends was avoided

during the tests, and thus linear elastic homogeneous isotropic material properties were used in the calculations.

Before bonding, a chemical treatment process was used to develop a thin layer of aluminum oxide that can provide strong bonding in either mode I or mode II loading. The adherends were abraded with #220 sandpaper, rinsed with de-ionized (DI) water for 2 minutes, and heated in an oven at 110 °C for 1 hour to remove moisture from their surfaces. The adherends were then chemically pretreated by placing them in a 10% (wt) NaOH solution for 10 minutes, rinsing with DI water, and then placing them in a solution of  $HNO_3 : H_2O = 1:1$  (v) for 2 to 3 minutes or until the gray surfaces regained a white metallic appearance. The adherends were rinsed again with DI water, and then placed in an oven heated to 110 °C for at least 1 hour.

Two commercially available toughened epoxy structural adhesives were used to bond the adherends. One is LORD 320/322 (LORD Corporation, USA), which was provided by the manufacturer. The other is J-B INDUSTRO-WELD (J-B Weld Company, USA) which was purchased locally.

Prior to bonding, two shims were placed at the two ends to control bondline thickness at 0.25 mm. After applying the adhesive, the two adherends were clamped to maintain alignment. All the specimens were cured at room temperature for 16 hours and postcured at 60 °C for 3 hours to guarantee the full development of the crosslinks prior to testing. These adhesives resulted in stable crack propagation in quasi-static tests, and no plastic deformation was induced to the aluminum adherends during the tests.

## **5.4 Analysis methods for determining fracture energy**

Several analysis procedures have been advocated for obtaining more accurate and consistent fracture energy results than obtained with simple beam theory[1]. Descriptions of the methods used herein to interpret experimental results are presented briefly in this section.

### **5.4.1 Corrected beam theory**

Using the loads and displacements recorded by the computer, as well as the crack lengths recorded manually using a magnifying lens or the naked eye in the tests, fracture energies and mode mixity angles can be calculated using corrected beam theory (CBT) [12, 28]. This theory includes a correction to the measured crack length due to the beam root rotation and displacement at the crack tip and the loading points, and has been implemented into the British Standard 7991:2001[29].

Under the assumption of linear elastic deformation, the stress fields resulting from mixed mode loadings can be obtained as a linear superposition of the stress fields resulting from the pure in-plane opening and in-plane shearing modes. Therefore, loads applied by the two hydraulic actuators can be partitioned into loads of mode I and mode II load components as follows:

$$F_I = (F_L + F_R) / 2 \quad (5.1)$$

$$F_{II} = (F_L - F_R) / 2 \quad (5.2)$$

where, subscripts I and II denote the mode I and mode II components, respectively, and subscripts L and R denote the left and right actuators, respectively. Positive values of  $F_L$  and  $F_R$  imply, respectively, forces acting outward. A schematic of this definition is shown in Figure 5.2. The mode I component of the applied or available strain energy release rate (SERR) can be calculated by [28],

$$G_I = \frac{12F_I^2(a+x)^2}{EB^2h^3} \quad (5.3)$$

where,  $E$  is the Young's modulus of the adherends,  $h$  is the thickness of each adherend,  $a$  is the crack length,  $B$  is the width of the adherends and the bond, and  $x$  is the correction to the crack length in mode I. This correction necessitates first testing a specimen in pure mode I before analyzing tests with other loading modes. Details are shown at the end of this section. Similarly, the mode II component of  $G$  is given by [12]:

$$G_{II} = \frac{9F_{II}^2(a+0.42x)^2}{EB^2h^3} \quad (5.4)$$

where the 0.42 factor is suggested by finite element calibration[30]. The global mode mixity angle,  $\psi$ , is defined as,

$$\psi = \arctan \sqrt{\frac{G_{II}}{G_I}} \quad (5.5)$$

The crack is assumed to propagate when the applied SERR  $G = G_I + G_{II}$  reaches the critical SERR or the fracture energy,  $G_c$ . In mixed mode tests, the fracture energy can be partitioned into a mode I component  $(G_c)_I$  and a mode II component  $(G_c)_{II}$ . Since  $G_c$  is the critical value of  $G$  associated with crack propagation, it can be evaluated by substituting the critical forces into equations of  $G_I$ , and  $G_{II}$  for any particular mode mixity. Then the total fracture energy is defined to be the sum of the mode I and mode II components:

$$G_c = (G_c)_I + (G_c)_{II} \quad (5.6)$$

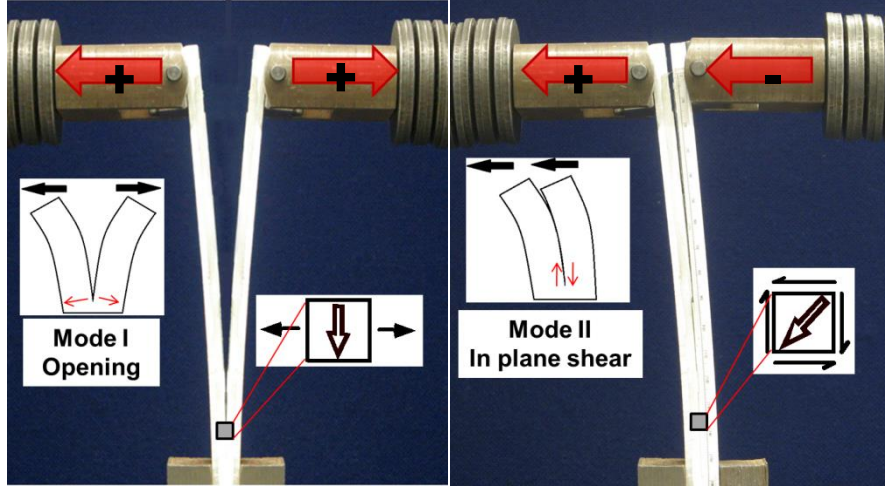


Figure 5.2. Definition of positive and negative loads in mode I and mode II tests.

#### 5.4.2 Compliance-based beam method

CBT introduces corrections to the crack length, as well as the effective stiffness, but still generally depends on manual crack readings. Obtaining accurate crack readings by visual observation is relatively easy for mode I tests, but identifying the real crack length in mixed mode tests, especially for mode II dominant loading, can be very challenging. Therefore, there is a need for methods that do not rely on manual crack readings. The compliance-based beam method (CBBM)[31] is one such method that uses Timoshenko beam theory and does not depend on manual crack reading. Using this technique, the fracture energy value can be calculated using only loads and displacements measured by the transducers. Though the crack lengths can also be read and recorded as markers when plotting the fracture energy curves, such readings are not actually used in the calculations. Instead, equivalent crack lengths will be calculated by knowing the loads and displacements. In brief, the loads and displacements provide all the information that is necessary to obtain the fracture energy. In the present work, CBBM is employed to compare with the results from CBT.

Based on the same partitioning of mode I and mode II components in equations (5.1) and (5.2) in CBT, the relationships between loads and displacements within CBBM can be expressed as follows,

$$\delta_L = \frac{(7a^3 + L^3)F_L}{2Bh^3E} + \frac{(a^3 - L^3)F_R}{2Bh^3E} + \frac{3[L(F_L - F_R) + a(F_L + F_R)]}{5BhG} \quad (5.7)$$

$$\delta_R = \frac{(7a^3 + L^3)F_R}{2Bh^3E} + \frac{(a^3 - L^3)F_L}{2Bh^3E} + \frac{3[L(F_R - F_L) + a(F_R + F_L)]}{5BhG} \quad (5.8)$$

$$C_I = \frac{\delta_I}{F_I} = \frac{8a^3}{Bh^3E} + \frac{12a}{5BhG} \quad (5.9)$$

$$C_{II} = \frac{\delta_{II}}{F_{II}'} = \frac{3a^3 + L^3}{2Bh^3E} + \frac{3L}{5BhG} \quad (5.10)$$

where,  $\delta_L$  and  $\delta_R$  are displacements of the left adherend and right adherend, respectively.  $C_I$  and  $C_{II}$  are compliances defined for mode I and mode II components, respectively.  $\delta_I$  and  $\delta_{II}$  are displacements defined for mode I and mode II components, respectively,

$$\delta_I = \delta_L + \delta_R \quad (5.11)$$

$$\delta_{II} = \frac{\delta_L - \delta_R}{2} \quad (5.12)$$

Based on the definition in [32],  $F_I$  and  $F_{II}$  are the same as used in CBT, the load in mode I and mode II[32].

The SERR can be calculated by the expression given by Irwin-Kies[33]:

$$G = \frac{P^2}{2B} \frac{dC}{da} \quad (5.13)$$

Similarly, using equation(5.9) and(5.10) for the compliances,

$$G_I = \frac{6F_I^2}{B^2h} \left( \frac{2a_{eI}^2}{h^2E} + \frac{1}{5G} \right) \quad (5.14)$$

$$G_{II} = \frac{9F_{II}^2 a_{eII}^2}{B^2 h^3 E} \quad (5.15)$$

where,  $a_{eI}$  and  $a_{eII}$  are equivalent crack lengths in mode I and mode II obtained by solving equations (5.9) and (5.10), respectively[32].

The CBBM is convenient to experimentalists because it would not require crack reading during the tests. However, when the error from the instrument compliances are involved in the real tests, some errors would be introduced to the equivalent crack lengths and fracture energies. Therefore, some correction to the specimen compliances would be helpful when using the CBBM. Details of the calibrations can be found in chapter 4, but some key points are shown briefly herein.

It is worth noting that the load frame compliance issues can affect both CBT (through effective slope measurement) and CBBM techniques. To show the influence of errors in the compliances, equations (5.9) and (5.10) were used to plot the relationships of crack length vs. compliance in Figure 5.3. The change in the compliance in mode I component is much steeper (proportional to  $a^3$ ) than mode II component (only 4 times that of the initial

value). For typical specimens considered herein, when the crack length increases from 100 mm to 200 mm,  $C_I$  increases by two times but  $C_{II}$  increases by around seven times. In other words, if the same amount of error in the compliance is assumed, the error introduced to  $a_{eII}$  is significantly larger than that in  $a_{eI}$ . Thus, when the CBBM is applied to the tests, some large errors would be found, especially for the mode II component of the fracture energy.

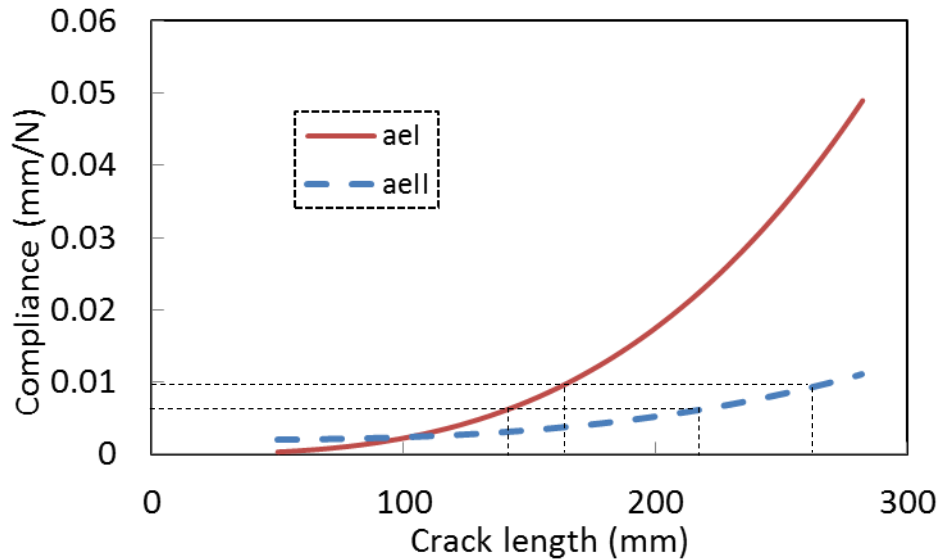


Figure 5.3. The effect of the error in compliance measurement to the calculation of the equivalent crack lengths.

Actually, when calculating the equivalent crack lengths using the CBBM, there are two equivalent crack lengths obtained, from mode I, and mode II components, respectively. Essentially, this is a mathematical problem with redundant equations (one variable but two equations). Since the compliances were used in this method, measurement of the small displacements is very important to the accuracy of the results. Therefore, the criterion to find a good estimation of the equivalent crack length is to choose the one that can best represent the crack length with the least error.

Therefore, some more corrections were required. The errors were introduced to the tests mainly through the compliances of the two cylinders, and the rotation in the clamp fixed at the platform. Finally, three steps were added to the calculation of fracture energy with this method:

- (1) Mode II components include both errors from the cylinder load train and rotation of the clamp, while mode I components include errors only from the cylinders. Also, the errors in the steel rods can be taken to be linear to the load, and are easier to be estimated. The error from the clamp was considered to be complex and nonlinear. Therefore, it is more convenient to use only  $a_{eI}$  to calculate both  $(G_c)_I$ , and  $(G_c)_{II}$ .

- (2) Test a DCB specimen with the same dimensions but without any crack in pure mode I, obtain the two compliances of the cylinders,  $C_L$ , and  $C_R$  while increasing the loads and displacements linearly. Theoretically, the compliances should be zero. Therefore these two values were used to be the two corrections to the compliances in the other tests.
- (3) When any of the loads of the cylinder changed from positive to negative, another error was introduced by the tolerance of the loading pins and holes. This correction to the displacement should also be considered.

Finally, after the modification in equations (5.9) and (5.11),

$$\frac{\delta_l}{F_l} - \frac{(C_L F_L + C_R F_R)}{F_l} + (1 - H(F_R)) \frac{T_R}{F_l} + (1 - H(F_L)) \frac{T_L}{F_l} = \frac{8a_e^3}{Bh^3 E} + \frac{12a_e}{5BhG} \quad (5.16)$$

where,  $H()$  is the Heaviside function,  $T_L$  and  $T_R$  are the tolerances of the left and right cylinder, respectively. In mixed mode tests, only one of the cylinders carries compressive load. Therefore,  $T_L$  and  $T_R$  will not be used at the same time. This equation was solved to get the equivalent crack length,  $a_e$ . Then, using  $a_{eI} = a_{eII} = a_e$ , the fracture energy and its two components were calculated by equations(5.6), (5.14), and (5.15), respectively.

### 5.4.3 Stability of the crack growth in mixed mode tests

Stability is also an important factor in designing and conducting fracture tests, and is dominated by the rate of change of SERR with respect to the crack length. The condition for stable crack growth is first shown by Williams [27]:

$$\left. \frac{dG}{da} \right|_{\delta=const} \leq 0 \quad (5.17)$$

Replacing  $P$  in equation(5.13) by  $P = \delta / C$ , where  $C$  is the compliance, and then taking the derivative of both sides, equation(5.17) becomes

$$\frac{CC''}{2C'^2} \leq 1 \quad (5.18)$$

where  $C'$  and  $C''$  are the first and second order derivative of  $C$  with respect to the crack length. Using this criterion for the loading case in the DALF, the critical crack length is calculated for any mode mixity angle in the dual actuator. This critical crack length for the tests on the DALF with the full range of mode mixity angle has not been reported by others, though Williams[27] and Davies[34] have showed some examples of different geometries by applying several different equations of  $C$  into equation (5.18). It is worth noting that, same to the statement in chapter 4, all the mixed mode tests on the DALF were conducted

by applying bending moments to the left, which is the positive direction we defined. In order to simplify the followed equations, a coefficient of  $-1 \leq k \leq 1$  is defined, such that

$$F_R = kF_L \quad (5.19)$$

Then, using equations (5.3) and(5.4), the mode mixity angle in equation (5.5) is

$$\psi = \arctan\left(\sqrt{\frac{3}{4} \frac{1-k}{1+k}}\right) \quad (5.20)$$

Thus,  $\mathcal{G}$  at any mode mixity can be calculated using the method introduced by Williams[27],

$$\mathcal{G} = \frac{a^2}{16BEI} (7F_L^2 + 7F_R^2 + 2F_L F_R) = \frac{a^2 F_L^2}{16BEI} (7 + 7k^2 + 2k) \quad (5.21)$$

Therefore, using equation(5.13),  $C' = dC / da$  and  $C$  can be calculated,

$$C' = \frac{2BG}{P^2} \quad (5.22)$$

$$C = \int_0^a \frac{2BG}{P^2} da + C_0 \quad (5.23)$$

where,  $C_0$  is the compliance when the crack length is zero. In this case, the total force that does work is  $P = F_L - kF_L = (1-k)F_L$ . Finally, the limit for stable crack propagation is obtained by,

$$\frac{a}{L} \geq \sqrt[3]{\frac{(1-k)^2}{2(7+7k^2+2k)}} \quad (5.24)$$

Obviously, when  $k = 1$  in pure mode I,  $a / L \geq 0$ . This means that the crack growth is always stable in pure mode I. In pure mode II,  $k = -1$ , and the criteria for stable crack growth is as same as that given by Williams[27].

$$\frac{a}{L} \geq \sqrt[3]{\frac{1}{6}} = 0.55 \quad (5.25)$$

The critical crack lengths at some mode mixity angles is shown in Table 5.1.

Table 5.1. Critical crack lengths at different mode mixity angles

Mode mixity angle (°)	Critical crack length (a/L)
0	0.00
20	0.27
40	0.41
60	0.50
80	0.54
90	0.55

Therefore, in this section, a more general equation for the critical crack lengths at different mode mixity angles is derived for the tests to be conducted on the DALF. However, the calculation above is only related to geometric instability, and is separate from material properties, temporal stability, or stick-slip behavior. Therefore, to avoid unstable crack propagation in mixed mode tests, the specimens were usually first tested in pure mode I to about halfway of the effective specimen length, and then loaded in mix mode as required.

## 5.5 Experimental results

The effective specimen length was  $L = 240mm$ , which was measured from the loading pin to the edge of the clamp at the base of the specimen. Based on the calculation for stable crack growth, the tests on the DALF were started by loading in pure mode I, until the crack length grew to just over halfway ( $\approx 130mm$ ). Figure 5.4 shows the fracture surfaces following a test conducted as shown in Figure 5.1. Crack propagation in these bonded DCB joints were always stable and many data points were recorded for each specimen.  $\mathcal{G}_c$  values at different mode mixity angles were calculated using both CBT and CBBM.

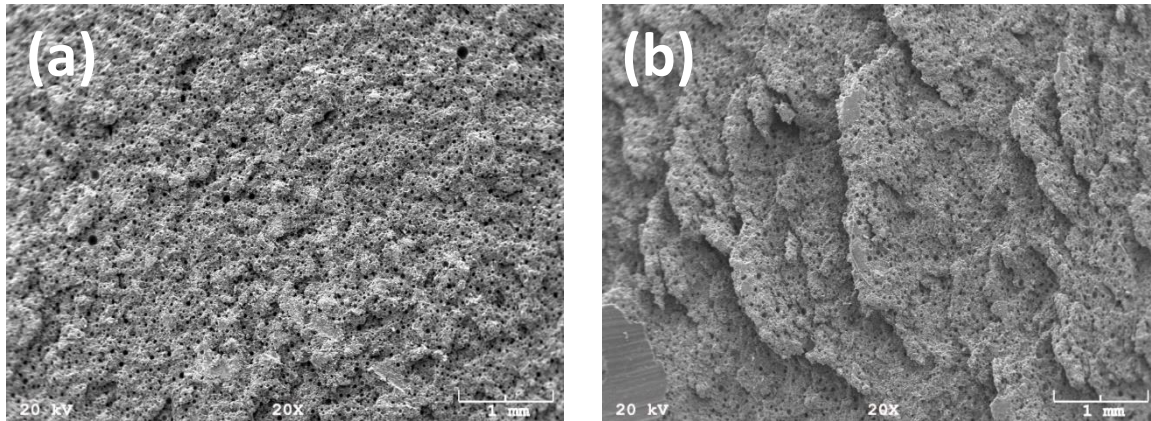


Figure 5.4. SEM pictures of the crack surfaces after the test of one JB Weld adhesive bonded specimen: (a) deformations were essentially pure mode I; (b) the mode mixity angle was around  $60^\circ$ .

The SEM pictures of representative fracture surfaces in Figure 5.4 for the JB Weld adhesive show that both mode I and  $60^\circ$  loaded specimens exhibited cohesive failures, which was also the case for all the following tests reported. Figure 5.4a reveals a representative fracture surface resulting from pure mode I loading (pure opening). Figure 5.4b was obtained in the region with higher mode mixity angle (less opening but more shearing) with characteristic hackles and microcracks. The LORD epoxy adhesive also showed similar crack surfaces as the JB Weld adhesive. Aiming to have stable crack growth, all the tests were executed in displacement control, with displacement rates of 0.1mm/min (crosshead displacement rate in mode I, left adherend displacement rate in mixed mode). Tests with constant mode mixity angles were also conducted in displacement control on the DALF, but with an extra sub-program in the controller of the DALF to read loads, calculate the mode mixity angle, and then adjust the displacements stably and automatically. A number of mixed mode tests were repeated and the fracture energy curves are shown in the following figures.

During the tests, the crack length was taken to be the distance from the center of the loading pin to the farthest microcrack observed using magnify lens by naked eye. Since it is very difficult to identify the main crack and the microcracks in a mixed mode test with such a thin adhesive layer, this crack-reading method may be the only practical one. Pictures and details were shown in the discussion. However, a pronounced resistance curve (R-curve) will be found when the mode mixity angle is changed, but this can be taken only as an intermediate value of the SERR before it reaches the fully developed plateau. It is reasonable to realize that if an increase in fracture energy occurs when changing from one mode mixity to another, a longer characteristic damage zone length in the adhesive layer is to be expected for the newly applied mode mixity angle. The fracture energy curves from the tests with constant mode mixity angles are shown first.

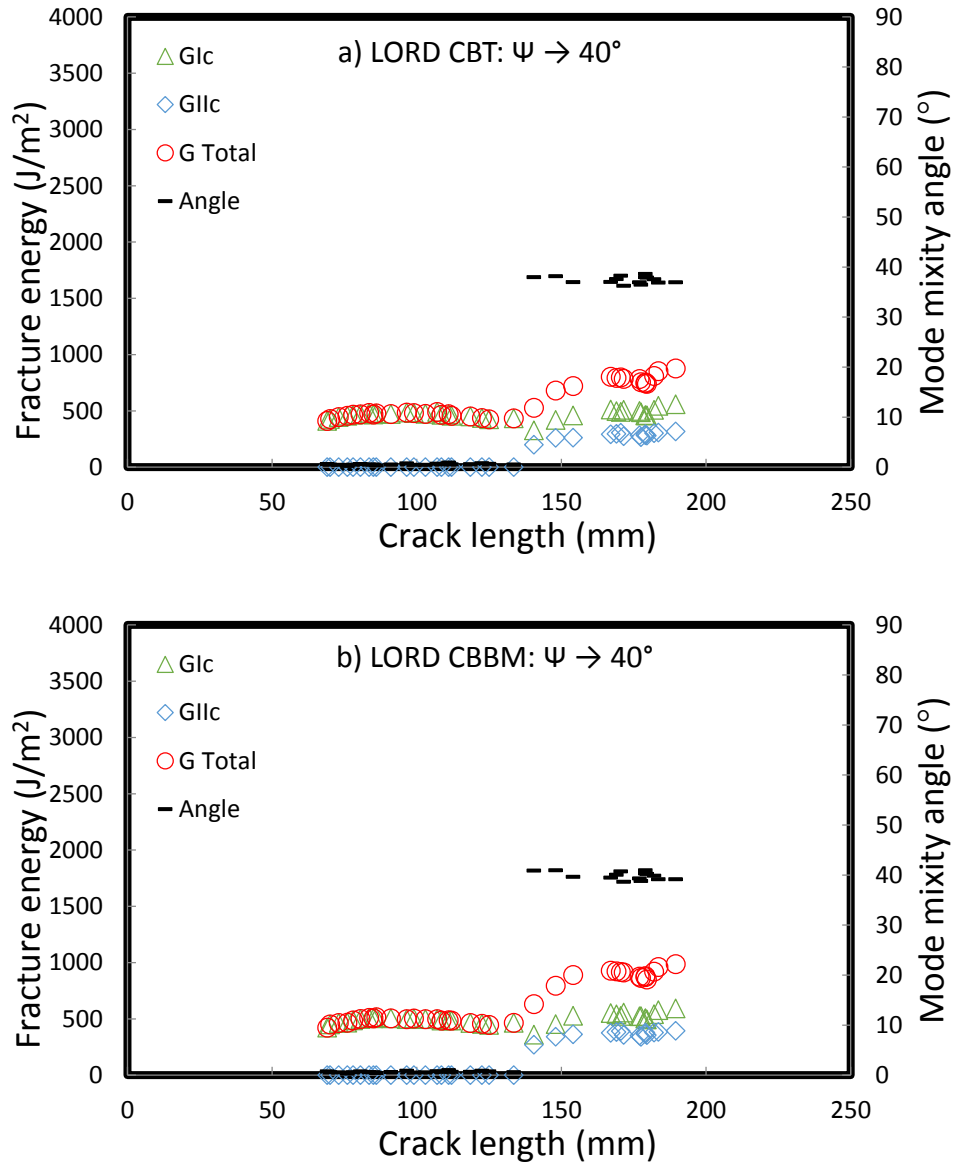


Figure 5.5. Fracture energy values from one test with mode I followed by constant nominal mode mixity angle of 40° (LORD): (a) CBT, (b) CBBM.

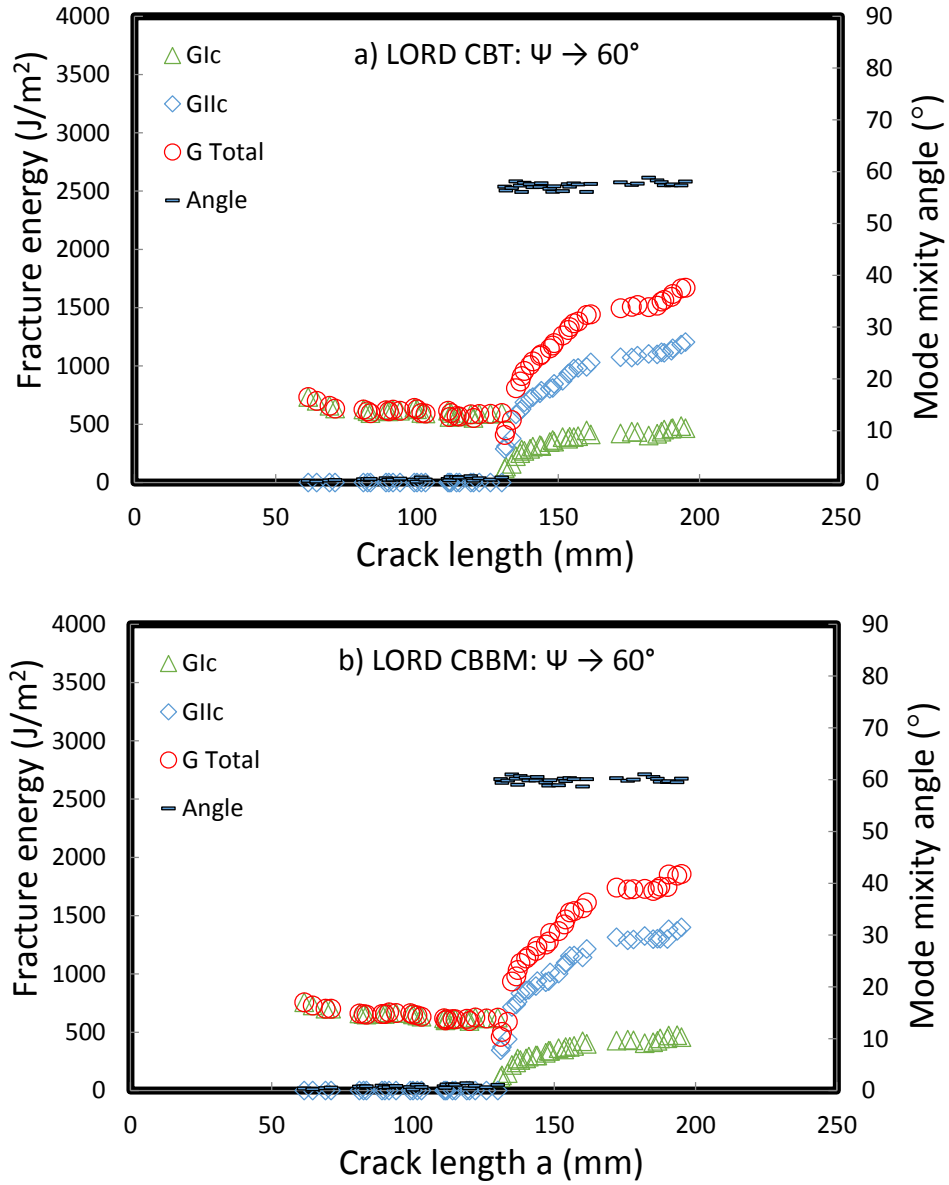


Figure 5.6. Fracture energy values from one test with mode I followed by constant nominal mode mixity angle  $60^\circ$  (LORD): (a) CBT, (b) CBBM.

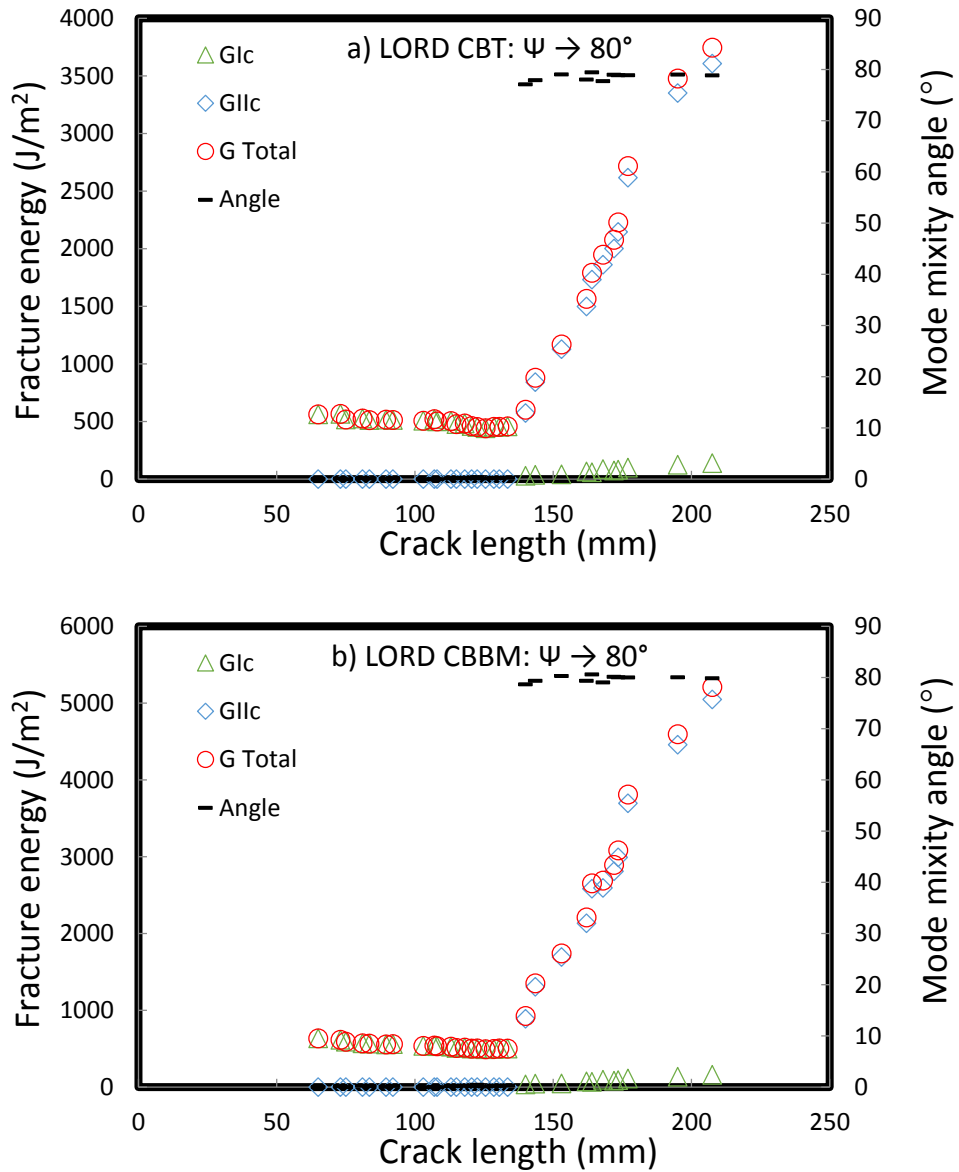


Figure 5.7. Fracture energy values from one test with mode I followed by constant nominal mode mixity angle  $80^\circ$  (LORD): (a) CBT, (b) CBBM.

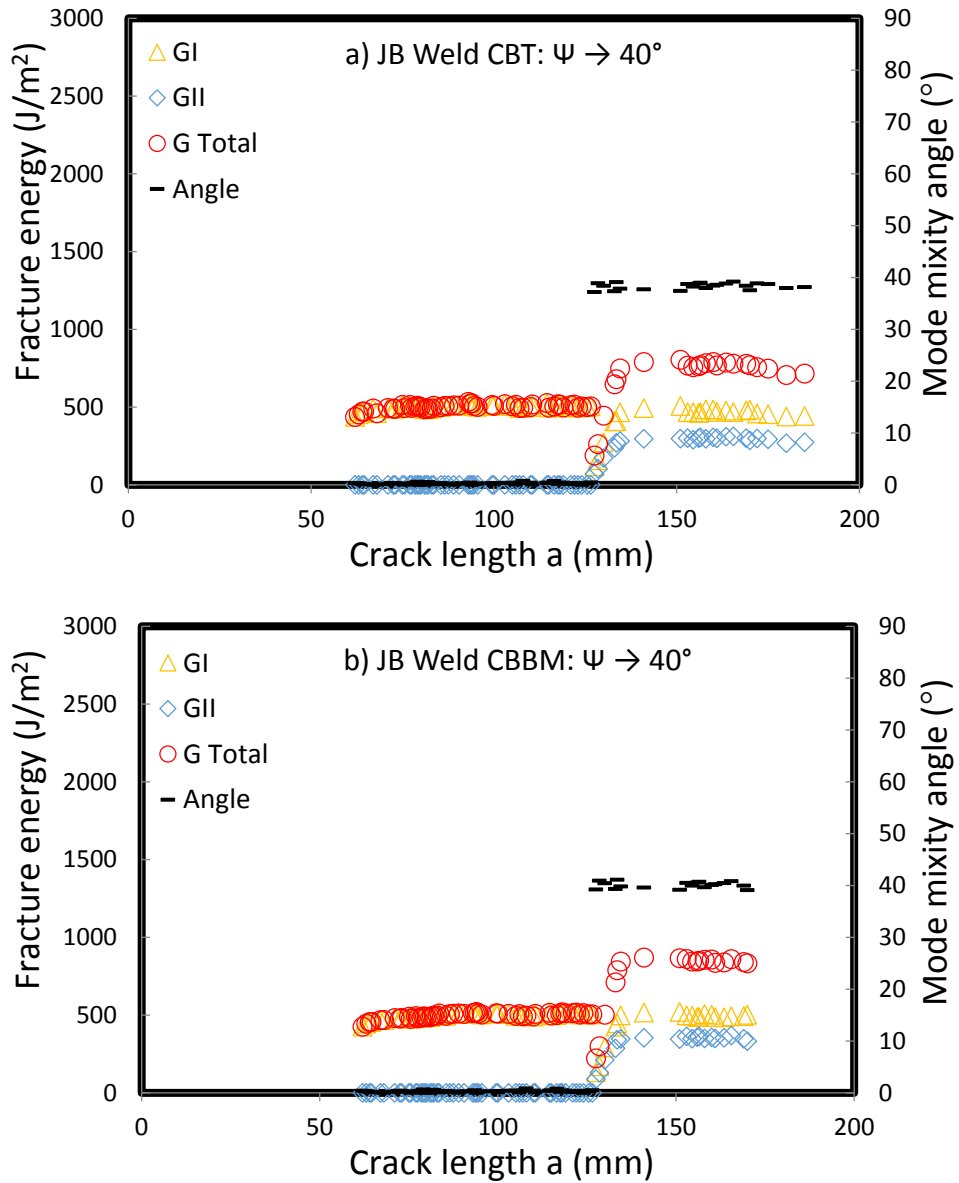


Figure 5.8. Fracture energy values from one test with mode I followed by constant nominal mode mixity angle  $40^\circ$  (JB Weld): (a) CBT, (b) CBBM.

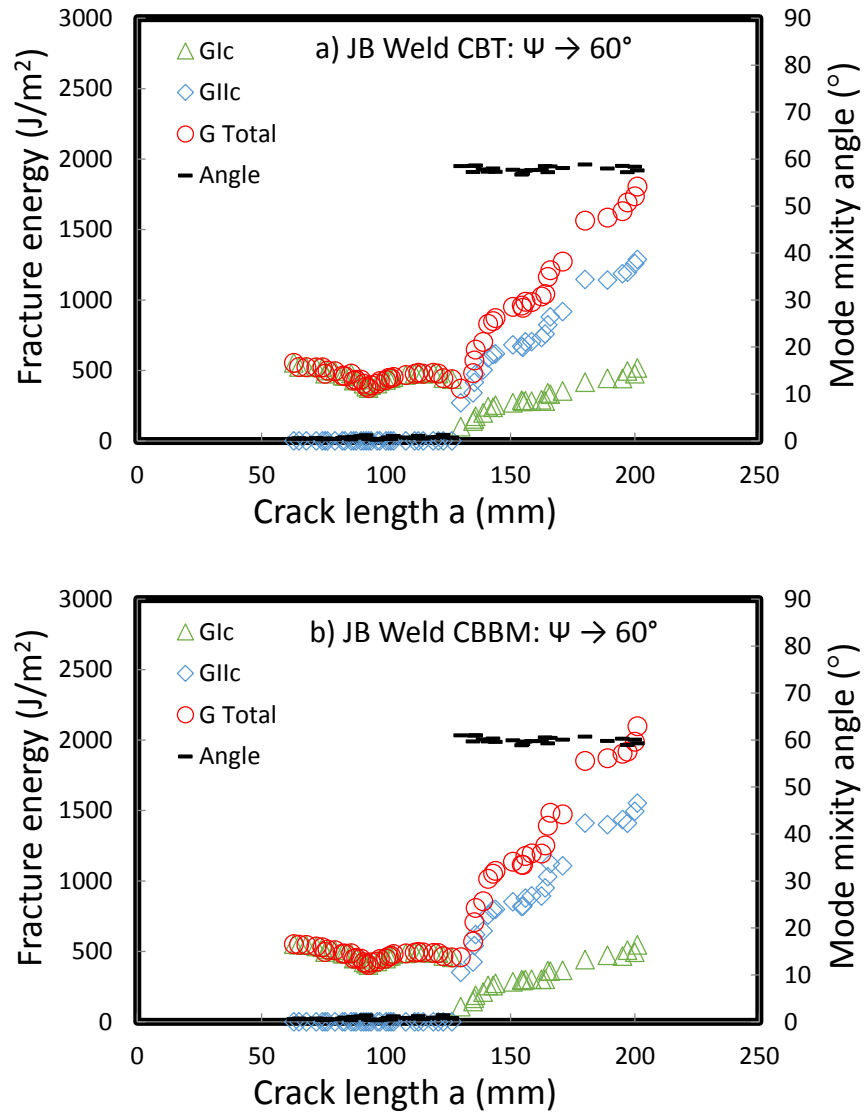


Figure 5.9. Fracture energy values from one test with mode I followed by constant nominal mode mixity angle  $60^\circ$  (JB Weld): (a) CBT, (b) CBBM.

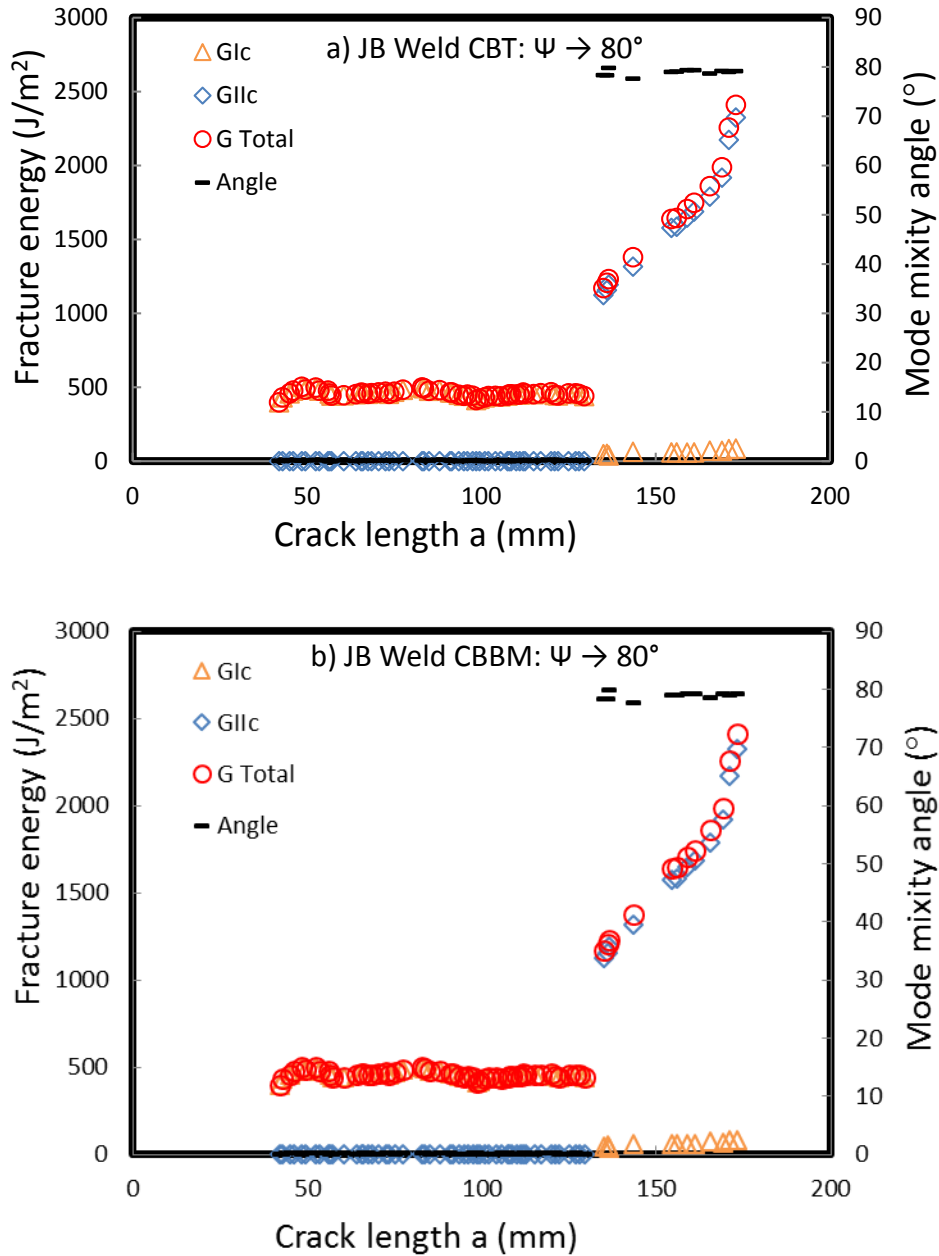


Figure 5.10. Fracture energy values from one test with mode I followed by constant nominal mode mixity angle  $80^\circ$  (JB Weld): (a) CBT, (b) CBBM.

Consistent with what is generally observed in much of the published literature, the figures indicate that the mixed mode  $G_c$  values are higher than those in pure mode I. As stated previously, when the crack length was taken to be the distance from the center of the loading pin to the farthest visible microcrack, apparent R-curves were found when the mode mixity angles were increased by a step function. After a certain distance, except for the  $80^\circ$  specimens, resistance curves reached a plateau value,  $G_c$ . The higher the mode mixity angle was, the longer the distance required to reach a plateau. The tests of specimens

prepared with LORD adhesive with mode mixity angle of  $40^\circ$  and  $60^\circ$  showed that the distances of the apparent R-curves are around 20mm, and 30mm, respectively. For specimens prepared with JB Weld adhesive and tested by changing the mode mixity angle from  $0^\circ$  directly to the designated angles of  $40^\circ$  and  $60^\circ$ , the distance ranged from 6mm to 25mm. The tests with a mode mixity angle of  $80^\circ$  didn't show plateaus for  $G_c$  for either the LORD or JB Weld specimens. The intermediate value of  $G$  kept increasing within the remaining length of the specimens. Therefore, since no plateaus were found in the fracture energy, the long apparent R-curves suggest that the damage zones in front of the main cracks were still developing. Thus the length of the damage zone is expected to be very large for high mode mixity tests.

In the present work, the crack tip damage zone is used to define the areas in the adhesive material where irreversible damage has been introduced. In order to clarify the definition, several other zones need to be explained. First, the K-dominant zone is defined as the region surrounding the crack tip wherein the stress intensity factors (SIFs) are sufficient to characterize the stress state. Then, within the K-dominant zone, there is a smaller zone where the material expresses nonlinear behavior, which is referred to as the plastic zone. Finally, in the immediate vicinity of crack tip, is the process zone, within which damage occurs and crack propagation proceeds. The process zone is usually neglected in both linear or nonlinear fracture mechanics, but is considered to be important if the local mechanisms of crack propagation are needed in simulating fracture [35]. Generally, the term damage zone includes both the plastic zone and the process zone. Therefore, it is reasonable to consider that, when loaded with a global mode mixity of  $80^\circ$ , the damage zones were not fully developed even after long distances ( $> 70mm$ ). More explanations are shown in the following discussion.

Another investigation is about the changing of mode mixity angles continuously. Since it would not be difficult to find some cracks in engineering bonded structures, which were initiated in mode I or low mode mixity angle, but gradually propagating with the mode mixity angle increases. Therefore, this study will convey some useful insights. Figure 5.11 shows one of the tests conducted with an increasing mode mixity angle, which is a specific capability of the dual actuator load frame. The specimen was also clamped at the bottom, and the different displacement rates were applied to the two adherends. Therefore, the mode mixity angle was changing while the two adherends were loaded. The rate of change of the mode mixity angle  $d\psi/da$  can be altered as needed by changing the two displacements or displacement rates during the tests. Similarly, another example is shown for JB Weld specimen in Figure 5.12.

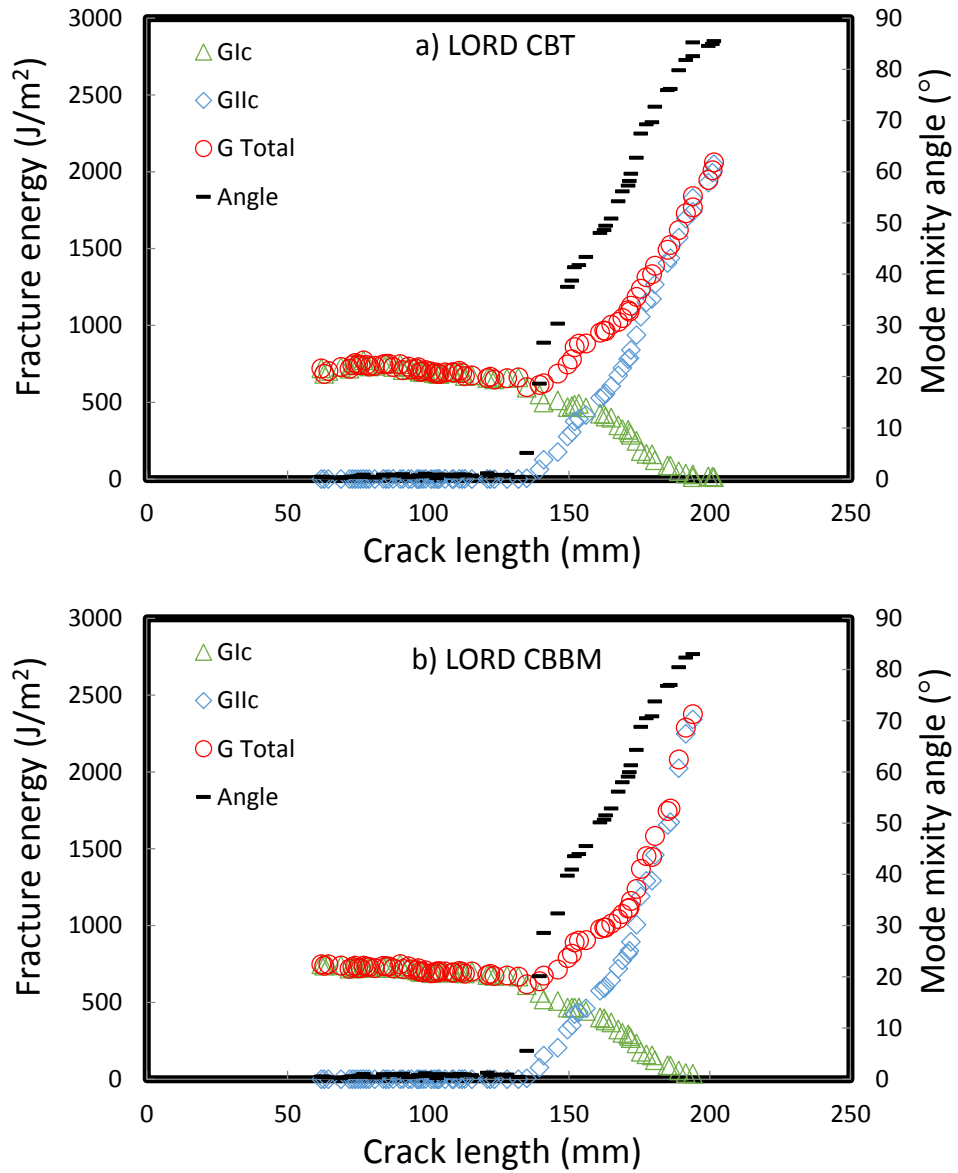


Figure 5.11. Fracture energy values from one test with increasing mode mixity angle (LORD): (a) CBT, (b) CBBM.

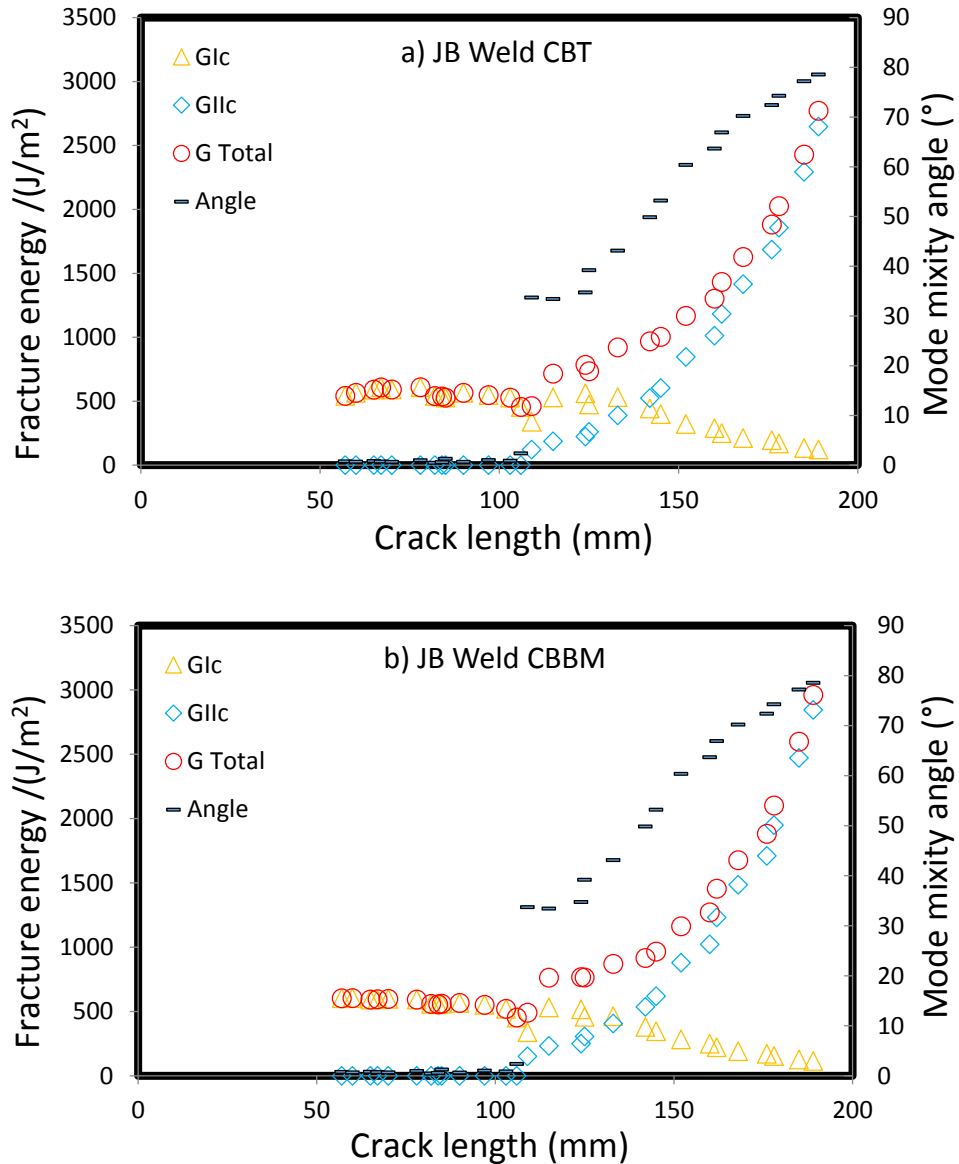
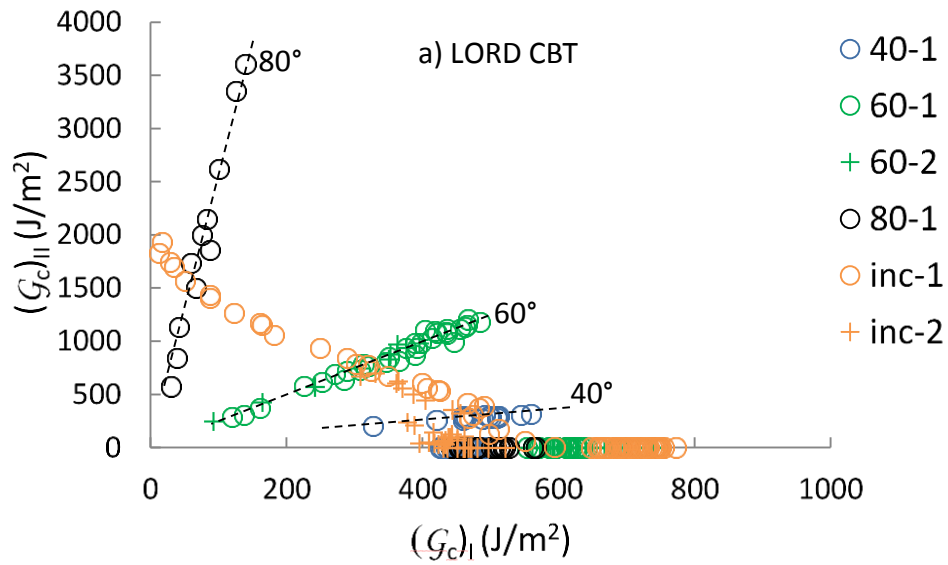


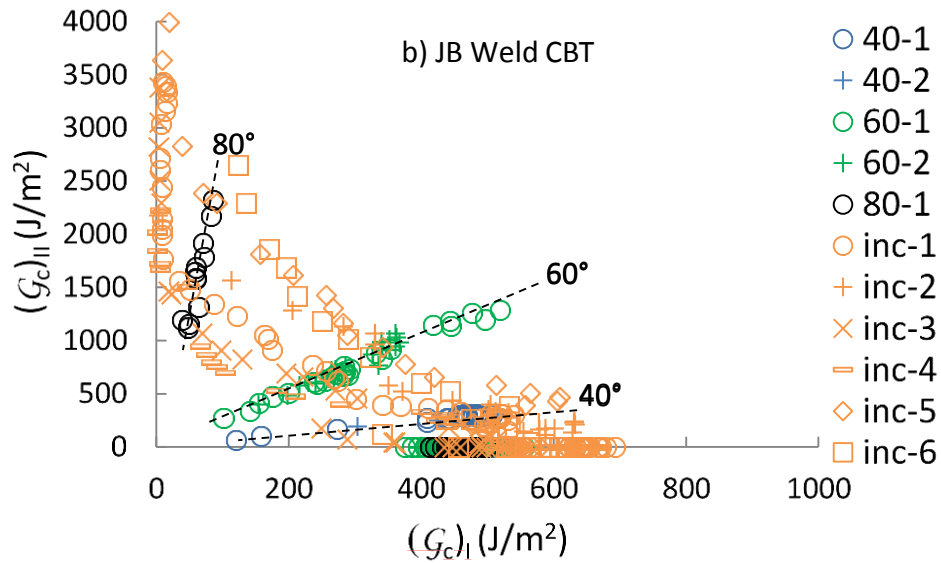
Figure 5.12. Fracture energy values from one test with increasing mode mixity angle (JB Weld): (a) CBT, (b) CBBM.

Figure 5.11 and Figure 5.12 show that the intermediate  $\mathcal{G}$  values obtained from a test conducted with increasing mode mixity angles were much lower than the plateau values of  $\mathcal{G}_c$  from constant mode mixity tests (as shown in Figure 5.5 to Figure 5.10). The higher the mode mixity angle is, the more significant the difference is. This is also considered to be the apparent R-curve effect. As the mode mixity angle changed, the new damage zone was developed as well. Therefore, the fracture energy value kept increasing. In order to show the behavior clearer, several tests were repeated and the combined plot of  $(\mathcal{G}_c)_I$  vs.  $(\mathcal{G}_c)_{II}$

is shown as a fracture envelope in Figure 5.13 (note that the scales in x-axis and y-axis are different).



(a)



(b)

Figure 5.13. Combined plot of failure envelopes with  $(G_c)_I$  vs.  $(G_c)_{II}$  for repeated tests: (a) LORD, (b) JB Weld.

These combined plots showed that, for both the JB Weld and the LORD 320/322 adhesives, the  $G_{IIc}$  values are much higher (5 to 10 times) than those of  $G_{Ic}$ . The fracture envelopes do not follow any significant unique law. Tests with increasing mode mixity

angle showed increasing intermediate  $G$  values. The toughening mechanisms may not be easily characterized by traditional relationships.

## 5.6 Discussion

It is worth noting that the apparent R-curves of both adhesives are quite high for mixed mode conditions. The following discussions will show possible reasons for these high values and lack of plateau at 80 °.

### 5.6.1 Friction and contact

For the analysis of the results in mixed mode tests, many researchers have considered the factors of friction and misreading of the crack lengths in mode II tests. Russell and Street [36] implied a maximum error of around 2% in  $G_{IIc}$  in composites if friction was ignored. Fernlund and Spelt [22] concluded that the effect of friction did exist but was relatively small in mode II ENF (end-notched flexure) and ELS (end-loaded split) tests. Davies[37] showed experimentally that frictional effects could account for up to 20% of the measured  $G_{IIc}$  values in the ENF test if PTFE spacers were not used in the region of loading pins. Blackman and Williams [38] considered friction effects by including a frictional shearing stress in the beam analysis. The effect of friction was shown to be significant for the composites studied, but the results were dependent upon the accuracy of both the corrected beam theory and experimental compliance data analysis methods. These methods, as shown in [12], are sensitive to errors in measured crack length. Other researchers [39, 40] have also indicated that a major cause of scatter and inconsistency in mode II data analyses may be the difficulty in determining the location of the crack tip. Since the DCB specimens were loaded by two cylinders on the dual actuator load frame, and most of the tests were mixed mode tests, there were still some opening between the opposite crack surfaces. Therefore, for the toughened adhesives used in our tests, friction is not expected to have been a major concern when the mode mixity angle is not very high. But if near 90 °, the two adherends are very close to each other and the rough hackles and microcrack feathers likely move against each other and larger resistances (including frictions and contacts) would be expected.

### 5.6.2 Toughening mechanisms and microcracks in adhesive

In some modified epoxies toughened with nano-silica particles (e.g. Nanopox F400[41, 42], or D.E.R. 331[5, 43]), the crack surfaces appeared smooth to the naked eye after pure opening. In the toughened epoxy adhesives used herein, several toughening mechanisms is expected to be employed to carry and distribute the loads, though the researchers don't know details about them. Therefore, the crack surfaces resulting from pure mode I loading were also tortuous (see Figure 5.4a). In mixed mode tests, the stage of the apparent R-curves was very long in the two epoxy adhesives tested herein. Usually, many microcracks were shown along the bondline, as shown in Figure 5.14, and more were found on the crack surfaces after the tests. Therefore, it is reasonable to expect microcracks inside the damage zones before the main crack propagates. As estimated by Lee[44] in mode II tests, the shear

stresses showed periodic peaks in the adhesive layer in front of the crack tip. Thus the microcracks were found throughout a long distance in the longitudinal direction. But these phenomena were only considered to be the response of the yielding areas, and therefore could not be taken as the propagation of the main crack. Then these microcracks developed and connected with each other, and then with the main crack. Only at this point would it be reasonable to consider that the main crack propagated.

Traditionally, from the viewpoint of energy dissipation, the measured fracture energy results from energy consumed in creating new crack surfaces. Actually, the dissipation is not only related to new crack surface development, but also other irreversible behaviors, such as plastic deformation. Many researchers have given insights into possible explanations for a strong mixed mode effects due to plasticity [45, 46]. These theories were also used to explain the results in the present work. Besides that, microcracks and hackle patterns were also considered. Though no details are provided, these toughening mechanisms are supposed to be spreading the deformations to the regions farther away from the crack tip. Therefore, the area with plastic deformation is enlarged more significantly when comparing to brittle epoxy adhesives such as D.E.R. 331. Thus, due to the toughening effects of the components in the adhesives, the energy is distributed throughout a large region, which develops lots of microcracks instead of driving the main crack to failure.

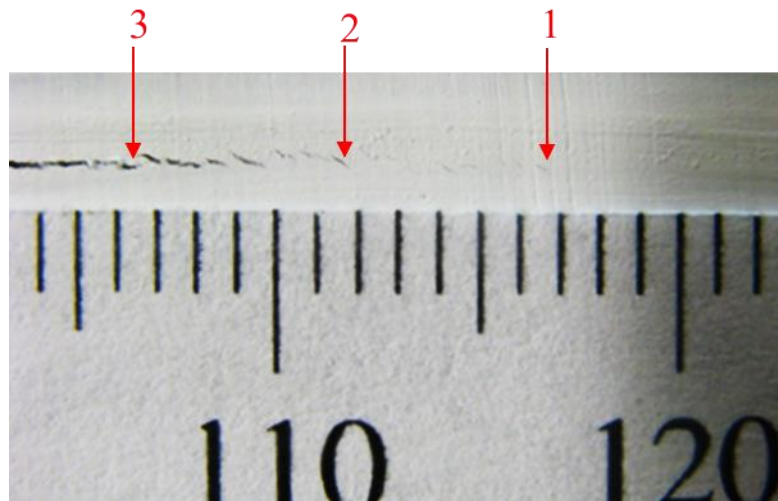


Figure 5.14. Main crack and microcracks observed along the correction fluid covered bondline during a  $60^\circ$  mixed mode test of a DCB specimen prepared with JB Weld adhesive: different “crack tip” criteria would lead to different crack reading at the location of (1) 117mm, (2) 112mm, and (3) 106.5mm.

Actually, the microcracks created in the adhesive layer may have similar spacing between one another, but may not be placed neatly along the thickness direction. The real array of microcrack would be similar to the one shown in Figure 5.14. Then, these microcracks would connect with each other to form some larger cracks. Also, it is worth noting that, the size of the minimum visible microcracks visible to naked eyes would be in the scale of 0.1mm, with the orientation of about  $45^\circ$ , which complies with the theoretical

value for deformable materials with shearing stresses. The small cracks shown in Figure 5.14 were not the minimum visible microcracks.

### 5.6.3 Effect of damage zone size in constrained joints

The diagrams in Figure 5.15 suggest a comparison of damage zone of bulk material and bonded joint when loaded in shear. In bulk materials, the plastic zone or damage zone was developed with no extra constraints. However, in bonded joints with thin adhesive layers, the development of the damage zone is strongly constrained by the adherends and the clamping at the bottom. Many relatively brittle adhesives exhibit large shear strains at break in constrained joints (some reported ultimate tensile strain is around 5% while ultimate shear strain is around 80%). Azari *et al.* have reported similar apparent R-curve for about 70 mm at the mode mixity angle of 65 [47]. They also studied the fracture of the adhesive they used by finite element analysis with plastic strain in the model[48]. They showed that the size of the plastic zone increases when the mode mixity angle increases. Similarly, in mixed mode tests herein, the damage zone was enlarged, and microcracks were created one after another, and then connected with each other. At the same time, the size of the plastic zones close to these microcrack tips was also developing. If different criteria for judging the crack length were applied, such as the three shown in Figure 5.14, different apparent R-curves would be plotted in Figure 5.15 when the mode mixity angle changed from A to B. It is also worth noting that, it is difficult to identify where the main/real crack tip is. Though they are more or less connected with each other, but it seems like that it is difficult to find a direct criteria to find the main crack tip. Of course, there are so many microcracks in actual mixed mode tests that detecting advancing crack propagation of the main crack is very difficult. Therefore, essentially, these dependencies make the apparent R-curve determination quite subjective rather than an objective material property.

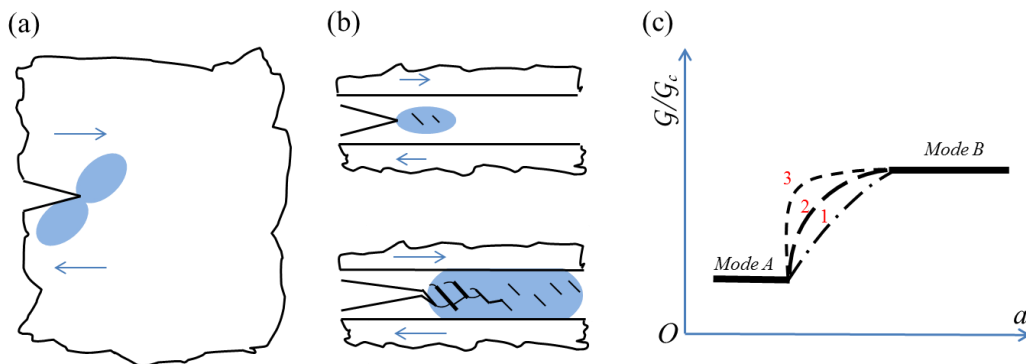


Figure 5.15. Diagrams to show the damage zone in (a) monolithic material, (b) thin adhesive layer and its evolution, and (c) different R-curves when using different criteria, the numbers are corresponding to the crack reading in Figure 5.14.

Alvarez, *et al.* have reported significant large damage zone in mode II fracture tests using ELS specimens [49]. They were using thicker (thus stiffer) adherends to test highly toughened adhesives to avoid plastic deformation of the adherends. However, these thicker adherends yield larger damage zones and thus reduce the ability to reach a stable, steady-state plateau in the test. Numerical analysis was employed in their study to determine the length of the damage zones (cohesive zones) in the specimen and it was shown that for the tough adhesive, the whole of the adhesive layer (from the crack tip to the clamp point) became part of the damage zone prior to crack initiation. Such behavior violates the assumptions of LEFM and explains the apparently strongly rising R-curves observed and the failure to reach a steady-state[49].

Thus, it is reasonable to conclude that it is the toughening effects of the two stiff adherends and the clamping at the bottom that introduced this difference in the mixed mode tests herein. Indeed, with the stiff adherends, strong constraint was applied through the interfaces to the adhesive. This limited the strain near the crack tip, and a larger area of the adhesive deformed and yielded simultaneously. Besides the plastic deformation, there were also lots of microcracks and hackles initiated and developed simultaneously within the enlarged damage zone. When larger volume of the adhesive involved in the yielding, the SERR calculated were much higher than those from pure mode I.

## 5.7 Conclusions

The process of testing a DCB specimen at different mode mixity angles or continuously changing mode mixity angles on the DALF was shown in detail. This method to obtain fracture envelopes of adhesively bonded joints is considered to be a reliable option because multiple loading modes can be easily applied to a given specimen having the same surface pretreatment and bonding procedures. In addition, a single fixture is used and a consistent set of equations is used to analyze the results obtained using two different approaches to calculate fracture energy over the range of mode mixity angles studied. Both the CBT and the CBBM analysis methods were employed, comparing and discussing their results. A discussion of the CBBM and beam compliance methods showed possible ways to improve the accuracy of the CBBM when calculating fracture energy in mixed mode tests. A general equation was derived for stable mixed mode tests of DCB specimens on the DALF, as well as other fixtures.

Tests at constant mode mixity angles showed apparent R-curve effects. The tests of specimens prepared with both adhesives studied at mode mixity angles of 40 ° and 60 ° showed plateaus for  $G_c$ . But no plateaus for  $G_c$  were seen in the tests with a mode mixity angle of 80 °. Tests with increasing mode mixity angle also showed increasing apparent  $G_c$  values, which are lower than that of the corresponding constant mode mixity tests.

The strong apparent R-curve effects are likely explained by the stiff adherends and the clamping at the bottom, which limited the strain near the crack tip. When the strong constraint was applied through the interfaces to the adhesive, a larger area of the adhesive deformed and yielded simultaneously. The whole of the adhesive layer (from the crack tip to the clamp point) apparently became part of the damage zone prior to crack propagation.

These experimental results showed that the behavior of bonded joints not only depends on the material properties of the adhesive, but is also related to the stiffness of the adherends and fixtures. The apparent R-curves were very long and the plateaus for  $G_c$  were very high when specimens were loaded in mixed mode conditions in stiffer adherends and fixtures. These points would be useful in understanding of the test results, as well as the engineering design of bonded joints.

## 5.8 References

- [1] H. J. Choi and G. H. Paulino, "Interfacial cracking in a graded coating/substrate system loaded by a frictional sliding flat punch," *Proceedings of the Royal Society a-Mathematical Physical and Engineering Sciences*, vol. 466, pp. 853-880, Mar 8 2010.
- [2] J. M. A. Reina, J. J. N. Prieto, and C. A. Garcia, "Influence of the Surface Finish on the Shear Strength of Structural Adhesive Joints and Application Criteria in Manufacturing Processes," *Journal of Adhesion*, vol. 85, pp. 324-340, 2009.
- [3] B. Chen, D. A. Dillard, J. G. Dillard, and R. L. Clark, "Crack path selection in adhesively bonded joints: the roles of external loads and specimen geometry," *International Journal of Fracture*, vol. 114, pp. 167-190, Mar 2002.
- [4] B. Chen and D. A. Dillard, "Numerical analysis of directionally unstable crack propagation in adhesively bonded joints," *International Journal of Solids and Structures*, vol. 38, pp. 6907-6924, SEP 2001.
- [5] B. Chen, D. A. Dillard, J. G. Dillard, and R. L. Clark, "Crack path selection in adhesively-bonded joints: The role of material properties," *Journal of Adhesion*, vol. 75, pp. 405-434, 2001.
- [6] D. A. Dillard, H. K. Singh, D. J. Pohlit, and J. M. Starbuck, "Observations of Decreased Fracture Toughness for Mixed Mode Fracture Testing of Adhesively Bonded Joints," *Journal of Adhesion Science and Technology*, vol. 23, pp. 1515-1530, 2009.
- [7] G. Fernlund and J. K. Spelt, "Mixed-Mode Energy-Release Rates for Adhesively Bonded Beam Specimens," *Journal of Composites Technology & Research*, vol. 16, pp. 234-243, JUL 1994.
- [8] A. J. Kinloch, *Adhesion and Adhesives: Science and Technology*. London: Chapman and Hall, 1987.
- [9] BS-7991, "Determination of the Mode I Adhesive Fracture Energy,  $G_{Ic}$ , of Structural Adhesives Using the Double Cantilever Beam (DCB) and Tapered Double Cantilever Beam (TDCB) Specimens," ed, 2001.
- [10] ASTM-D3433-99, "Standard Test Method for Fracture Strength in Cleavage of Adhesives in Bonded Metal Joints," in *Annual Book of ASTM Standards*, ed West Conshohocken, PA, 1999 (Reapproved in 2005).
- [11] F. Ducept, P. Davies, and D. Gamby, "Mixed mode failure criteria for a glass/epoxy composite and an adhesively bonded composite/composite joint," *International Journal of Adhesion and Adhesives*, vol. 20, pp. 233-244, Jun 2000.
- [12] B. R. K. Blackman, A. J. Kinloch, and M. Paraschl, "The determination of the mode II adhesive fracture resistance,  $G_{IIc}$ , of structural adhesive joints: an

- effective crack length approach," *Engineering Fracture Mechanics*, vol. 72, pp. 877-897, Apr 2005.
- [13] R. Duer, D. Katevatis, A. J. Kinloch, and J. G. Williams, "Comments on mixed-mode fracture in adhesive joints," *International Journal of Fracture*, vol. 75, pp. 157-162, 1996.
- [14] B. D. Davidson and V. Sundararaman, "A single leg bending test for interfacial fracture toughness determination," *International Journal of Fracture*, vol. 78, pp. 193-210, 1996.
- [15] G. Fernlund and J. K. Spelt, "Failure Load Prediction of Structural Adhesive Joints .2. Experimental-Study," *International Journal of Adhesion and Adhesives*, vol. 11, pp. 221-227, Oct 1991.
- [16] Y. H. Lai, M. D. Rakestraw, and D. A. Dillard, "The cracked lap shear specimen revisited - A closed form solution," *International Journal of Solids and Structures*, vol. 33, pp. 1725-1743, May 1996.
- [17] S. Mall and N. K. Kochhar, "Criterion for Mixed Mode Fracture in Composite Bonded Joints," *NASA/CR-178112*, 1986.
- [18] S. Park and D. A. Dillard, "Development of a simple mixed-mode fracture test and the resulting fracture energy envelope for an adhesive bond," *International Journal of Fracture*, vol. 148, pp. 261-271, Dec 2007.
- [19] J. R. Reeder and J. H. Crews, "Mixed-Mode Bending Method for Delamination Testing," *AIAA Journal*, vol. 28, pp. 1270-1276, Jul 1990.
- [20] J. R. Reeder and J. H. Crews, "Redesign of the Mixed-Mode Bending Delamination Test to Reduce Nonlinear Effects," *Journal of Composites Technology & Research*, vol. 14, pp. 12-19, Spr 1992.
- [21] J. R. Reeder and J. J. H. Crews, "Non-linear Analysis and Redesign of the Mixed-mode Bending Delamination Test," *NASA/TM-102777*, 1991.
- [22] G. Fernlund and J. K. Spelt, "Mixed-Mode Fracture Characterization of Adhesive Joints," *Composites Science and Technology*, vol. 50, pp. 441-449, 1994.
- [23] M. Papini, G. Fernlund, and J. K. Spelt, "The Effect of Geometry on the Fracture of Adhesive Joints," *International Journal of Adhesion and Adhesives*, vol. 14, pp. 5-13, Jan 1994.
- [24] F. J. P. Chaves, M. F. S. F. de Moura, L. F. M. da Silva, and D. A. Dillard, "Numerical validation of a crack equivalent method for mixed-mode I plus II fracture characterization of bonded joints," *Engineering Fracture Mechanics*, vol. 107, pp. 38-47, Jul 2013.

- [25] H. K. Singh, A. Chakraborty, C. E. Frazier, and D. A. Dillard, "Mixed mode fracture testing of adhesively bonded wood specimens using a dual actuator load frame," *Holzforschung*, vol. 64, pp. 353-361, Apr 2010.
- [26] H. K. Singh, P. Soojae, D. C. Ohanehi, and D. A. Dillard, "A design space for a novel dual-actuator mixed-mode test frame," *Proceedings of the 29th Annual Adhesion Society Meeting, Jacksonville, FL, 2006*.
- [27] J. G. Williams, "On the Calculation of Energy-Release Rates for Cracked Laminates," *International Journal of Fracture*, vol. 36, pp. 101-119, Feb 1988.
- [28] B. R. K. Blackman, A. J. Kinloch, M. Paraschi, and W. S. Teo, "Measuring the mode I adhesive fracture energy,  $G(IC)$ , of structural adhesive joints: the results of an international round-robin," *International Journal of Adhesion and Adhesives*, vol. 23, pp. 293-305, Aug 2003.
- [29] "Determination of the mode I adhesive fracture energy,  $GIC$ , of structural adhesives using the double cantilever beam (DCB) and tapered double cantilever beam (TDCB) specimens," ed: BSI, 2001, p. 32.
- [30] Y. Wang and J. G. Williams, "Corrections for Mode-Ii Fracture-Toughness Specimens of Composites Materials," *Composites Science and Technology*, vol. 43, pp. 251-256, 1992.
- [31] M. F. S. F. de Moura and A. B. de Morais, "Equivalent crack based analyses of ENF and ELS tests," *Engineering Fracture Mechanics*, vol. 75, pp. 2584-2596, Jun 2008.
- [32] F. J. P. Chaves, M. F. S. F. de Moura, L. F. M. da Silva, and D. A. Dillard, "Numerical analysis of the dual actuator load test applied to fracture characterization of bonded joints," *International Journal of Solids and Structures*, vol. 48, pp. 1572-1578, May 15 2011.
- [33] G. R. Irwin, "Fracture dynamics," *Fracturing of Metals, American Society for Metals*, pp. 147-166, 1948.
- [34] P. Davies, B. R. K. Blackman, and A. J. Brunner, "Mode II delamination," in *European Structural Integrity Society, D. R. Moore, et al., Eds., ed: Elsevier, 2001*, pp. 307-330.
- [35] S. Pommier, A. Gravouil, A. Combescure, and N. Moes, *Extended finite element method for crack propagation*. Hoboken, NJ 07030: John Wiley & Sons, Inc., 2011.
- [36] A. J. Russell and S. K. N., "Factors affecting the interlaminar fracture energy of graphite/epoxy laminates," presented at the ICCM-IV, Tokyo, Japan, 1982.
- [37] P. Davies, "Influence of ENF specimen geometry and friction on the mode II delamination resistance of carbon/PEEK," *Journal of Thermoplastic Composite Materials*, vol. 10, pp. 353-361, Jul 1997.

- [38] B. R. K. Blackman and W. J. G., "On the mode II testing of carbon–fibre polymer composites," presented at the ECF12 fracture from defects, Sheffield, UK, 1998.
- [39] A. J. Brunner, "Experimental aspects of Mode I and Mode II fracture toughness testing of fibre-reinforced polymer-matrix composites," *Computer Methods in Applied Mechanics and Engineering*, vol. 185, pp. 161-172, 2000.
- [40] A. J. Brunner, B. R. K. Blackman, and J. G. Williams, "Calculating a damage parameter and bridging stress from G(IC) delamination tests on fibre composites," *Composites Science and Technology*, vol. 66, pp. 785-795, May 2006.
- [41] B. R. K. Blackman, A. J. Kinloch, J. S. Lee, A. C. Taylor, R. Agarwal, G. Schueneman, and S. Sprenger, "The fracture and fatigue behaviour of nano-modified epoxy polymers," *Journal of Materials Science*, vol. 42, pp. 7049-7051, Aug 2007.
- [42] B. B. Johnsen, A. J. Kinloch, R. D. Mohammed, A. C. Taylor, and S. Sprenger, "Toughening mechanisms of nanoparticle-modified epoxy polymers," *Polymer*, vol. 48, pp. 530-541, 2007.
- [43] B. Chen, D. A. Dillard, J. G. Dillard, and R. L. Clark, "Crack path selection in adhesively bonded joints: the roles of external loads and specimen geometry," *International Journal of Fracture*, vol. 114, pp. 167-190, MAR 2002.
- [44] S. M. Lee, "Mode II delamination failure mechanisms of polymer matrix composites," *Journal of Materials Science*, vol. 32, pp. 1287-1295, Mar 1 1997.
- [45] K. M. Liechti and Y. S. Chai, "Asymmetric Shielding in Interfacial Fracture under Inplane Shear," *Journal of Applied Mechanics-Transactions of the Asme*, vol. 59, pp. 295-304, Jun 1992.
- [46] V. Tvergaard and J. W. Hutchinson, "The Influence of Plasticity on Mixed-Mode Interface Toughness," *Journal of the Mechanics and Physics of Solids*, vol. 41, pp. 1119-1135, Jun 1993.
- [47] S. Azari, M. Eskandarian, M. Papini, J. A. Schroeder, and J. K. Spelt, "Fracture load predictions and measurements for highly toughened epoxy adhesive joints," *Engineering Fracture Mechanics*, vol. 76, pp. 2039-2055, 2009.
- [48] S. Azari, M. Papini, and J. K. Spelt, "Effect of adhesive thickness on fatigue and fracture of toughened epoxy joints – Part II: Analysis and finite element modeling," *Engineering Fracture Mechanics*, vol. 78, pp. 138-152, 2011.
- [49] D. Alvarez, B. R. K. Blackman, F. J. Guild, A. J. Kinloch, A. C. Taylor, and S. Osiyemi, "Mode II Fracture in Adhesive Joints," in *The 36th Annual Meeting of the Adhesion Society*, Daytona, FL, 2013.

# Chapter 6 A numerical study of crack path selection in mode I and mixed mode loading conditions using cohesive zone models

---

(Paper prepared for submission to the *Engineering Fracture Mechanics*)

## **Abstract:**

Damage evolution and the possibility of fracture remain significant concerns in the engineering design of adhesively bonded joints and composite materials. One area of interest is crack path selection, which is important because failures along different crack paths may offer different resistances to fracture, affecting the resulting performance and durability. In the present study, numerical simulations are conducted to investigate the influence of locally weakened interfacial regions on crack path trajectories of propagating cracks in adhesive bonds. The numerical model of adhesively bonded double cantilever beam (DCB) specimens with an initial crack in the middle of the adhesive layer is developed in ABAQUS®. Besides the two strong interfaces between the adhesive and the adherends, a weakened interfacial area is introduced along a portion of one of the strong interfaces, simulated through reduced properties. Two cohesive zone models (CZMs) are used: cohesive elements are used for the interfaces, and the extended finite element method (XFEM) is employed for the bulk adhesive material. Under globally mode I loading, the resulting crack paths demonstrated significant differences due to the interaction between the main (cohesive) crack and the weakened interface. The maximum traction of the CZM at these weakened interfaces appears to be the controlling parameter for altering crack path selection in bonded joints, as exceeding this traction allows additional compliance and induces shear stresses that direct the growing crack toward the weakened interface. The fracture energy of the weakened interface was of secondary importance, but it can affect the results when it is particularly small (e.g. 1% of the adhesive fracture energy). Under globally mixed mode loadings, the competition between the loading and weakened interface affects the shear stress distribution and thus changes the crack path in the adhesive layer. Higher mixed mode loadings in the opposite direction of the weakened interface are predicted to drive the crack away from the weak interface, potentially avoiding failure within these regions.

## **Keywords:**

Crack path selection, locally weakened interface, cohesive zone model(CZM), cohesive element, extended finite element method(XFEM), damage evolution, maximum traction, fracture energy, double cantilever beam, adhesively bonded joint, mixed mode.

## 6.1 Introduction

Damage and cracks are occasionally found in structural adhesives or bonded joints, especially in detrimental service situations, or in response to a variety of environmental challenges. If the cracks have been initiated, the next step is to evaluate the service life, or to study if the crack can be steered to some tougher regions so as to extend the service life. Some engineers may want to direct cracks in certain ways to control locus of failure, increase or decrease resistance to failure. In addition, scientists would also like a deeper understanding of the fundamental mechanisms of fracture such as factors that affect crack path selection. If more understanding to the crack path selection can be found, engineers would have the chance to make use of it in designs, or control it when possible. Therefore, knowledge of crack path selection in bonded joints could have potential applications in the future.

Besides the initial cracks, some improper bonding procedures would leave some partially contaminated interfacial regions in the bonded joints, which could potentially do harm to the whole structure or system. Damage or cracks can form from environmental degradation, fatigue, or mechanical overload. Though these weakened interfaces might not fail in a short time, it could accelerate the damage process of the structure when some neighbor crack is propagating.

In this chapter, for more insight into crack path selection in bonded joints with partially weakened interface, numerical simulations were conducted in ABAQUS®. The interaction of an initial crack and a partially weakened interface is studied by a series of numerical experiments with different remote loading modes. Cohesive zone based models (CZMs) in ABAQUS® are used: cohesive elements are used for the simulation of interfacial fracture, while the (extended finite element method) XFEM is used for the simulation of the crack propagating within the bulk adhesive. Some important factors that could influence the crack path selection in adhesively bonded joints are revealed in the study.

## 6.2 Background on crack path selection

In modern material science, fracture mechanics is an important tool for studying and improving the mechanical performance of engineering materials, structures, and complements can. The history of fracture mechanics has been filled with challenges, many developments can be found in textbooks[1] and will not be reviewed in detail. Generally, there are at least two broad approaches to fracture mechanics. One is based on linear elastic fracture mechanics (LEFM). This approach regards the crack tip as infinitely sharp, therefore the singularity of the stress field is found at the crack tip but a finite energy release rate can often be calculated. Therefore, crack stability and equilibrium can be written by pre-factors such as the stress intensity factor, or the strain energy release rate. The other approach involves the use of a traction-separation law at the crack tip, a method that avoids the singularity at the crack tip. As a result, finite stresses remain, and the sharp crack tip is replaced by a cohesive zone. In the linear-elastic case for example, when the size of the cohesive zone is very small, these two approaches give

asymptotically identical results[2]. However, when the size of the plastic zone is large or considered to be important, the cohesive zone model (CZM) is very useful. The CZM approach has been widely applied to many engineering materials, including concrete, metals, ceramics, polymers, and soft gels. Details on the CZM will be discussed in the next section.

Fracture in monolithic materials is categorized in three modes: mode I (in-plane opening), mode II (in-plane shearing or sliding), and mode III (out-of-plane shearing). These pure modes, as well as their combined contributions for the mixed mode loading, can drive cracks to propagate, though often at different fracture energy values depending on the mode mixity[3]. Usually, the two in-plane modes, mode I and mode II, are of the greatest interest since they represent many practical loading scenarios, lend themselves to simple 2-D (plane stress or plane strain) simulation, and are often easier to experimentally measure. Besides, mode I is considered to be important because the mode I fracture resistance is often smaller than for other modes, thereby providing conservative results (though exceptions have been noted[4]). To characterize combinations of in-plane modes in fracture mechanics, the mode mixity angle is defined as

$$\psi = \arctan \sqrt{\frac{G_{II}}{G_I}} \quad (6.1)$$

where  $G_I$  and  $G_{II}$  are mode I and mode II components of the strain energy release rates (SERR), respectively.

The mode mixity angle plays an important part in the crack path selection of propagating cracks. Fundamentally, three criteria have been proposed to determine the direction of crack propagation. The first criteria, proposed by Erdogan & Sih[5], is that a crack will propagate in the direction that is perpendicular to the maximum opening stress. Palaniswamy & Knauss[6] suggested that propagation would occur in the direction that maximizes the strain energy release rate. The third criteria, advocated by Goldstein & Salganik[7] and Cotterell & Rice[8], is that a crack will grow in a direction such that mode I fracture is maintained at the crack tip, i.e. such that the local  $K_{II} = 0$ . Though seemingly very different criteria, they all yield similar results. No experimentally distinguishable differences have been observed [9-11]. According to these criteria, a propagating crack can veer or kink into a different direction, depending on the mode mixity of the local stress state at the crack tip.

Applications of these concepts in multi-layered material systems become more complex. It is worth noting that the global loading mode would be different from the local mode adjacent to the crack tip due to the geometric configuration, mismatch of material properties, and the existence of interfaces. For example, a mode II component is usually induced in what appears globally to be pure mode I conditions, since the material properties are asymmetric with respect to the interface. A mismatch of Young's modulus, Poisson's ratio, or the resulting Dundur's parameters changes the mode mixity angle on the interface when the material system is subjected to external loads[11].

Besides these concepts and criteria in fracture mechanics, numerical methods are also important to the simulation of the crack path selection in bonded joints. More backgrounds about the mathematical model and the numerical simulation is shown in the next section.

### **6.3 Background on the CZM**

The finite element method (FEM) is one of the powerful tools to simulate material behavior numerically. Several methods to evaluate fracture mechanics parameters have been integrated in the FEM under a continuum mechanics framework. Among them, linear elastic fracture mechanics has been widely applied and proven to be useful for crack simulation, but the nonlinear zone ahead of the crack tip is ignored. These methods work well for brittle materials but need to be augmented when dealing with materials where the size of the plastic/nonlinear zone is not negligible in comparison with other dimensions. There has been a lot of work on fracture of materials with plasticity since 1948, when Griffith's model was advanced by Irwin[12], Dugdale[13], Barenblatt[14], and Wells[15] by correcting for yielding at the crack tip. The Irwin plastic zone correction was a relatively simple extension of LEFM, while Dugdale and Barenblatt each developed more elaborate models based on a narrow strip of yielded material at the crack tip. Wells proposed the displacement of the crack faces as an alternative fracture criterion when significant plasticity precedes failure. His observations led to the development of the parameter now known as the crack tip opening displacement (CTOD). Williams[16] also derived a crack tip solution using a different method, but essentially identical to Irwin's. In 1968, Rice[17] developed another parameter, the  $J$  integral, which Hutchinson[18], Rice and Rosengren[19] related it to crack tip stress fields in nonlinear materials.

These developments have all proven successful in engineering designs, but interest remains in the search for methods that could be easily applied in simulations with finite element methods. Since fracture processes of polymers is usually quite complicated, with the movement and breakage of molecular chains, initiation of microcracks, and plastic deformation, as well as other nonlinear behaviors, the cohesive zone model (CZM) is useful for providing an alternative method that smears the details of these complicated mechanisms by replacing them with a prescribed "traction-separation law" that effectively models the response. The CZM is a general model which can deal with the nonlinear zone ahead of the crack tip—due to plasticity or microcracking—present in many materials.[20] The basis for CZM can be traced back to the work of Dugdale (1960)[13] and Barenblatt (1962)[14]. Usually, a bilinear traction-separation law is taken as a material property that describes the constitutive behavior. Calculations of crack initiation and crack growth are possible for both ductile and brittle materials. The implementation of these cohesive zone models is rather straightforward in commercial FEM software such as ABAQUS®.

One implementation of CZM in ABAQUS is the cohesive element [21-33]. The cohesive element is able to simulate cracks growing along the boundaries of elements, i.e. a pre-defined crack path. This is a drawback for the simulation of cracks in bulk

materials, where the crack path may not be known a priori, but is quite useful for fracture along bonded interfaces. One layer of cohesive elements along the interface of two bulk materials is capable of simulating a debonding or delamination process. This method assumes a linear elastic traction-separation law prior to damage, and assumes that failure of the elements is characterized by progressive degradation of the material stiffness, which is driven by a damage process. This damage parameter is referred to as SDEG (scalar stiffness degradation at integration points) in ABAQUS and varies from zero when there is no damage to unity when the element totally fails. Figure 6.1 shows a typical traction-separation response. Subscripts n, s, and t, indicate normal, in-plane shear, and out-of-plane shear directions, respectively. The symbols  $t^o$  and  $\delta^o$  are the traction, and separation, respectively, when damage starts.  $\delta^f$  is the final separation when the crack totally fails.

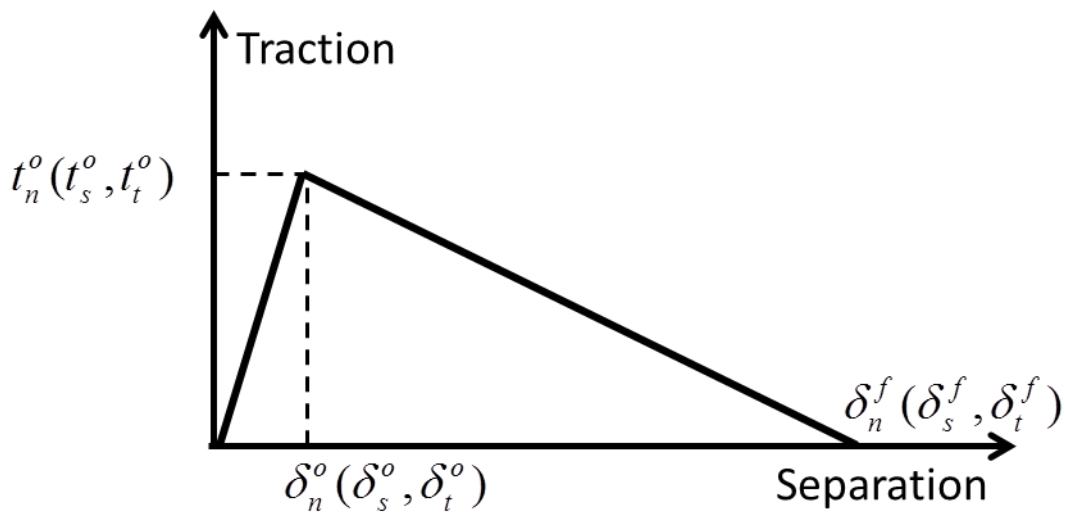


Figure 6.1. Typical traction-separation law.

The initial response of the cohesive element is assumed to be linear and several researchers have studied the effect of the initial stiffness for cohesive elements. They recommended that the penalty stiffness should be very large to guarantee small strain of the interfaces, but not too large to cause problems of convergence[34]. Once a damage initiation criterion is met, material damage evolves according to the damage evolution law defined a priori.

Based on the CZM framework, there is another method developed for fracture in bulk materials/elements known as the extended finite element method (XFEM)[25, 35], which is an extension of the conventional finite element method based on the concept of partition of unity [35, 36]. It allows for the presence of discontinuities in an element by enriching degrees of freedom with special displacement functions, but does not require the mesh to match the geometry of the discontinuities. In brief, XFEM is a relatively new application that enables crack propagation within the elements and determination of crack path automatically by some criterion. Therefore, the XFEM can be used to simulate crack

initiation and propagation along an arbitrary, solution-dependent path in bulk materials, since the crack propagation is not tied to the element boundaries in a mesh. In this case the near-tip asymptotic singularity is not needed, and only the displacement jump across a cracked element is considered. In ABAQUS®, the XFEM does not need remeshing after each step of crack propagation. But some phantom nodes, which are superposed on the original real nodes, are introduced to represent the discontinuity of the cracked elements, as illustrated in Figure 6.2. When the element is intact, each phantom node is completely constrained to its corresponding real node. When one element is broken by a crack, the cracked element splits into two parts. Each part is formed by a combination of some real and phantom nodes depending on the orientation of the crack. Each phantom node and its corresponding real node are no longer tied together and can move apart. These capabilities greatly facilitate the simulation of crack path selection. By default in ABAQUS, the crack propagates normal to the direction of the maximum tangential stress. This process can be repeated several times within one element by small increments of crack, so as to provide a relatively continuous crack path.

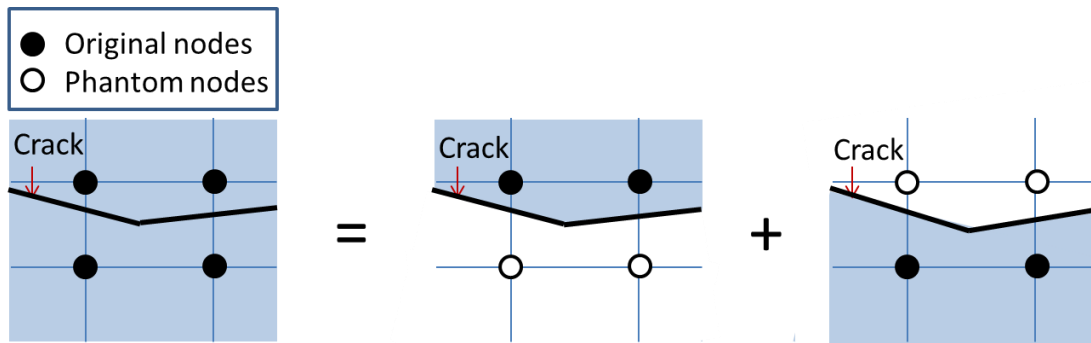


Figure 6.2. Phantom nodes created in the ABAQUS when simulating crack propagation using XFEM.

In the XFEM with traction-separation laws, the first stage is elastic until the stress approaches to the maximum traction. The slope of this line is related to the Young's modulus of the bulk material, rather than being a fictitious stiffness as for the cohesive element method. Since strains remain elastic in this stage, no damage will be initiated. The second stage involves the softening law, which defines how the traction drops to zero as the displacement increases to the critical displacement (or the SERR approaches to the critical value). Therefore, the area beneath the lines in Figure 6.1 is the critical strain energy release rate (SERR).

Based on these fundamental principles of fracture mechanics, crack path selection in adhesively bonded joints is investigated herein by numerical simulations with CZM in ABAQUS®. The interaction of a growing crack within an adhesive layer with the surrounding interfaces is considered. Since both strong and weakened interfaces are simulated in the model, one of the most interesting cases will be how the main crack in an adhesive layer propagates when it is passing near a partially weakened interface. The weakened area is used to simulate an interface that is neither very strong nor very weak; such reduced adhesion might be typical of a contaminated bonding surface in real bonding situations, or could be intentionally introduced in order to control adhesion.

When the main crack is approaching a weakened interface, the changing traction exerted by the damaged interface will influence the stress field adjacent to the tip of the main crack. Therefore, the behavior of the weak interface results in the selection of different crack paths in the adhesive layer than predicted when no weakening is present. The geometry, material properties, boundary conditions, and the other details on the modeling process are shown in the next section.

## 6.4 Modeling

Without loss of generality, a model of an adhesively bonded joint was built to study the crack path selection in multiple-layered material systems. The material properties of aluminum alloy were applied to the adherends, while those of a typical epoxy resin were applied to the adhesive layer. Additionally, several different parameters were also assumed for the interfaces to study the resulting influence on crack path selection. In summary, both the cohesive element method and XFEM are based on the CZM framework: the cohesive element is used for interfacial fracture, while the XFEM is used for the cracks propagating within the bulk adhesive. Therefore, by changing parameters of the geometry and the material properties of the weakened interface, crack path selection is investigated by numerical experiments. Generally, there are two categories in this study: cracks approaching a long weakened area (semi-infinite or extending to the end of the specimen), and cracks approaching a short weakened area (of finite length ranging from  $\frac{1}{4}$  to 1 bondline thickness in length). Therefore, the effect of the length of the weakened interface is also included in this study.

A sketch of the model in ABAQUS is shown in Figure 6.3, which was built referring to the DCB specimen in ASTM D3433-99(2012) with nominal dimensions of  $150 \times 25.4 \times 12.7$  mm for each adherend. The dimension of the adhesive layer is  $150 \times 25.4 \times 0.25$  mm, i.e. the thickness of adhesive is 0.25 mm. The initial crack is located in the middle of the adhesive layer, from 0 mm to 58 mm, and the distance between the initial crack tip and the start of the weakened interface is 2 mm further along the bondline direction (8 bondline thicknesses away). This configuration is such that initial crack growth within the model is unperturbed by proximity of the weak zone, so that the entire history of crack path selection can be recorded and studied. Indeed, the following simulations show that this 2 mm gap (8 times the adhesive layer thickness) is sufficiently large to avoid effects of the weakened zone to the initial crack. For the model with a long or semi-infinite weakened area, the weakened area extends from 60 mm to the end of the DCB specimen. For the short weakened interfacial areas, the lengths are 0.25 mm, 0.125 mm, and 0.0625 mm, respectively. To facilitate the general analysis, these lengths were normalized by the thickness of the adhesive layer, i.e. 0.25 mm, in subsequent figures. Residual stresses were assumed to be zero throughout this chapter. The boundary conditions were applied to the nodes near the loading points by assigning symmetric displacements (up and down) and fix the horizontal positions, as shown in Figure 6.3.

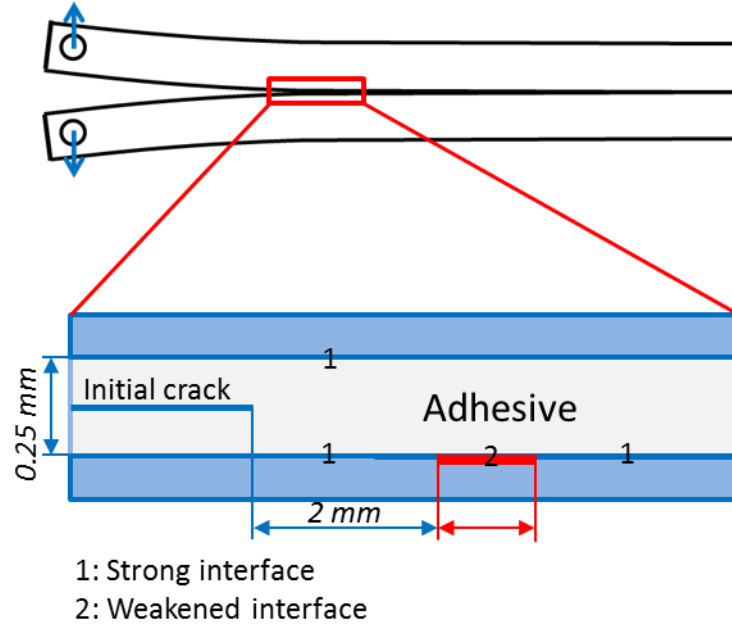


Figure 6.3. Location of the weak interface in the DCB specimen model with initial crack.

Within the CZM framework, the XFEM is applied to simulate crack propagation in the adhesive layer, and cohesive elements were used to simulate the debonding process of interface. Representative material properties were chosen as follows: Young's modulus  $E = 70GPa$ , Poisson's ratio  $\nu = 0.33$  for aluminum; and  $E = 3GPa$ ,  $\nu = 0.35$  for the adhesive. No inelastic behavior is included. Fracture properties for the CZM were obtained from previous experimental results of this material system[37]. The averaged values of the fracture energies for cohesive failures within the adhesive layer were used:  $500 J/m^2$  for pure mode I,  $2500J/m^2$  for pure mode II; the maximum traction is 11.6 MPa, which was optimized from several load-displacement curves from DCB tests. Though the value of the maximum traction is lower than the yield stress of the epoxy, it is still reasonable and has provided good agreement with experimental results[37]. Blackman, *et al*, also showed that there's no simple relationship between the maximum traction and the yield stress[38].

The criterion for crack initiation is the maximum principal stress,  $\sigma_{\max}^o$ , in equation(6.2). The symbol " $\langle \rangle$ " represents the Macaulay bracket, which results in zero if  $\sigma_{\max}$  is negative and keeps its original value if is positive. They are used to signify that a pure compressive deformation or stress state does not initiate damage in this model. The criterion for failure is the energy-based criterion in equation(6.3).  $G_I$  and  $G_{II}$  are the strain energy release rate for mode I and mode II, respectively.  $G_{Ic}$  and  $G_{IIc}$  are the fracture energy for mode I and II, respectively.

$$\left\{ \frac{\langle \sigma_{\max} \rangle}{\sigma_{\max}^o} \right\} = 1 \quad (6.2)$$

$$\frac{G_I}{G_{Ic}} + \frac{G_{II}}{G_{IIc}} = 1 \quad (6.3)$$

However, the CZM parameters for the strong and partially weakened interfaces are difficult to estimate by experimental results when the crack does not propagate along them. Therefore, the CZM parameters for these interfaces are assumed, guided by the CZM parameters of the adhesive in reference [37]. The fracture energy of the strong interface is assumed to be higher than that of the adhesive, while the fracture energy of the weakened interfaces is assumed to be lower than that of the adhesive. Similar criteria were applied when choosing maximum tractions for the strong and weakened interfaces. All these CZM parameters were found within the range that discussed in other articles [34, 38]. The criterion for the crack initiation is the maximum nominal stress criterion in

$$\max \left\{ \frac{\langle t_n \rangle}{t_n^o}, \frac{t_s}{t_s^o} \right\} = 1 \quad (6.4)$$

where  $t_n$ , and  $t_s$  are the normal traction, and in plane shear traction, respectively;  $t_n^o$ , and  $t_s^o$  represent the peak values of them, respectively, when the deformation is either purely normal to the interface or purely in the first or the second shear direction, respectively. The criterion for the failure of all the interfaces is also the mode dependent equation (6.3).

Empirically, the CZM parameters for the strong interfaces should be equal to or exceed those for the adhesive layer. The maximum traction is taken as 20 MPa, which is larger than that for adhesive so as to make sure that there is no interfacial damage when the crack in the adhesive propagates. The fracture energy is assumed to be 500 J/m<sup>2</sup>, which is the same value for the adhesive. Parameters for the long weakened areas are listed in Table 6.1. Parameters for short weakened areas are listed in Table 6.2. These parameters were chosen to cover most possible cases for weakened surfaces. One of the combinations of the CZM parameters for the adhesive layer, strong interface, and weakened interfaces is shown schematically in Figure 6.4. The three small triangles with the same heights, or  $T_{\max}$ , represent the behavior of the three presumed weakened interfaces. They are all lower and smaller than those for the adhesive or the strong interface. This schematic may be useful in understanding the interaction and the competition process among them when a crack propagates.

Table 6.1. CZM parameters for the long weakened areas.

Maximum traction (MPa)	Fracture energy (J/m <sup>2</sup> )
10	250
5	50
2.5	5

Table 6.2. CZM parameters for the short weakened areas.

Maximum traction (MPa)	Fracture energy (J/m <sup>2</sup> )	Length of weakened interface (mm)
5	250	1/16
2.5	50	1/8
0.25	5	1/4

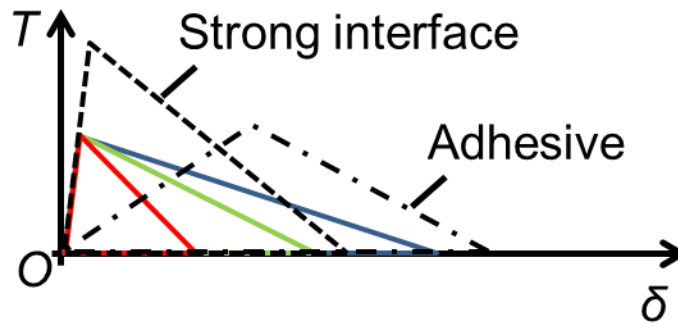


Figure 6.4. Schematic of the CZM traction-separation laws for the adhesive layer, strong interface, and several weakened interfaces.

A scalar damage variable,  $D$ , which evolves monotonically from 0 to 1 upon further loading after the initiation of damage is used to represent the averaged overall damage of cracked elements. This variable is the same as the SDEG (scalar stiffness degradation variable) for cohesive elements in ABAQUS. A mathematical interpretation of this is shown in equation (6.7) after the following introductions. The normal and shear stress components are affected by the damage according to

$$\begin{aligned}
t_n &= \begin{cases} (1-D)T_n, & T_n \geq 0 \\ T_n, & T_n < 0 \end{cases} \\
t_s &= (1-D)T_s, \\
t_t &= (1-D)T_t,
\end{aligned} \tag{6.5}$$

where  $T_n$ ,  $T_s$ , and  $T_t$  are the normal and shear stress components predicted by the elastic traction-separation behavior for the current separations without damage. To describe the evolution of damage under a combination of normal and shear separations across an interface, an effective separation,  $\delta_m$ , is defined as

$$\delta_m = \sqrt{\langle \delta_n \rangle^2 + \delta_s^2 + \delta_t^2} \tag{6.6}$$

where  $\delta_n$ ,  $\delta_s$ , and  $\delta_t$  are the normal and shear separation components. For linear softening, ABAQUS uses the evolution of the damage variable,  $D$ , that reduces (in the case of damage evolution under a constant mode mixity angle, temperature, and field variables) to the expression proposed by Camanho and Davila[39], namely:

$$D = \frac{\delta_m^f (\delta_m^{\max} - \delta_m^o)}{\delta_m^{\max} (\delta_m^f - \delta_m^o)} \tag{6.7}$$

In the preceding expression,  $\delta_m^{\max}$  refers to the maximum value of the effective displacement attained during the loading history. The assumption of constant mode mixity at a material point between initiation of damage and final failure is customary for problems involving monotonic damage (or monotonic fracture).

When studying the debond process of the interfaces, the compliance of the interface or cohesive element layer is not considered to influence the bulk materials. Visual thickness of the cohesive element in the model is not required to be accurately equal to the one in reality. Indeed, the real thickness of an interface is difficult to be measured. Therefore, in ABAQUS, visual thickness will not be taken into account in the simulation, and can be modified to be zero (by modifying the coordinates of the nodes of the cohesive elements). Again, it is worth noting that this is merely a post processing artifact, showing up only in visual outputs.

The interfacial elastic stiffness for a traction-separation based on the cohesive element model can be better understood by studying the equation that represents the displacement of a truss of length  $L$ , elastic stiffness  $E$ , and original area  $A$ , due to an axial load  $P$ :

$$\delta = \frac{PL}{EA} = \frac{S}{K} \tag{6.8}$$

where,  $S = P/A$  is the nominal stress and  $K = E/L$  is the stiffness that relates the nominal stress to the displacement. The above equations suggest that the actual length  $L$  may be replaced with 1.0 (to ensure that the strain is the same as the displacement, regardless of the units) if the stiffness is appropriately reinterpreted. In particular, the stiffness is  $K = E/L$ , where the true length of the truss is used in these equations. Usually, the stiffness can be a very high value only if it will not be too high to cause convergence problem.

Although XFEM has alleviated the shortcomings associated with refining the mesh in the neighborhood of the crack front due to the added asymptotic fields, a sufficient number of elements around the crack front must be generated to obtain path-independent contours. The group of elements within a small radius from the crack front are enriched and become involved in the contour integral calculations. The default enrichment radius is three times the typical element characteristic length in the enriched area. However, in order to obtain the stress field precisely near the crack, the mesh should still be very fine in the adhesive layer. Effective connections between the relatively coarse mesh and the very fine mesh in the adhesive layer are required so as to obtain numerical results with high precisions. The mesh is shown in Figure 6.5 in three levels, since the scale from adherend to the adhesive layer is very large.

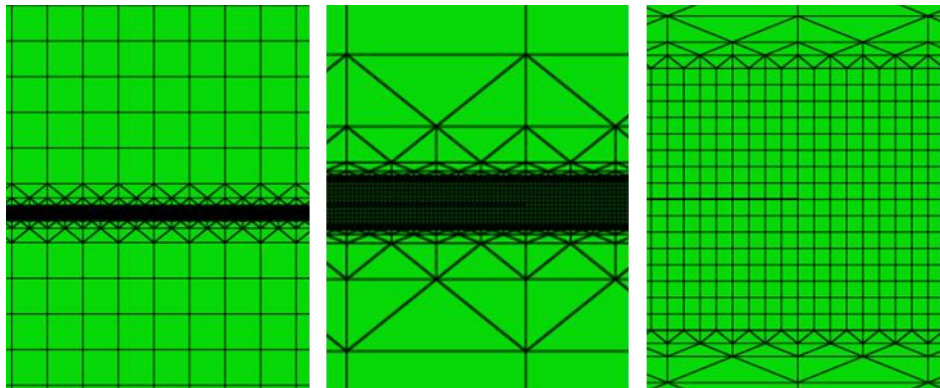
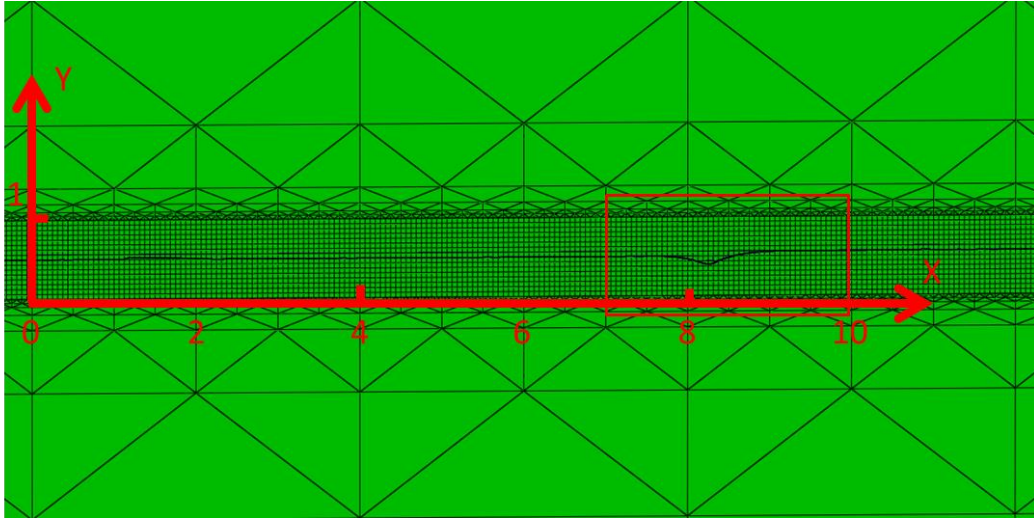


Figure 6.5. Mesh connectivity of the DCB model at three levels: Zooming in (in the pictures located from the left to the right).

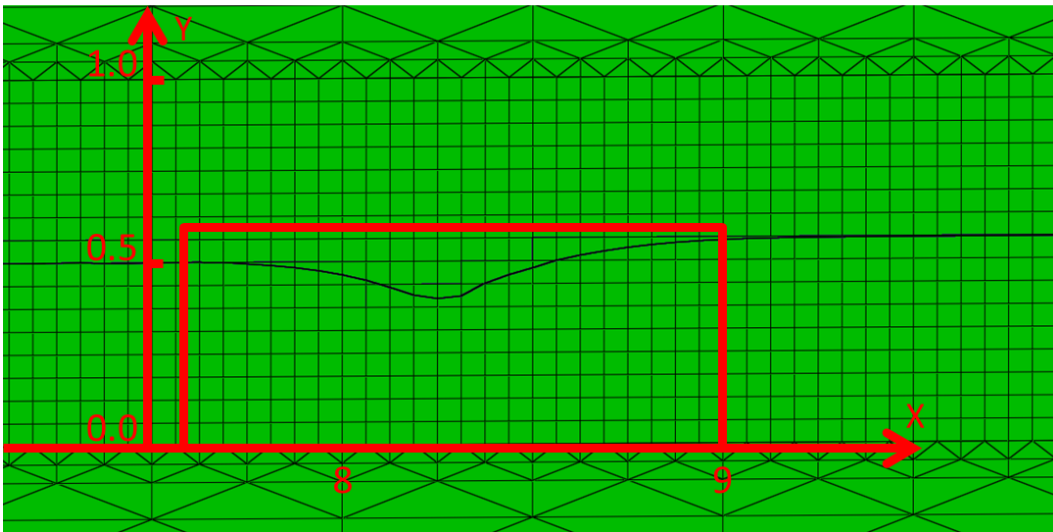
## 6.5 Results with mode I loadings

Since the crack path selection predictions are expected to be sensitive to the stresses and mesh size, it is reasonable to determine the mesh refinement required to accurately evaluate the stress field with relatively low costs in time and space in computer. Therefore, adhesive layer elements with different size and type are applied for one case. The case used to determine the mesh size effect involves a 0.125 mm long weakened interface on one side, which is located at 2 mm in front of the initial crack tip. The thickness of the adhesive layer is  $H = 0.25\text{mm}$ . The fracture energy for weak interface is  $50\text{ J/m}^2$ , and the maximum traction is 5 MPa. The crack path together with the meshes in

the undeformed shape is shown in Figure 6.6. The coordinate system normalized by  $H$  is also shown:  $X = x/H, Y = y/H$  (“ $x, y$ ” are the global coordinates in mm, “ $X, Y$ ” are the normalized coordinates), therefore, the crack initiates at  $X = 0$ , the weakened interface starts from  $X = 8$ . The red frame in Figure 6.6b is used for the following plot of crack paths for all the cases.



(a)



(b)

Figure 6.6. Example of a grown crack path with meshes and normalized coordinate system.

All of the material parameters and geometric dimensions are the same except for the size and type of elements in the adhesive layer. The result of the crack path is shown in Figure 6.7.<sup>2</sup>

In ABAQUS, CPE4 corresponds to plane strain 4-nodes element with full integration, and CPE4R means plane strain 4-nodes element with reduced integration. Essentially, more elements through the thickness of the adhesive layer should give more accurate results. However, the time and space required by the calculation will be increased enormously. Since the results from the model with 16 CPE4 elements through the thickness of the adhesive layer is very close to those with 32 and 64 elements, it is reasonable to choose 16 CPE4 elements through the thickness for the subsequent simulations. The key finding here is relative insensitivity to mesh sizes considered and the significant effect of full integration.

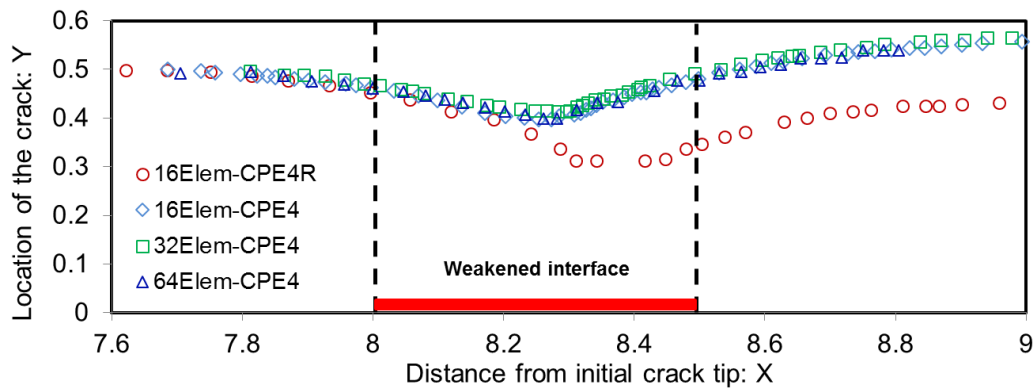
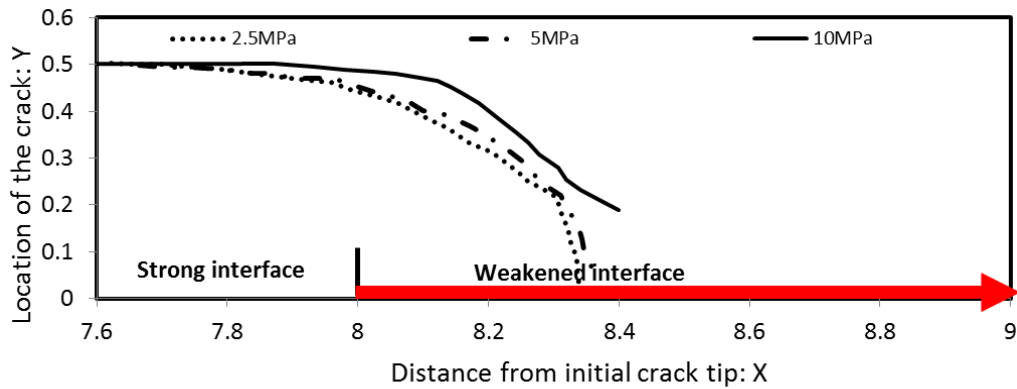


Figure 6.7. Comparison of crack path selection with same geometric and material parameter but different mesh size and element type.

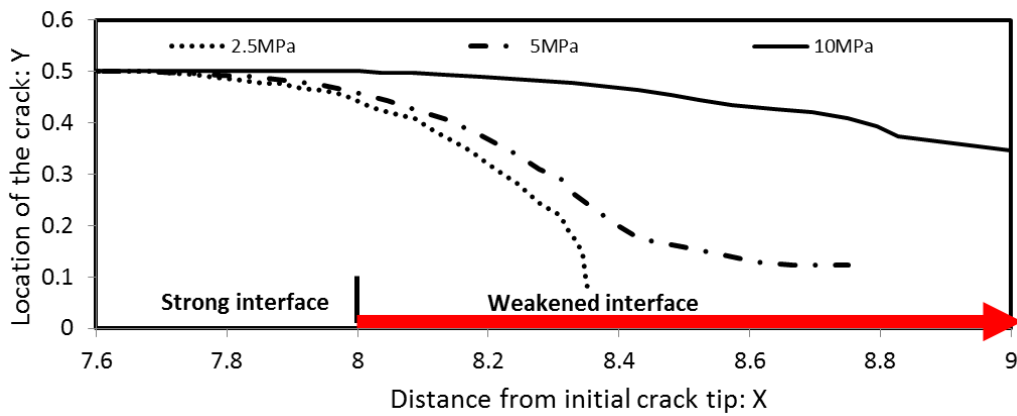
<sup>2</sup> It is worth noting that the crack plateaus higher than it enters on the left. This is considered to be related to the criterion of crack direction when it propagates, as well as the stability in the middle of the adhesive layer<sup>1</sup>. First, the flexible adhesive layer near the weakened interface exerts shear stresses that drive the crack to the weakened interface. Then when the crack is leaving the weakened interface, based on the criterion for the crack direction, the shear stresses in the opposite direction drive the crack back to the central line. However, when it arrives at the central line, the shear stress is still affecting the crack tip and the crack doesn't turn back to the horizontal direction. Thus, it moves on across the central line to the other side slightly. When the crack direction finally turns to horizontal, the deviation from the central line is so small that there is very little motivation for the crack to go back to the central line. Further simulation showed that, the crack keeps this slight deviation for at least 17.3 mm without significant change. Since this is not the main focus of this chapter, the figure is not shown. Similar to a ball rolling in a shallow groove, there is a relative wide region near the central line at the bottom for the ball to keep its direction stably. In summary, the crack would keep its direction stably even if there is small deviation from the central line.

### 6.5.1 Crack path selection with long weakened interface

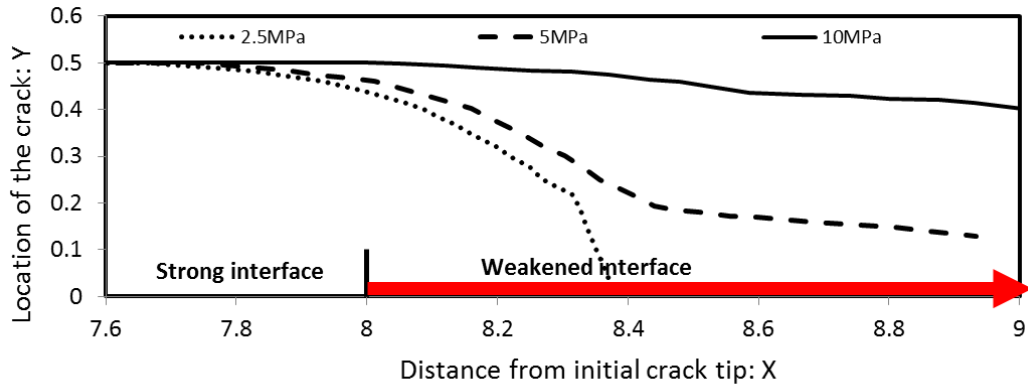
In this model, the weakened area, starting from 2 mm ( $x=8$  in the following figures) ahead of the initial crack tip, extends to the end of the specimen. The purpose of this study is to investigate if the veering angle would be significantly changed by different CZM parameters of the weakened interface. Figure 6.8 and 6.9 show the crack paths simulated by ABAQUS, but categorized in different ways.



(a)



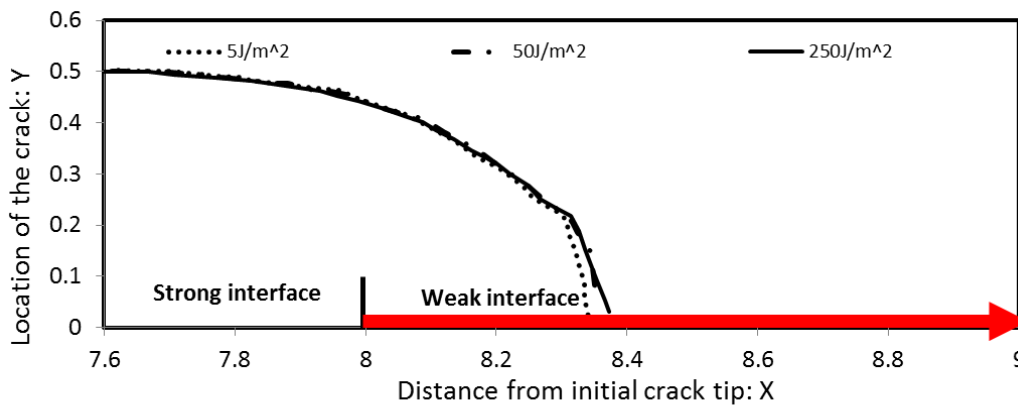
(b)



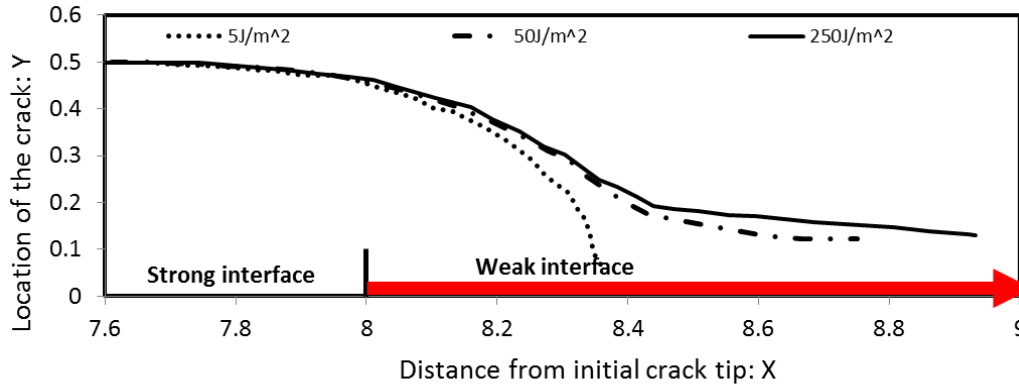
(c)

Figure 6.8. The crack path with long weakened interface and maximum traction: (a) 5 J/m<sup>2</sup>, (b) 50 J/m<sup>2</sup>, (c) 250 J/m<sup>2</sup>.

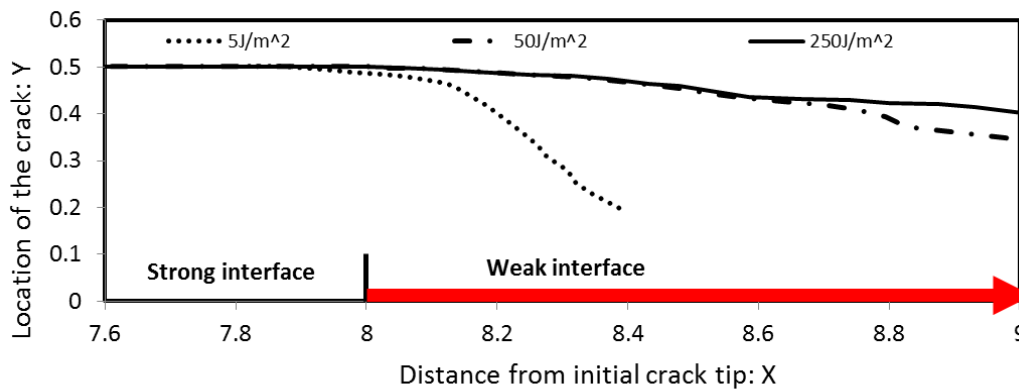
The crack paths in Figure 6.8 show that all these cracks veer towards the long weakened interfaces. When  $T_{\max}$  is small, the main cracks veer and approach the weakened interface quickly. When  $T_{\max}$  is larger, the main crack veers gently and the distance traveled before reaching the interface is longer. Evidently, a low  $T_{\max}$  means the failure of the weakened interface is usually easy. In some situations, many of these cohesive elements will totally fail even when the main crack is still of certain distance to the left of the beginning of the weak zone. Thus, the reduction (due to softening) or release (due to total failure) of the traction to the adhesive layer prior to the approaching of the main crack shears the surrounding adhesive and attracts the main crack to veer into the interface steeply. Therefore, the maximum traction  $T_{\max}$  plays a very important part in the crack path selection in DCB bonded joints with long weakened interfaces.



(a)



(b)

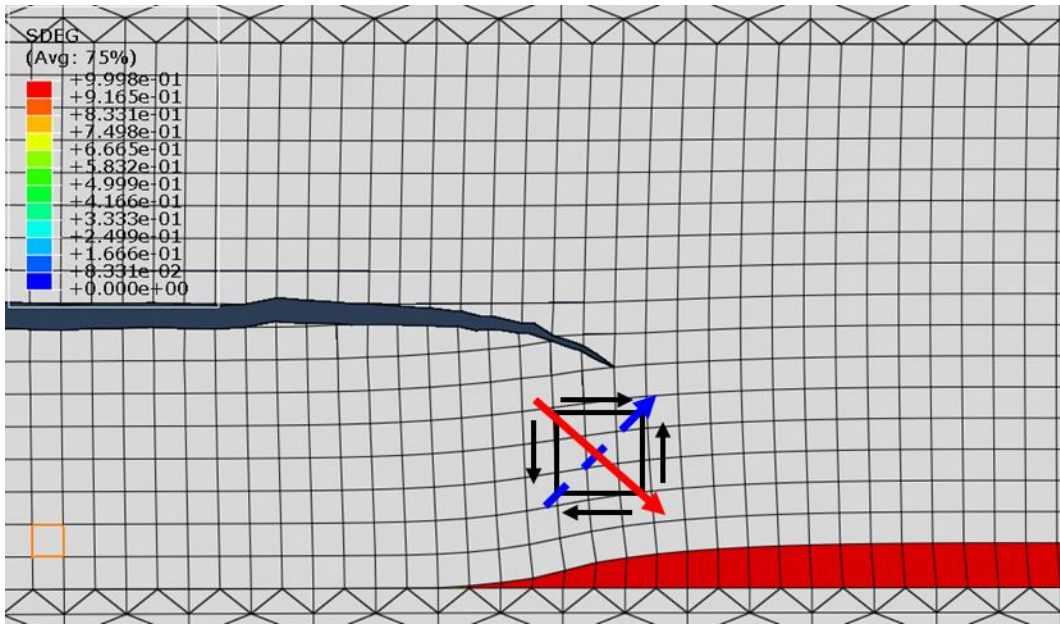


(c)

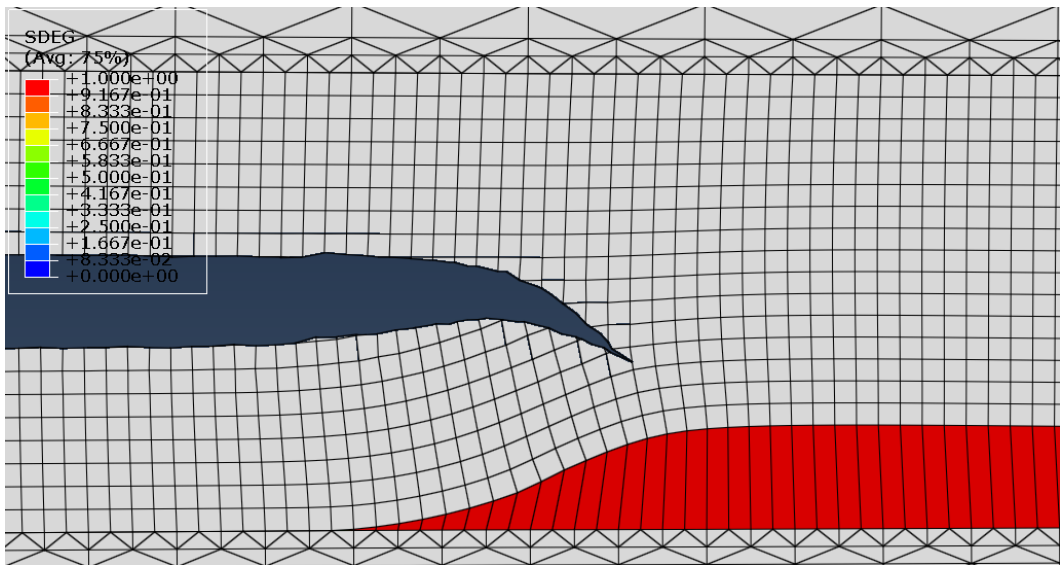
Figure 6.9. Crack path with long weakened interface and maximum traction: (a) 2.5 MPa, (b) 5 MPa, (c) 10 MPa.

Fracture energy is another factor that alters the path, as shown in Figure 6.9. When  $T_{\max}$  is very small, such as in Figure 6.9a, fracture energy values exert little influence until the last stage of the propagation when the growing cohesive crack is about to reach the weakened interface. When  $T_{\max}$  is larger, such as in Figure 6.9b and c, the difference exerted by the values of fracture energy is larger. This is because the fracture energy controls the maximum distance when the weakened interface approaches total failure. In summary, the chosen interfacial fracture energy values have little effect at the beginning of the veering propagation, but make some difference in the last stage of the propagation.<sup>3</sup>

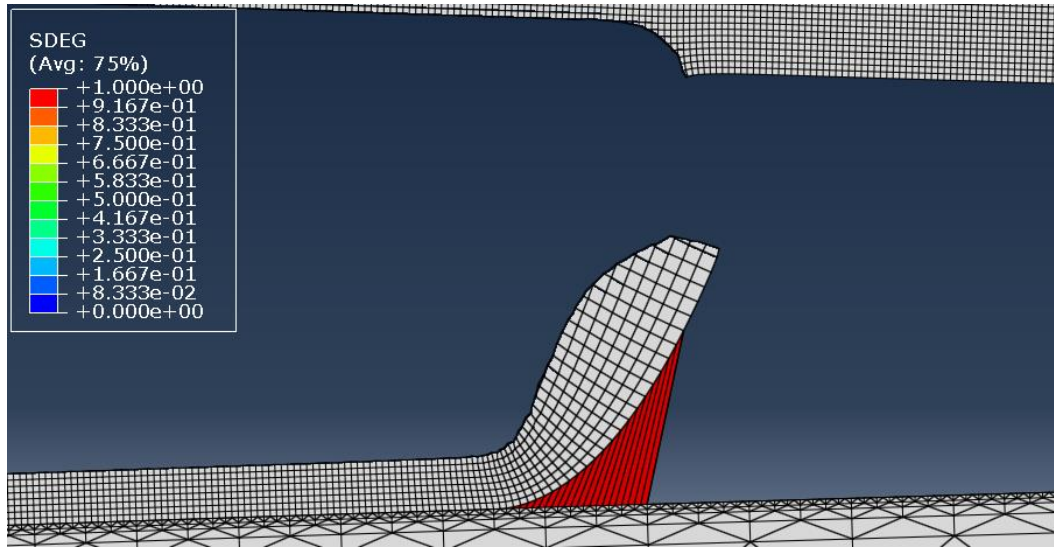
<sup>3</sup> The real focus of these work will be on whether growing cracks can sense weakened zones and veer toward them or not. The final stage where the last ligament falls is beyond the discussion of this chapter, but will be researched in the future.



(a)



(b)



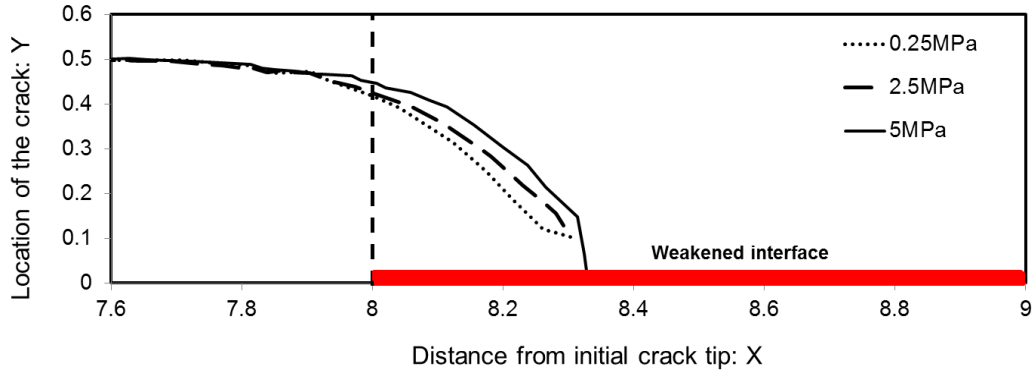
(c)

Figure 6.10. The main crack propagation and damage evolution of a long weakened interface: (a) the main crack senses and veers to the weakened interface, the interface is damaging, (b) large scale of damage is found when the main crack is closer, (c) the main crack veers into and connects with the interface, interfacial crack is developed.

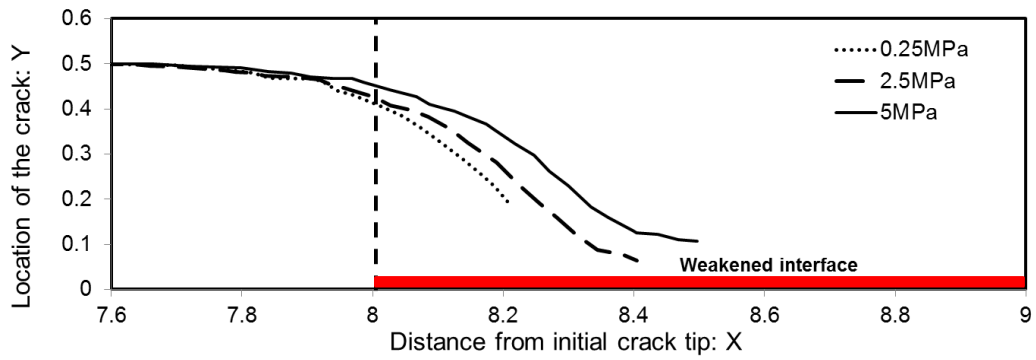
Figure 6.10 shows the process of crack propagation for one case (fracture energy:  $50\text{J/m}^2$ , maximum traction:  $5\text{MPa}$ ). For all the print screens with deformed shapes from ABAQUS, the deformations have been magnified by 20 times in ABAQUS so as to show the interaction of the main crack and the long weakened interface. Since the weakened interface debonds as the external load increases, the local shearing effectively “attracts” the main crack to turn quickly and almost perpendicular to the interface.

### 6.5.2 Crack path selection with short weakened interface

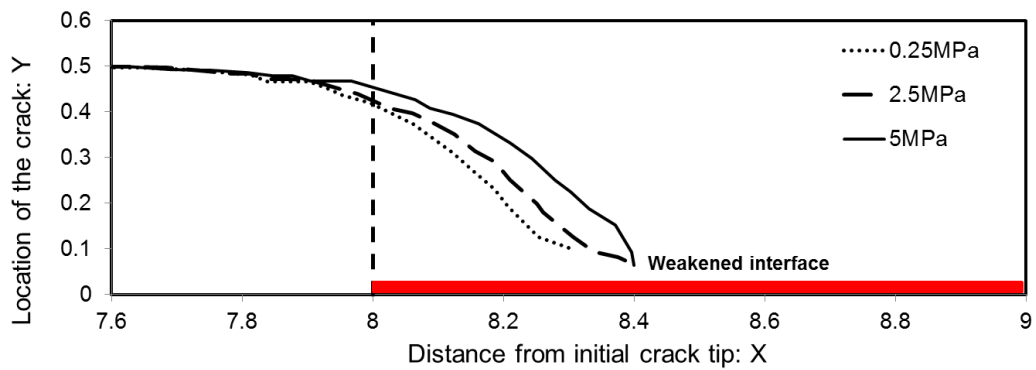
In the models with short weakened interfaces, the lengths of weakened areas considered include  $0.0625\text{ mm}$ ,  $0.125\text{ mm}$ , and  $0.25\text{ mm}$ . Since the previous model showed a significant influence of the weakened interface on the resulting crack path, the next question would be: how long does a weak interface of given properties need to be for the main crack to “detect” its existence.



(a)



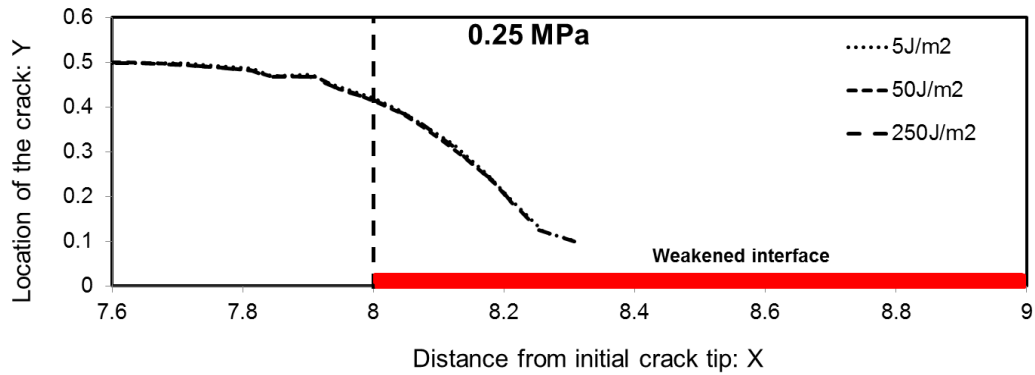
(b)



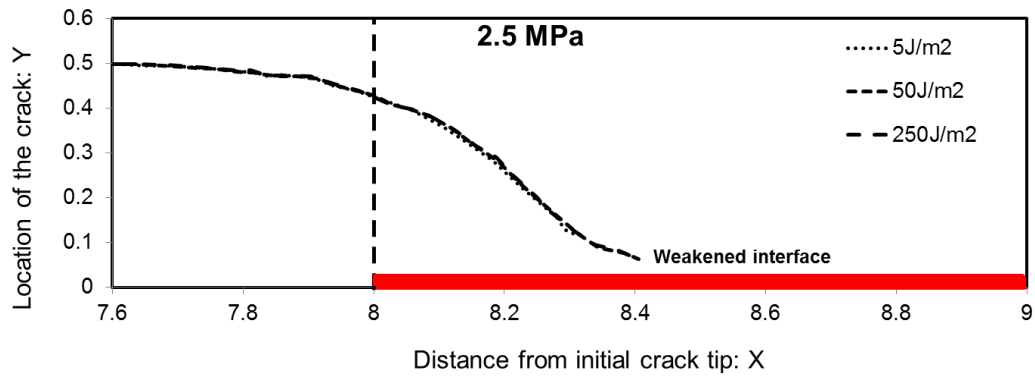
(c)

Figure 6.11. Crack paths with 0.25 mm weakened interface and fracture energy of: (a) 5 J/m<sup>2</sup>, (b) 50 J/m<sup>2</sup>, (c) 250 J/m<sup>2</sup>.

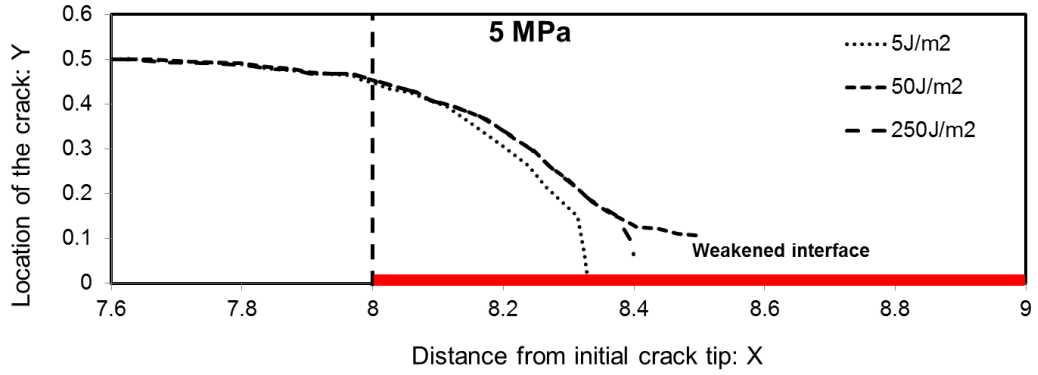
Figure 6.11 shows that the weakened interface of length equal to the adhesive layer thickness (0.25 mm) is long enough and thus all these crack paths are strongly attracted by the weakened interface. If these curves are rearranged by the same values of the maximum tractions, as seen in Figure 6.12, it is easy to find that the curves are quite similar, even though the fracture energy values differ significantly.



(a)

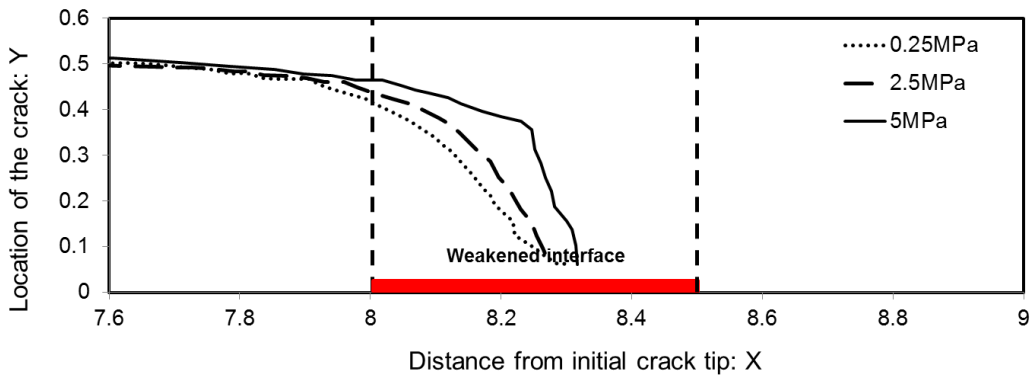


(b)

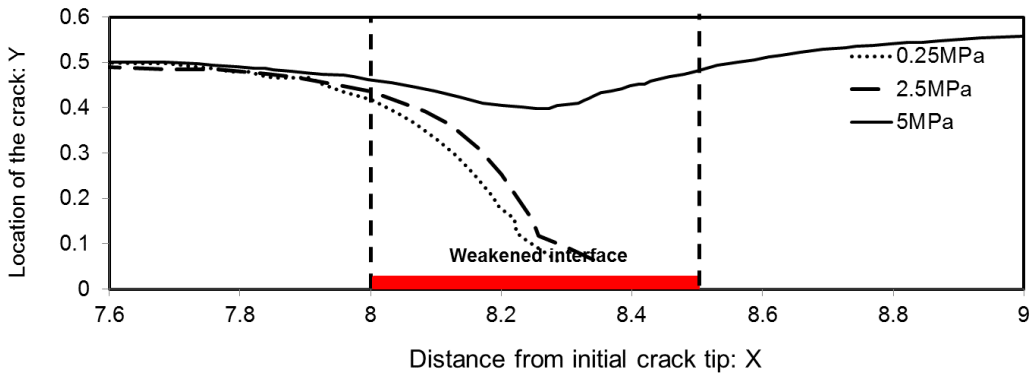


(c)

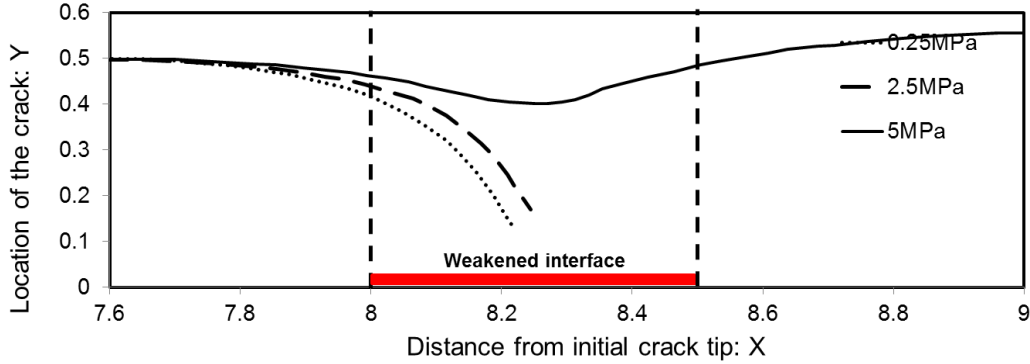
Figure 6.12. Crack paths with 0.25 mm weakened interface and the maximum traction of: (a) 0.25 MPa, (b) 2.5 MPa, (c) 5 MPa.



(a)



(b)

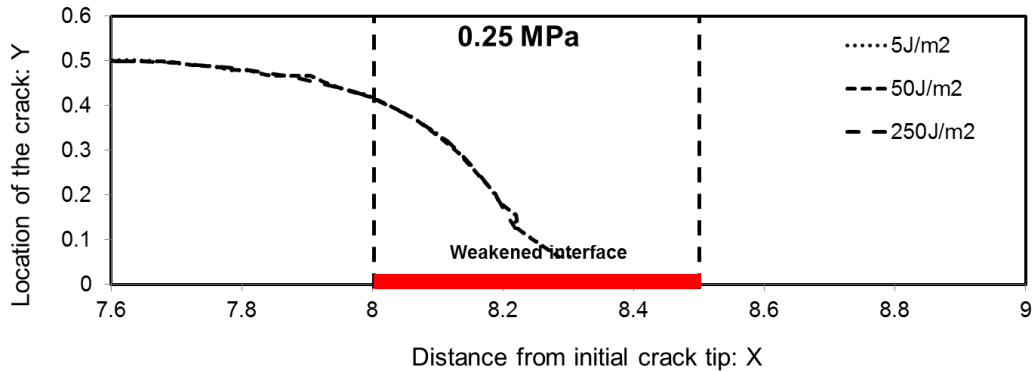


(c)

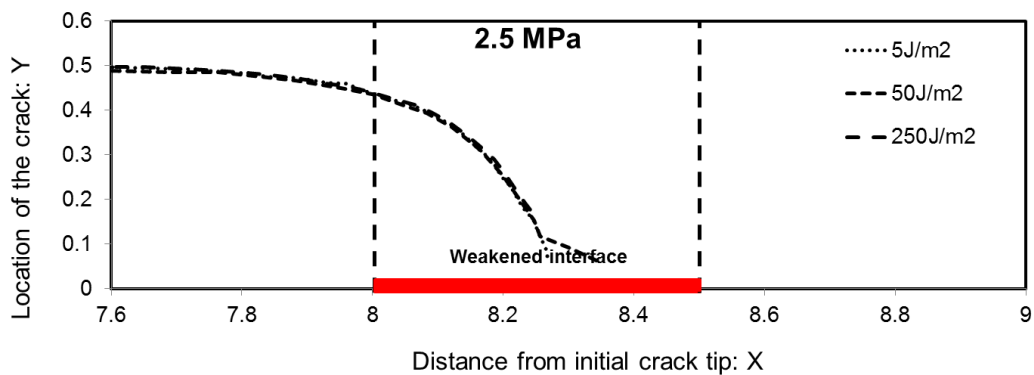
Figure 6.13. Crack paths with 0.125 mm weakened interface and fracture energy of: (a) 5 J/m<sup>2</sup>, (b) 50 J/m<sup>2</sup>, (c) 250 J/m<sup>2</sup>.

Figure 6.13 shows that, for the most part, a weakened interface length equal to the adhesive thickness is sufficiently long to cause the growing cohesive crack to veer into the weakened interface. However, Figures 6.13b and c suggest that when the maximum traction is 5 MPa, the crack path returns to the central line of the adhesive layer after initially veering toward the weakened interface. Figure 6.14 reorganizes these curves by the maximum tractions. Generally, the crack paths do not change significantly when the fracture energy increases. Though the crack path changed in Figure 6.14c when the fracture energy increases from 5 J/m<sup>2</sup> to 50 J/m<sup>2</sup>, but does not change anymore from 50 J/m<sup>2</sup> to 250 J/m<sup>2</sup>. In other words, the fracture energy of the weakened interface can barely influence the crack path when  $T_{\max}$  of the weakened interface is sufficiently small (e.g.  $T_{\max} \leq 2.5\text{MPa}$ , or 22% of that of the bulk adhesive in our simulations). Mostly, the fracture energy of the weakened interface changes the profile of the crack path slightly when it is about to reach the edge of the adhesive layer.

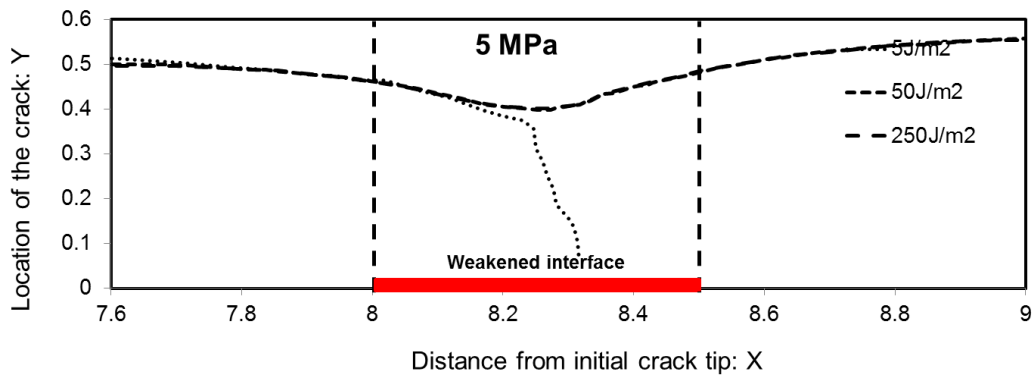
This indicated that most of the crack path selection process is less sensitive to reductions in the fracture energy, or the critical displacement of the weakened interface. Early stage damage of the weakened interface, which is dependent on  $T_{\max}$ , is more important in influencing crack path selection than further damage and displacement of the weakened interface. In other words, it is the increased compliance of weakened interfaces that locally shears the adhesive ahead of the growing crack and effectively directs the growing crack towards the weakened region.



(a)



(b)

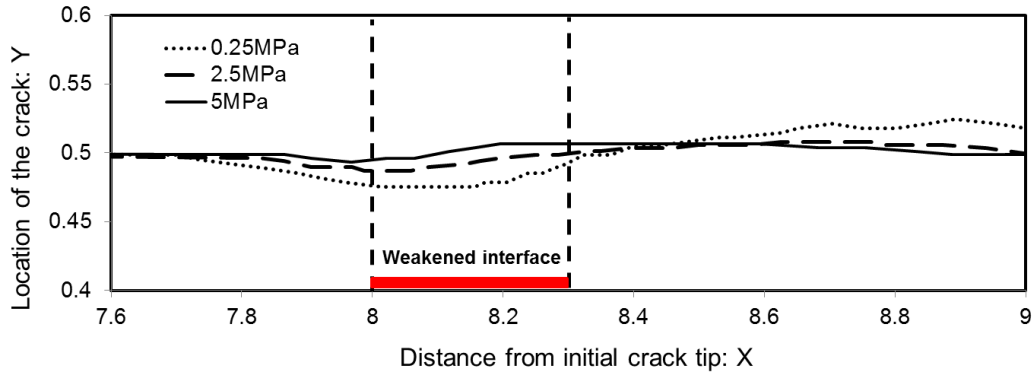


(c)

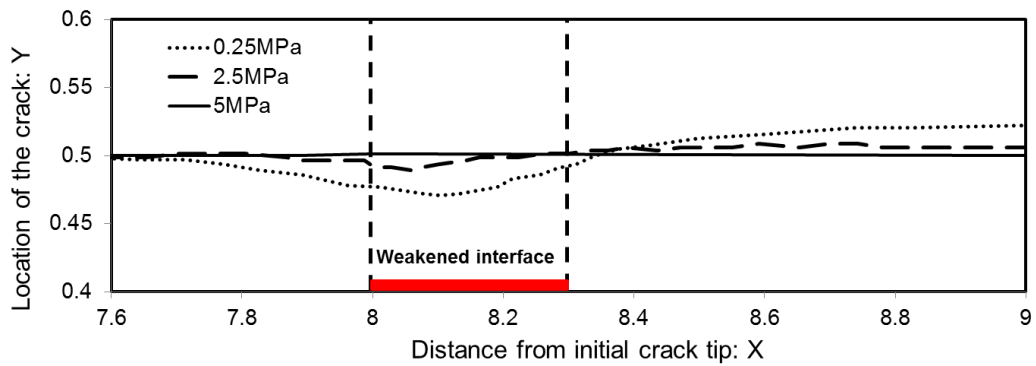
Figure 6.14. Crack paths with 0.125 mm weakened interface and the maximum traction of: (a) 0.25 MPa, (b) 2.5 MPa, (c) 5 MPa.

Figure 6.15 shows that, when the length of the weakened interface is  $\frac{1}{4}$  the adhesive thickness, to the influence on the main crack is very weak, resulting in only a very localized disturbance. Note that, in order to show the small crack path deviations clearly, the scale in the y-direction is different from the previous figures. The crack only veers slightly and then goes back to the central line and moves forward. When the main cracks

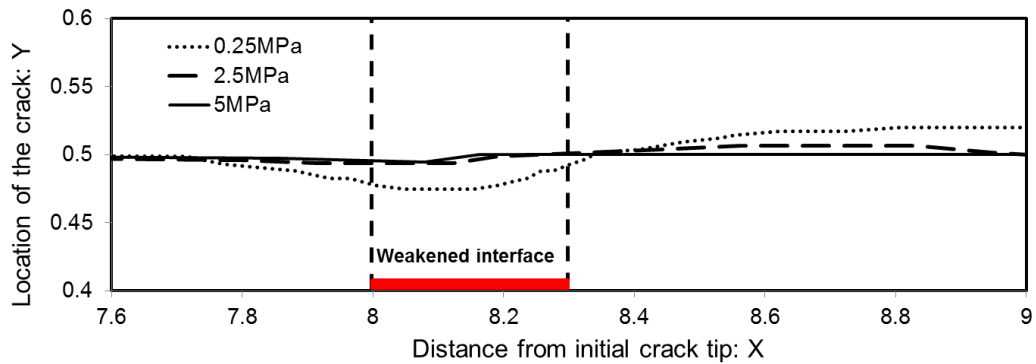
turn back to the central line of adhesive layer, the weakened interface is still exerting some shear stress though in the opposite direction. Therefore the main cracks go over the central line a little and then gradually come back. Figure 6.16 organizes these curves by different maximum tractions, showing the trends more clearly.



(a)

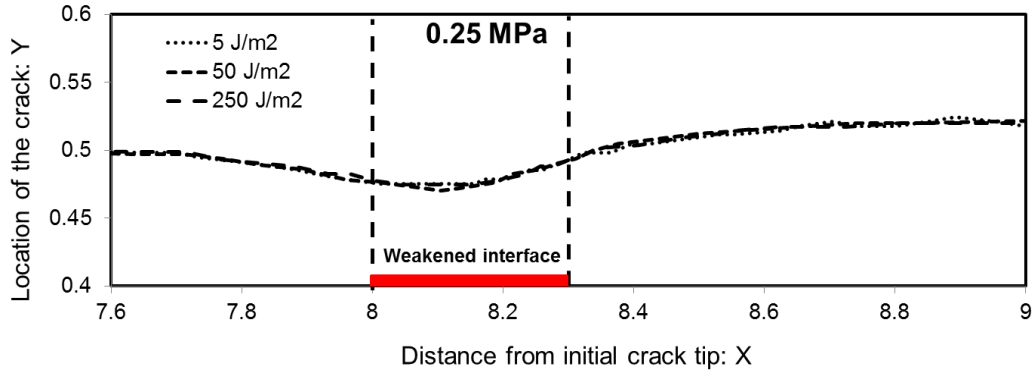


(b)

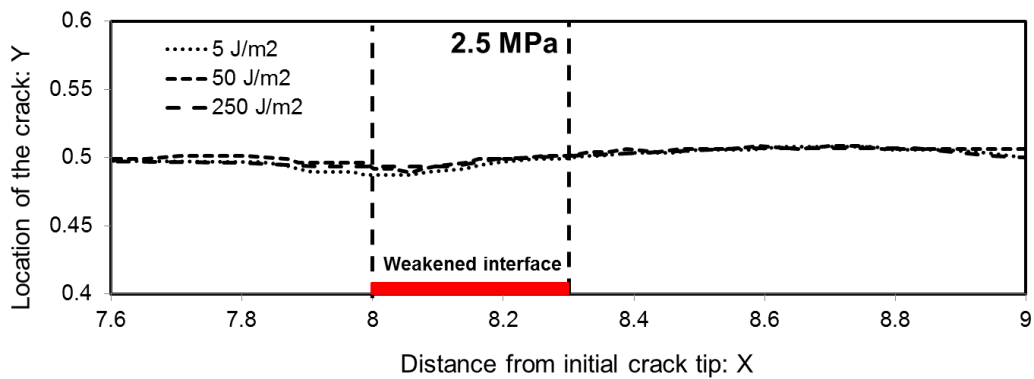


(c)

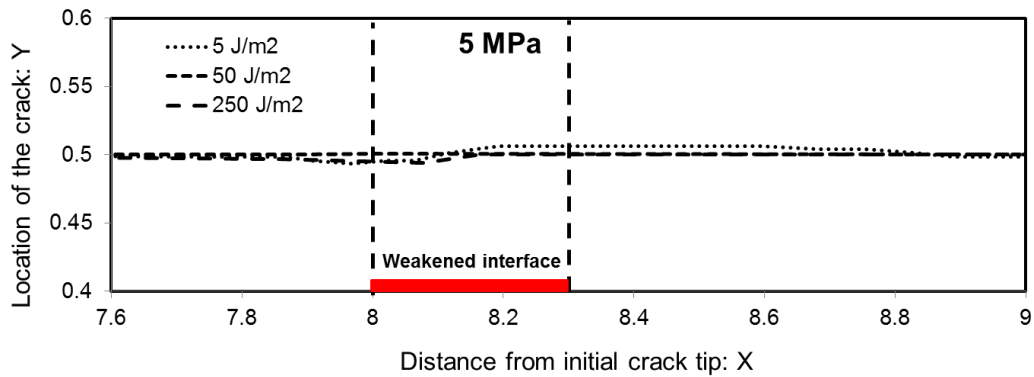
Figure 6.15. Crack paths with 0.0625 mm weakened interface and fracture energy of: (a) 5 J/m<sup>2</sup>, (b) 50 J/m<sup>2</sup>, (c) 250 J/m<sup>2</sup>.



(a)



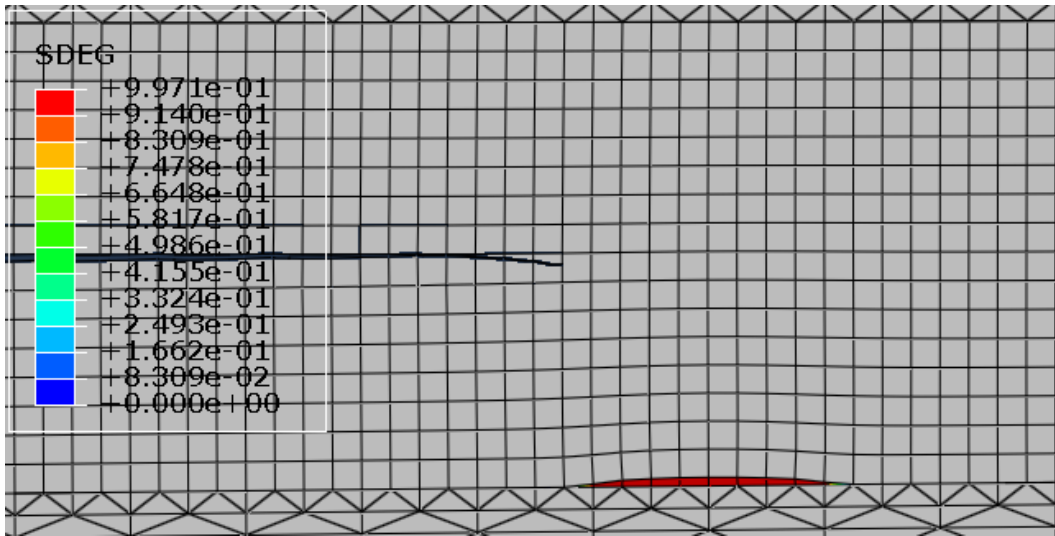
(b)



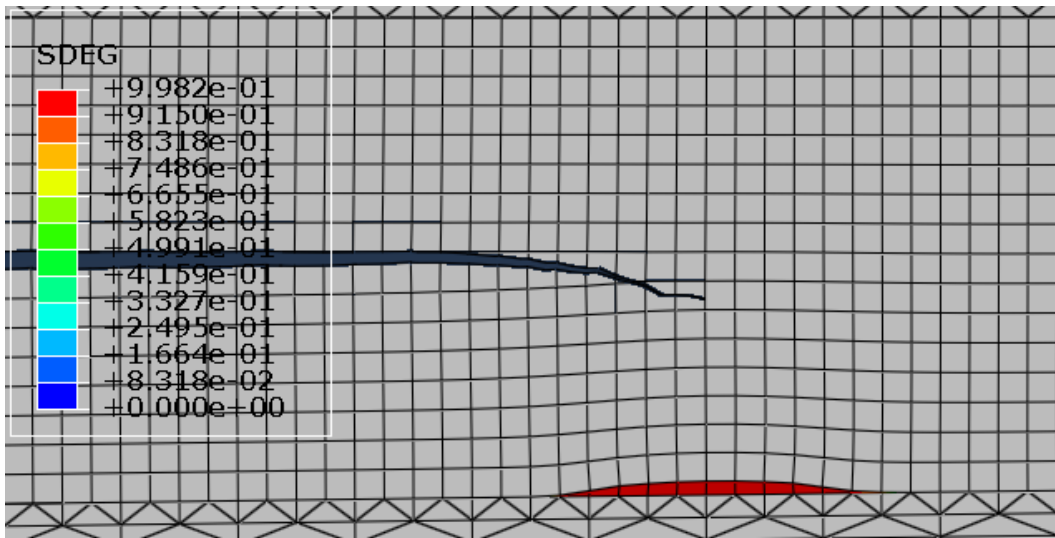
(c)

Figure 6.16. Crack paths with 0.0625 mm weakened interface and the maximum traction of: (a) 0.25 MPa, (b) 2.5 MPa, (c) 5 MPa.

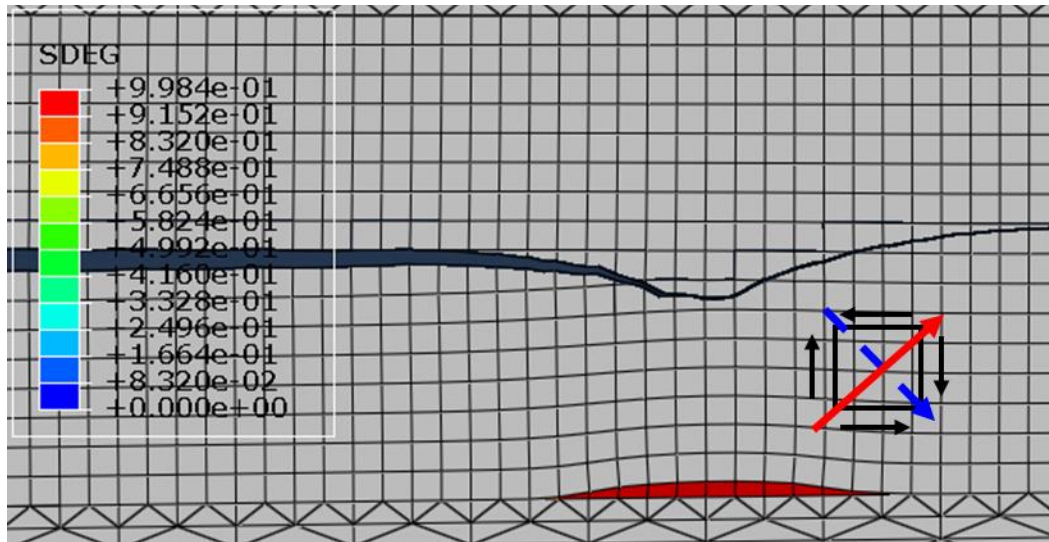
To show more details of the crack propagation and the influence of the weakened area, one crack propagation process is shown in Figure 6.17, with 20 times magnified deformation to reveal the interaction between the main crack and weakened interface (length: 0.125mm, fracture energy: 50J/m<sup>2</sup>, maximum traction: 5MPa).



(a)



(b)



(c)

Figure 6.17. The main crack propagation and damage evolution of a short weakened interface: (a) the main crack senses and veers to the weakened interface, the interface starts to damage, (b) the main crack veers more closely to the interface, (c) the main crack passes over the short weakened interface and veers back to the center line, the short interface does not totally fail.

## 6.6 Modelling and results with mixed mode loadings

It has been found in the numerical simulation that, when there is a weakened interfacial area in an adhesively bonded joint that is loaded in pure mode I, the crack path in the adhesive layer can be affected by the weakened area. It is also of interest to investigate predicted crack paths if the model is subjected to mixed mode loading scenarios. In this section, the crack paths influenced by both weakened interfaces and globally mixed mode loading, are investigated. The boundary conditions are similar to the one for pure mode I in Figure 6.3: displacements were applied at the nodes close to the two loading points (as shown by the up and down arrows in Figure 6.3), and fixed the nodes at the bonded end (on the right hand side in Figure 6.3) in x and y directions.

Referring to the numerical experiments in the previous sections for globally mode I loading, two model configurations are selected for study: in the first model, the main crack goes into the weakened interface; in the second model, the main crack veers to the weakened interface but goes back thereafter to the center of the bondline. These two crack paths are both believed to be possible and serve as representative models to be studied in bonded joints. The parameters for the two selected configurations are shown in Table 6.3.

Table 6.3. Parameters for the two models used for the study of the effect of mixed mode loadings.

Weakened interfaces	Length (mm)	$T_{max}$ (MPa)	$G_c$ (J/m <sup>2</sup> )
Model 1	0.25	2.5	5
Model 2	0.125	5	50

Based on the previous model built for the study of mode I loading, mode mixity was realized by changing the displacements applied to the two loading points, with the bonded end of the DCB specimen fixed. Though forces can be easily calculated and applied to the loading points for any specific mode mixity angle, it is not realistic to apply this boundary condition (BC) to a DCB joint because the critical forces required for crack propagation drop as the crack grows longer, resulting in catastrophic rather than controlled failure. Therefore, displacement loading is experimentally preferred, since crack propagation will cease after traveling for some distance when some constant displacement is applied to the model. The mode mixity angles were calculated after the simulation using the reaction forces obtained at the two loading points. (Though the mode mixity angle will change slightly when the crack propagates in these cases, it has been proven to be insignificant if the crack propagates by only a few millimeters.) Including the previous results for pure mode I, 11 loading cases to the two models given in Table 6.3. Refer to the coordinate system defined previously; the specimen is horizontal, with positive X direction to the right, and positive Y direction to the top. These cases are listed in Table 6.4, where a positive displacement means a movement to the right, a negative displacement means a movement to the left. The displacements on the upper and lower loading points show the ratios for each case. In some of these cases, if the crack does not propagate far enough, larger displacements were applied but the ratio was kept constant so as to provide consistency in the mode mixity angle.

Table 6.4. Displacements and mode mixity angle applied to the models.

Case	1	2	3	4	5	6	7	8	9	10	11
Upper /mm	0.2	0.2	0.2	0.2	0.2	0.2	0.15	0.05	-0.05	-0.15	-0.2
Lower /mm	0.2	0.15	0.05	-0.05	-0.15	-0.2	-0.2	-0.2	-0.2	-0.2	-0.2
Mode Angle /°	90	63	25	10	3	0	-4	-10	-25	-63	-90

Weakened area and mode mixity are the two major influences for the main crack propagation in the present work, and the former has been investigated in the previous

section. Therefore, in order to make comparisons to the crack paths when considering both of the two influences, the effect of the mode mixity angle needs to be studied separately before the combination of the two influences. These crack paths are shown in Figure 6.18. They are fairly straight since the mode mixity angle is almost constant and there is no weakened interface to disturb the propagation for each case.

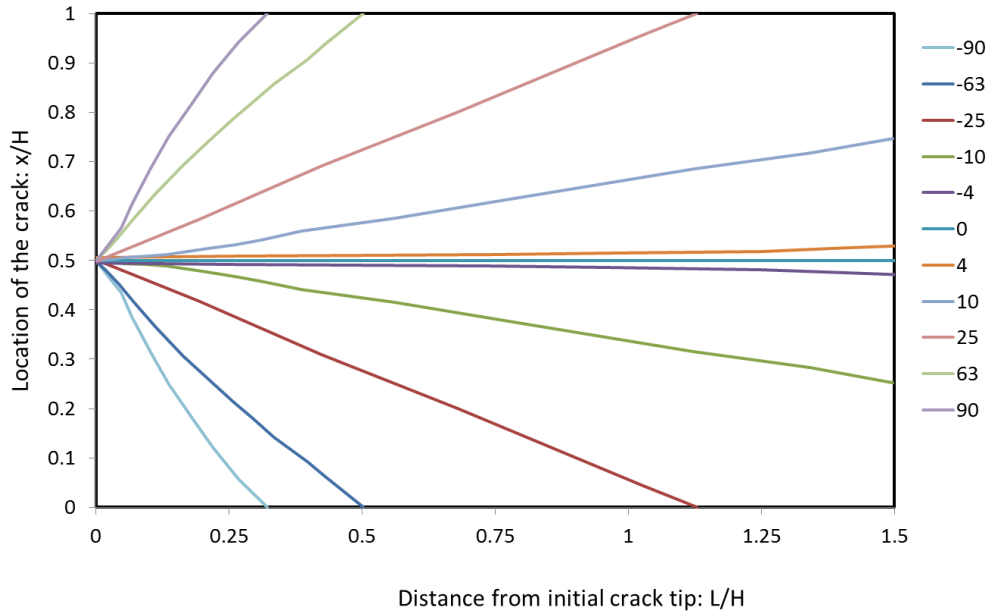


Figure 6.18. The crack paths when loaded in different mode mixities but without any weakened interface in the model in ABAQUS.

The crack paths in Figure 6.18 also shows that the main crack starts to veer initially, regardless of the distance from the weakened interface region. Therefore the weakened interface should be put close to the initial crack tip when studying the influence from both mode mixity and the weakened interface. It was found in the previous section that the main crack can sense the existence of the weakened interface when they are approximately 0.5H (i.e. half of the thickness of the adhesive layer) away in the X direction. Therefore, consistent with the previous coordinate system and non-dimensional scale, the crack tip is located at  $X=7.5H$ , as seen in Figure 6.19. This location of the crack tip was applied to all of the following cases and models.

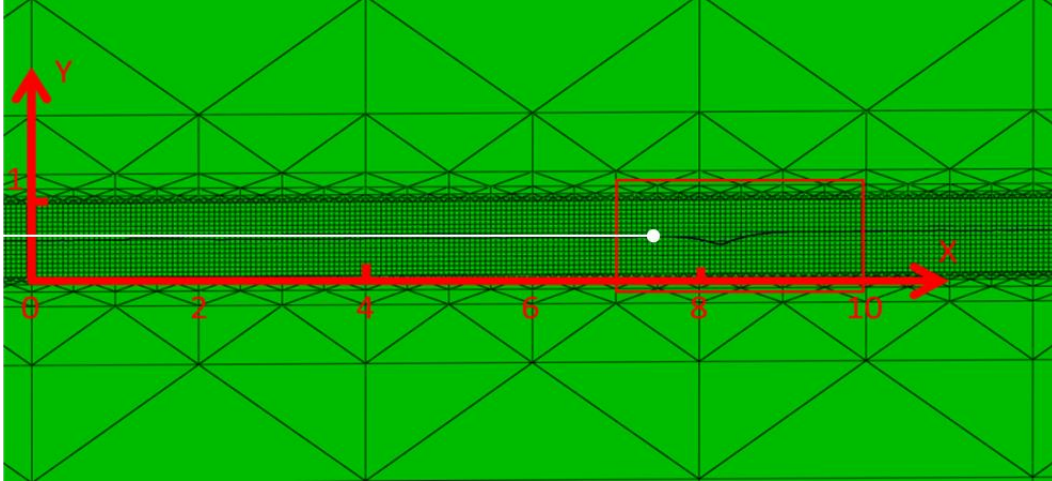


Figure 6.19. Location of the crack tip when the weakened interface starts to affect the main crack.

As was predicted, the mixed mode loadings produced different crack paths for these two models. One comparison for model 1 is shown in Figure 6.20. When loaded in pure mode I, the crack veered into the weakened interface. When loaded in  $-25^\circ$  (towards the weakened area), the main crack veered more rapidly and reached the weakened interface more directly. When loaded in  $25^\circ$  (opposite to the weakened area), the main crack was steered away from the weakened interface and grew towards the stronger interface.

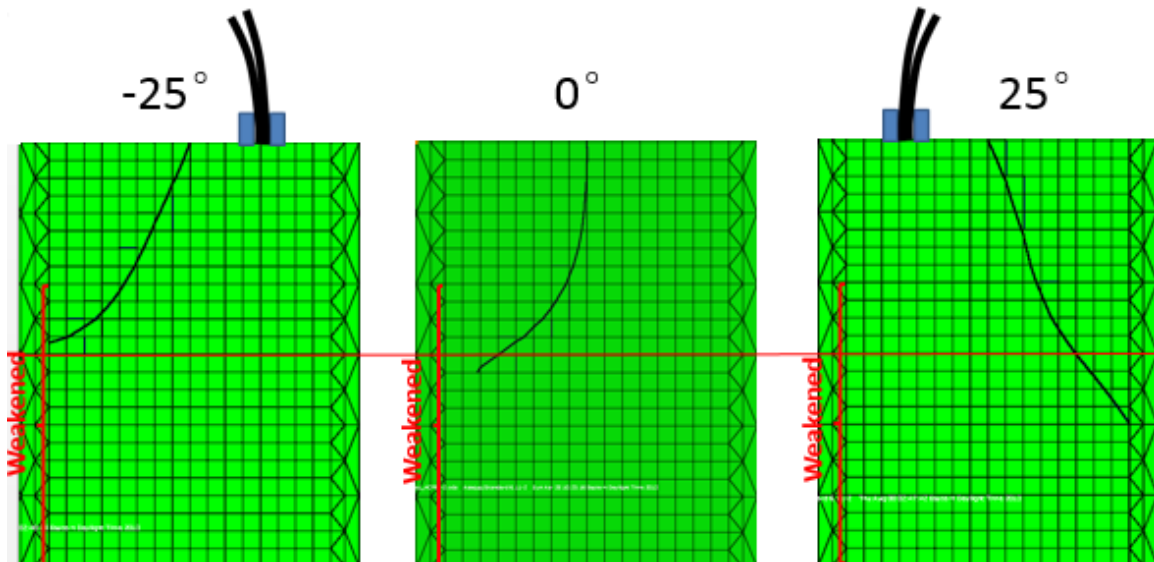


Figure 6.20. The different crack paths resulting when mixed mode loads were applied to model 1 that has a 0.25mm weakened interface on the left hand side. The horizontal red line is shown as a reference for comparisons of crack paths.

Crack paths for all 11 cases for model 1 are shown in Figure 6.21. The group of crack paths indicates that the mode mixity angle applied from the loading points far away can

change the crack paths significantly. Though the shearing effect of the weakened area is strong, sufficiently high positive mode mixity angles are capable of driving the crack path away from the weakened area in model 1.

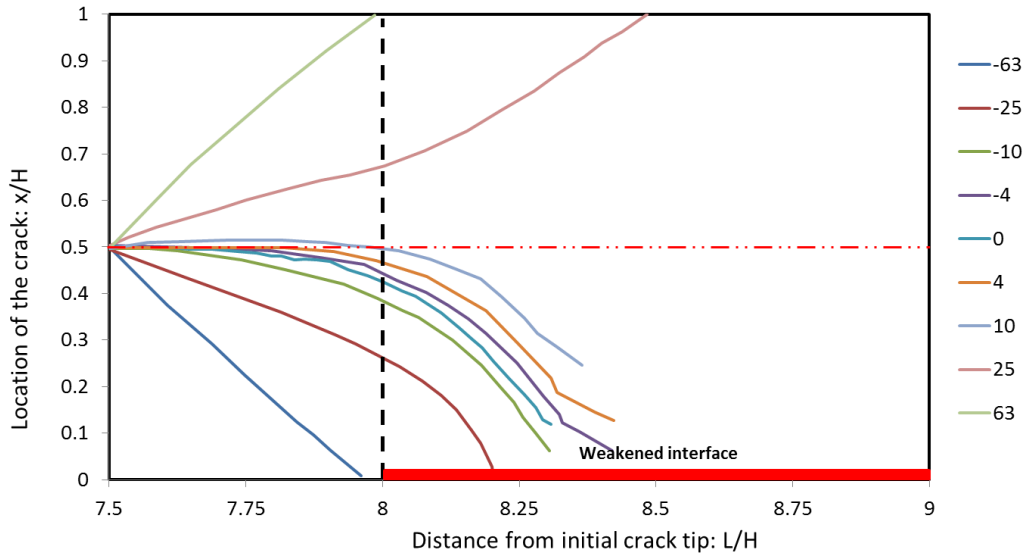


Figure 6.21. The different crack paths obtained when the 11 loading cases were applied to model 1 that has a 0.25mm weakened interface on one side. The horizontal dash-dot red line is shown as a reference for the comparisons.

Similarly, in model 2 with the finite length weakened zone, the mode mixity angle can also influence the crack paths significantly, as seen in Figure 6.22. When loaded in pure mode I for model 2, the crack path deviated to the weakened interface by some distance and then came back to the center thereafter. When loaded at  $-10^\circ$  (towards the weakened area), the main crack veered into the weakened interface quickly. When loaded in  $+10^\circ$  (opposite to the weakened area), the main crack was slightly affected by the weakened interface at the beginning, but was steered away from the weakened interface later.

Crack paths for all the 11 loading cases of model 2 are shown in Figure 6.23. The group of crack paths also shows that there was some strong influence from the mode mixity applied on the loading points. The remote mixed mode loading is capable of either steering the crack into the weakened area, or away from it. Therefore, these results indicate that the shear stresses resulting from the remote loadings and the damaged weakened area are combined. Finally, the new shear stress ahead of the crack tip drives the crack to a new direction, which is different from those without the remote mixed mode loading.

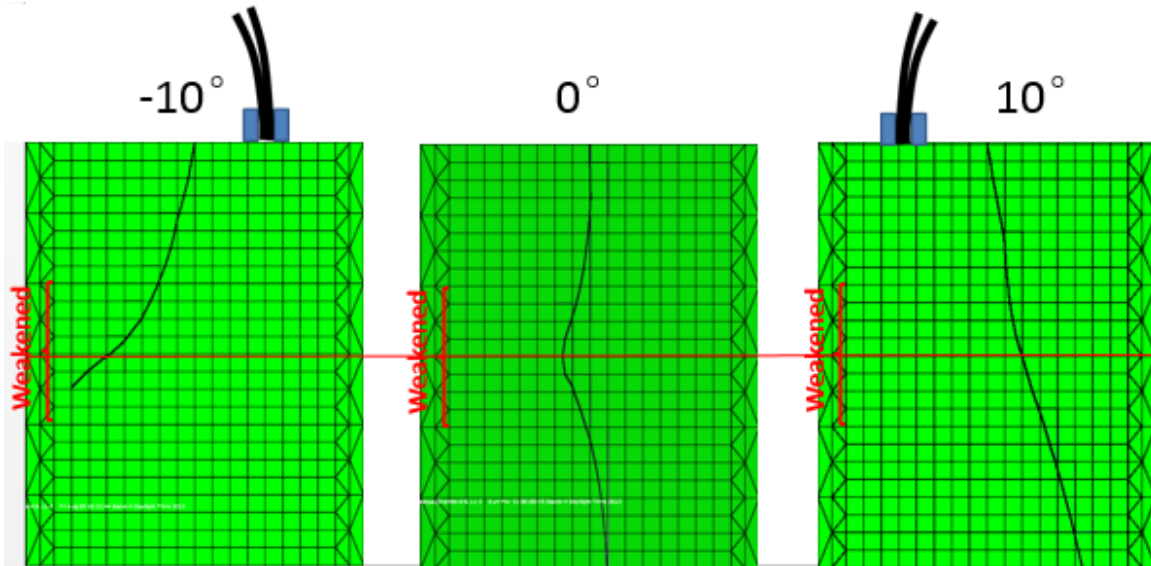


Figure 6.22. The different crack paths when mixed mode loads were applied to model 2 that has a 0.125mm weakened interface on the left hand side. The horizontal red line is shown as a reference for the comparisons of crack paths.

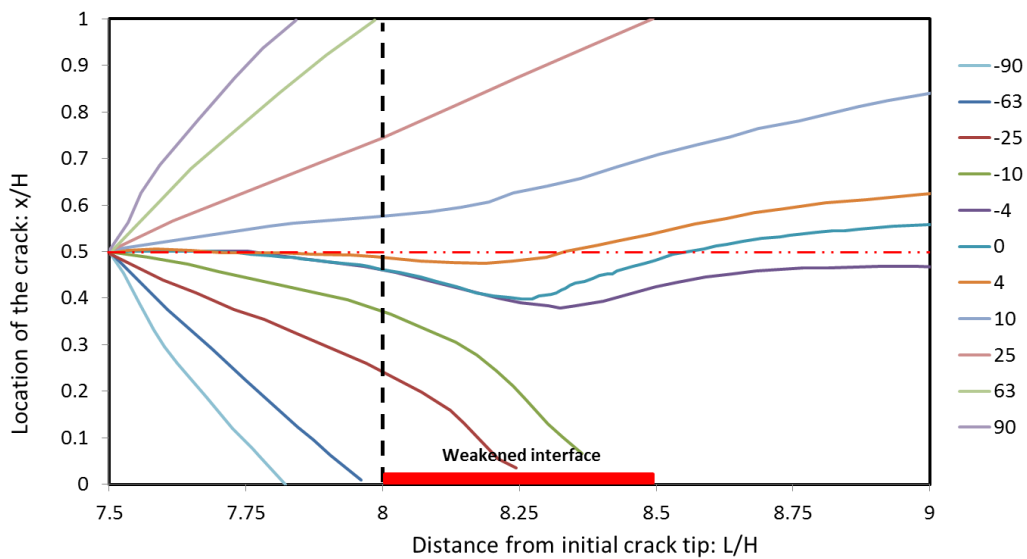


Figure 6.23. The different crack paths when the 11 cases of mixed mode loads were applied to model 2 that has a 0.125mm weakened interface on one side. The horizontal dash-dot red line is shown as a reference for the comparisons.

## 6.7 Discussion

Many researchers who studied DCBs, as well as other bonded joints, with the CZM approach agreed that the fracture energy played a more important role than the maximum traction in simulating the load-displacement curves. However, maximum traction is

difficult to measure experimentally, and some other researchers found that the values reported are somewhat lower than might be expected by a comparison with the seemingly related transverse tensile strength[40]. Since there is no direct experimental interpretation [38], most of researchers estimate the maximum traction by data fitting of load-displacement curves for fracture specimens or by making certain assumptions. The importance of the maximum traction has not been demonstrated adequately. However, in the study of crack path selection, the maximum traction is shown to be quite important to the veering of the crack path. Indeed, the maximum traction determined when the damage would start, since the flexibility of the adjacent adhesive layer would be quite different before and after the initiation of the damage process. Thus, the crack paths would be evidently different when the value of the maximum traction is different.

In general, crack path selection is considered to be influenced by the stress field ahead of the crack tip. Residual stresses were assumed to be zero throughout this chapter. When damage is initiated in the weakened area, the traction applied from the weakened interface to the adjacent adhesive boundary decreases as the displacement increases. Then the adhesive adjacent to this region is becoming more and more flexible, until traction free when the interface totally fails. Therefore, shear stress is exerted around the crack tip, which veers the crack path towards the weakened interface. The crack will propagate to the new direction, which is perpendicular to the maximum opening stress ahead of the crack tip.

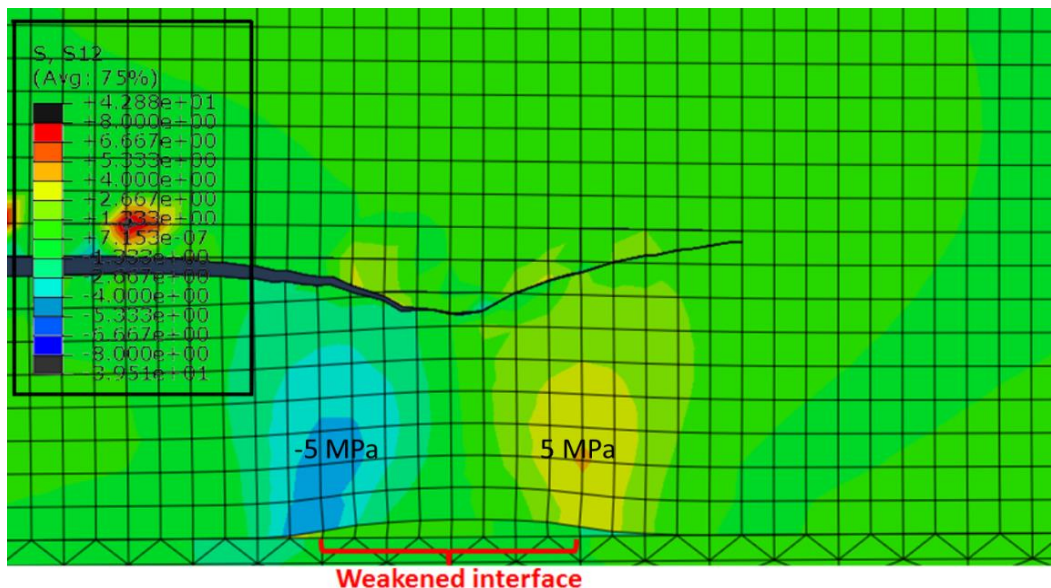


Figure 6.24. Shear stress distribution in the adhesive layer when the main crack is propagating.

The deformed mesh in Figure 6.24 shows the shear stress in the adhesive layer. Evidently, the high shear stress region at the front of the weakened interface effectively deflects the crack towards the interface slightly as the growing cohesive crack approaches the region above the weakened area. Then shear stresses in the opposite direction at the right end of the weakened region effectively drive the crack up away from the weakened

zone. Similar stress distributions are found for other cases analyzed. But if the distance between these two shear regions (one is positive and the other is negative) is sufficiently long, the main crack does turn into the interface.

Based on this analysis, the maximum traction strongly affects the initiation of damage of the interfaces. If the maximum traction is smaller, the damage starts before the main crack comes closer, and the adhesive layer next to the weakened interface is more flexible, thus the influence to the main crack is more significant. On the other hand, the fracture energy value determines when the interface would totally fail, and is equivalent to the maximum displacement on failure.

In summary, all these reasoning processes were made based on the assumptions of the CZM. Though the CZM parameters used for this numerical study are assumed values, the logic would be reasonable. Since the CZM has been widely accepted to be a good approach to the constitutive behavior of an interface, the crack path selection and the interaction of the main crack and the partially weakened interface obtained herein may prove useful in understanding and interpreting the effects of locally weakened interfacial regions.

## 6.8 Conclusions

Crack path selection in adhesively bonded joints with partially weakened interfaces was studied numerically using XFEM for bulk adhesive and cohesive elements for the interfaces. The maximum traction in the CZM model, the fracture energy, and the length of the assumed weakened interfacial regions were changed to alter the response of the main cohesive crack propagating within the adhesive layer as it interacts with the weakened interface. Several discrete values of these parameters have been used to compute results and cover a wide range of values of parameters. The role of the CZM parameters, as well as the size of the initial weakened area, are summarized as follows:

(1) The maximum traction of the weakened interface was shown to be the most important parameter affecting crack path selection. The main crack veers to the weakened interface steeply when  $T_{\max}$  of the interface is sufficiently small in comparison to that of the bulk material. For example, of the cases simulated herein, this occurred for  $T_{\max} \leq 5\text{MPa}$  (43% that of the bulk  $T_{\max}$ , which was 11.6 MPa). There is still some influence on the crack path even if  $T_{\max}$  of the weakened interface equals 86% of that of the bulk adhesive, though the slopes of the crack paths are relatively small.

(2) The fracture energy of the weakened interface also influences the crack path but is of secondary importance, though a particularly small value (e.g.  $G_c = 5\text{J}/\text{m}^2$ , which is 1% that of the bulk adhesive) can significantly affect the crack paths in some cases. The fracture energy of the weakened interface can barely influence the crack path when  $T_{\max}$  of the weakened interface is sufficiently small (e.g.  $T_{\max} \leq 2.5\text{MPa}$ , or 22% of that of the bulk adhesive in our simulations). Mostly, the fracture energy of the weakened interface

changes the profile of the crack path slightly when it is about to reach the edge of the adhesive layer.

(3) The size of the weakened area is also an important factor to the crack path when  $T_{\max}$  of the weakened interface is small enough (e.g.  $T_{\max} \leq 5MPa$ , or 43% of that of the bulk adhesive in our simulations). Long weakened interfacial regions can strongly influence the crack path in these cases. But if the size of the weakened area is very small (e.g. shorter than 25% of the adhesive thickness in our models), the main crack is not changed significantly even if  $T_{\max}$  and  $G_c$  of the weakened interface are very small, resulting in the weakened interface being essentially “ignored” by the growing cohesive crack. However, in the other cases where the length of the weakened interface is either 50% or 100% of the adhesive thickness, different crack path patterns can be found. The influence does depend on the CZM parameters of the weakened interface.

Assumptions of the CZM imply that the stiffness of the weakened interface decreases as damage evolution progresses. The damaged interface relaxes constraint on the adjacent adhesive layer, which shears in a manner that drives the main crack towards the weakened interface. When remote mixed mode loading is applied, the shear stress due to the applied load is increased by the weakened interface, further altering the crack path.

## 6.9 References

- [1] T. L. Anderson, *Fracture Mechanics: Fundamentals and Applications*, 2nd ed. Boca Raton: CRC Press, 1995.
- [2] C. Y. Hui, A. Ruina, R. Long, and A. Jagota, "Cohesive Zone Models and Fracture," *Journal of Adhesion*, vol. 87, pp. 1-52, 2011.
- [3] N. Choupani, "Interfacial mixed-mode fracture characterization of adhesively bonded joints," *International Journal of Adhesion and Adhesives*, vol. 28, pp. 267-282, Sep 2008.
- [4] D. A. Dillard, H. K. Singh, D. J. Pohlit, and J. M. Starbuck, "Observations of Decreased Fracture Toughness for Mixed Mode Fracture Testing of Adhesively Bonded Joints," *Journal of Adhesion Science and Technology*, vol. 23, pp. 1515-1530, 2009.
- [5] V. F. Erdogan and G. C. Sih, "On Crack Extension in Plates Under Plane Loading and Transverse Shear," *Trans. ASME J. Bas. Eng.*, vol. 85, pp. 519-527, 1963.
- [6] K. Palaniswamy and W. G. Knauss, "On the Problem of Crack Extension in Brittle Solids Under General Loading," *Mechanics Today*, vol. 4, pp. 87-148, 1978.
- [7] R. V. Goldstein and R. L. Salganik, "Brittle Fracture of Solids with Arbitrary Cracks," *International Journal of Fracture*, vol. 10, 1974.
- [8] B. Cotterell and J. R. Rice, "Slightly Curved or Kinked Cracks," *International Journal of Fracture*, vol. 16, pp. 155-169, 1980.
- [9] A. R. Akisanya and N. A. Fleck, "Brittle-Fracture of Adhesive Joints," *International Journal of Fracture*, vol. 58, pp. 93-114, NOV 15 1992.
- [10] P. H. Geubelle and W. G. Knauss, "Crack-Propagation at and near Bimaterial Interfaces - Linear-Analysis," *Journal of Applied Mechanics-Transactions of the Asme*, vol. 61, pp. 560-566, SEP 1994.
- [11] J. W. Hutchinson and Z. Suo, "Mixed-Mode Cracking in Layered Materials," *Advances in Applied Mechanics, Vol 29*, vol. 29, pp. 63-191, 1992.
- [12] G. R. Irwin, "Fracture dynamics," *Fracturing of Metals, American Society for Metals*, pp. 147-166, 1948.
- [13] D. S. Dugdale, "Yielding in Steel Sheets Containing Slits," *Journal of the Mechanics and Physics of Solids*, vol. 8, pp. 100-104, 1960.
- [14] G. I. Barenblatt, "The Mathematical Theory of Equilibrium Cracks in Brittle Fracture," *Advances in Applied Mechanics*, vol. 7, pp. 55-129, 1962.

- [15] A. A. Wells, "Unstable Crack Propagation in Metals: Cleavage and Fast Fracture," *Proceedings of the Crack Propagation Symposium*, vol. 1, 1961.
- [16] M. L. Williams, "On the stress distribution at the base of a stationary crack," *Journal of Applied Mechanics*, vol. 24, pp. 109-114, 1957.
- [17] J. R. Rice, "A Path Independent Integral and the Approximate Analysis of Strain Concentration by Notches and Cracks," *Journal of Applied Mechanics*, vol. 35, pp. 379-386, 1968.
- [18] J. W. Hutchinson, "Singular behaviour at the end of a tensile crack in a hardening material," *Journal of the Mechanics and Physics of Solids*, vol. 16, pp. 13-31, 1// 1968.
- [19] J. R. Rice and G. F. Rosengren, "Plane strain deformation near a crack tip in a power-law hardening material," *Journal of the Mechanics and Physics of Solids*, vol. 16, pp. 1-12, 1// 1968.
- [20] M. Elices, G. V. Guinea, J. Gomez, and J. Planas, "The cohesive zone model: advantages, limitations and challenges," *Engineering Fracture Mechanics*, vol. 69, pp. 137-163, Jan 2002.
- [21] G. Alfano and M. A. Crisfield, "Finite element interface models for the delamination analysis of laminated composites: Mechanical and computational issues," *International Journal for Numerical Methods in Engineering*, vol. 50, pp. 1701-1736, Mar 10 2001.
- [22] Y. Mi, M. A. Crisfield, G. A. O. Davies, and H. B. Hellweg, "Progressive delamination using interface elements," *Journal of Composite Materials*, vol. 32, pp. 1246-1272, 1998.
- [23] A. Needleman, "A Continuum Model for Void Nucleation by Inclusion Debonding," *Journal of Applied Mechanics-Transactions of the Asme*, vol. 54, pp. 525-531, Sep 1987.
- [24] V. K. Goyal, E. R. Johnson, and C. G. Davila, "Irreversible constitutive law for modeling the delamination process using interfacial surface discontinuities," *Composite Structures*, vol. 65, pp. 289-305, Sep 2004.
- [25] P. P. Camanho, C. G. Davila, and M. F. de Moura, "Numerical simulation of mixed-mode progressive delamination in composite materials," *Journal of Composite Materials*, vol. 37, pp. 1415-1438, 2003.
- [26] A. Turon, P. P. Camanho, J. Costa, and C. G. Davila, "A damage model for the simulation of delamination in advanced composites under variable-mode loading," *Mechanics of Materials*, vol. 38, pp. 1072-1089, Nov 2006.
- [27] V. Tvergaard and J. W. Hutchinson, "The Relation between Crack-Growth Resistance and Fracture Process Parameters in Elastic Plastic Solids," *Journal of the Mechanics and Physics of Solids*, vol. 40, pp. 1377-1397, Aug 1992.

- [28] X. P. Xu and A. Needleman, "Numerical Simulations of Fast Crack-Growth in Brittle Solids," *Journal of the Mechanics and Physics of Solids*, vol. 42, pp. 1397-1412, Sep 1994.
- [29] W. C. Cui and M. R. Wisnom, "A Combined Stress-Based and Fracture-Mechanics-Based Model for Predicting Delamination in Composites," *Composites*, vol. 24, pp. 467-474, Sep 1993.
- [30] J. C. J. Schellekens and R. Deborst, "A Nonlinear Finite-Element Approach for the Analysis of Mode-I Free Edge Delamination in Composites," *International Journal of Solids and Structures*, vol. 30, pp. 1239-1253, 1993.
- [31] J. Chen, M. Crisfield, A. J. Kinloch, E. P. Busso, F. L. Matthews, and Y. Qiu, "Predicting progressive delamination of composite material specimens via interface elements," *Mechanics of Composite Materials and Structures*, vol. 6, pp. 301-317, Oct-Dec 1999.
- [32] M. V. C. Alfaro, A. S. J. Suiker, R. de Borst, and J. J. C. Remmers, "Analysis of fracture and delamination in laminates using 3D numerical modelling," *Engineering Fracture Mechanics*, vol. 76, pp. 761-780, Apr 2009.
- [33] W. G. Jiang, S. R. Hallett, B. G. Green, and M. R. Wisnom, "A concise interface constitutive law for analysis of delamination and splitting in composite materials and its application to scaled notched tensile specimens," *International Journal for Numerical Methods in Engineering*, vol. 69, pp. 1982-1995, Feb 26 2007.
- [34] A. Turon, P. P. Camanho, J. Costa, and J. Renart, "Accurate simulation of delamination growth under mixed-mode loading using cohesive elements: Definition of interlaminar strengths and elastic stiffness," *Composite Structures*, vol. 92, pp. 1857-1864, 2010.
- [35] R. D. S. G. Campilho, M. D. Banea, F. J. P. Chaves, and L. F. M. da Silva, "eXtended Finite Element Method for fracture characterization of adhesive joints in pure mode I," *Computational Materials Science*, vol. 50, pp. 1543-1549, Feb 2011.
- [36] E. Giner, N. Sukumar, J. E. Tarancón, and F. J. Fuenmayor, "An Abaqus implementation of the extended finite element method," *Engineering Fracture Mechanics*, vol. 76, pp. 347-368, 2009.
- [37] C. L. Tsai, Y. L. Guan, D. C. Ohanehi, J. G. Dillard, D. A. Dillard, and R. C. Batra, "Analysis of Cohesive Failure in Adhesively Bonded Joints with SSPH Meshless Method," *International Journal of Adhesion and Adhesives*, vol. In review, 2013.
- [38] B. R. K. Blackman, H. Hadavinia, A. J. Kinloch, and J. G. Williams, "The use of a cohesive zone model to study the fracture of fibre composites and adhesively-bonded joints," *International Journal of Fracture*, vol. 119, pp. 25-46, Jan 2003.

- [39] P. P. Camanho, and C. G. Davila, "Mixed-Mode Decohesion Finite Elements for the Simulation of Delamination in Composite Materials," 2002.
- [40] A. J. Kinloch, G. K. A. Kodokian, and J. F. Watts, "The Adhesion of Thermoplastic Fiber Composites," *Philosophical Transactions of the Royal Society of London Series a-Mathematical Physical and Engineering Sciences*, vol. 338, pp. 83-112, Jan 15 1992.

# **Appendix A Rate dependent tests on crack path selection in epoxy adhesive bonded joints with weakened interfaces**

---

Epoxy resins are widely used as structural adhesives, efficiently facilitating the assembly of materials with less weight and simpler designs. Though significant improvements have been made in bonding techniques, adhesive performance, and joint design, there are still a number of uncertainties, including environmental degradation and fracture resistance over the range of conditions experienced by adhesive bonds in service. Therefore, the presence and propagation of cracks in bonded joints remain of concern. Adhesives are often formulated to result in cohesive failure and to avoid the interfacial failures that make bonding particularly suspect. This appendix presents preliminary results for adhesively bonded double cantilever beam (DCB) specimens formed using one adherend that had been discretely contaminated to reduce interfacial adhesion to explore how a growing cohesive crack may interact with a locally weakened interface. Quasi-static tests were performed in mode I to investigate crack path selection (cohesive failure or adhesive failure). The effects of bonding strength of interfaces and rate of propagation of cracks on the interaction between a cohesive crack and weakened interfaces are discussed.

## **A.1 Experimental works with graphite and silicone tape contaminated interfaces**

The specimens were made of 6061-T6 aluminum alloy, and bonded with one of the two epoxy adhesives. All adherends were first treated by placing them in a 10% (wt) NaOH solution for 10 minutes, and then in 50% (v) HNO<sub>3</sub> for 3 minutes, with distilled water rinse after each step. Some initial mode I DCB tests showed that bonding to the interfaces was strong, resulting in only cohesive failures within the adhesive layer. The average value of the fracture energy was found to be 500 J/m<sup>2</sup> and appeared to be independent of crack propagation rate over the range of the tests conducted. Initially a lead pencil was manually used to locally contaminate strips on the adherend surface with graphite particles. Subsequently the joints were bonded with epoxy adhesive, and tested in pure mode I loading.

This local contamination, resulting in areas of reduced adhesion, was found to affect the path followed by the growing crack in some situations. There are at least four factors that may influence the crack path selection: the width of the weakened strips, the distance between them, the degree of contamination, and, as reported here, the effective crack propagation rate at the crack tip. In order to obtain insights to guide the plans for further study, several patterns were applied on a single specimen. Out of the five approximately 5 mm wide weak zones, as shown in Figure A.1, four were clearly discovered by the growing crack, resulting in what is apparently a failure within the weakened interfacial areas. But the fifth one was only partially detected by the growing crack tip. This test was repeated

on another specimen with the same pattern and the same result was obtained. Because this DCB specimen was loaded at a constant crosshead displacement rate, the crack propagation rate was higher at the beginning but decreased as the crack length increased. The results suggested possible rate dependence for the detection of the weakened regions, as borne out further in the tests described below.

To verify this idea, other specimens with the same pattern of contaminated interfaces were tested at a constant crack propagation rate that was applied based on simply beam theory through custom function implemented in the controller used with the DALF. If constant fracture energy ( $G_{lc} = 500 \text{ J/m}^2$ ) can be assumed for a DCB specimen, the crack propagation rate can be shown to be proportional to the reciprocal of the crack length  $a$ , as well as the crosshead displacement rate:

$$\dot{a} = \frac{\dot{\Delta}}{2a} \sqrt{\frac{EI}{G_{lc} B}} \quad (1.9)$$

where  $\dot{a}$  is the crack propagation rate,  $\dot{\Delta}$  is the crosshead displacement rate,  $EI$  is the stiffness of the aluminum adherend,  $B$  is the width of the adherends, as well as the bond width. Therefore, by using this equation, an approximately constant  $\dot{a}$  was attained by adjusting  $\dot{\Delta}$  after every 1 mm increment in  $a$  manually. (Up to now, the crosshead displacement is calculated automatically and suggested, but applied by the user manually in order to avoid potential safety issue resulted from uncertainties during the tests.)

The initial crosshead displacement rate of 0.12 mm/min in these tests was gradually increased to 2 mm/min for  $a = 60 \text{ mm}$  to maintain a nearly constant crack propagation rate along the entire specimen length.

In summary, it was found that higher crack propagation rates appear much more likely to detect the weakened interfacial zones for these bonded joints. However, these weak zones were detected at low crack propagation rates. Similarly, most of the narrow weak zones ( $\approx 1 \text{ mm}$ ) were not detected by the main crack when the propagation rate was low. But they were clearly identified when the growth rate was high in Figure A.1b.

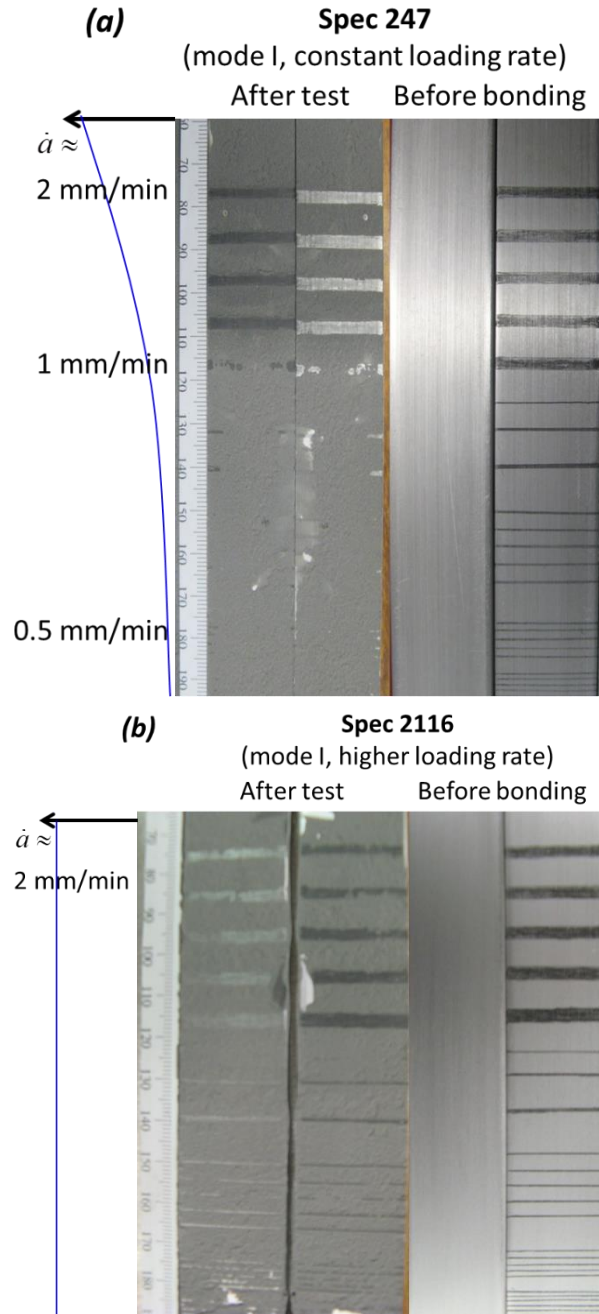


Figure A.1. Crack path selection at different displacement rates in toughened epoxy adhesive bonded DCB joints: (a) constant crosshead loading rate: 0.1 mm/min, (b) constant crack propagation rate. (On the surfaces before bonding, the black bands were weakened areas, theoretically predicted crack propagation speed curves are shown on the left side of each picture).

Similar rate dependency was also found in specimens contaminated by silicone tapes from the 3M®. The silicone tapes were applied to the treated (by base and acid solution) and dried aluminum (the same aluminum alloy as used in the previous tests) surfaces manually, and then removed after 1 minute. The size of the silicone contaminated areas

was 25mm by 25 mm, and the spaces between these areas were also 25 mm. Therefore, some silicone contamination was potentially transferred to the three areas on the adherends.

Then the joints were bonded using the same method as shown at the beginning of this chapter. Quasi-static DCB test was conducted at a crosshead displacement rate of 0.1 mm/min. After the test, it was found that the first and second weakened areas were detected by the main crack in the adhesive layer, where the crack propagation rate is relatively fast. However, the third one, where the crack propagation rate is slower, was not detected by the main crack. This test was also repeated and similar result were found, though these manually controlled contamination were not sophisticated.

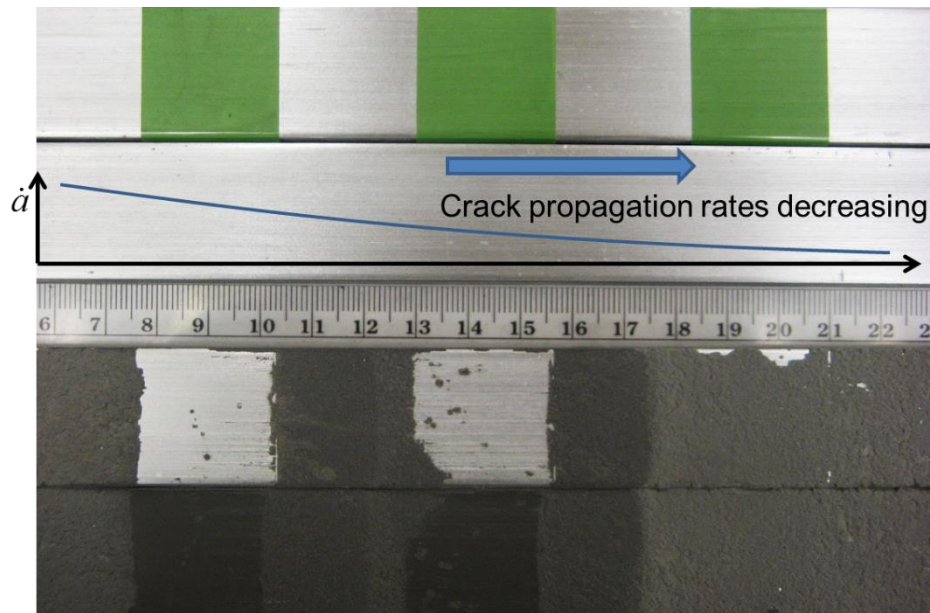


Figure A.2. Rate dependent detection of weakened interfacial areas in bonded joints prepared by JB Weld epoxy adhesive, the crosshead displacement rate is 0.1 mm/min, and the crack propagation rate is decreasing.

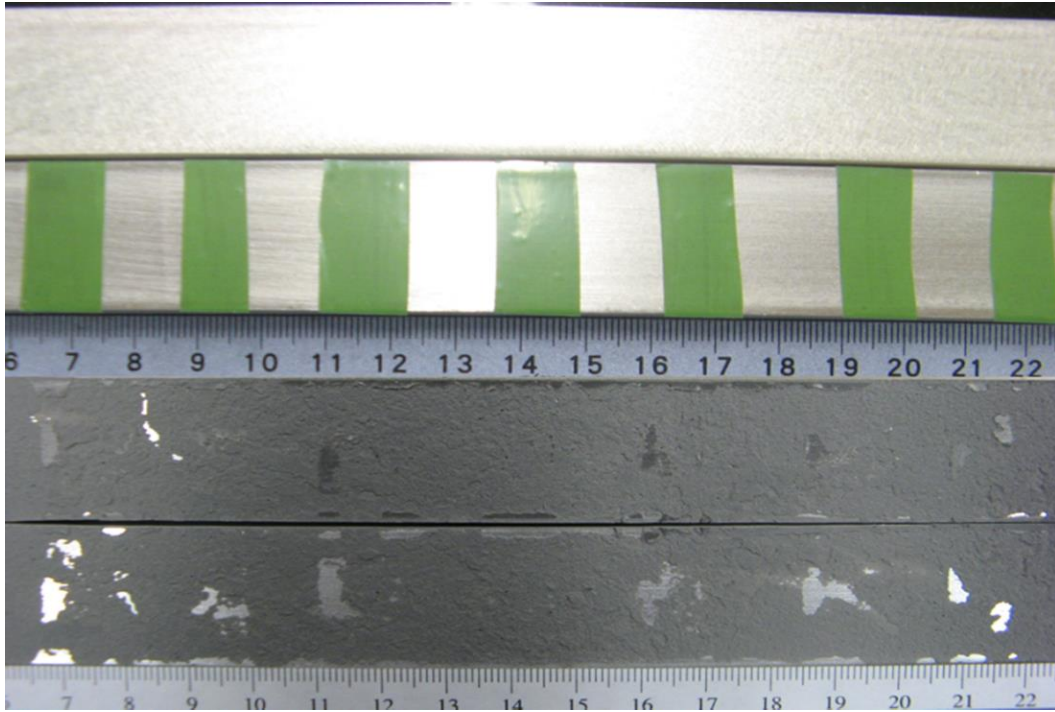


Figure A.3. Rate dependent detection of weakened interfacial areas in bonded joints prepared by JB Weld epoxy adhesive, the crosshead displacement rate is 0.002 mm/min and no clear detection in this case.

These tests showed that the weakened area detection is a rate dependent phenomena. Stimulated by these results, some more sophistic tests were conducted thereafter.

Graphite was used again to prepare contaminated areas with better spacing control. Some half millimeter graphite lines with 8.5 mm spacing were applied to the treated and dried adherends. Six of these DCB specimens were bonded with the JB Weld epoxy, and six more were bonded with the LORD epoxy. Again, these specimens were tested at different crosshead displacement rates: some of them at 0.001 mm/min, some of them at 100 mm/min. After the DCB tests, specimens bonded with different epoxies showed different results. For the specimens bonded with the JB Weld epoxy, high propagation rate tests detected almost all the weakened interfaces clearly, but low propagation rate tests didn't find any of them. For the specimens bonded with the LORD epoxy, neither the high propagation rate tests nor the low propagation rate tests detected the weakened interfaces clearly. In summary: for a common general-purpose epoxy such as the JB Weld adhesive, the crack path is quite sensitive to the graphite contamination on the interface; for a more highly formulated commercial adhesive such as the LORD epoxy, however, the crack path in the adhesive layer appears less sensitive to the graphite contamination on the interface. The fracture energy curve is shown in Figure A.5, which is slightly higher than those quasi-static DCB tests conducted previously at the crosshead displacement rate of 0.1 mm/min.

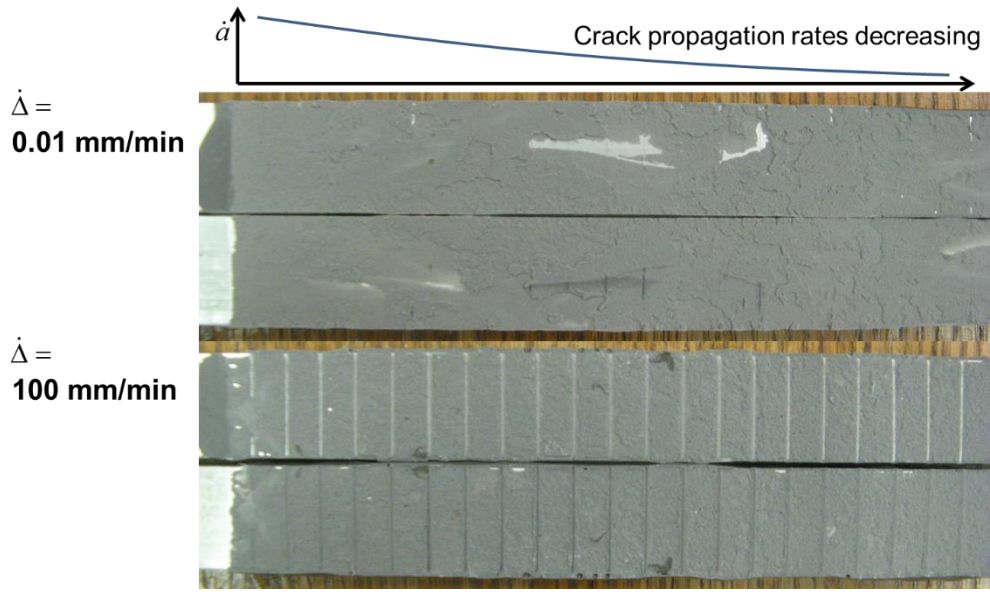


Figure A.4. Rate dependent detection of weakened interfacial areas in bonded joints prepared by the JB Weld epoxy adhesive, the crosshead displacement rates are 0.01mm/min, and 100 mm/min, respectively. High propagation rate tests detected almost all the weakened interfaces clearly, but low propagation rate tests didn't find any of them.

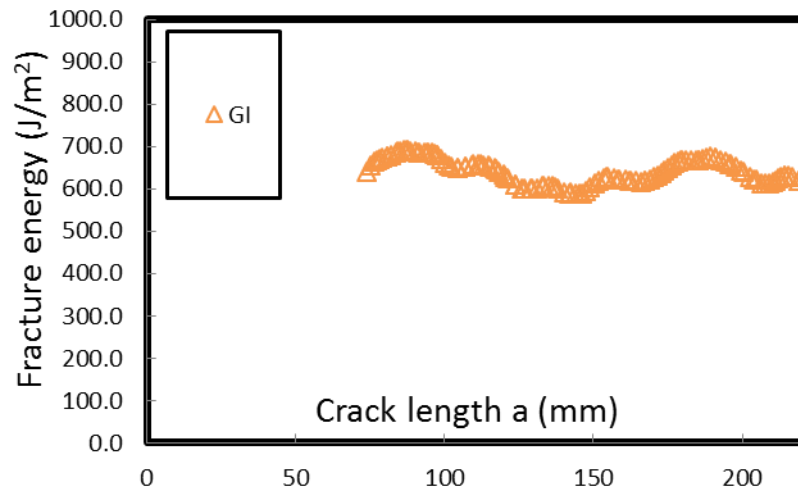


Figure A.5. Fracture energy curve for one high propagation rate tests of specimens bonded with the JB Weld epoxy.

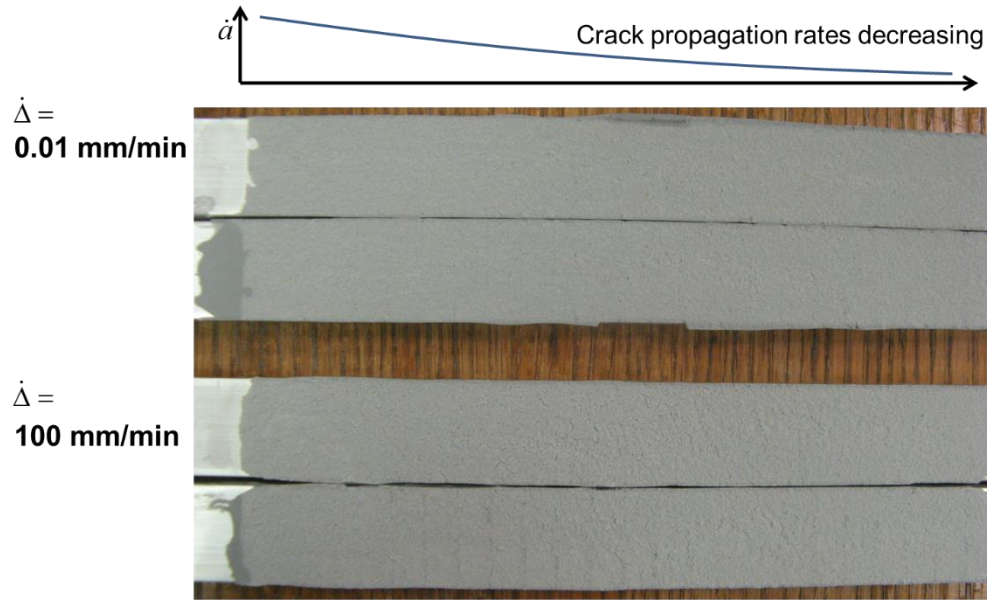


Figure A.6. Rate dependent detection of weakened interfacial areas in bonded joints prepared by the LORD epoxy adhesive, the crosshead displacement rates are 0.01mm/min, and 100 mm/min, respectively. Neither the high propagation rate tests nor the low propagation rate tests find the weakened interfaces clearly.

## A.2 Experimental works with silane weakened interfaces

Some of the adherends were weakened by silane solution to provide lower bonding strength and affect the crack path selection. Different silane solutions were used to provide a unique treatment on a large area, avoiding inconsistency in the contamination process. In principle, if the surface was very weak, the crack in the adhesive should turn into the interface. If the surface is not so weak, the crack in adhesive could, sometimes, ignore the weak surfaces and remain cohesive within the adhesive when loaded in pure mode I. The contact angle between the water drop and aluminum beam was used to estimate the bonding strength: smaller angle meant stronger bonding and higher surface energy.

For some of the tests, propyltrimethoxysilane (PS) was used to weaken the adhesion to one adherend, while 3-aminopropyltrimethoxysilane (APS) was used to strengthen it. Both of the treatments are the same and can be applied through the same process:

- (1) Complete abrading and base-acid treatments as above, but without drying.
- (2) In a beaker prepare a solution of approximately 5% (v/v) PS in 100% (200 proof) ethanol.
- (3) To 100 mL of the solution prepared above, add about 5 mL of 0.1 M acetic acid. Stir this solution for about 10 min. (Solution A)

(4) In a separate beaker, add 5 mL of 0.1 M acetic acid to 100 mL of ethanol (Solution B). Immerse the adherends in Solution B for about 10 min with stirring.

(5) Add 100 mL of Solution A to Solution B, and continue stirring the combined solutions. Allow this derivatization reaction to continue at room temperature for at least 30 min.

(6) Remove the adherends from the derivatization reaction vessel, rinse the adherends with DI water and dry the adherends in an oven at 110 C for at least 30 min.

In order to obtain the bonding strength in different levels, propyltrimethoxysilane (PS) and 3-amino propyltrimethoxysilane (APS) were used and mixed. The process of silane treatment is shown above, but the only difference in this study is: some mixture of PS and APS with different ratios were used. Some of the pictures from the tests were shown in Figure A.7. It is worth noting that, when the contact angle changed from  $67^\circ$  to  $83^\circ$ , for the specimens tested, different crack paths were found after pure mode I tests.

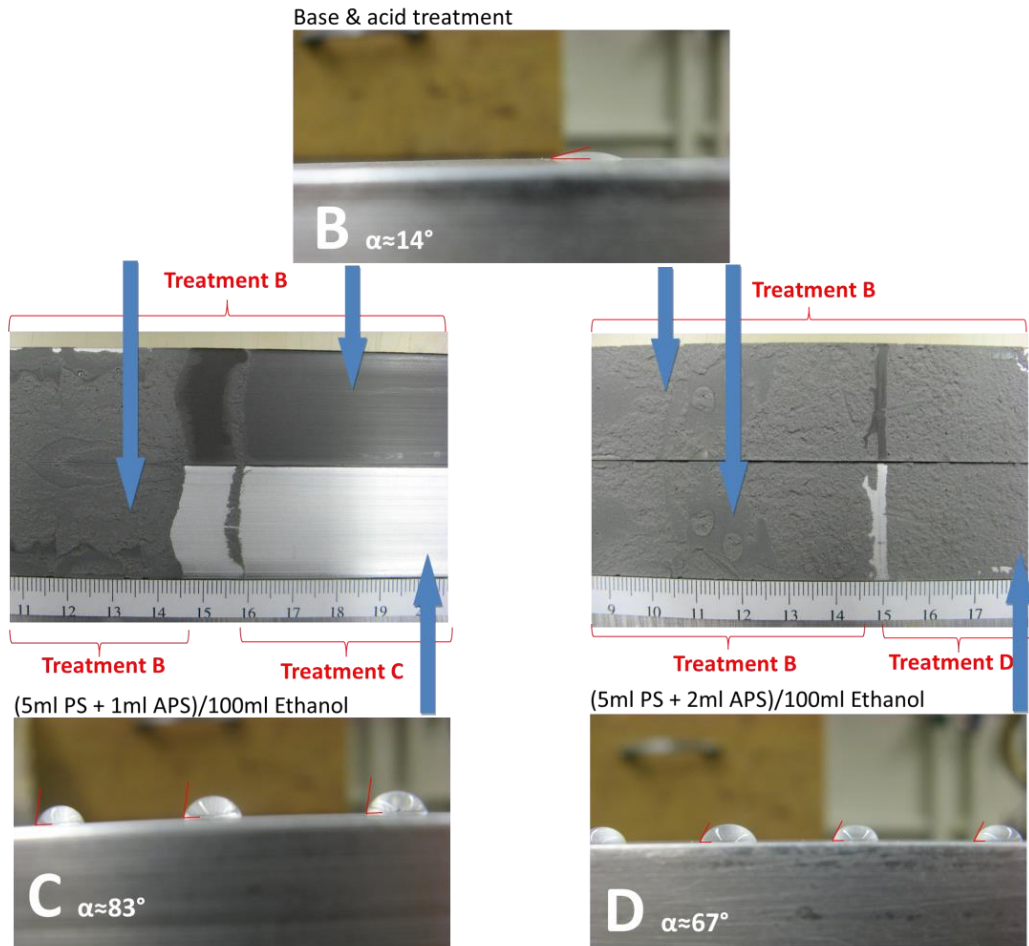
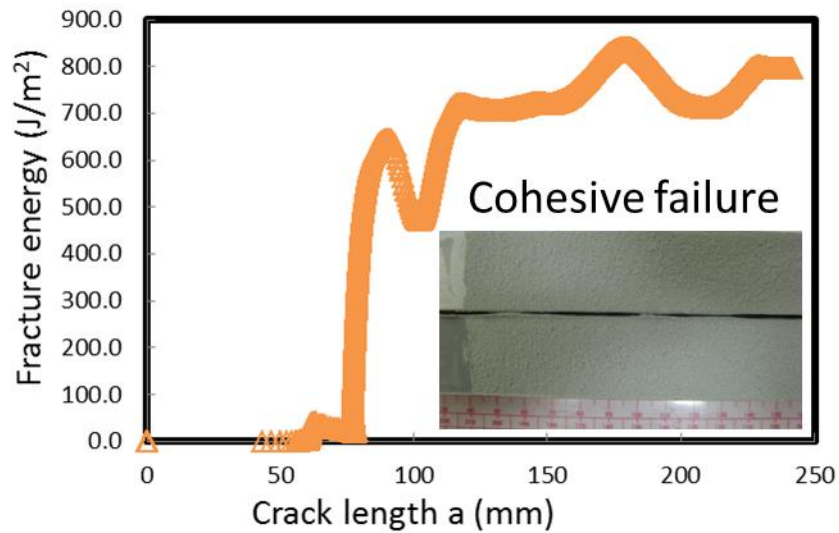


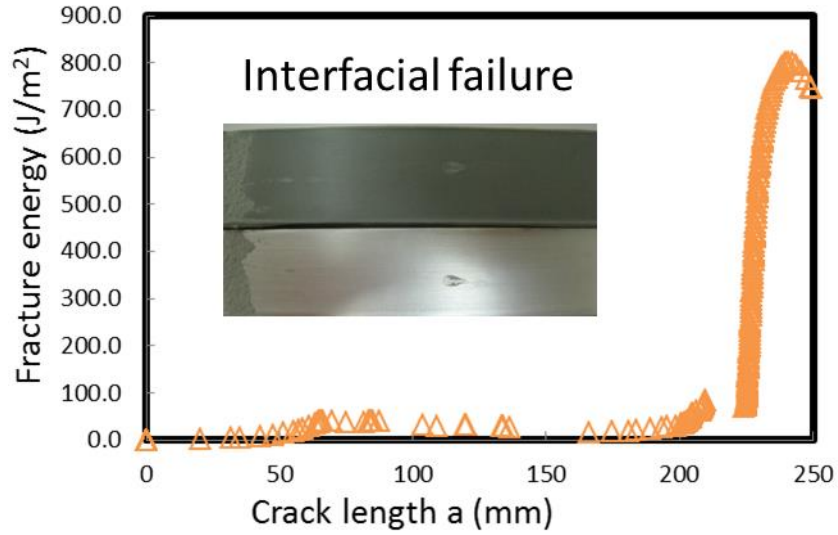
Figure A.7. Relationships between the water drop contact angle and the failure modes: cohesive failure when the contact angle is smaller than  $67^\circ$ ; interfacial failure when the contact angle is larger than  $83^\circ$ .

Therefore, to obtain a partially weakened interfacial area (neither very strong nor very weak) for this study, the water drop contact angle needed is between 67 °and 83 °for the JB Weld epoxy/aluminum oxide interface. However, repeated tests indicated that this range of contact angle does not work for the LORD epoxy/aluminum oxide interface.

Then, a new mixture with different silanes was developed for the LORD epoxy/aluminum oxide interface. The mixture consists of 1 ml APS and 5 ml Hexyltrimethoxysilane (HS). The contact angle is  $\alpha \approx 90^\circ$  . Again, six specimens prepared with the LORD epoxy were tested at different crosshead displacement rates: three of them at 0.01 mm/min, three of them at 100 mm/min. Some of the DCB test results is shown in Figure A.8. In summary, according to our tests, LORD 320/322 epoxy adhesive is better because it requires less strong interface (higher contact angle) than the JB Weld epoxy adhesive.



(a)



(b)

Figure A.8. One fracture energy curve of the DCB specimens prepared by the LORD epoxy tested at: (a) 0.01 mm/min (cohesive failure); (b) 100 mm/min (interfacial failure).

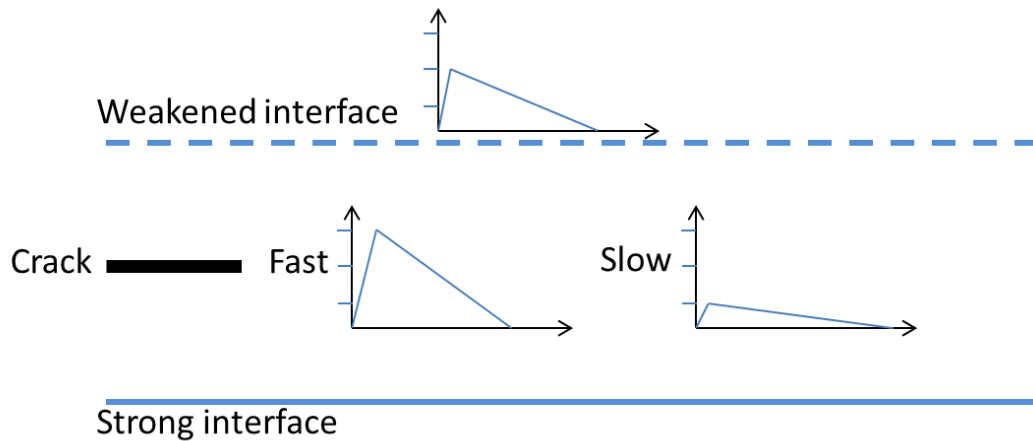


Figure A.9. Schematic of the explanation to the rate dependency of the crack path selection using the CZM for adhesive layer, and weakened interface.

### A.3 Summary

In summary, these tests showed significant rate dependence of the crack path selection. Therefore, an explanation to these phenomena is required. One explanation can be found by applying the CZM to the adhesive and the weakened interface, as shown in Figure A.9. The ultimate stress of epoxy material is considered to be high at high loading

rates but low at slow loading rates. When the loading rate is high, the maximum traction of the LORD epoxy is higher than that of the weakened interface. However, when the loading rate is slow, the maximum traction is lower than that of the weakened interface. Therefore, when the crosshead displacement rate was changed from 100 mm/min to 0.01 mm/min, the failure mode changed from interfacial failure to cohesive failure.

## Appendix B Calculation of the T-stress using contour integration in ABAQUS®

---

This section discusses the T-stress calculated in ABAQUS by contour integration in the CT (compact tension) specimen models shown in Chapter 2. The goal of this section is to keep a record of what has been done for the calculation of the T-stress using ABAQUS®, though the contour integration failed in providing consistent T-stresses at the crack tips in the models of CT specimen.

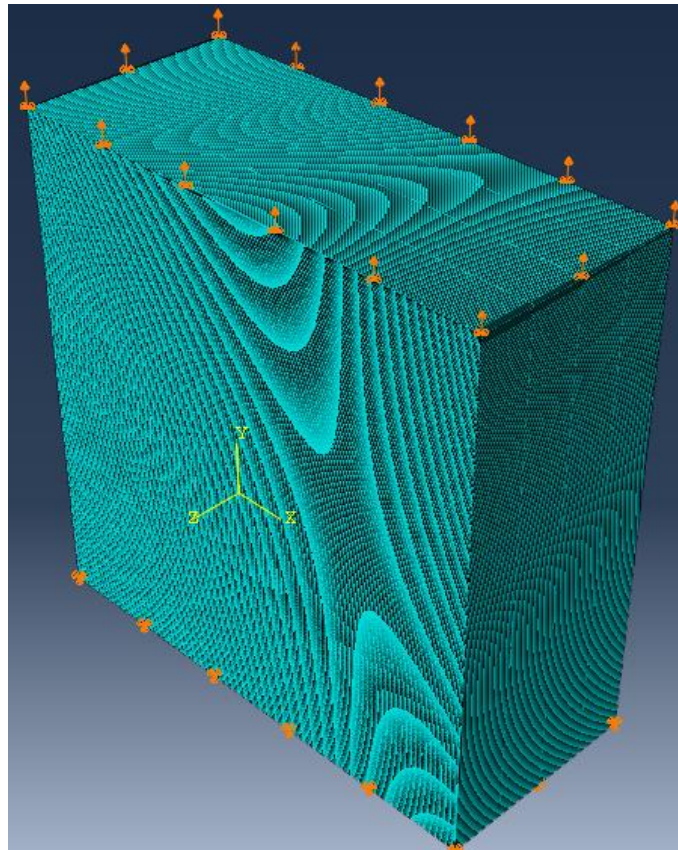
### B.1 Calculation of the T-stress in front of the crack tip in an infinite plate

Finer meshes were applied so as to obtain more accurate stress field, especially near the crack tip. For example, the contour integration for the T-stress in ABAQUS is very sensitive to the mesh size, symmetry of the model, etc. The mesh size in the 3D models for T-stress calculation is  $0.1 \times 0.1 \times 3$  mm. The ABAQUS Documentation states that, J-integral can be calculated very accurately even with relatively coarse mesh, but T-stress is usually very sensitive[1].

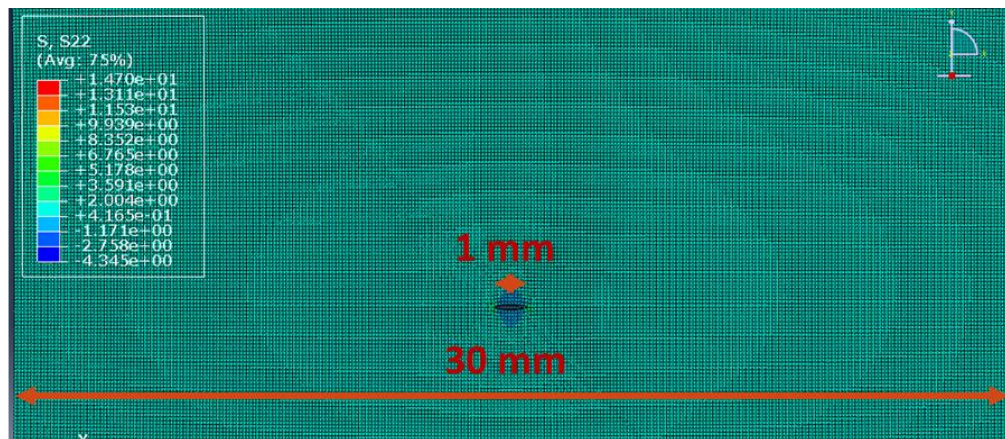
According to the ABAQUS Documentation[1], the T-stress is computed with new axes parallel and perpendicular to the most recent segment of the crack path, instead of along the global X and Y axes. The ABAQUS Documentation also states that, in general, the T-stress has larger domain dependence or contour dependence than the J-integral and the stress intensity factors. Numerical tests in SIMULIA® suggest that the estimates from the first two rings of elements abutting the crack tip or crack line generally do not provide accurate results. Sufficient contours extending from the crack tip or crack line should be chosen so that the T-stress can be determined to be independent of the number of contours, within engineering accuracy. Particularly for axisymmetric models, the closer the crack tip is to the symmetry axis, the more refined the mesh in the domain should be to achieve path independence of the contour integral[1]. Since most of the models in this chapter are asymmetric, the values of the T-stress need some verifications.

A model simulating crack in infinite plate was developed so as to verify the values of the T-stress obtained from ABAQUS. This model in ABAQUS is actually not infinite, but consists of a PMMA block ( $30 \times 30 \times 12.7$  mm), and a 1 mm crack located in the middle of the block. The block is fixed on the bottom and loaded on the top with 0.01 mm displacement upwards. Since the Young's modulus of the PMMA is 3 GPa, and the strain is  $0.01/30 = 0.000333$ , the average stress applied to the block is 1 MPa. The stress applied to the crack plane is  $1 \text{ MPa} \times 30 / (30 - 1) = 1.03 \text{ MPa}$ . So this model is considered to be close to "infinite plate" Using the equation (2.2) for the T-stress parallel to the crack

tip, T-stress = -1.03 MPa is the analytical solution (for infinite sheet). The mesh size in the 3D models for T-stress calculation is  $0.1 \times 0.1$  mm, as shown in Figure B.1.



(a)



(b)

Figure B.1. The symmetrically loaded block with a symmetric initial crack in the middle, (a): fixed bottom plane and the 0.01 mm displacement applied to the top plane, (b): zoom-in of the mesh ( $0.1 \times 0.1 \times 3$  mm) near the crack.

The T-stresses given by ABAQUS are shown in Figure B.2. In this 3D model, there are three nodes through the thickness (12.7 mm) direction and eight contours integrations were requested. Therefore, 24 values are plotted in Figure B.2.

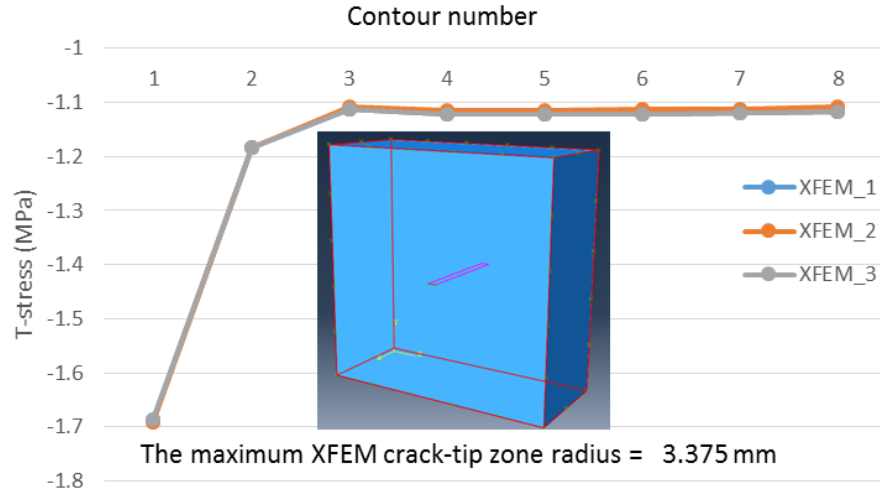


Figure B.2. The T-stress calculated by contour integration in ABAQUS for the symmetric model shown in Figure B.1.

For further verification, the symmetric initial crack was moved up to 2/3 of the height of the PMMA block, and the T-stresses were calculated again with the same boundary conditions and the same mesh size. The new T-stresses are shown in Figure B.3. It is worth noting that the location of the initial crack in the y-axis is as same as those in the asymmetric CT specimens.

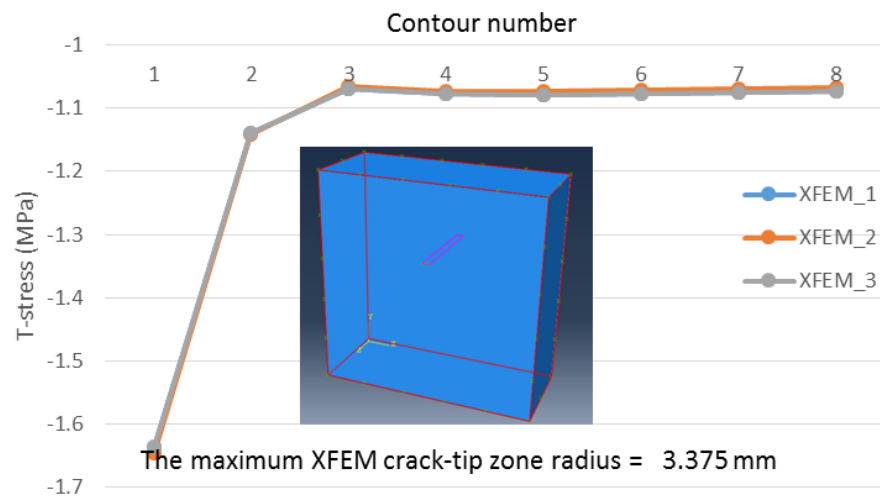


Figure B.3. The T-stress calculated by contour integration in ABAQUS for the symmetric model but with the initial crack moved up to 2/3 of the height.

The T-stress calculated by contour integration in ABAQUS approximates but is not exactly equal to the analytical solution (-1.03 MPa), but instead is about 6.8% larger. Possible reasons for this discrepancy are because the model is not really infinite comparing with the length of the crack in the center, or because the constant displacement applied on the boundary introduces some inconsistent stress distribution.

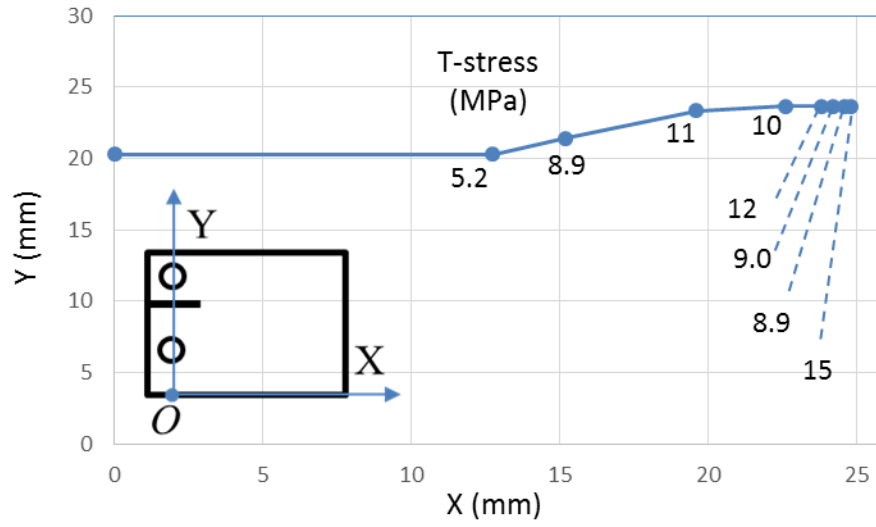
Since the two cases with symmetric PMMA blocks resulted in the converged values of the T-stress when using the mesh size of  $0.1 \times 0.1 \times 3$  mm, this mesh size is applied to the other models of asymmetric CT specimens. Though these convergences in Figure B.2 and B.3 can not guarantee the convergence in the other models, these works still demonstrated that a mesh size of  $0.1 \times 0.1 \times 3$  mm, and the location of the horizontal initial crack should not be the reasons to the convergence of the T-stress. Since the algorithm in ABAQUS is unknown, and limited analytical solution to the T-stress is reported, the verification is suspended until other example is found.

## **B.2 Calculation of the T-stress in front of the crack tip in the asymmetric CT specimens**

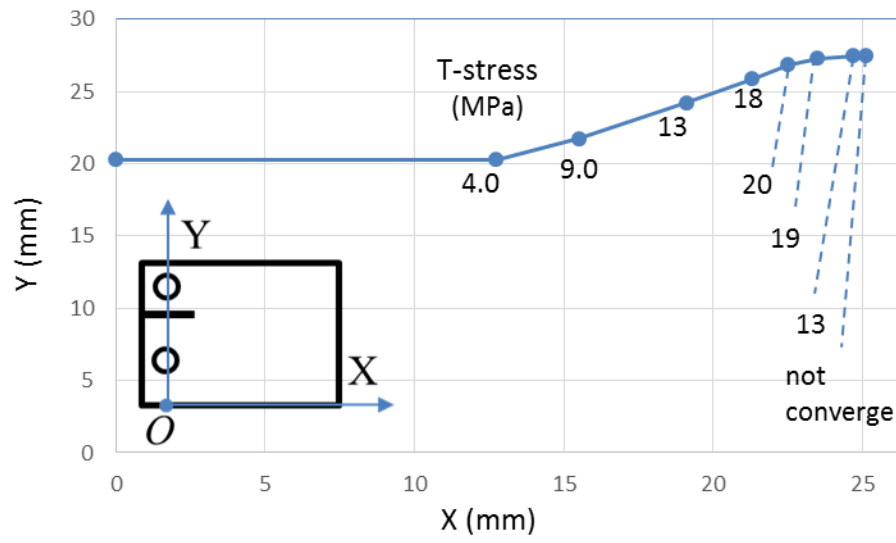
In order to explain the directional stability of the cracks, the values of the T-stress parallel to the crack front were calculated. Indeed, as stated previously, positive T-stress values indicate unstable cracks. Eight points were selected, corresponding to the eight crack tips when the crosshead displacements ranged from 0.25 mm to 2 mm with the increment of 0.25 mm between them. Attached to the crack tips, the T-stresses were shown together in Figure B.4. Note that this doesn't mean that the crack propagated in straight lines between these eight points, there are actually lots of sub-steps in these processes. These actual crack trajectories obtained from ABAQUS are the same as shown in Figure 2.12.

As described in the ABAQUS documentation, the T-stress is calculated by contour integration near the stationary crack tip in 3D model when using X-FEM with traction-separation law. Therefore, corresponding to the previous simulation in the 2D models, some 3D models were created using the crack paths obtained from the 2D models. In these 3D models, the cracks are not allowed to propagate and only used to calculate the T-stress. The values of the T-stress in Figure B.4 were obtained by applying contour integration with different radius loops so as to find the converged value.

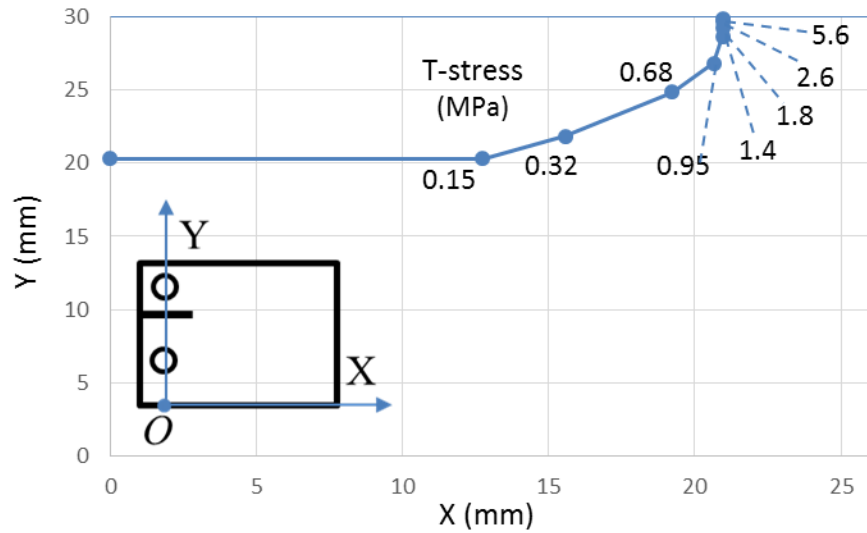
In Figure B.4c, obviously, all the values of the T-stress are positive and mostly increase monotonically. Therefore, the crack propagation is unstable and the crack veers to the upper edge. Similarly, in Figure B.4a and b, most of the values of the T-stress are positive. Though the T-stresses are not increasing or decreasing monotonically, these positive signs indicated that the crack would be unstable and change its direction when propagating in each of these sub-steps.



(a)



(b)



(c)

Figure B.4. T-stress obtained from ABAQUS during the crack propagations when W is: (a) 25.7 mm, (b) 26.2 mm, (c) 26.4 mm.

The meshes were refined further for all these models shown previously. The minimum mesh size in x, and y direction is 0.05mm, and 0.015mm, respectively. Since the initial crack length is 12.7mm, these lengths are 0.4%, and 0.1% of the initial crack length. The same result was obtained in the infinite plate model, and similar results (with inconsistent values of the T-stress) were obtained in the asymmetric CT specimen models.

It is worth noting that, the value of the T-stress is not directly related to the crack propagation angle. According to the ABAQUS documentation, the crack propagates normal to the direction of the maximum tangential stress. Therefore, regarding to the accurate prediction of the critical specimen length, and the agreements of the crack paths, the simulation in this section showed that the CZM works quite well for the crack path selection in generic monolithic materials.

## **B.3 References**

- [1] ABAQUS 6.11 Documentation Section 11.4.2 [Online].

# Appendix C The simulation of 2D bridging problem in ABAQUS using cohesive elements

---

This section shows the crack propagation sequences studied in Chapter 3 concerning the 2D bridging problem, but using a simulation in ABAQUS® with cohesive elements instead of the analytical solution in Mathematica®. Comparisons of the numerical results herein and the one in Chapter 3 show good agreement, which indicates that the analysis in Chapter 3 is reasonable.

## C.1 Modelling of the 2D bridging problem in ABAQUS®

In order to verify the predictions of the propagation process in the 2D bridging problems in Chapter 3 by other methods, ABAQUS® was employed again. In this simulation, besides the application of commonly used 4-node-plane-stress elements (CPS4), cohesive elements (COH2D) were also used to apply the cohesive zone model (CZM) to the fracture simulation of the interfaces. In this numerical model, interfacial damage initiation and evolution laws were introduced.

Since the cohesive elements are used to simulate the thin interfaces, the thickness is considered to be very small. Details about the thickness definition of interface in ABAQUS® can be found in Chapter 6. When the external load is increased, the stress of the cohesive element increases and then decreases after reaching the peak stress. The strain keeps increasing until the strain energy release rate (SERR) or the displacement in the thickness direction of the cohesive element reaches the fracture energy. Damage is aggregating in this process. In ABAQUS®, there is an output field variable called SDEG (scalar stiffness degradation variable) that shows the degree of damage in the cohesive element. There's no damage when  $SDEG = 0$ , and the element fails when  $SDEG = 1$ . The stiffness of all the elements with  $SDEG=1$  will be set to be 0 by ABAQUS, so as to effectively “remove” the elements.

In general, the model developed in this section (both geometry and the boundary conditions) is similar to the one used in Chapter 6 for crack path selection in pure mode I. The sketch of the geometry for the simulation conducted in ABAQUS is shown in Figure C.1, which assumes the DCB specimen configuration recommended in ASTM D3433-99(2012) with nominal dimensions of  $300 \times 25.4 \times 12.7$  mm for each adherend. The dimension of the adhesive layer is  $300 \times 25.4 \times 0.25$  mm, i.e. the thickness of adhesive is 0.25 mm. Representative material properties were chosen as follows: Young's modulus  $E = 70GPa$ , and Poisson's ratio  $\nu = 0.33$  for aluminum;  $E = 3GPa$ , and  $\nu = 0.35$  for the adhesive. Consistent with the fracture energy used in Chapter 3, the fracture energy for the interfacial failure is  $300 J/m^2$ . The maximum traction is assumed to be 8 MPa, which is considered to be reasonable for relatively weak interfaces[1]. A mode independent failure criterion is chosen, as shown in equation C.1. Discussions about CZM, softening laws, and the parameters can be found in Chapter 2 and Chapter 6. Mesh connectivity is shown in Figure C.1 as well.

$$\frac{G_I + G_{II}}{G_c} = 1 \quad (C.1)$$

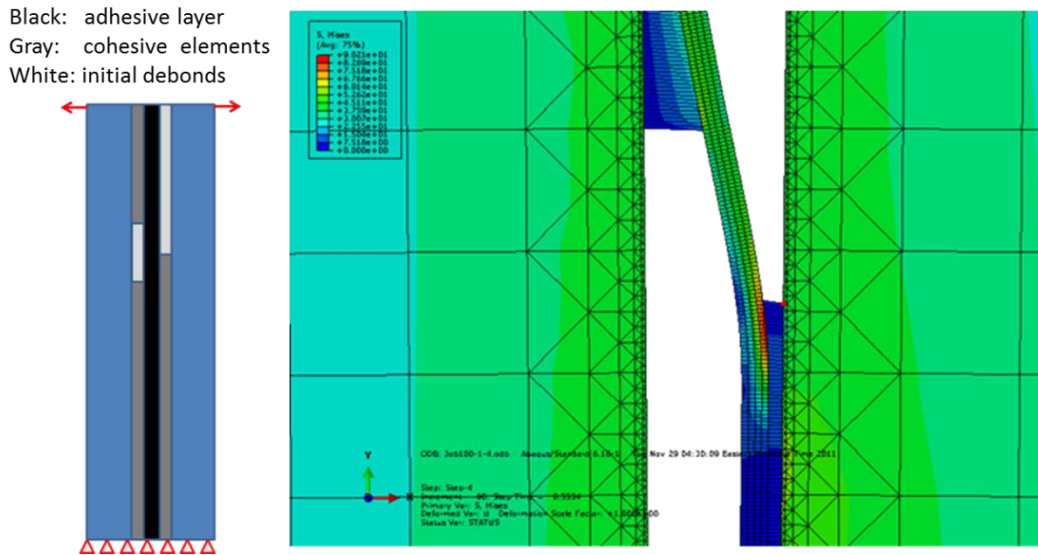


Figure C.1. Geometry, boundary conditions, and mesh connectivity of the 2D bridging model in ABAQUS®.

With the same crack lengths used in the results from the analytical solution in Chapter 3, the ABAQUS® gave similar answers for the propagation processes. With the crack length  $a_1$  fixed, curves of  $a_2$  vs.  $a_3$  are very close to those obtained from the analytical solution in Chapter 3, though ABAQUS encountered convergence problem with the crack 3 is long<sup>4</sup>.

<sup>4</sup> As shown in Figure C.2, both crack 2 and crack 3 propagate. Crack 3 is the longest one when comparing with crack 2 and crack 1 (Definition of crack 1, crack 2, and crack 3 are shown in Chapter 3). Since the propagation of crack 2 is usually much shorter than that of crack 3, the most significant phenomena in the simulation is that, when crack 3 propagates for certain long distance, ABAQUS® encounters the convergence problem, and none of the cracks would propagate.

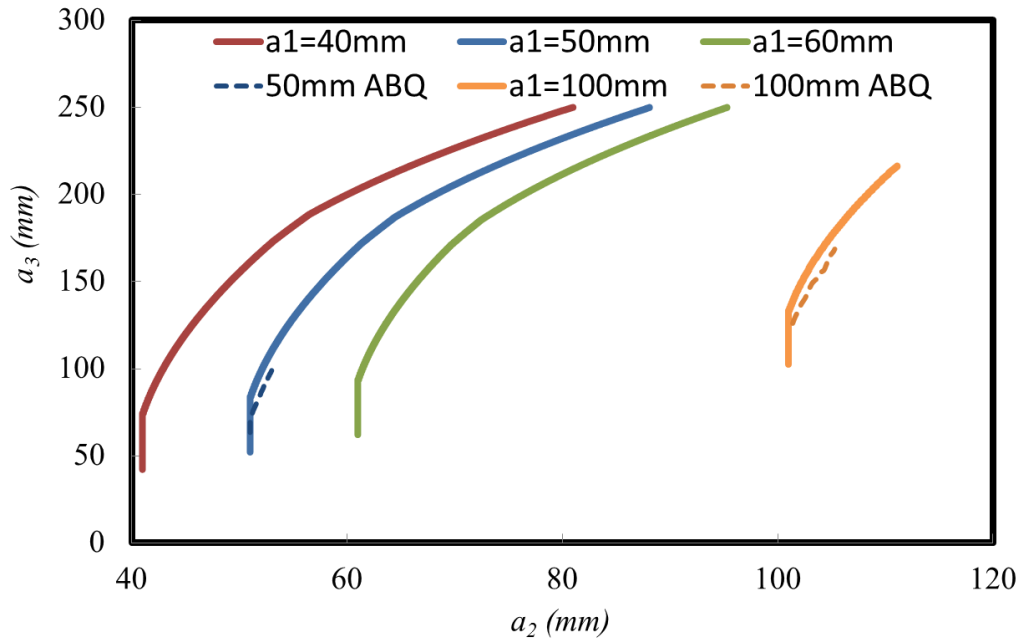


Figure C.2. When the initial  $a_1$  values are assumed, the relationship between the crack lengths  $a_3$  and  $a_2$  is fixed during the propagation process. Solid lines are the solution using the numerical integration in Chapter 3; dashed lines are the relationship simulated by ABAQUS using cohesive elements.

Two initial debonding values of  $a_1$  were tried, several attempts (with modifications in mesh sizes, element types, boundary conditions, etc.) have been conducted, but neither of them can overcome the difficulty in convergence when  $a_3$  is long. The minimum increment in these analysis were  $1e-9$ , (and  $1e-12$  was also tried). Because of these unsuccessful trials, the other values of  $a_1$  were not tried. The reason for the convergence issue in ABAQUS is unknown. The messages shown in ABAQUS® include:

- (1) THE SOLUTION FAILS TO CONVERGE IN THE MAXIMUM NUMBER OF EQUILIBRIUM ITERATIONS ALLOWED.
- (2) ERROR: TIME INCREMENT REQUIRED IS LESS THAN THE MINIMUM SPECIFIED.

In summary, simulations in ABAQUS® using cohesive elements were also employed to predict the debonding process in the 2D bridging problem. The results are very close to those calculated in Chapter 3 (with only a few millimeters difference, as shown in Figure C.2). The good agreement indicates that the calculation in Chapter 3 is reasonable, and the accuracy is verified by commonly used commercial software.

## C.2 References

- [1] A. Turon, P. P. Camanho, J. Costa, and J. Renart, "Accurate simulation of delamination growth under mixed-mode loading using cohesive elements: Definition of interlaminar strengths and elastic stiffness," *Composite Structures*, vol. 92, pp. 1857-1864, 2010.